UNIVERSITY OF SOUTHAMPTON

FACULTY OF ENGINEERING & THE ENVIRONMENT

INSTITUTE OF SOUND AND VIBRATION RESEARCH

Application and Assessment of Time-Domain DGM for Intake Acoustics Using 3D Linearized Euler Equations

by

Zbigniew Rarata

Thesis for the degree of Doctor of Philosophy

August 2014

UNIVERSITY OF SOUTHAMPTON

ABSTRACT

FACULTY OF ENGINEERING AND THE ENVIRONMENT

Institute of Sound and Vibration Research

Computational Aeroacoustics

Thesis for the degree of Doctor of Philosophy

Application and Assessment of Time-Domain DGM for Intake Acoustics Using 3D Linearized Euler Equations

Zbigniew Rarata

Fan noise is one of the major sources of aircraft noise. This can be modelled by means of frequency and time domain CAA methods. Frequency domain methods based on the convected Helmholtz equation are widely used for noise propagation and radiation from turbofan intakes. However, these methods are unsuited to deal easily with turbofan exhaust noise and presently unable to solve large 3D (three-dimensional) problems at high frequencies. In this thesis the application of time-domain Discontinuous Galerkin Methods (DGM) for solving linearized Euler equations is investigated. The research is focused on large 3D problems with arbitrary mean flows. A commercially available DGM code, Actran DGM, is used.

An automatic procedure has been developed to perform the DGM simulations for axisymmetric and 3D intake problems by providing simple control of all the parameters (flow, geometry, liners). Moreover, a new method for integrating source predictions obtained from CFD calculations for the fan stage of a turbofan engine with the DGM code to predict tonal noise radiation in the far field has been proposed, implemented and validated.

The DGM is validated and benchmarked for intake and exhaust problems against analytical solutions and other numerical methods. The principal properties of the DGM are assessed, best practice is defined, and important issues which relate to the accuracy and stability of the liner model are identified. The accuracy and efficiency of the CFD/CAA coupling are investigated and results obtained are compared to rig test data.

The influence of the 3D intake shapes and the mean flow distortion on the sound field is investigated for static rig and flight conditions by using the DGM approach. Moreover, it is shown that the mean flow distortion can have a significant effect on the sound attenuation by a liner.

Contents

List of tables

List of figures

DECLARATION OF AUTHORSHIP

I, Zbigniew Rarata, declare that the thesis entitled
Application and Assessment of Time-Domain DGM for Intake Acoustics Using 3D Linearized Euler Equations
and the work presented in the thesis are both my own, and have been generated by me as the result of my own original research. I confirm that:

- this work was done wholly or mainly while in candidature for a research degree at this University;
- where any part of this thesis has previously been submitted for a degree or any other qualification at this University or any other institution, this has been clearly stated;
- where I have consulted the published work of others, this is always clearly attributed;
- where I have quoted from the work of others, the source is always given. With the exception of such quotations, this thesis is entirely my own work;
- I have acknowledged all main sources of help;
- where the thesis is based on work done by myself jointly with others, I have made clear exactly what was done by others and what I have contributed myself;
- parts of this work have been published as:

Z. Rarata, R. J. Astley, G. Gabard, R. Sugimoto "Validation of a Discontinuous Galerkin Method for turbofan nacelle acoustics", 15th CEAS-ASC Workshop, 13-14 October, 2011, Lausanne, Switzerland.

Z. Rarata, G. Gabard, R. Sugimoto, J. Coupland, R.J. Astley, H. Namgoong, P.J.G. Schwaller "Integrating CFD source predictions with time-domain CAA for intake fan noise prediction", AIAA 2014-2456, 20th AIAA/CEAS Aeroacoustics Conference, 16-20 June 2014, Atlanta, USA.

Signed: ……..

Date:……

Acknowledgements

I gratefully acknowledge the financial support by Rolls-Royce plc at the Rolls-Royce University Technology Centre in Gas Turbine Noise at the Institute of Sound and Vibration Research, University of Southampton and by the UK Government Technology Strategy Board through the SILOET (Strategic Investment in Low-carbon Engine Technology) programme. The research was also supported by European Commission through FP7 Marie-Curie IAPP Programme PARNAS during my secondment at Free Field Technologies SA, Belgium.

I wish to thank my academic supervisors, Prof Jeremy Astley, Dr Gwenael Gabard and Dr Rie Sugimoto, for their professional support and guidance of the PhD research. It is greatly appreciated experience on both the professional and personal level. I would also like to thank my industrial supervisors Dr John Coupland and Dr Howoong Namgoong for many fruitful discussions in our research meetings.

I also wish to thank Prof Jean-Louis Migeot and Prof Jean-Pierre Coyette for giving the opportunity to participate in some research activities undertaken in the development of Actran DGM and Dr Gregory Lielens for useful discussions.

During this research many meetings and personal discussions took place, therefore I would like to greatly appreciate the invaluable contributions to the project by Dr Peter Schwaller, Dr Christoph Richter and Dr Yves Detandt.

Last but not least, I would like to express my deepest gratitude to my family, particularly my wife and son, parents and sister for their patience and support during this project.

Zbigniew Rarata, August 2014

Definitions and Abbreviations

Symbols

(x, y, z)	Cartesian coordinate system
(r, θ, z)	cylindrical coordinate system
(ξ, η, ζ)	local Cartesian coordinate system
(r'', θ'', z'')	rotating cylindrical coordinate system
$A_{m\mu}$, $B_{m\mu}$	modal wave amplitude
α	order of the damping increase in the buffer zone
b, R_0	inner and outer radii of a straight duct
b	basis function (DGM)
B	basis function (NURBS)
$\mathbf{B}_{edge}$	edge matrix for semi discrete linearized Euler equations
β	cavity reactance (liner model)
c	speed of sound
c_p	specific heat capacity at constant pressure
c_v	specific heat capacity at constant volume
$\boldsymbol{C}$	parameterized curve
γ	ratio of specific heats, $\gamma = c_p/c_v$
d	the space dimension
δ	the Dirac delta function
δ_{bl}	boundary layer thicknesses
Δ	finite element in the local coordinate system
$\partial\Delta$	finite element edge in the local coordinate system
e	internal energy per unit mass
E	energy
ε	damping in the fluid cavity (liner model)
ϵ	steady flow distortion parameter
$\mathbf{f}$	fluxes for Euler equations
f	frequency
f_c	cut-on frequency
$\boldsymbol{F}$	fluxes for linearized Euler equations
$\boldsymbol{F}^R$	Riemann flux for linearized Euler equations
$\boldsymbol{G}$	vector contains terms associated with the mean flow gradients
h	element size

H	cavity depth (liner model)
θ_{mode}	axial propagation angle (mode angle), for the case of uniform mean flow it is defined as $\sin\theta_{mode} = \mp\frac{k_r}{k_0}\sqrt{1-M^2}$
i	imaginary unit, $i^2 = -1$
$\boldsymbol{I}$	intensity vector
$\mathrm{J}_m, \mathrm{Y}_m$	Bessel functions of the first and second kinds of the order m
k	free field wave number, $k = \frac{\omega}{c}$
k_z	axial wavenumber
k_r	radial wavenumber
$\mathbf{K}$	stiffness tensor for semi discrete linearized Euler equations
κ	fixed constant describing accuracy within an element
l	the Lagrange polynomial
$\boldsymbol{L}$	position vector in volume coordinates
L_b	length of the buffer zone
L_c	unknown coefficients in the CFD-CAA matching
λ	wavelength
m	azimuthal mode order
m	mass reactance (liner model)
M	Mach number, $M = u/c$
$\mathbf{M}$	mass matrix for semi discrete linearized Euler equations
μ	radial mode order
$\boldsymbol{n}$	wall normal vector
p	element order or polynomial degree
p	pressure
$\boldsymbol{P}, w$	NURBS control points and its weight, respectively
$P_{m\mu}$	radial eigenfunction
$\boldsymbol{q}$	solution vector for linearized Euler equations
$\boldsymbol{q}_f$	solution vector for Euler equations
$\boldsymbol{Q}$	discrete points defining geometry
R	face resistance (liner model)
R_{fan}	fan duct outer radius
R_g	ideal gas constant
ρ	density
$\boldsymbol{S}$	parameterized surface
σ	damping function

t	time
T	time period
T	temperature
T_f	transmission factor
$\boldsymbol{u}$	velocity vector
u_g, v_g	non-dimensional parameters defining NURBS geometry
$\boldsymbol{U}, \boldsymbol{V}$	NURBS knot vectors
ϕ	velocity potential
w	arbitrary smooth test function
y^+	a non-dimensional distance of the first grid point off the wall
Z	complex impedance
z	inverse Fourier-transform of Z
ω	angular frequency
Ω	shaft speed
Ω	finite element in the global coordinate system
$\partial\Omega$	finite element edge in the global coordinate system

Operators

$\frac{d_0}{dt}$	material derivative
Im	imaginary part of a complex number
J	Jacobian
Re	real part of a complex number

Superscripts

$'$	unsteady perturbations
$''$	value related to the rotating coordinate system
$*$	complex conjugate
$\bar{}$	time-averaged value
$\sim$	complex amplitude
ω	source angular frequency

Subscripts

0	steady mean flow/average flow state
∞	infinite number

CAA	obtained from the CAA simulations
CFD	obtained from the CFD simulations
m	azimuthal component
m, μ	azimuthal and radial mode order of a modal source
n	normal component

Abbreviations

ACARE	Advisory Council for Aeronautics Research in Europe
APE	Acoustic Perturbations Equations
ASCII	American Standard Code for Information Interchange
BC	Boundary Condition
BEM	Boundary Elements Method
BPF	Blade Passing Frequency
CAA	Computational AeroAcoustics
CAD	Computer Aided Designing
CAE	Computer Aided Engineering
CFD	Computational Fluid Dynamics
CFL	Courant Friedrichs Lewy
CPU	Central Processing Unit
DES	Detached Eddy Simulation
DGM	Discontinuous Galerkin Method
DRP	Dispersion Relation Preserving
EPNL	Effective Perceived Noise Level
EO	Engine order
ESS	Engine Section Stators
FE	Finite Element
FEM	Finite Element Method
FAA	American Federal Aviation Administration
FFT	Free Field Technologies
FDM	Finite Difference Methods
FWH	Ffowcs-Williams and Hawkings
FVM	Finite Volume Methods
GPU	Graphics Processing Units
GUI	Graphical User Interface
ICAO	International Civil Aviation Organization

IE	Infinite Element
IEM	Infinite Element Method
ISVR	Institute of Sound and Vibration Research
LEE	Linearized Euler Equations
LES	Large Eddy Simulation
MPT	Multiple Pure Tones
NASA	National Aeronautics and Space Administration
NDOF	Number of degrees of freedom
NRBC	Non-Reflecting Boundary Conditions
NURBS	Non-uniform rational B-spline
OGV	Outlet Guide Vanes
OPENAIR	EC 7th Framework Programme "Optimisation for low environmental noise impact aircraft"
PDE	Partially Differential Equations
PML	Perfectly Matched Layer
RAM	Random Access Memory
RANS	Reynolds Averaged Navier-Stokes
RK-DGM	Runge-Kutta Discontinuous Galerkin Method
SILENCE(R)	EC 5th Framework Programme "Significantly lower community exposure to aircraft noise"
SPL	Sound Pressure Level
SRA	Strategic Research Agenda
1D	1 Dimensional
2D	2 Dimensional
3D	3 Dimensional

1. Introduction

1.1 The problem of noise in Aviation

The widespread use of jet engines for civil aviation in the 1960s caused a noise problem in the vicinity of airports. The International Civil Aviation Organisation (ICAO) deals with international noise regulations in civil aviation. In the US, compliance with the regulations of American Federal Aviation Administration (FAA) is obligatory. These are closely aligned with those of the ICAO. In 1971 the first recommendations for noise emissions were published by the FAA. Similar regulations were also published by the ICAO as the ICAO Annex 16, chapter 2. Since then it has evolved through a chapter 3 [1], and the ICAO Annex 16, chapter 4 is currently mandatory. These rules apply only to new aircraft, designed after January of 2006. Therefore, chapter 3 is still valid for older aircraft.

The standards are based on three measurement points: Flyover, Lateral and Approach to landing as illustrated in figure 1.1. At each of these points the Effective Perceived Noise Level (EPNL) is measured for which the unit of measure is EPNdB [2]. Figure 1.2 shows the maximum permitted noise levels prescribed in chapter 3 of the ICAO Annex 16 at the three certification reference points [1] [3] [4]. In chapter 4 the total reduction at three measuring points in relation to the maximum noise levels specified in chapter 3 must be at least 10 EPNdB. In addition, the noise at each point cannot exceed the levels prescribed in chapter 3, and the sum of any two differences must be lower by at least 2 EPNdB [1] [3] [4].

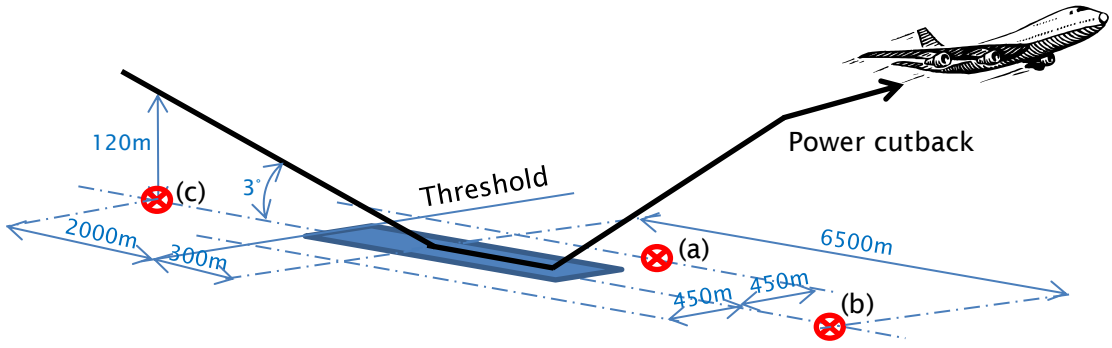

Figure 1.1: Reference noise measurement points in certification process: (a) lateral full-power reference, (b) flyover reference, (c) approach reference.

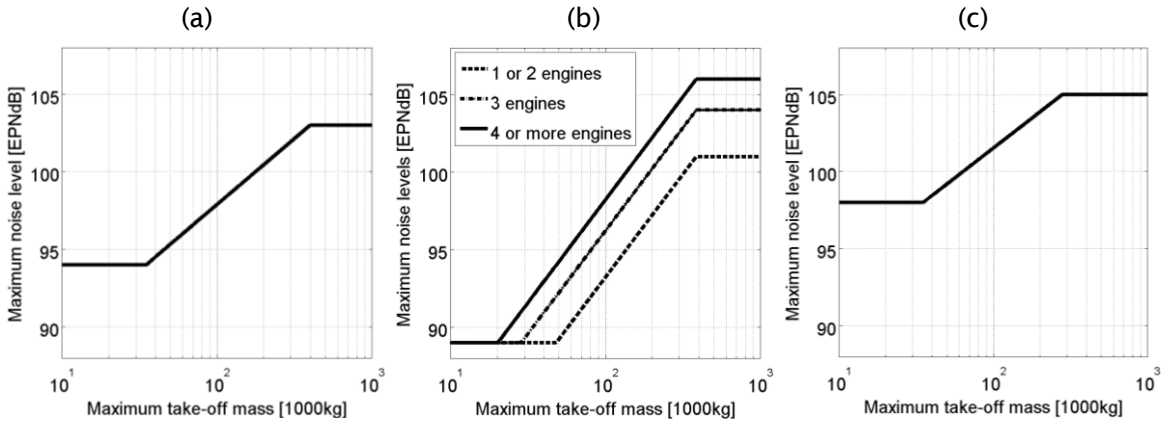

Figure 1.2: Maximum noise levels from chapter 3 of the ICAO Annex 16 at reference noise measurement points: (a) lateral full-power reference, (b) flyover reference, (c) approach reference.

Noise regulations, airport constraints and public pressure have forced airframe and engine manufacturers to reduce aircraft noise significantly over the last forty years. In 2001, the Advisory Council for Aeronautics Research in Europe (ACARE) proposed a Strategic Research Agenda (SRA) to better address the society's needs and improve the European Aeronautics competitive position in global markets [5]. In the area of the environment, ACARE aims to encourage manufacturers to reduce air pollutions and noise. The goals are: reducing CO_2 emissions by 50 percent per passenger kilometre, reducing NO_x emissions by 80 percent, and reducing perceived aircraft noise by 50 percent below a 2000 baseline by 2020. These figures are further strengthened in the vision for 2050 [6]. As an example, the noise reduction over the latest Rolls-Royce large turbofan engines as well as the ACARE goal for 2020 is shown in figure 1.3.

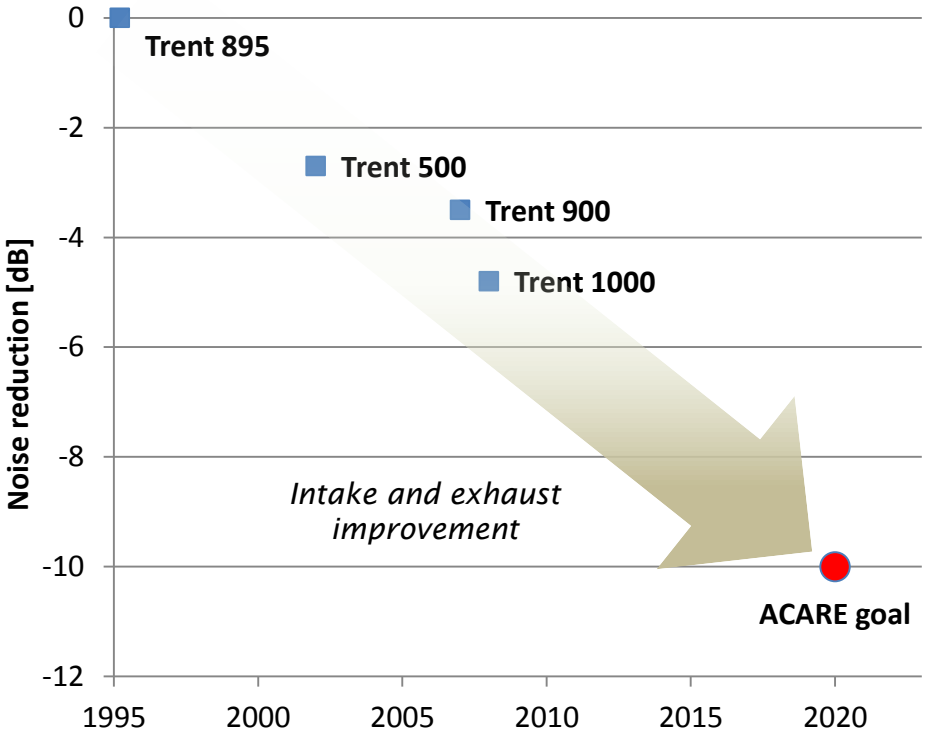

Figure 1.3: Noise reduction in dB over the latest Rolls-Royce large turbofan engines towards ACARE goal, reproduced from [7]. Corrected for aircraft weight.

1.2 Sources of noise in a turbofan engine

In the nineteen sixties the aircraft noise was dominated by the noise from the exhaust jet (jet noise). This situation changed with the introduction of turbofan engines with bypass ducts. Since that time, a "revolution" has taken place in the reduction of aircraft noise. A comparison of noise sources of a single-stream turbo-jet engine and a turbofan engine is shown in figure 1.4. The sources are grouped into four major sources of a typical jet engine, i.e. Fan, Compressor, Turbine & Combustor, and Jet noise. The strength of each source is represented by the size of the corresponding arrow [8]. Increases in the bypass ratio enabled a significant reduction in noise by reducing the overall speed of the exhaust flow. However, this led to the increase of the fan noise contribution, especially in the rear arc.

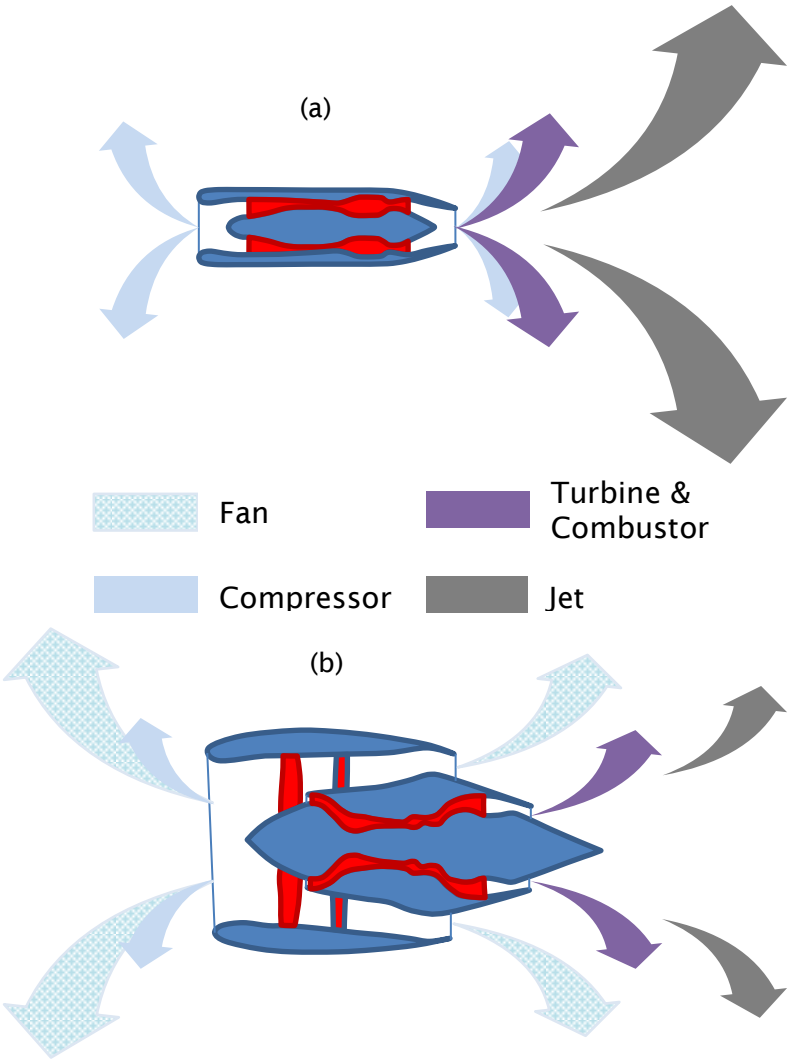

Figure 1.4: A noise pattern comparison for single stream turbojet and dual flow turbofan engines. (a) Typical 1960s single stream jet engine, (b) Modern, dual stream turbofan engine.

A noise reduction of up to 20EPNdB in each of the three flight conditions in the certification process has been achieved over the last 30 years [9]. The progress made in noise reduction over the last 50 years is shown in figure 1.5. The reference value in the figure is the current chapter 4 level. This significant achievement has been realized by a reduction of the jet velocity, lowered fan speed, improved acoustic treatment in the inlet and bypass duct, low-noise design of fan and stators as well as selection of optimal numbers of fan blades and stator vanes.

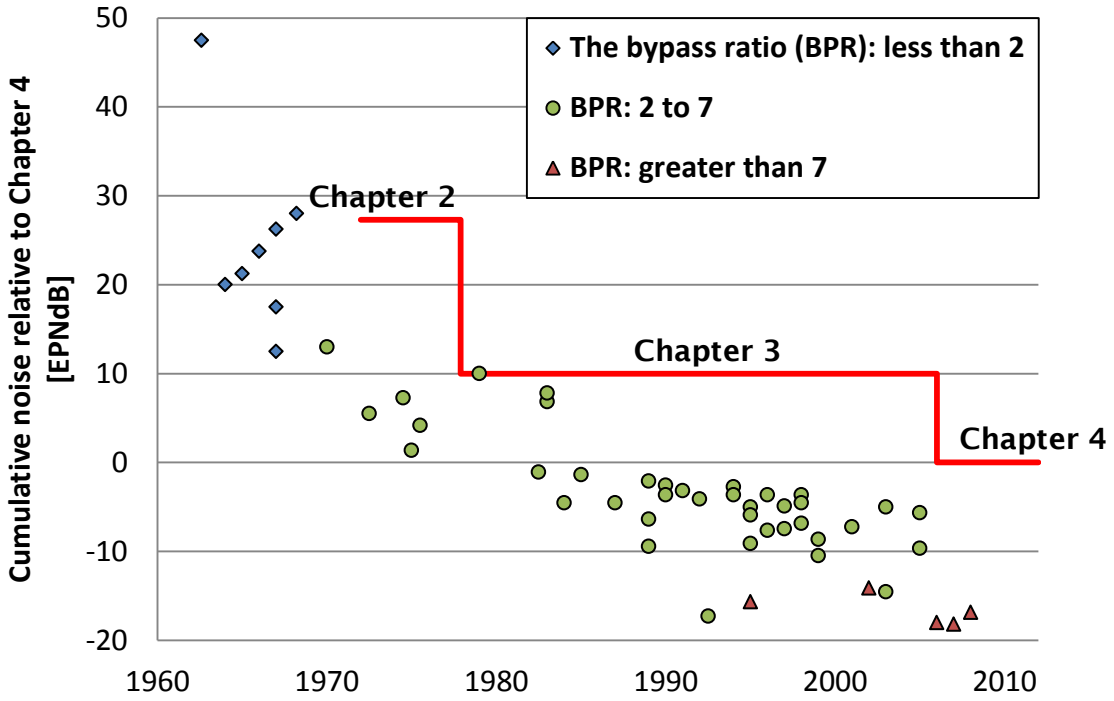

Figure 1.5: The progress made in noise reduction over the last years with respect to chapter 4 noise level, reproduced from [9]**.**

1.2.1 Fan and compressor noise

The noise from the fan and compressor contains both tonal [1] and broadband[2] components. Within tonal noise we can define the four following components:

- Rotor alone tones
- Interaction tones
- Distortion tones
- Buzz-saw noise

The rotor alone tones are modes locked to the rotation of the fan. They can only radiate strongly to a far-field observer if any point on the rotor moves with supersonic speed, e.g. supersonic tip speed. If the fan rotates with subsonic speed then they decay exponentially (evanescent modes) with distance from the source. This will be discussed in section 2.6. Further information can be found in [10] [11]. A typical far field turbofan sound power spectra at approach

[1] The tonal noise is by definition the noise with discrete frequencies
[2] The broadband noise refers to the situation where the sound energy is spread over a wide band of frequencies

(subsonic tip speed) and take-off (supersonic tip speed) are illustrated in figure 1.6. The rotor alone tones can be seen in figure 1.6 (b) at the blade passing frequency (BPF) and its harmonics.

Interaction tones occur due to the interaction between rotor and stator. This type of source was first identified by Tyler and Sofrin [12]. They derived a formula for modes scattered by stator vanes. The tones at the blade passing frequency (BPF) and its harmonics are evident above the broadband noise, as illustrated in figure 1.6 (a) [13] [10]. It is worth mentioning that some of the interaction modes can propagate even when the rotor-locked engine order tones are evanescent.

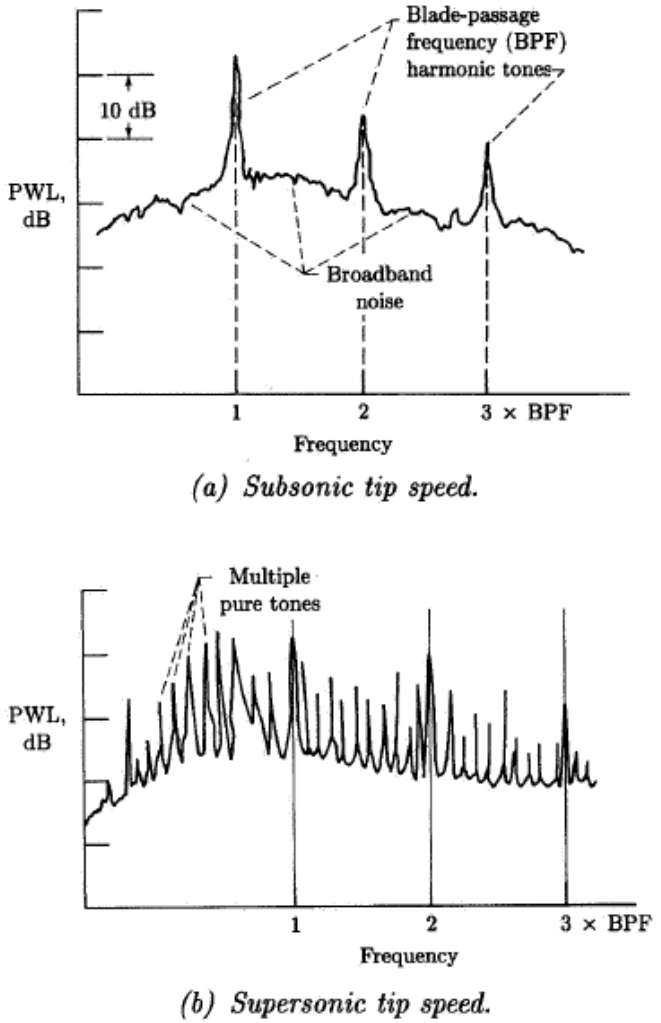

Figure 1.6: A typical turbofan sound power spectra at far field for approach (subsonic tip speed) and takeoff (supersonic tip speed) [10].

Distortion tones are generated when there are velocity non-uniformities in the inflow.

A typical spectra for buzz-saw noise [10] [13] [2], also known as Multiple Pure Tones (MPT), is illustrated in figure 1.6 (b). This type of noise is a result of supersonic fan tip speeds and blade-to-blade differences in blade stagger angle. In the case of an ideal fan where all blades are identical, the tones are generated only at the blade passing frequency and its harmonics. Real fans, however, have blades which are not identical in every respect. For example, they can differ very slightly in shape and stagger angle. The rotating pressure field is not then perfectly periodic with the blade spacing. This generates pressure components of lower azimuthal order rotating all at the shaft speed. Due to the non-linear propagation this leads to differences in the strength and shape of the shock waves. As a result, the tone amplitudes are not regular and they are distributed over all engine orders[3] (EO).

Broadband fan noise is more complex than tonal noise and is due to turbulence. It can be categorized into the following groups:

- Rotor self-noise
- Rotor interaction with inflow turbulence
- Rotor – Stator interaction
- Boundary layer interaction

The self-noise is a result of a number of mechanisms. The most important for ducted fans is trailing-edge noise. It is due to the boundary layer turbulence on the blade, which results in randomly distributed sound sources when passing the trailing edge of the blade.

The interaction of the rotor with the ingested turbulence creates broadband noise as the rotor blades cut turbulent eddies to create random pressure fluctuations [10] [13].

The rotor-stator interaction broadband noise is due to the interaction of stator vanes with the turbulent scales in the wakes shed by the rotor blades [13] [14].

[3] Engine order is an integer multiple of the shaft rotation frequency

Boundary layer interaction broadband noise is a result of the interaction of the rotor-tip with the turbulence in the casing boundary layer [13] [14] [15].

1.2.2 Turbine noise

The mechanisms of noise generations from a turbine are very similar to those of the fan or compressor. Due to the smaller spacing between the rows, tonal noise is more dominant than for fan or compressor. In the case of noise from the turbines, noise propagates only in the direction of the exhaust nozzle [2] [10]. This is a result of choked outflow from the combustor chamber.

1.2.3 Jet Noise

The schematic diagram of the structure of a single jet is presented in figure 1.7. The jet plume consists of five regions. The potential core is a region where the jet velocity is preserved approximately at the same level as that of the nozzle exit. The turbulence is created by shear layers due to instabilities induced by strong mean flow gradients. The fully developed jet is reached when self-similarity between mean flow components, turbulent fluctuations, shear stresses and kinetic energy is achieved. The jet noise can be characterised by scaling law from the Lighthill's analogy. In theory the sound power varies with the eighth power of the jet velocity [16] [17] [18] [19], but in practice more complex behaviour is observed [20].

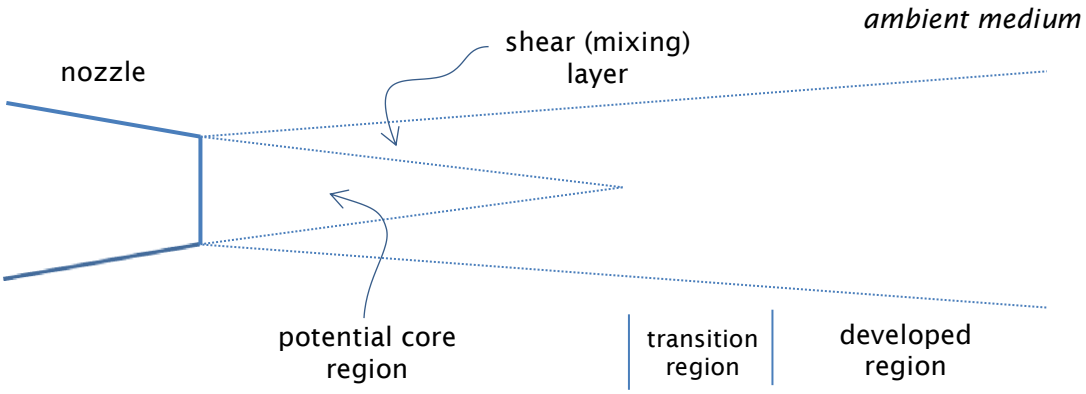

Figure 1.7: A schematic diagram of the jet.

1.2.4 Combustion Noise

Direct combustion noise is generated by unsteady heat supply at constant pressure, which results in monopole source, and the high intensity turbulent mixing of hot gases. The noise intensity is amplified by flame tube devices, which increases combustion efficiency and reduces emissions of harmful gases [21] [2].

Indirect combustion noise is generated as the hot gases pass through the turbine stages and exhaust nozzle [21] [2].

1.3 Computational AeroAcoustics (CAA)

In general, CAA has evolved from Computational Fluid Dynamics (CFD). The generation and propagation of the noise could be predicted by solving one system of the compressible Navier-Stokes Equations. This is, however, a highly challenging task mainly due to the high CPU time and memory requirements. Therefore this approach is not yet available for the industrial applications such as the nacelle acoustics, especially in cases where a three-dimensional radiation model is needed. In practice the sound generation (noise source), acoustic propagation and radiation to the far-field are achieved separately by applying different methods. A typical model used for the fan stage tonal noise generation, propagation and radiation from a turbofan engine is presented in figure 1.8.

The acoustic sources are obtained in many ways, i.e. analytical methods, experimental data, numerical calculations or hybrid approaches. The methods based on the Reynolds-averaged Navier–Stokes equations (RANS-CFD) are commonly used to predict fan stage tone sources (figure 1.8) [22] [23]. Low order models are generally used for such calculations. The prediction of the resulting rotor-locked and interaction tones presents a computational challenge for the frequencies of interest in terms of CPU time and memory requirements. RANS-CFD coupled with Lighthill's analogy is a good example of hybrid modelling for jet mixing noise [24]. Large and Detached Eddy Simulation (LES/DES) can also be used to determine noise sources [25] [26] [27]. It has been found that well-resolved LES gives accurate results. However, high-resolution computational meshes are required at relatively low Reynolds numbers.

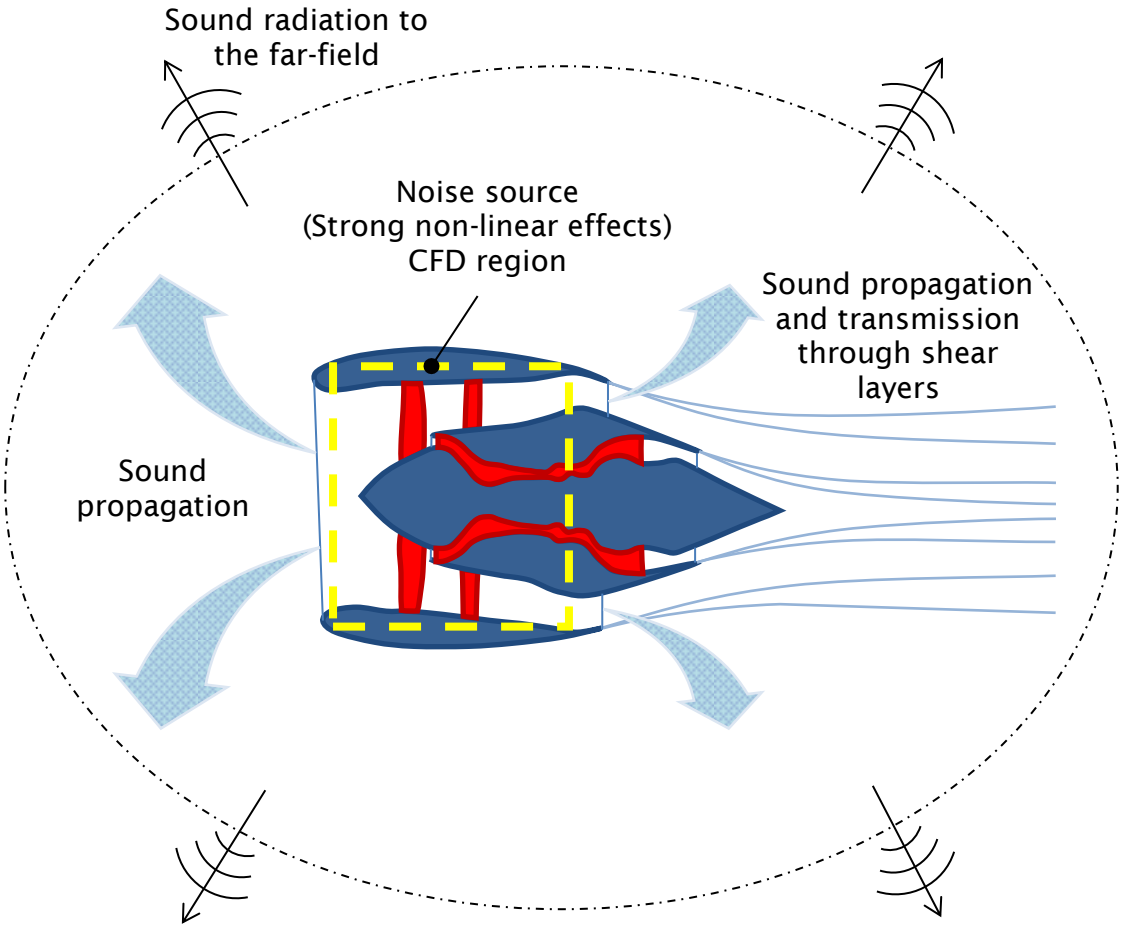

Figure 1.8: A schematic diagram of the fan stage tonal noise generation, propagation and radiation from a turbofan engine.

In order to model acoustic propagation, high accuracy numerical schemes are necessary. Low order CFD finite difference schemes are not sufficiently accurate for CAA propagation problems [28], unless very fine grids are used. This is due to high dispersion and dissipation errors (phase and amplitude) in low order methods. The errors can be controlled by applying high order or optimised numerical schemes [28] [29] [30]. This is further discussed in section 1.3.1.

In most methods, the acoustic radiation is computed separately from near field solution. It would be highly ineffective to propagate the sound to the far field using numerical methods due to high computational cost. This is not a case in some Finite/Infinite element approaches [31] where special interpolation schemes are used. In the other methods additional computations are necessary. In most cases an integral must be performed over a near field

surface. The Kirchhoff integral method [32] or the Ffowcs-Williams and Hawkings (FWH) equation [33] [34] are often used.

1.3.1 Numerical approaches for sound propagation

There are many schemes available for CAA. A review of CAA methods for turbofan applications has been given by Astley [35]. The Finite/Infinite Element approach (FEM/IEM) based on the convected Helmholtz equation in the frequency domain is one of the most widely used method for turbofan applications [31] [36] [37]. The method has proved its effectiveness for noise radiation from turbofan intakes when irrotational mean flow is assumed. Nevertheless, this approach has some significant limitations. The irrotational character of mean flow makes it difficult to apply to turbofan exhaust propagation [38] [39]. However, a modification of the method based on Möhring's formulation has recently been developed and shown to give promising results. It also requires a direct solver of which the memory usage increases very rapidly with the number of degrees of freedom (NDOF), therefore is not practically applicable for large 3D (three-dimensional) problems at high frequencies.

Methods based on the linearized Euler equations (LEE) have also been developed for CAA propagation. Rotational mean flows can be modelled by using this approach. The equations can be solved in the frequency [40] [41] or time domains [42] [43] [44]. Time domain solvers are favoured because of their ability to use explicit schemes. As a result, they consume less memory and are more suitable for multithreaded computations. This is particularly important for large applications in three dimensions.

Another categorization these methods can be made with respect to type of spatial meshes used for the discretisation, i.e. structured and unstructured. A mesh is structured if it can be mapped to a uniform Cartesian mesh by using an arbitrary mapping function.

Structured approaches include high-order finite difference schemes such as the Dispersion-Relation-Preserving (DRP) scheme developed by Tam and Webb in early 90s [28] and compact schemes such as that of Lele [45], and Ashcroft and Zhang [30]. Both methods use high-order interpolation of order 4 or greater. They can be effectively used for problems of wave propagation

based on Linearized Euler Equations (LEE), both in the frequency domain [41], and in the time domain [46]. These methods allow efficient parallelization in the time domain [47]. Moreover, they can be implemented on the Graphics Processing Units (GPU) [48].

The Discontinuous Galerkin Method (DGM) offers an alternative high-order, time-domain method for the Linearized Euler Equations (LEE) and is readily implemented on unstructured grids [44] [49] [50] [51]. This method can be regarded as a generalization of conventional low order finite volume schemes. In contrast to finite volume methods, the DG methods can use high order polynomial bases for the interpolation in space and permit unstructured grids. Unstructured grids are often preferred for real applications, like turbofan acoustics, since the process of grid creation is fast and easily automated. This is a significant advantage over the structured methods, which require high quality problem dependent multi-blocks grids or overlapping grids. Moreover, the DGM, due to its discontinuity property, is well suited for parallel computing on the CPUs [44] [51] [52], and on the GPUs [53] [54] [55].

1.3.2 The discontinuous Galerkin method

The Discontinuous Galerkin Method (DGM) is a variant of the continuous Galerkin Method (GM) developed at the beginning of 20th century. The discontinuous Galerkin method was first proposed by Reed and Hill in 1973 to solve the neutron transport equation [56].

The DGM has three properties which make it particularly attractive for applications such as the nacelle acoustics. These are: a capacity to deal with complex geometries, an ability to use explicit schemes, and high accuracy and hp-adaptivity[4]. On the other hand, most of the well-known numerical schemes for solving Partially Differential Equations (PDE) are not, in practice, capable of providing these features simultaneously. The Finite Difference Method (FDM) requires structured meshes which cannot be applied so directly to complex geometries. Mapped and overlapping meshes are generally needed, which must be designed for a specific geometry. The Finite Volume Method (FVM) is a low order method with poor dispersion and dissipation characteristics. This

[4] The hp-adaptivity is an approach allowing finite elements with variable size and polynomial orders to optimise the overall accuracy and performance of the numerical scheme [183].

can be partly compensated by using very fine meshes but this increases problem size. The finite element methods are based mainly on implicit schemes and, therefore, are not well suited for time-dependent problems.

A fundamental property of the DGM is the discontinuity of the trial solution at element boundaries. Information is exchanged between elements by means of numerical fluxes. Different polynomial orders can be used in adjacent elements. This allows the use of different element orders in a single grid, which can be non-conformal. It gives many advantages: DGM is fully stabilized by fluxes, and the boundary conditions are satisfied only by fluxes [57]. Therefore, the method is well suited for parallelization [52].

The DG method has been extensively applied to the solution of hyperbolic equations since the 1990s. Cockburn, Shu et al. [58] [59] [60] [61] implemented an explicit Runge-Kutta discontinuous Galerkin method (RK DGM) for solving compressible Euler equations. A comprehensive review on RK DGM and limiters is given by Cockburn and Shu [62]. In order to reduce RAM consumption and computational cost a quadrature-free formulation was proposed by Atkins and Shu [63].

The DG method gives good accuracy, due to its low dispersion and low dissipation when high polynomial orders are used which are crucial for wave propagation problems. This was first studied by Hu et al. [64]. They showed that the dispersion relation and dissipative rate depend highly on flux type, i.e. upwind flux or centred flux. The DGM was also found to be easily implemented on unstructured grids. This work was continued by Hu and Atkins [65] [66]. They formulated an eigenvalue problem of wave propagation based on Linearized Euler Equations (LEE). They found an exponential convergence for propagating physical waves and showed analytically that the numerical dispersion relation is locally accurate to order $2p+2$, where p is maximum element order. This was also confirmed by Ainsworth [67]. Additionally an approximation was proposed, for choosing discretization parameters to obtain the exponential convergence of dispersion and dissipation parameters at assumed accuracy. The method can be implemented on unstructured, conformal or non-conformal tetrahedral grids. The high accuracy is maintained [49]. Moreover, the hp adaptivity can be easily implemented [68]. The

quadrature free formulation is commonly used for wave propagation problems. This is mainly due to low/moderate RAM and computational cost requirements.

Chevaugeon et al. [44] demonstrated that the DG method can be an efficient approach for turbofan nacelle acoustics. Leneveu, Schiltz et al. [69, 52, 70] also reported that it is an accurate and efficient approach for exhaust noise radiation simulations with strong shear layers. In theory the time domain DG method is an ideal method for the broadband noise simulations over a wide range of frequencies. Manera et al. [38], however, found that the classical finite/infinite element approach can be still more efficient for axisymmetric realistic applications. An interesting study of broadband slat noise modelling was performed by Bauer et al. [50]. They applied the DG method for solving the APE (Acoustic Perturbations Equations). More recently Rinaldi et al. [51] solved both APE and LEE in uniform and non-uniform flows using DGM with a PML (Perfectly Matched Layer) as a non-reflecting boundary conditions. It was shown that the DG method can be successfully implemented for airframe and duct aeroacoustic propagation. However, these numerical studies were performed for hard-walled problems. A nearly ideal parallel speedup of the quadrature free formulation was also confirmed.

1.4 Aims and motivation

Fan noise has become more important in relation to other main sources with each new generation of turbofan engines. The reason for this lies in the fact that the higher demands for increased performance and efficiency has led to higher bypass ratios. In conventional turbofan engine architectures, the only way to increase the bypass ratio is by increasing the fan diameter which increases the fan-noise component of whole aircraft noise.

Turbofan nacelle CAA radiation calculations are currently performed by using a variety of numerical methods. The frequency domain Finite/Infinite approach has been found to be a robust tool, especially for acoustic treatment design and optimisation [71], but the method is limited to potential mean flow. This is often acceptable in intakes, but less so in the bypass duct and in the exhaust where strong shear flows exists. In order to address this problem the time-domain Discontinuous Galerkin Method (DGM) has been proposed [69]

[52] [70]. The DGM brings several benefits compared to existing CAA methods currently in use:

- The ability to solve very large 3D (three-dimensional) problems due to relatively low memory consumption compared to other methods and good scaling in parallel computations.
- It is directly applicable to sheared flows such as jet shear layers.
- Fully unstructured grids can be used. These greatly simplify the mesh generation for complex geometries.

The main objective of the research in this thesis has been to industrialize a time-domain Computational AeroAcoustics (CAA) modelling tool based on the Discontinuous Galerkin Method (DGM). A commercially available DGM code Actran DGM [72] developed by Free Field Technologies (FFT) is used. The following topics are considered:

- Development of modelling capabilities for inlet, bypass and exhausts noise radiation for axisymmetric and 3D geometries.
- Comparison of the Discontinuous Galerkin method with other CAA methods, e.g. finite element/infinite element method (Actran TM), for performance, accuracy, etc.
- Identification of best practice in terms of mesh generation, flow calculation, post-processing and high performance capabilities.
- Development of a shell program to perform automated analysis with the DGM code for intake problems by providing simple control of all the parameters (flow, geometry, liners).
- Integration of the DGM code with unsteady CFD to predict the generation and propagation of fan stage tonal noise.

1.5 Original contributions

The thesis contains several original contributions which are listed below:

I. An automatic procedure is developed in order to perform efficiently the DGM simulations for axisymmetric and 3D non-axisymmetric turbofan intakes with complex mean flows. Moreover, a novel approach to convert a simple geometric description of a realistic intake to a 3D freeform NURBS surface is proposed and implemented.

II. The DGM is validated and benchmarked for intake and exhaust problems against analytical solutions and other numerical methods. The principal properties of the DGM are assessed, best practice is defined, and important issues which relate to the accuracy and stability of the Myers boundary condition are identified.

III. A new method is proposed for integrating a source prediction obtained from a CFD model for the fan stage of a turbofan engine with the DGM propagation code to predict tonal noise radiation in the far field. The accuracy and efficiency of this approach are investigated and results obtained are compared to measured data from a fan rig.

IV. The influence of the 3D intake shapes and the mean flow distortion on the sound field is investigated for static rig and flight conditions by using the DGM approach. It is shown that for rotor-alone tones at the blade passing frequency, the intake shape and the mean flow distortion play a major role in shaping the sound field inside and outside the nacelle.

V. It is also shown that the mean flow distortion can have a significant effect on the sound attenuation by a liner.

1.6 Outline of the thesis

This research investigates the application of time-domain Discontinuous Galerkin Methods (DGM) to solve large 3D wave propagation problems.

Chapter 1 presents an introduction to the problem of aircraft noise, sources of noise in a turbofan engine, and computational aeroacoustics (CAA) methods. Special attention is paid to methods used to solve wave propagation problems, and particularly to the discontinuous Galerkin methods. The motivation, objectives and original contributions of this research are also given.

In chapter 2, the derivation of the linearized Euler equations and the linearized potential theory in the time and frequency domains are given. The acoustic duct modes are introduced, and the boundary conditions are presented, with special attention to time-domain impedance boundary conditions. The general and quadrature-free formulations of the DGM, basis functions and space discretization, numerical fluxes, and time integration are

discussed. The implementation of the impedance boundary condition in the DGM is also described.

In chapter 3, we describe in detail the application of the discontinuous Galerkin method for turbofan acoustics. The physical problem and numerical models used for the mean flow calculations and acoustic simulations are discussed, including the far-field reconstruction. Spatial discretisation, time integration, computational meshes, and the mean flow interpolation onto acoustic meshes are also discussed.

In chapter 4, a brief description of a scheme for automated 3D CAA noise radiation calculations is provided. An illustration of the whole process is also given.

In chapter 5, the DGM is validated and benchmarked for intake and exhaust problems against analytical solutions and other numerical methods. Special attention is paid to lined intakes in the presence of mean flow. Applicability of the DG method is demonstrated for a 3D non-axisymmetric intake at realistic frequencies and flow conditions. Moreover, a performance study of the numerical method is performed.

In chapter 6, a new method for coupling the CFD and CAA for the fan stage tone noise predictions is proposed. The accuracy and efficiency of the CFD/CAA coupling are investigated and results obtained are compared to measured data from a fan rig. The method is then used to obtain modal sources used in chapter 7.

In chapter 7, numerical studies are performed by means of the DGM approach to explore sound propagation and radiation from turbofan intakes to understand the effects of complex 3D shapes and mean flows on the sound field at realistic frequencies. A semi-analytical method and the frequency-domain finite element method are also used for a simplified intake problem to validate the DGM approach for sound propagation through distorted flows, and to investigate the impact of the mean flow distortion on sound absorption by liners.

Finally in chapter 8, summary, conclusions and outlook are given.

2. Time-domain discontinuous Galerkin methods for flow acoustics

2.1 Introduction

In this chapter the discontinuous Galerkin method is presented in the context of its application to acoustic propagation in turbofan engine nacelle. Sound propagation and radiation in the presence of non-uniform mean flow and impedance boundary conditions are considered.

2.2 Acoustic propagation

2.2.1 Euler equations

Propagation models in aeroacoustics are generally based on the full or linearized Euler equations. It is assumed that the effects of viscosity and heat transfer can be neglected. The equations of conservation of mass (continuity), momentum and energy can be written for a perfect gas as shown below [73].

Mass:

$$\frac{\partial \rho}{\partial t} + \nabla \cdot (\rho \boldsymbol{u}) = 0. \tag{2.1}$$

Momentum:

$$\frac{\partial (\rho \boldsymbol{u})}{\partial t} + \nabla \cdot (\rho \boldsymbol{u}\boldsymbol{u}^T) + \nabla \mathrm{p} = \boldsymbol{0}, \tag{2.2}$$

where $\boldsymbol{u}\boldsymbol{u}^T$ is a matrix multiplication which is equivalent to the outer product.

Energy:

$$\frac{\partial E}{\partial t} + \nabla \cdot [\boldsymbol{u}(E + \mathrm{p})] = 0. \tag{2.3}$$

The total energy E is given by

$$E = \rho e + \frac{1}{2}\rho|\boldsymbol{u}|^2, \tag{2.4}$$

for the perfect gas (or ideal gas) the internal energy per unit mass is given by

$$e = \mathrm{T}c_v. \tag{2.5}$$

The Euler equations described as above can be rewritten in vector form as [74]

$$\frac{\partial \boldsymbol{q}_\mathrm{f}}{\partial t} + \nabla \cdot \mathbf{f} = \mathbf{0}, \tag{2.6}$$

where

$$\boldsymbol{q}_\mathrm{f} = \begin{bmatrix} \rho \\ \rho u_x \\ \rho u_y \\ \rho u_z \\ E \end{bmatrix},$$

$\mathbf{f}$ is flux matrix where each column is defined by

$$\mathbf{f}_x = \begin{bmatrix} \rho u_x \\ \mathrm{p} + \rho {u_x}^2 \\ \rho u_x u_y \\ \rho u_x u_z \\ u_x(E + \mathrm{p}) \end{bmatrix}, \mathbf{f}_y = \begin{bmatrix} \rho u_y \\ \rho u_x u_y \\ \mathrm{p} + \rho {u_y}^2 \\ \rho u_y u_z \\ u_y(E + \mathrm{p}) \end{bmatrix}, \mathbf{f}_z = \begin{bmatrix} \rho u_z \\ \rho u_x u_z \\ \rho u_y u_z \\ \mathrm{p} + \rho {u_z}^2 \\ u_z(E + \mathrm{p}) \end{bmatrix}.$$

From equations (2.4), (2.5), and equation of state $\mathrm{p} = \rho R_g \mathrm{T}$ the pressure p can be written as

$$\mathrm{p} = \frac{R_g}{c_v}\left(E - \frac{1}{2}\rho\left(u_x^2 + u_y^2 + u_z^2\right)\right), \tag{2.7}$$

where R_g and c_v are perfect (ideal) gas constants.

2.2.2 Linearized Euler equations

A linearized version of the above equations is derived from a flow decomposition, which separates the steady flow from time dependent small perturbations. The decomposition is given by

$$\begin{aligned} \mathrm{p}(\boldsymbol{x},t) &= \mathrm{p}_0(\boldsymbol{x}) + \mathrm{p}'(\boldsymbol{x},t), \\ \rho(\boldsymbol{x},t) &= \rho_0(\boldsymbol{x}) + \rho'(\boldsymbol{x},t), \\ \boldsymbol{u}(\boldsymbol{x},t) &= \boldsymbol{u}_0(\boldsymbol{x}) + \boldsymbol{u}'(\boldsymbol{x},t). \end{aligned} \tag{2.8}$$

where the quantities with subscript "0" refer to a steady mean flow and with superscript "′" to unsteady perturbations, which are small compared to the mean components.

The linearization of the Euler equations can be now performed by substituting expressions (2.8) into the full Euler equations and neglecting non-linear terms of p', ρ' and $\boldsymbol{u}'$.

The resulting linearized equations derived from equations (2.1), (2.2), and (2.3) are given below [75].

Conservation of mass:

$$\frac{d_0\rho'}{dt} + \mathbf{u}' \cdot \nabla\rho_0 + \rho_0 \nabla \cdot \boldsymbol{u}' + \rho' \nabla \cdot \boldsymbol{u}_0 = 0. \tag{2.9}$$

Conservation of momentum:

$$\rho_0 \frac{d_0\boldsymbol{u}'}{dt} + \rho_0 \boldsymbol{u}' \cdot \nabla \boldsymbol{u}_0 - \frac{\rho'}{\rho_0} \nabla \mathrm{p}_0 + \nabla \mathrm{p}' = \mathbf{0}. \tag{2.10}$$

The energy equation:

$$\frac{d_0\mathrm{p}'}{dt} + \boldsymbol{u}' \cdot \nabla \mathrm{p}_0 + \gamma \mathrm{p}_0 \nabla \cdot \boldsymbol{u}' + \gamma \mathrm{p}' \nabla \cdot \boldsymbol{u}_0 = 0. \tag{2.11}$$

These equations can also be written in vector form as

$$\frac{\partial \boldsymbol{q}}{\partial t} + \nabla \cdot \boldsymbol{F} + \boldsymbol{G} = \mathbf{0}, \tag{2.12}$$

where

$$\boldsymbol{q} = \begin{bmatrix} \rho' \\ \rho_0 u'_x \\ \rho_0 u'_y \\ \rho_0 u'_z \\ \mathrm{p}' \end{bmatrix},$$

$$\boldsymbol{F}_x = \begin{bmatrix} \rho' u_{0x} + \rho_0 u'_x \\ u_{0x}\rho_0 u'_x + \mathrm{p}' \\ u_{0x}\rho_0 u'_y \\ u_{0x}\rho_0 u'_z \\ u_{0x}\mathrm{p}' + \gamma \mathrm{p}_0 u'_x \end{bmatrix}, \boldsymbol{F}_y = \begin{bmatrix} \rho' u_{0y} + \rho_0 u'_y \\ u_{0y}\rho_0 u'_x \\ u_{0y}\rho_0 u'_y + \mathrm{p}' \\ u_{0y}\rho_0 u'_z \\ u_{0y}\mathrm{p}' + \gamma \mathrm{p}_0 u'_y \end{bmatrix}, \boldsymbol{F}_z = \begin{bmatrix} \rho' u_{0z} + \rho_0 u'_z \\ u_{0z}\rho_0 u'_x \\ u_{0z}\rho_0 u'_y \\ u_{0z}\rho_0 u'_z + \mathrm{p}' \\ u_{0z}\mathrm{p}' + \gamma \mathrm{p}_0 u'_z \end{bmatrix},$$

$$\boldsymbol{G} = \begin{bmatrix} 0 \\ (\rho_0 u'_x + \rho' u_{0x})\dfrac{\partial u_{0x}}{\partial x} + (\rho_0 u'_y + \rho' u_{0y})\dfrac{\partial u_{0x}}{\partial y} + (\rho_0 u'_z + \rho' u_{0z})\dfrac{\partial u_{0x}}{\partial z} \\ (\rho_0 u'_x + \rho' u_{0x})\dfrac{\partial u_{0y}}{\partial x} + (\rho_0 u'_y + \rho' u_{0y})\dfrac{\partial u_{0y}}{\partial y} + (\rho_0 u'_z + \rho' u_{0z})\dfrac{\partial u_{0y}}{\partial z} \\ (\rho_0 u'_x + \rho' u_{0x})\dfrac{\partial u_{0z}}{\partial x} + (\rho_0 u'_y + \rho' u_{0y})\dfrac{\partial u_{0z}}{\partial y} + (\rho_0 u'_z + \rho' u_{0z})\dfrac{\partial u_{0z}}{\partial z} \\ (\gamma - 1)(\mathrm{p}' \nabla \cdot \boldsymbol{u}_0 - \boldsymbol{u}' \cdot \nabla \mathrm{p}_0) \end{bmatrix}.$$

The vector $\boldsymbol{q}$ contains the unsteady fluctuations, the tensor $\boldsymbol{F}$ contains the Eulerian fluxes and the vector $\boldsymbol{G}$ contains terms associated with the mean flow gradients. The constant γ is the ratio of specific heats (1.4 for the air).

2.2.3 Linearized potential theory

The linearized energy equation (2.11) can be further simplified if the acoustic perturbations are isentropic and the mean flow is assumed homentropic, i.e. the entropy is uniform and constant. The energy equation is then replaced by the following algebraic relationship [76],

$$\mathrm{p}' = c_0^2 \rho'. \tag{2.13}$$

In case of irrotational ($\nabla \times \boldsymbol{u}_0 = \boldsymbol{0}$) flow the acoustic velocity vector can be described by an acoustics velocity potential, $\boldsymbol{u}' = \nabla \phi'$ where ϕ' is the potential. The linearized momentum equation (2.10) can be replaced by Bernoulli's equation.

$$\frac{\mathrm{p}'}{\rho_0} = -\left(\frac{\partial}{\partial t} + \boldsymbol{u}_0 \cdot \nabla\right)\phi'. \tag{2.14}$$

Combining equations (2.14) and (2.9) using equation (2.13) the acoustic velocity potential then satisfies

$$\frac{\partial}{\partial t}\left(-\frac{\rho_0}{c_0^2}\frac{d_0\phi'}{dt}\right) + \nabla \cdot \left(\rho_0 \nabla\phi' - \frac{\rho_0}{c_0^2}\frac{d_0\phi'}{dt}\boldsymbol{u}_0\right) = 0. \tag{2.15}$$

2.2.4 Frequency domain analysis

The linearized Euler equations and their potential version can be solved in the time or frequency domains. In the frequency domain, the acoustic perturbation vector is assumed to be time-harmonic of the form

$$\boldsymbol{q}'(\boldsymbol{x}, t) = Re\{\tilde{\boldsymbol{q}}(\boldsymbol{x})\mathrm{e}^{\mathrm{i}\omega t}\}, \tag{2.16}$$

where $\tilde{\boldsymbol{q}}(\boldsymbol{x})$ is the complex amplitude vector of a vector (or scalar) variable $\boldsymbol{q}'$.

Equation (2.12) can then be rewritten,

$$\mathrm{i}\omega\tilde{\boldsymbol{q}} + \nabla \cdot \tilde{\boldsymbol{F}} + \tilde{\boldsymbol{G}} = \boldsymbol{0}, \tag{2.17}$$

where $\tilde{\boldsymbol{F}}(\boldsymbol{x})$ and $\tilde{\boldsymbol{G}}(\boldsymbol{x})$ are the complex amplitude vectors of the tensor $\boldsymbol{F}$ and vector $\boldsymbol{G}$, respectively. In similar way the velocity potential equation (2.15) can be rewritten as a convected Helmholtz equation;

$$\frac{\rho_0}{c_0^2}\left(\omega^2\tilde{\phi} - \mathrm{i}\omega\boldsymbol{u}_0 \cdot \nabla\tilde{\phi}\right) + \nabla \cdot \left(\rho_0\nabla\tilde{\phi} - \frac{\rho_0}{c_0^2}\left(\mathrm{i}\omega\tilde{\phi} + \boldsymbol{u}_0 \cdot \nabla\tilde{\phi}\right)\boldsymbol{u}_0\right) = 0, \tag{2.18}$$

where $\tilde{\phi}$ is the complex amplitude of the acoustic velocity potential. This is the equation which is solved in the finite/infinite element codes [31] [36] [37] for acoustic propagation.

2.3 The hard-wall boundary conditions

The hard-wall boundary condition is obtained by applying the condition that $\boldsymbol{u}' \cdot \boldsymbol{n} = 0$ at the wall, where $\boldsymbol{u}'$ is the acoustic velocity vector and $\boldsymbol{n}$ is the unit locally normal vector with respect to the wall.

2.4 Impedance boundary conditions

2.4.1 Impedance boundary conditions – Frequency domain

An impedance boundary condition defines a relationship between the acoustic pressure and normal acoustic velocity on a boundary. In the frequency domain, the relationship can be written as

$$\mathrm{Z}(\omega) = \frac{\tilde{\mathrm{p}}}{\tilde{\boldsymbol{u}} \cdot \boldsymbol{n}}, \tag{2.19}$$

where $\mathrm{Z}(\omega)$ is a frequency dependent impedance.

This impedance model can be used for zero mean flow or for mean flow with a non-slip, zero flow velocity at the wall. It cannot be used directly for base flows when there is non-zero slip velocity at the wall. However, an infinitely thin boundary layer can be assumed [77, 78]. A modification of the impedance condition for cases where a slip velocity exists at the walls is given by Ingard [79] and Myers [80],

$$\tilde{\boldsymbol{u}} \cdot \boldsymbol{n} = [\mathrm{i}\omega + \boldsymbol{u}_0 \cdot \nabla - \boldsymbol{n} \cdot (\boldsymbol{n} \cdot \nabla \boldsymbol{u}_0)] \frac{\tilde{\mathrm{p}}}{\mathrm{i}\omega \mathrm{Z}(\omega)}. \tag{2.20}$$

This includes the effect of an infinitely thin boundary layer with continuous pressure and normal displacement across the vortex sheet. It is valid for curved surfaces and non-uniform flows.

2.4.2 Impedance boundary conditions – Time domain

The frequency impedance model for zero mean flow (Eq. 2.19) can be converted into an equivalent time domain condition by using the convolution theorem for Fourier transforms. This gives

$$\mathrm{p}'(\boldsymbol{x},t) = \frac{1}{2\pi}\int_{-\infty}^{+\infty} z(\boldsymbol{x},t-\tau)(\boldsymbol{u}'(\boldsymbol{x},\tau)\cdot\boldsymbol{n})d\tau, \tag{2.21}$$

where $\mathrm{p}'(\boldsymbol{x},t)$ and $\boldsymbol{u}'(\boldsymbol{x},t)$ are the inverse Fourier transforms of $\tilde{\mathrm{p}}(\boldsymbol{x},\omega)$ and $\tilde{\boldsymbol{u}}(\boldsymbol{x},\omega)$ defined as:

$$\mathrm{p}'(\boldsymbol{x},t) = \int_{-\infty}^{+\infty} \tilde{\mathrm{p}}(\boldsymbol{x},\omega)\mathrm{e}^{\mathrm{i}\omega t}d\omega, \qquad \boldsymbol{u}'(\boldsymbol{x},t) = \int_{-\infty}^{+\infty} \tilde{\boldsymbol{u}}(\boldsymbol{x},\omega)\mathrm{e}^{\mathrm{i}\omega t}d\omega. \tag{2.22}$$

The integral in equation (2.21) is the convolution product of $\mathrm{z}(\boldsymbol{x},t)$ and $\boldsymbol{u}'(\boldsymbol{x},t)$, where $\mathrm{z}(\boldsymbol{x},t)$ is the inverse Fourier transform of $\mathrm{Z}(\boldsymbol{x},\omega)$.

The impedance modelling in the time domain involves, however, some problems. The impedance $\mathrm{Z}(\boldsymbol{x},\omega)$ is usually defined in a narrow range of real frequencies. In order to obtain the inverse Fourier transform a physical model of the impedance is necessary in the full field of complex number frequencies.

The impedance models for aeroacoustic applications are comprehensively reviewed by Fung and Ju [82], and Richter et al. [48]. The model proposed by Özyörük and Long [83] assumes that $\mathrm{Z}(\boldsymbol{x},\omega)$ is modelled by a rational function of ω. The z-transform is used to mitigate the problem of computing a convolution sum in the time-domain. Özyörük et al. [84] validated the method against experimental data for the NASA Langley flow-impedance tube. Tam and Auriault [85] proposed a model based on the analogy to mass-spring-damper system (three parameter model). The extended Helmholtz resonator model using the z-transform was proposed by Rienstra [81]. The mass-spring-damper model [85] and the extended Helmholtz resonator model [81] are commonly used. A comparison of these models was performed by Richter et al. [86] to simulate data from the NASA grazing flow impedance tube [87]. They have shown that for single frequency there is reasonably good agreement between the two models and experiment data. They also confirmed that the extended Helmholtz resonator model can be implemented for broadband frequency problems. Further developments of the mass-spring-damper model [85] were also proposed by Fung et al. [88], Ju and Fung [89] and Reymen et al. [90]. More recently Li et al. [91] presented an improved multi-pole broadband impedance model. They validated the improved model for NASA Grazing Flow Impedance Tube data against multi-frequency input. A good agreement to the analytical and experimental data was observed for flow and zero flow cases.

2.4 Impedance boundary conditions

The extended Helmholtz resonator model proposed by Rienstra [81] was implemented by Chevaugeon et al. [92] in the DGM framework. Schiltz et al. [70] validated this implementation against the classical frequency domain FEM code (Actran TM [93]) and the analytical mode-matching solutions for a straight annular duct with and without flow, and for different modes at various frequencies. They also validated the impedance condition against Airbus' ACTIPOLE BEM code for realistic 3D turbofan exhaust problems with zero flow, and demonstrated its ability to deal with 3D complex flows. This impedance model is used in the DG method applied later in this thesis, and its implementation is discussed in more detail in section 2.7.6.

An important issue in time-domain impedance models is modelling of the mean flow boundary layer, which has to be included in the acoustic model. It is usually realized by the Ingard/Myers boundary condition [79, 80] which assumes an infinitely thin boundary layer (see section 2.4.1). Assuming the no-penetration condition for the mean flow ($\boldsymbol{u_0} \cdot \boldsymbol{n} = 0$) and uniform impedance, the following form can be obtained in the time domain [81]:

$$\frac{1}{2\pi}\int_{-\infty}^{+\infty} \mathrm{z}(t-\tau)\frac{\partial}{\partial\tau}(\boldsymbol{u}'(\boldsymbol{x},\tau)\cdot\boldsymbol{n})d\tau = \frac{\partial}{\partial t}\mathrm{p}' + \boldsymbol{u}_0\cdot\nabla\mathrm{p}' + \boldsymbol{u}_0\cdot(\boldsymbol{n}\cdot\nabla\boldsymbol{n})\mathrm{p}'. \tag{2.23}$$

The Myers boundary condition provides a stable and accurate solution in the frequency domain [40, 71, 94], but may result in instability along the lined surface in the time domain [85, 83, 89, 92, 86]. It is believed that the instability is inherent to the Myers formulation rather than to a numerical scheme as indicated by analytical studies in [95, 96, 97]. Moreover, Brambley [98] showed that the Myers boundary condition is ill-posed, since there are no regular solutions for large wave numbers (the growth rate of the instability tends to infinity), and the corresponding stability analysis cannot be applied. This implies that the instabilities may arise in numerical simulations in the time-domain when sufficiently high spatial resolution is applied. In order to address the ill-posedness, a modified (well-posed) Myers boundary condition which replaces the mean flow boundary layer with a thin but non-zero boundary layer thickness, instead of the infinitely thin boundary layer, has been proposed by Brambley [99]. The method of matched asymptotic expansions has been used to incorporate the finite-thickness boundary layer within the boundary condition. This has been shown for a straight cylindrical

duct with thin boundary layers. The problem of the instability has also been further investigated by Rienstra and Darau [100], who studied the hydrodynamic stability of the shear layer over the liner model in the limit of incompressible flow. They confirmed the ill-posedness of the Myers boundary condition when the boundary layer thickness tends to zero, and proposed a corrected boundary condition, which includes the finite-thickness boundary layer. Since the finite boundary layer thickness is incorporated within the modified boundary conditions, the slip boundary condition is still valid in the numerical simulations. Recently, Gabard [101] compared these two modified boundary conditions to the standard Myers boundary condition and validated against an exact solution for the case of the reflection of a plane wave by a lined plane surface.

The presence of the hydrodynamic instability over the lined surfaces with the mean flow has also been confirmed experimentally under certain conditions [102, 103]. Theoretical stability analyses performed by Marx [104] for an extended version of the boundary layer model by Rienstra and Darau [100] have shown that certain properties of the liner and the mean flow can give rise to instability. It has also been confirmed that the absolute instability is unlikely to occur in industrial practice due to the boundary layer thicknesses, which are relatively thick compared to those considered in the analytical studies. However, it is likely that the convective instability can occur. It has also been shown by Brambley [105], using the surface mode dispersion relation, that varying the boundary layer thickness leads to different behaviour of the convective and absolute instabilities.

More recently, Gabard and Brambley [106] performed dispersion analysis to investigate the properties of the instability in the numerical model when using the Myers boundary condition. The studies have been performed on the whole numerical model. They confirmed that the instability observed over the lined surfaces in the time domain numerical simulations is indeed associated with the Myers boundary condition. However, the growth rate of the instability in the numerical simulations is bounded due to the spatial discretisation. Therefore, a further refinement of the mesh leads to an increase in the growth rate of the instability. Moreover, they observed that the unstable mode in the numerical simulations corresponds to the absolute instability, which means that the instability in the numerical model spreads out rapidly over the whole

computational domain. They also showed that depending on the implementation of the impedance condition other numerical instabilities can also be observed.

The instability associated with the Myers boundary condition can be prevented by using an implicit discretization [83], an artificial damping [107] or a spatial filter [86, 92] to stabilize the convective term (Eq. 2.23). The dispersion analysis performed by Gabard and Brambley [106] confirmed that the spatial filtering can be an efficient approach to deal with the instability. However, a special attention should also be given to the mesh refinement along the liner. It should also be noted that in some cases the spatial filtering can lead to inaccurate acoustic solution, e.g. due to the scattering at the liner discontinuities.

An alternative approach to the slip boundary condition is to resolve the mean flow with a finite-thickness boundary layer (no-slip boundary condition). This approach has been studied in [108, 109] using sheared mean flows with a parabolic velocity profile. These studies have been performed to simulate data from the NASA grazing flow impedance tube [110]. A good agreement has been found between the numerical simulations and experimental data. Moreover, the studies have shown that the numerical instabilities can be alleviated by applying zero flow velocity at the wall.

Non-linear effects, which are due to high acoustic amplitudes and flow influence on acoustic liner performance, are not accounted in the approaches described above. These effects can be implicitly included by induction of impedance model parameters from measured data [48]. On the other hand, liner properties can also be determined computationally [112, 113].

There also exist other approaches suitable for the simulation of attenuation in lined ducts [114, 115]. In these models the attenuation of noise is achieved by using the liner resistance to compute the pressure drop across the porous sheet, whereas the normal velocity is obtained by solving 1D Euler equations within the liner cavity.

2.5 Non-reflecting boundary conditions

Non-reflecting boundary conditions are necessary to ensure an anechoic termination of the physical zone. This is crucial for wave propagation problems. The physical domain can be significantly reduced when an effective numerical termination is applied.

The non-reflecting boundary conditions for 1D (one-dimensional) wave propagation problems are relatively straightforward to implement [116]. They are known as 1D characteristics or Riemann invariants. Outgoing wave amplitude is computed based on the information from physical zone, whereas the amplitudes of any incoming waves are set to zero. In case of 3D modelling, it is still an efficient approach when the incident direction is approximately normal to the boundary. In case of non-normal incident waves artificial reflections occur [117].

In order to minimize the reflections, many types of absorbing boundary conditions have been developed. They are comprehensively reviewed by; Hixon [117]; Hu [118], and Colonius [119].

The Perfectly Matched Layer (PML) [118] is an effective approach. The concept of the PML for Maxwell's equations has been introduced by Berenger [120]. Hu [121] implemented the PML for 2D (two-dimensional) wave propagation problem with uniform flow, based on the Linearized Euler Equations (LEE). It was shown that, in theory, the non-reflecting condition can be ensured for acoustic and hydrodynamic waves at any angle of incident and frequency. In practice, however small numerical reflections exist. They depend on the PML thickness. Tam et al. [122] showed that when mean flow is present the PML supports an unstable solution. Hu [123] confirmed that the instabilities are caused by inconsistent group and phase velocities for acoustic waves. A new stable PML formulation was proposed, and then extended for non-uniform flows [124].

The buffer zone boundary condition is a strategy where the numerical solution is artificially damped across an added buffer zone. The resulting solution in the buffer zone does not have to be physical. However, its impact on the physical zone must be minimized. Several techniques of the buffer zone exist [125] [126]. This discussion is continued in section 2.7.4.2 to focus on

the buffer zone technique which is used in the DGM simulations presented later in this thesis.

2.6 Duct modes

For the case of a time-harmonic solution within a duct of constant cross-sectional area, and with boundary conditions that are independent of axial position, the acoustic field can be represented as a superposition of an infinite number of modes [76]. The eigenvalue problem can be formulated by using the linearized Euler equations (2.9 – 2.11). In case of a uniform flow, three types of disturbances can be identified, entropy, vorticity and acoustical waves. The entropy and vorticity waves are convected with the mean flow whereas acoustical waves propagate with the speed of sound relative to the mean flow. The entropy waves contain only density component in the solution vector $\boldsymbol{q}$. For the vorticity waves, three velocity components are present. The acoustical waves involve all five variables. In the case of a homentropic flow only vorticity (hydrodynamic) and acoustical waves propagate. None of the three types of waves exist individually for non-uniform flows. In the case of parallel shear flow a third-order equation for the acoustic pressure (the Pridmore-Brown equation) can be derived [127]. For more general problems, numerical solutions may be the only alternative.

In case of uniform axial flow, the equations of continuity (2.9), momentum (2.10) and energy, assuming homentropic flow, (2.13) can be combined to obtain the convected wave equation:

$$\frac{1}{c_0^2}\left(\frac{\partial}{\partial t}+u_{0z}\frac{\partial}{\partial z}\right)^2 \mathrm{p}' - \nabla^2 \mathrm{p}' = 0, \tag{2.24}$$

where the z axis is the duct axis. This equation can be solved for rigid or lined walls. In case of rigid walls the following relation must be satisfied at the wall $\boldsymbol{u}' \cdot \boldsymbol{n} = 0$. When the impedance boundary conditions are considered, the Ingard/Myers condition has to be applied, equation (2.20).

In case of circular or annular duct with hard walls and uniform mean flow, the acoustic pressure field can be given by the following sum of modes of azimuthal order (m) and radial order (μ);

$$\mathrm{p}'(z,r,\theta,t) = \sum_{m=-\infty}^{+\infty}\sum_{\mu=0}^{+\infty}\left(A_{m\mu}\mathrm{e}^{-\mathrm{i}k_{z,m\mu}^{+}z} + B_{m\mu}\mathrm{e}^{-\mathrm{i}k_{z,m\mu}^{-}z}\right)P_{m\mu}(r)\,\mathrm{e}^{\mathrm{i}\omega t-\mathrm{i}m\theta}. \tag{2.25}$$

$A_{m\mu}$ and $B_{m\mu}$ are the modal amplitudes, $P_{m\mu}(r)$ is the radial eigenfunction, and $k_{z,m\mu}^{\pm}$ is an axial wave number given by

$$k_{z,m\mu}^{\pm} = \frac{-k_0 M \pm \sqrt{k_0^2 - (1-M^2)k_{r,m\mu}^2}}{1-M^2}, \tag{2.26}$$

where $k_{r,m\mu}$ is a radial wavenumber. For a circular, hard-walled duct, $P_{m\mu}(r)$ is given by the Bessel function of the first kind $\mathrm{J_m}\left(k_{r,m\mu}r\right)$. The eigenvalue $k_{r,m\mu}$ is obtained from the boundary condition at the outer wall, and is given by $k_{r,m\mu} = \mathrm{j}'_{m\mu}/R_0$, where $\mathrm{j}'_{m\mu}$ is the n$^{\text{th}}$ root of $\mathrm{J}'_m\left(k_{r,m\mu}R_0\right) = 0$, and R_0 is the wall radius.

In case of annular, hard-walled duct, $P_{m\mu}(r)$ is a linear combination of Bessel functions of the first and second kinds, $A\mathrm{J}_m\left(k_{r,m\mu}r\right) + B\mathrm{Y}_m\left(k_{r,m\mu}r\right)$.The eigenvalue $k_{r,m\mu}$ is then the n$^{\text{th}}$ root of:

$$\mathrm{J}'_m\left(k_{r,m\mu}R_0\right)\mathrm{Y}'_m\left(k_{r,m\mu}\mathrm{b}\right) - \mathrm{J}'_m\left(k_{r,m\mu}\mathrm{b}\right)\mathrm{Y}'_m\left(k_{r,m\mu}R_0\right) = 0, \tag{2.27}$$

where R_0 and b are the outer and inner radii, respectively.

The axial wave number $k_z^{\pm}$ is either pure real or pure imaginary. For real axial wave number, the mode amplitude is constant along the axis. In case of complex axial wave number, the amplitude decays exponentially along the duct. In first case the mode is said to be 'cut on' whereas in second it is 'cut off'. k_z is real when the following inequality is fulfilled, $k_0^2 > (1-M^2)k_r^2$. The frequency above which, each mode is cut-on, termed the cut-on frequency for that mode can be expressed as

$$f_c = \frac{c_0 k_r}{2\pi}\sqrt{1-M^2}. \tag{2.28}$$

It can be seen that for a given frequency the number of cut-on modes increases when the Mach number increases. The limit is reached for sonic flow velocity (M =1).

2.7 The DGM formulation applied to the linearized Euler equations

The space discretisation of the linear Euler equations (2.12) is performed for each element Ω by using the discontinuous Galerkin method formulation. The weak variational formulation can be obtained by multiplying the non-conservative form of the LEE (Eq. 2.12) by any arbitrary smooth test function w.

$$\int_{\Omega} \left(\frac{\partial \boldsymbol{q}}{\partial t} + \nabla \cdot \boldsymbol{F}(\boldsymbol{q}) + \boldsymbol{G}(\boldsymbol{q}) \right) \mathrm{w} d\Omega = 0, \tag{2.29}$$

for ∀w.

The solution vector $\mathbf{q}$ is approximated on each element as a linear combination of basis functions given by

$$\boldsymbol{q}(\boldsymbol{x}, t) \cong \sum_{l=1}^{N(p,d)} \boldsymbol{q}_l(t) b_l(\boldsymbol{x}), \tag{2.30}$$

where $\boldsymbol{q}_l(t)$ is a vector of unknowns at the element node. $b_l(\boldsymbol{x})$ is the l^{th} basis function, and $N(p,d)$ is the number of basis functions on each element. For tri and tetrahedral elements the number is given by [128] $\prod_{i=1}^{d} \frac{p+i}{i}$, where p is maximum polynomial order, and d is the space dimension.

The test function can be represented by each basis function b_k and the equation (2.29) can be written for each element Ω as follows:

$$\int_{\Omega} \left(\sum_{l=1}^{N(p,d)} \frac{d\boldsymbol{q}_l}{dt} b_l + \nabla \cdot \boldsymbol{F}(\boldsymbol{q}) + \boldsymbol{G}(\boldsymbol{q}) \right) b_k d\Omega = 0, \tag{2.31}$$

where $k = 1, .., N(p,d)$.

The divergence part of the equation (2.31) is integrated by parts to give

$$\int_{\Omega} \left(\sum_{l=1}^{N(p,d)} \frac{d\boldsymbol{q}_l}{dt} b_l \right) b_k d\Omega - \int_{\Omega} \nabla b_k \cdot \boldsymbol{F}(\boldsymbol{q}) d\Omega + \int_{\partial\Omega} \boldsymbol{F}(\boldsymbol{q}) \cdot \boldsymbol{n} b_k d\partial\Omega + \int_{\Omega} \boldsymbol{G}(\boldsymbol{q}) b_k d\Omega = 0, \tag{2.32}$$

where $k = 1,..,N(p,d)$, and $\partial\Omega$ corresponds to the boundary of the element.

In order to allow exchange information between elements the flux function, $\boldsymbol{F}(\boldsymbol{q})$ in the third term in equation (2.32) at element edges is replaced by the Riemann flux, $\boldsymbol{F}^R(\boldsymbol{q}^-, \boldsymbol{q}^+)$ [129] (for further comments, see section 2.7.2).

2.7.1 Basis functions and space discretization

Polynomial basis functions are commonly used for interpolation within a finite element. Lagrange polynomials were used by Hesthaven and Warburton [130] as a space discretization for time-domain solution of Maxwell's equations. They were found to be robust and accurate for unstructured tetrahedral grids [130] [49]. Jacobi polynomials can also be used as basis functions. They are orthogonal. This property simplifies considerably the DGM formulation [131]. Legendre polynomials which can be regarded as a subcase of Jacobi polynomials were shown to simplify p-adaptivity [132]. The basis functions can be also represented by the plane waves [133]. For some applications this approach reduces significantly problem size, while maintaining required accuracy.

In the DG method applied later in this thesis the space discretisation is based on Lagrange polynomials defined on triangular and tetrahedral elements with equally spaced-nodes along edges and on faces. An example of a cubic tetrahedron is shown in figure 2.1.

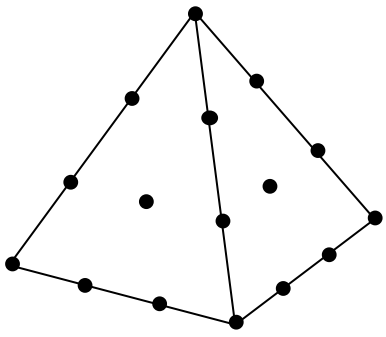

Figure 2.1: An example a cubic tetrahedron.

The Lagrange polynomials in one volume coordinate [128] are given by

$$l_p(x) = \prod_{\substack{0 \le k \le N \\ k \neq p}} \frac{L_1 - L_{1_k}}{L_{1_p} - L_{1_k}}. \tag{2.33}$$

The elements orders in the whole computational mesh are determined by using the global accuracy relation proposed by Ainsworth [67]. In this case the flow convection effect is associated with a wavenumber.

$$2p + 1 \approx \kappa h k, \tag{2.34}$$

where p is an element order, h is an element size, k is the highest wavenumber and κ is a fixed constant describing accuracy. The elements orders vary in order to ensure similar accuracy within the whole mesh.

2.7.2 The numerical fluxes

Due to the discontinuity in interpolation, there is no unique value for the dependent variables at element interfaces. This is addressed by means of the numerical fluxes at the element interfaces. As in many finite difference and finite volume methods the fluxes in the DG method are based on exact or approximate Riemann solvers [129]. A comprehensive review and performance study of different numerical fluxes for DGM were performed by Qiu et al. [134]. They tested, among others the common Lax–Friedrichs (LF) numerical flux and Godunov flux. The former is based on the approximate Riemann solver and the latter on the exact solver. They found that the Lax–Friedrichs is quickest but their results are least accurate. The Godunov flux appears much more accurate but requires longer CPU time.

The Godunov, first order, upwind scheme is applied in the Actran DGM formulation [72] used in this thesis.

The Godunov intercell numerical flux for the Riemann problem is given by [135] [129]

$$\boldsymbol{F}^R(\boldsymbol{q}^-, \boldsymbol{q}^+) = \boldsymbol{F}\big(\boldsymbol{q}^*(\boldsymbol{q}^-, \boldsymbol{q}^+)\big), \tag{2.35}$$

where $\boldsymbol{F}^R(\boldsymbol{q}^-, \boldsymbol{q}^+)$ is the Riemann flux, and $\boldsymbol{q}^*(\boldsymbol{q}^-, \boldsymbol{q}^+)$ is a vector of unknowns at the interface between elements, where $\boldsymbol{q}^-$ if $x < 0$, and $\boldsymbol{q}^+$ if $x > 0$.

For the linear, eigenvalue problem there is a closed form solution of the local Riemann problem. The upwind, first order, Godunov flux can be expressed as [136] [72]

$$\boldsymbol{F}^{R}(\boldsymbol{q}^{-},\boldsymbol{q}^{+}) = \boldsymbol{R}\boldsymbol{\Lambda}^{+}\boldsymbol{R}^{-1}\boldsymbol{q}^{-} + \boldsymbol{R}\boldsymbol{\Lambda}^{-}\boldsymbol{R}^{-1}\boldsymbol{q}^{+}, \tag{2.36}$$

where $\boldsymbol{R}$ is the eigenvector matrix of the Jacobian matrix $\boldsymbol{A} = \partial\boldsymbol{F}/\partial\boldsymbol{q}$ of the Euler system (Eq. 2.12). $\boldsymbol{\Lambda}$ is a diagonal matrix of the eigenvalues of $\boldsymbol{A}$ corresponding to $\boldsymbol{R}$.

2.7.3 Time integration

The Runge-Kutta method is most commonly used as a time integrator for DGM [137]. A study on low dissipation and low dispersion RK methods for CAA was performed by Hu et al. [138]. They showed that in comparison to CFD applications a much smaller time step is required to satisfy dissipation and dispersion criteria for DGM, although stability limits allow larger time steps. They proposed optimised schemes with low storage requirements. More recently a study of the performance of the explicit R-K methods for wave propagation problems has been performed by Toulorge [139]. The time step in explicit R-K schemes is limited by the smallest element size. This results in long CPU time for fine meshes. In order to overcome this drawback, multi-time stepping methods can be considered. Liu et al. [140] proposed explicit Runge-Kutta method with non-uniform time steps. In this approach the correct communication of the solution between elements with different time step sizes is achieved assuming minimal dissipation and dispersion errors at the interfaces. Multi-rate methods use different time steps for groups of mesh elements [141]. The time step of each mesh subsystem is an integer multiple of the smallest element size.

The standard Runge-Kutta 4th order, 4 sub-step (RK4) numerical integrator is used for the Actran DGM computations which are presented later in this thesis [72]. In this approach a single uniform time step, corresponding to the smallest element size, is used. It is determined by the stability limit on the Courant–Friedrichs–Lewy (CFL) number given by

$$CFL = v\frac{\Delta t}{\Delta x}, \tag{2.37}$$

where v is the propagation speed, Δt is the time step, and Δx is the grid interval size. The limit on the CFL number for the Runge-Kutta Actran DGM scheme used in this work is given in section 3.4.6.

2.7.4 Non-reflecting boundary conditions and modal excitations

In all of the DGM analysis presented later in this thesis the non-reflecting boundary conditions and modal excitations are realized by a buffer zone with a 1D characteristic boundary at its outer edge, as presented in figure 2.2.

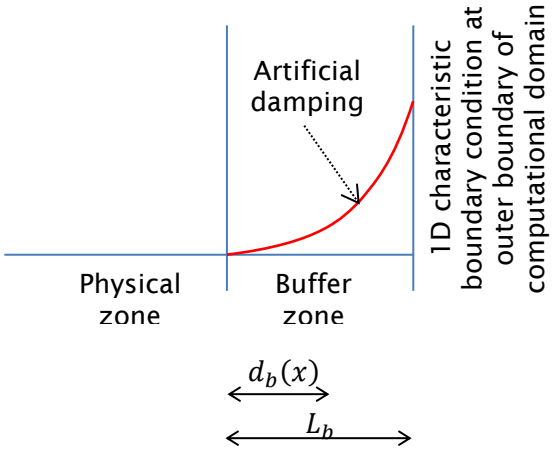

Figure 2.2: The non-reflecting boundary conditions used in this study.

2.7.4.1 Characteristic boundary conditions

The characteristic boundary conditions [116] for one-dimensional wave propagation problems are straightforward to implement into the DGM framework. This is due to the fact that the Riemann fluxes (Eq. 2.36) at the element interfaces are split into outgoing and incoming waves. Therefore, the non-reflecting boundary condition is satisfied by setting $\boldsymbol{q}^+$ to zero, and the modal excitation is realized by setting $\boldsymbol{q}^+$ to the value of the target to obtain the prescribed incoming waves (incident modes).

2.7.4.2 Buffer zone

In this approach the numerical solution (Eq. 2.12) is artificially damped to the target solution across the buffer zone at each time step according to

$$\overline{\boldsymbol{q}}^{n+1} = \boldsymbol{q}^{n+1} - \sigma(x)\left(\boldsymbol{q}^{n+1} - \boldsymbol{q}_{target}\right). \tag{2.38}$$

The vector $\boldsymbol{q}$ contains the unsteady fluctuations. $\boldsymbol{q}_{target}$ is a target vector solution. The target vector $\boldsymbol{q}_{target}$ is used either to introduce the prescribed acoustic waves (incident modes) into the domain, or to damp the outgoing waves when it is set to zero. $\sigma(x)$ is a damping function defined as follows:

$$\sigma(x) = \sigma_{max}\left|\frac{d_b(x)}{L_b}\right|^{\alpha}, \tag{2.39}$$

where σ_{max} is the maximum value of the damping factor, L_b is the length of the buffer zone, $d_b(x)$ is the local distance from the edge of the physical zone, and α is the order of the damping increase. The maximum value of the damping factor, σ_{max} can be computed for fixed L_b and α by assuming a certain value of the transmission factor, which is given by

$$T_f = \prod_{n=1}^{n_p}\{1 - \sigma(x_n)\}, \text{where } x_n = nv\Delta t, \tag{2.40}$$

where n_p is the number of time steps elapsed within the buffer zone $\left(\frac{L_b}{v\Delta t}\right)$, Δt is the time step, and v is the characteristic propagation speed which is defined as the sum of acoustic propagation and flow convective effect. Optimal buffer zone parameters can be estimated. An efficient buffer zone for typical wave propagation problems is achieved for: α = 2, T_f = 0.005, n_p = 400, and the length L_b at least twice the longest wavelength involved in the problem. These buffer zone parameters are used in the DGM analysis presented later in this thesis.

2.7.5 Reflecting wall

In order to obtain the hard-wall (reflection) boundary condition in the DGM framework the external state $\boldsymbol{q}^{+}$ is assumed to be the mirror picture of the internal state $\boldsymbol{q}^{-}$ when computing the Riemann flux at the wall, equation (2.36). This implies that the normal acoustic velocity is zero ($\boldsymbol{u}' \cdot \boldsymbol{n} = 0$).

2.7.6 Impedance boundary conditions

The extended Helmholtz resonator model proposed by Rienstra [81] has been used to obtain the results presented in this thesis. The impedance is defined as follows:

$$\mathrm{Z}(\omega) = R + i\omega\mathrm{m} - i\beta cot\left(\frac{\omega}{c_0}H - i\frac{1}{2}\varepsilon\right), \tag{2.41}$$

where R and m are face-sheet resistance and mass reactance, respectively. β is the cavity reactance, ε is the damping in the fluid cavity, and H is the cavity depth. The following conditions must be satisfied to ensure, that the model is passive and causal [81].

$$R \geq 0, \tag{2.42}$$

$$\mathrm{m} \geq 0, \tag{2.43}$$

$$\beta > 0, \tag{2.44}$$

$$\varepsilon > 0. \tag{2.45}$$

These passive and causal conditions lead to the following model [81]

$$\mathrm{Z}(\omega) = R + i\omega\mathrm{m} + \beta + 2\beta\sum_{n=1}^{\infty} e^{-in2H\omega/c_0 - \varepsilon n}. \tag{2.46}$$

The z-transform is used to mitigate the problem of computing a convolution sum in the time-domain as proposed by Özyörük and Long [83]. The inverse Fourier transform of the impedance is now given by

$$\frac{\mathrm{z}(t)}{2\pi} = (R + \beta)\delta(t) + \mathrm{m}\frac{\partial}{\partial t}\delta(t) + 2\beta\sum_{n=1}^{\infty} e^{-\varepsilon n}\delta(t - n\nu\Delta t). \tag{2.47}$$

where $\nu\Delta t = 2H/c_0$ represents multiple of time step which is needed by a traveling-wave to cover two cavity depths. Finally, using the sifting property of the Dirac delta function, a relationship between acoustic pressure p' and normal velocity v' in the time domain is given for no-flow case as follows

$$\mathrm{p}'(t) = (R+\beta)v'(t) + \mathrm{m}\frac{\partial}{\partial t}v'(t) + 2\beta\sum_{n=1}^{\infty} e^{-\varepsilon n}v'(t-n\nu\Delta t), \tag{2.48}$$

The impedance boundary condition is implemented in the DGM framework by imposing fluxes normal to the boundary face. The normal fluxes are computed by using an updated value of the acoustic pressure obtained from the equation (2.48), and the acoustic field is assumed to be continuous across the boundary [92]. The inertia term, which is a second term in the equation (2.48) must be solved implicitly in order to obtain stable solution [92]. The time derivative is treated as an unknown vector. This implies that each element attached via one of its faces to the liner model has additional terms in the mass matrix associated with the time derivative terms. The last term in the equation (2.48) is a memory term. It is shown in [92] that only ν number of values (n=1) must be stored for each point of an element face, which belongs to the liner model. The special treatment of the inertia and memory terms gives a slight worsening of the performance and an increase in the memory usage, whereby it should be noted that the number of elements associated with lined surfaces is usually small comparing to the overall size of the model therefore the impact on the overall performance is acceptable.

In case of the mean flow the Ingard/Myers boundary condition is applied [79, 80]. In that case the extended Helmholtz resonator is defined as follows [81]:

$$\frac{\partial}{\partial t}\mathrm{p}'(t) = (R+\beta)\frac{\partial}{\partial t}v'(t) + \mathrm{m}\frac{\partial^2}{\partial t^2}v'(t) + 2\beta\sum_{n=1}^{\infty} e^{-\varepsilon n}\frac{\partial}{\partial t}v'(t-n\nu\Delta t) - \boldsymbol{u}_0\cdot\nabla\mathrm{p}'. \tag{2.49}$$

The curvature term in the Ingard/Myers boundary condition (Eq. 2.23) is neglected. Therefore it is valid for liner models with not too large geometric curvature. In order to obtain stable solution, the time derivative terms in the equation (2.49) are computed similarly as the inertia term in the equation (2.48) for the non-flow case, i.e. implicitly by using modified mass matrix for elements associated with lined surfaces. The second time derivative can be avoided by applying $\mathrm{m}=0$ [81]. The convective term, which is the last term in the equation (2.49), is computed on a lined surface using the tangential gradient of the acoustic pressure since the no-penetration condition for the mean flow ($\boldsymbol{u_0}\cdot\boldsymbol{n}=0$) is assumed. This is performed on each element surface

which belongs to the lined surface by using the spatial discretization and the acoustic pressure which is approximated by taking the value at the previous time step, as described in [92]. Moreover, since the acoustic field is discontinuous at the element interfaces, the acoustic pressure at the interfaces is matched by using the arithmetic mean.

As already discussed in section (2.4.2), the current implementation of the Ingard/Myers boundary condition may suffer from the instability along the lined surface in the time domain. In the DGM code used in this work, a spatial filter is applied to the convective term ($\boldsymbol{u}_0 \cdot \nabla p'$) in the equation (2.49) to deal with the instability. This is achieved through the integration of the acoustic field over a disc of fixed radius (which is the filtering parameter) along the discretized lined surface and the space-averaged field is used for the next time step. Therefore, wavelengths shorter than the disc radius are filtered out. Further details on the smoothing procedure can be found in [92].

2.7.7 Quadrature-Free Formulation

The equation (2.32) could be solved by evaluating the integrals in the global coordinate system however it is much convenient to map every element to the reference element (master element) and evaluate the integrals in this way. The mapping is shown in figure 2.3. The master element is unit right tetrahedral with its origin at the origin of a local coordinate system (ξ,η,ζ) [136].

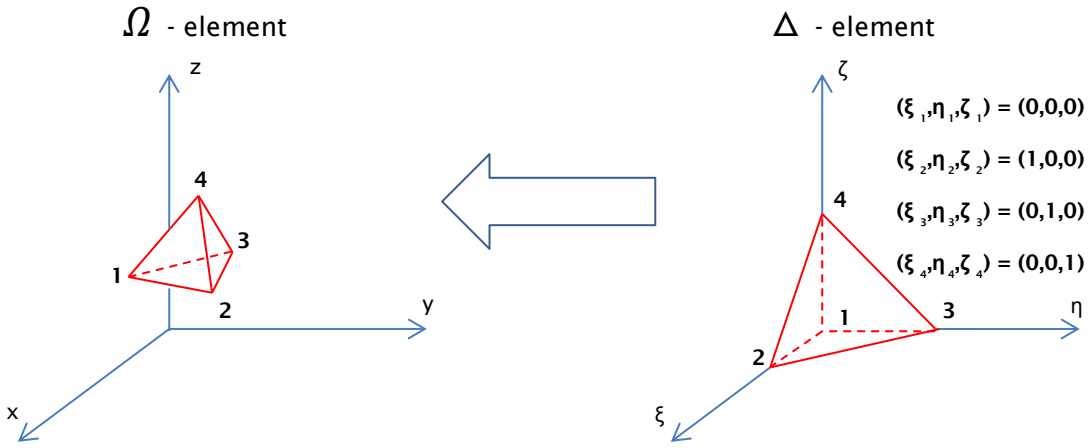

Figure 2.3: Transformation from global coordinate system, (x,y,z) to local (element) coordinate system, (ξ,η,ζ).

The quadrature-free DGM formulation is used in the DGM code (Actran DGM) used to obtain the results presented in this thesis. In the quadrature-free formulation the mapping shown in figure 2.3 is linear. This results in constant Jacobian, but it requires that the elements must have straight edges and plane faces. Based on this assumption the quadrature-free formulation can be now written for each element in a local coordinate system as follow [63] [57]:

$$\int_{\Delta}\left(\sum_{l=1}^{N(p,d)}\frac{d\boldsymbol{q}_l}{dt}b_l\right)b_k|J|d\,\Delta-\int_{\Delta}\boldsymbol{J}^{-1}\nabla b_k\cdot\boldsymbol{F}|J|d\,\Delta+$$
$$\int_{\partial\Delta}b_k\boldsymbol{F}^R\cdot\boldsymbol{n}|J_{\partial\Delta}|d\partial\,\Delta+\int_{\Delta}\boldsymbol{G}b_k|J|d\,\Delta=0. \tag{2.50}$$

The Jacobian, J is constant, so it can be taken out of the integrals. It means that the integrals can be evaluated on the reference element prior to numerical computations. Assuming that the fluxes are also approximated by basis functions, the integrals can be divided into the three following forms

$$\int_{\Delta}b_l b_k|J|d\,\Delta=\mathbf{M}|J|, \tag{2.51}$$

$$\int_{\Delta}J^{-1}\nabla b_k b_l|J|d\,\Delta=|J|\mathbf{K}\boldsymbol{J}^{-\mathbf{1}}, \tag{2.52}$$

$$\int_{\partial\Delta}b_k b_l|J_{\partial\Delta}|d\partial\,\Delta=|J_{\partial\Delta}|\mathbf{B}_{edge}, \tag{2.53}$$

where, $\mathbf{M}$, $\mathbf{K}$, $\mathbf{B}_{edge}$ are mass matrix, stiffness tensor and edge matrix respectively. This leads to a final set of time-domain semi discrete equations which can be integrated by using the Runge-Kutta method

$$\mathbf{M}|J|\frac{d\boldsymbol{q}}{dt}-|J|\mathbf{K}\boldsymbol{J}^{-\mathbf{1}}\cdot\boldsymbol{F}+\sum_{edges}|J_{\partial\Delta}|\mathbf{B}_{edge}\boldsymbol{F}^R\cdot\boldsymbol{n}+\mathbf{M}|J|\boldsymbol{G}=0. \tag{2.54}$$

3. Application of the Discontinuous Galerkin Method for turbofan acoustics

3.1 Introduction

In this chapter the application of the discontinuous Galerkin method to turbofan nacelle acoustics is addressed. Actran DGM, a commercial DG code which solves the Linearized Euler Equations (LEE) in the time domain as detailed in section 2.7 is used. This model is able to deal with rotational flow, shear layers, temperature gradients and non-homentropic mean flows. It is, therefore, well suited for acoustic propagation and radiation from intakes and bypass ducts. It can solve 2D, axisymmetric and 3D problems. Unstructured grids can be used. There are additional advantages for practical applications since unstructured meshes are more easily generated automatically for complex geometries.

The physical problem of noise propagation and radiation from a turbofan engine is illustrated in figure 3.1. A typical turbofan architecture is considered which consists of the engine and nacelle. The installation effects are not studied. Therefore, the installation elements such as pylon, lower and upper bifurcations and struts are not included in the model shown in figure 3.1. The fan stage of the engine, which is regarded here as a noise source, consists of the fan and Outlet Guide Vanes (OGV). Tonal noise components are considered, i.e. rotor alone harmonics of the blade passing frequency and other rotor-locked tones at lower engine orders (buzz-saw tones); interaction tones and distortion tones due to the flow non-uniformity. Noise propagates and radiates into the forward-arc through the intake duct and into the rear-arc through the bypass duct and the shear layers of the jet.

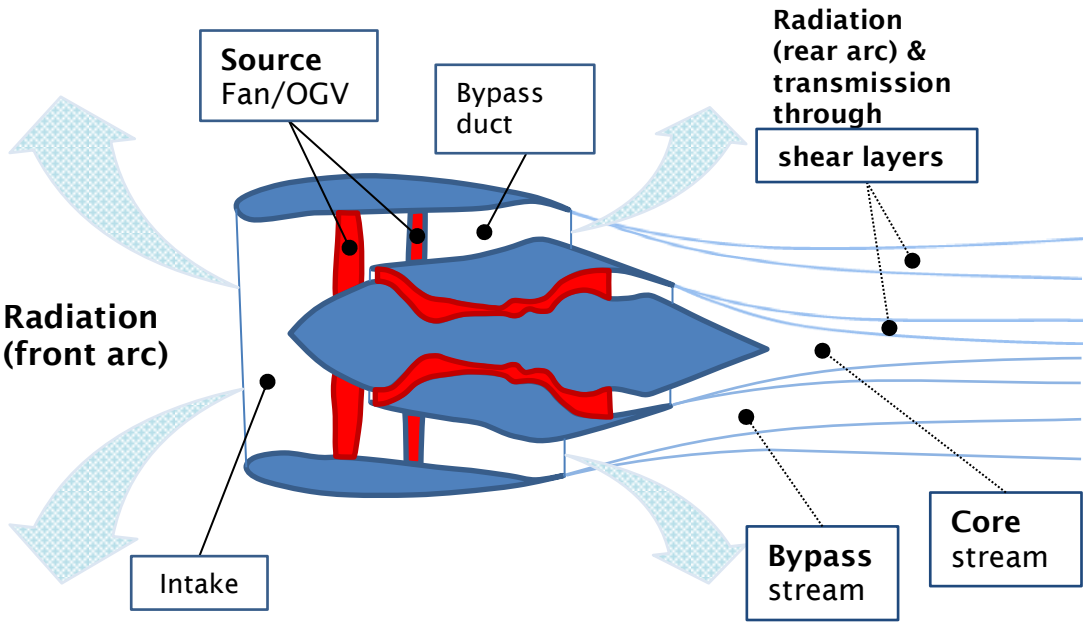

Figure 3.1: A physical problem of the fan stage tonal noise propagation and radiation from a turbofan engine.

3.2 The numerical model

The problem considered is that of noise propagation and radiation in the presence of subsonic mean flow in the intake and bypass duct of a turbofan engine. The mean flow and acoustic calculations are treated separately. The numerical models for the mean flow and acoustics analyses are illustrated in figure 3.2.

In the mean flow model, figure 3.2 (a), the flow equations are solved in the physical zone. Boundary conditions are imposed at uniform inflow & outflow (e.g. constant velocity at fan and OGV faces), free field static or uniform flow, and rigid walls. A detailed description of different mean flow models is given in section 3.3.

The linearized Euler equations are used to model the acoustic perturbations. They are solved in the physical zone of the acoustic model, figure 3.2 (b). Acoustical boundary conditions are satisfied at hard and acoustically lined walls and at non-reflecting terminations. The acoustic excitation is realized by analytical modes imposed to specified zones (see section 3.4 for details).

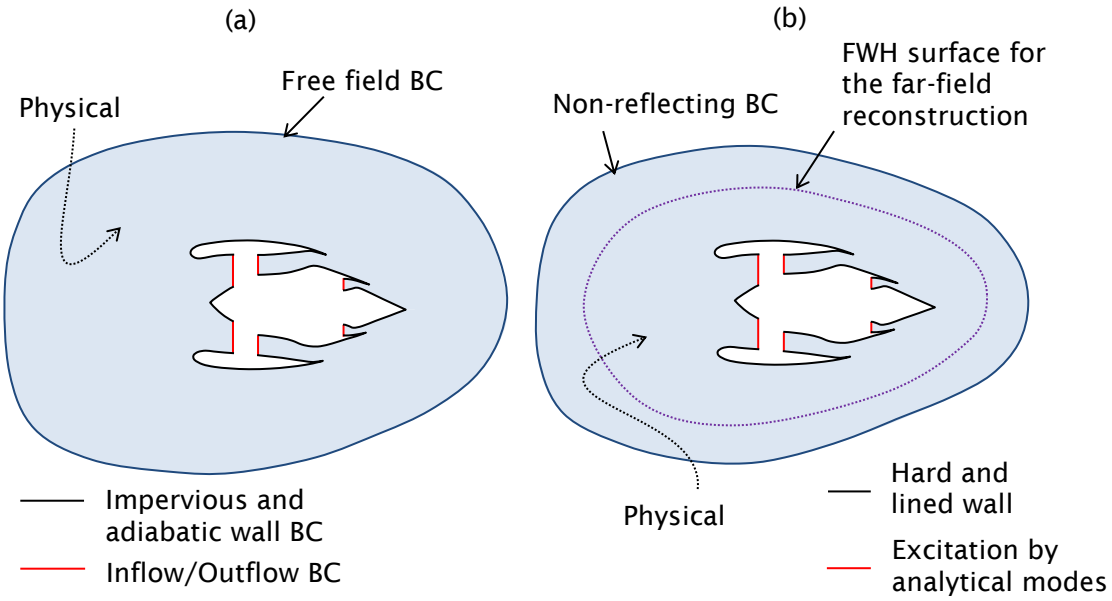

Figure 3.2: The CFD and CAA numerical models: (a) mean flow model (CFD), (b) acoustic model (CAA).

The far-field solution is calculated by solving Ffowcs-Williams and Hawkings (FWH) equation [33]. Data collected on a permeable surface (FWH surface in figure 3.2 (b)) in the acoustical physical region is used.

3.3 The mean flow computations

Four types of the mean flow will be considered: uniform, potential, Euler and Reynolds-averaged Navier–Stokes (RANS).

3.3.1 Uniform flow

This is set directly at the CAA mesh nodes, no calculations are needed. For example, it is often used when idealized models are considered.

3.3.2 Potential flow

This type of mean flow is obtained as a solution of the velocity potential equation for a steady irrotational compressible flow [31] which is solved iteratively. The boundary conditions on rigid surfaces correspond to zero normal velocity condition at walls ($u_{0_n} = 0$). The velocity potential ϕ_0 is specified at inflow boundaries and the normal velocity is imposed at outflow boundaries as shown in figure 3.3. Second order, quadratic finite elements are used to perform this calculation. The size of the finite elements is determined

by a characteristic lengthscale for variations in the mean flow caused by the problem geometry. In case of an intake, the maximum element size is taken to be 1/50th of the fan diameter.

3.3.3 Euler flow

This mean flow is obtained by solving the steady Euler equations by means of a Finite Volume Method (FVM). The CFD solver Fluent with an implicit second-order upwind scheme is used [142]. The fluid is modelled as an ideal gas. A diagram of the CFD model for a typical turbofan intake is shown in figure 3.3. At the free field boundary the static pressure, Mach number and flow direction are specified. The outflow boundary conditions require imposing an averaged surface static pressure. The walls, i.e. spinner and nacelle are modelled as slip walls. Additionally, in the case of an axisymmetric calculation a symmetry axis is specified. This approach requires higher mesh refinement than the potential flow calculation based on the standard finite element method, because of the low-order approximation which is inherent to the finite volume method. The element size inside an intake should be at least 1/100th of the fan diameter. The mesh can become coarser in the far field where the flow gradients decrease. An example of a 3D CFD mesh is presented in figure 3.4.

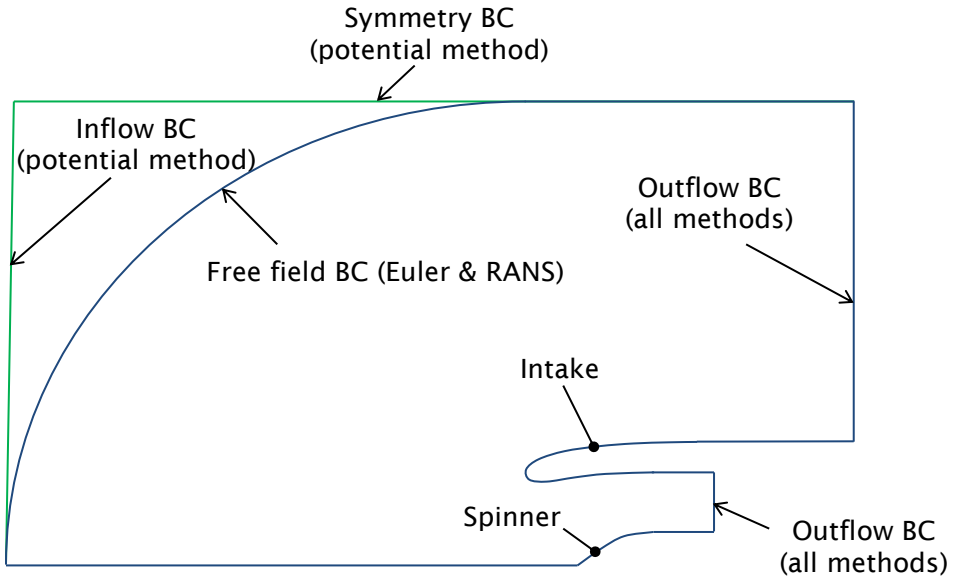

Figure 3.3: Computational domain and boundary surfaces for the CFD model used for mean flow calculations.

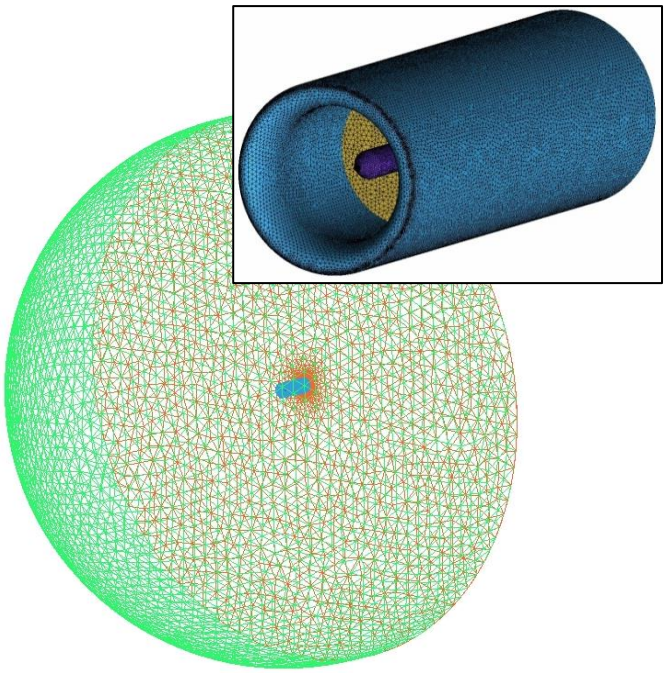

Figure 3.4: An example of a 3D CFD mesh model used for an Euler flow calculation.

It is an unstructured tetrahedral mesh. The main picture in figure 3.4 illustrates the whole computational domain, whereas the top picture shows the zoomed intake mesh. The shape of the computational domain is given by a combination of spherical and cylindrical surfaces. The size of the computational domain is determined by an integer multiple of the fan diameter in both the radial and axial directions. The integer is usually taken to be 25. The intake surface is discretized with uniformly sized elements. It is, however, further refined with respect to local radius of curvature of the surface.

3.3.4 Reynolds-averaged Navier-Stokes turbulent flow

Fluent is again used as a RANS solver [142]. Viscous and time-averaged turbulent stresses are modelled with a turbulence model. In this thesis the turbulent stresses will be modelled with a k-ε turbulence model [143]. An ideal-gas model is also assumed. The boundary conditions differ from those of the Euler flow calculation since the walls are modelled with a no-slip condition. In the RANS approach, the boundary layer must also be resolved. Therefore an extra refinement at the walls is necessary. It is defined by a number of cells representing the boundary layer, usually 10 are sufficient, but 20 are recommended [142]. This gives the location of the first cell at y^+ approximately equal to 1.

3.4 The Acoustic model

The acoustic field is solved using Actran DGM, a quadrature-free, time-domain Runge-Kutta, Discontinuous Galerkin Method [61] [44] [72]. A typical CAA model for turbofan intake propagation and radiation is presented in figure 3.5. The computational mesh consists of three main zones: admission, physical and buffer zones. Boundary conditions are applied at rigid and impedance walls, and at non-reflecting terminations. The acoustic excitation is imposed by analytical modes applied through the admission zone. The non-reflecting BC and buffer zone are added at the outer boundary of the physical zone to ensure minimum reflections. The buffer and admission zones are specified in terms of their lengths (thicknesses). The minimum length should be at least two times the largest wavelength involved in the problem. The physical zone is specified by its radius. In the absence of flow, it can be as small as required to include all geometry features. When the mean flow is present, significant variations in mean flow quantities should be included within the physical zone.

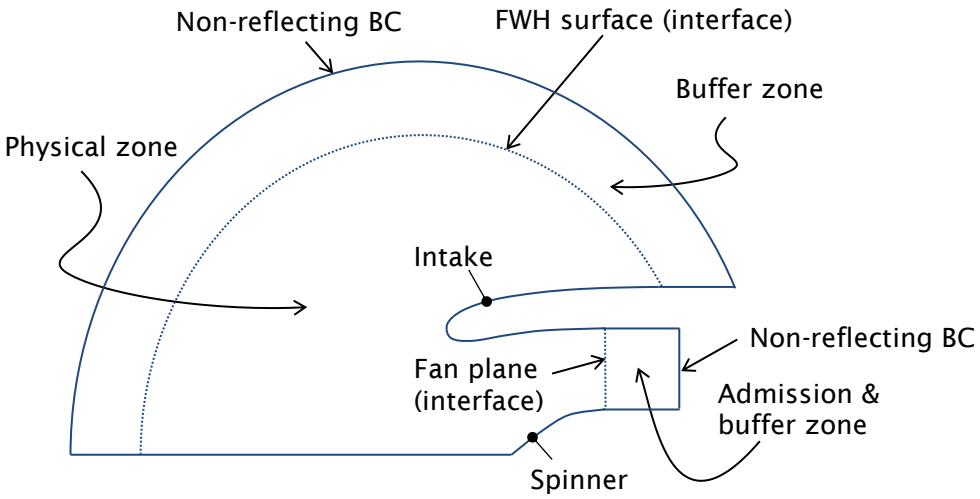

Figure 3.5: DGM model for a turbofan intake.

3.4.1 The physical domain

This is a computational domain where the LEE equations are solved. Three types of mean flow can be specified:

- Isentropic – the flow is assumed to be isentropic along streamlines. In this case the full LEE are solved. Temperature gradients are allowed (see section 2.2.2).
- Homentropic – the entropy is constant in space and time. The energy equation reduces to, $\mathrm{p}' = c_0^2 \rho'$. Temperature gradients are not allowed (see section 2.2.3).
- Constant (Uniform) – all flow gradient terms are removed (the vector $\boldsymbol{G}$ in equation (2.12) is zero vector).

3.4.2 Non-reflecting terminations and admission zone

A one dimensional characteristic non-reflecting boundary enclosing a buffer zone is used as a non-reflecting termination for the physical zone and to model the admission zone as indicated in figure 3.5 (see section 2.7.4).

3.4.3 Hard and lined wall boundary conditions

The boundary condition on a rigid impervious surface is satisfied by setting $\boldsymbol{u}' \cdot \boldsymbol{n} = 0$, where $\boldsymbol{u}'$ is an acoustic velocity vector and $\boldsymbol{n}$ is a locally normal vector with respect to the wall.

The extended Helmholtz Resonator Model [81] [92] is used to model the impedance of the lined wall. The Myers' boundary condition is applied to correct for the effect of grazing flow [80]. Further details are given in section 2.7.6.

3.4.4 Far-field calculation

The Ffowcs-Williams and Hawkings method [33] is used to reconstruct the far-field solution. This is numerically implemented in the frequency domain by using formulation 1A of Farassat [34]. The input data for the FWH integration is collected at the interface (FWH surface) between the physical and buffer zones as indicated in figure 3.5. The position of the interface is acceptable in the DGM due to its discontinuity property (see section 1.3.2 for details). Information is exchanged between elements only by means of numerical fluxes. Moreover, buffer zone parameters are optimised to minimize impact of the damping across the buffer zone on the physical zone including the FWH surface. Thus, any impact from the buffer zone on the far-field calculation is

minimal, and can be neglected in practice. The data is recorded in a progressing time interval (time window) at each mesh point on the FWH surface, on the side of the physical zone. It is approximated over a single time period of the exciting source by a harmonic solution $f(t) = (A + Bi)e^{i\omega t}$. A least squares method is used to fit the above solution to the measured data. If the fitting error is sufficiently small [72] (default normalized value is 10^{-4}) the solution is assumed to have converged. Fourier transform of the approximated harmonic solution is then performed and the far field is reconstructed by solving the FWH equation. This approach has been validated [52] [70] for exhaust noise predictions.

3.4.5 Spatial discretisation

The DGM solution in each element is approximated by Lagrange polynomials. The polynomial orders may vary within a mesh and they are computed a priori (see section 2.7.1). This allows an estimation of the element orders automatically based on element size and the acoustic wavelength. Actran DGM permits the use of element orders in the range from 1 to 16 [72].

3.4.6 Time integration

The time integration is performed explicitly by applying the Runge-Kutta 4th order, 4 sub-step (RK4) scheme. This executes four evaluations of the differential equations (2.54) per time step [72]. The local time step is defined to be

$$\Delta t = CFL(p)\frac{h}{|\boldsymbol{u}_0| + c_0}, \tag{3.1}$$

where, $CFL(p) \cong \frac{1}{2p+1}$ denotes for a stability condition, p is an element order, h is an element size which is defined to be the radius of a circle inscribed in the element, $|\boldsymbol{u}_0|$ is the magnitude of the mean flow velocity, and c_0 is a local speed of sound.

The smallest value of expression (3.1) over the whole mesh determines the overall time step for the DGM simulations [72].

3.4.7 Computational meshes

Much coarser meshes can be used for the DG method than for classic finite volume method. This is a result of high-order approximation within an element used in the DG formulation. Refinement of approximately 1-2 elements per wavelength is generally sufficient [49] [72]. This corresponds to element orders between 5 and 7. Further refinements are necessary in regions of highly curved geometry. This is due to the quadrature-free formulation of the DGM which requires elements with straight edges and flat faces (see section 2.7.7). Firstly, the intake surface mesh is uniformly refined in the azimuthal direction, usually, to approximately four elements per maximum mode azimuthal order involved in the problem. It is then, if necessary, further refined with respect to the local radius of curvature of the geometry surface. As a rule of thumb, element sizes must be less than the local radius of curvature (one radius or slightly below is usually sufficient). A mesh created according to the above specification is presented in figure 3.6.

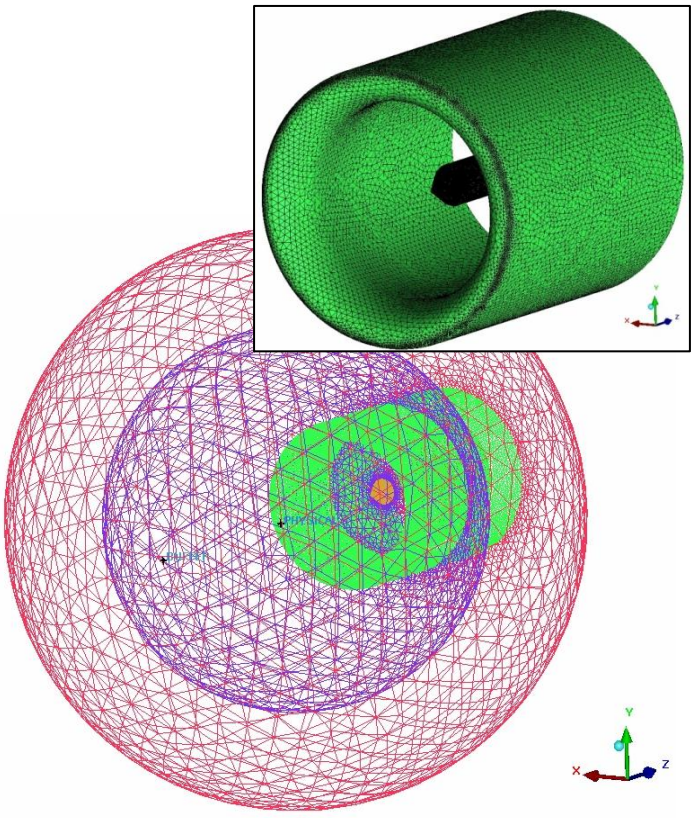

Figure 3.6: An example of DGM intake mesh.

This is a fully unstructured mesh which consists of tetrahedral elements. The main picture shows the whole mesh, and the top picture shows the intake surface mesh. The outer diameter of the computational domain is determined as a multiple of the fan diameter, usually taken to be between two and three.

In order to post-process the DGM results a separate post-processing mesh is required. The acoustic field obtained by using the DGM is interpolated onto the post-processing mesh [72]. Since linear tetrahedral elements are used while post-processing, much finer meshes are necessary. Therefore, if one would like to obtain sufficient spatial resolution to visualize the acoustic field a minimum refinement of approximately 7-10 elements per wavelength should be used.

3.4.8 Interpolation of the mean flow

The pre-calculated mean flow is necessary as input data for the CAA simulations. The flow is interpolated onto an intermediate mesh, which corresponds to the CAA mesh in terms of its size and refinement. The size of elements must also be sufficient to capture the flow properties. Quadratic tetrahedral elements are used. The Actran utility, iCFD is applied to map the CFD solution to the intermediate mesh [72]. In the case of flow containing viscous boundary layers, e.g. RANS CFD, the boundary layer is replaced with an equivalent slip boundary as shown in figure 3.7. It is necessary, since it is impractical to construct a sufficiently fine acoustic mesh to resolve the acoustical field within a thin boundary layer of the order of a few percent of the intake radius. Additionally, an interpolation error is eliminated, which occurs when large elements are used in vicinity of the walls. The following, types of regularization are available in Actran DGM [72]:

- Standard: The mean flow velocity vector at wall is assumed tangent to the wall and equal to an arithmetic average of the closest non-wall nodes, figure 3.7.

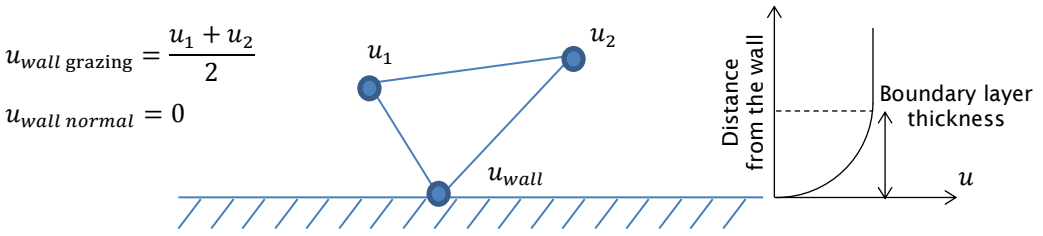

Figure 3.7: The standard mean flow regularization.

- Smoothing: It is performed to improve a quality of the mean flow when CFD mesh is coarser than CAA mesh.
- Standard & Smoothing: It activates both methods described above simultaneously.

4. A scheme for automated 3D CAA noise radiation calculations

4.1 Introduction

A scheme for automated 3D CAA noise radiation calculations for turbofan intakes has been developed and is briefly described in this chapter. The procedure described here is used to perform the CAA computations presented later in this thesis. This allows a large number of study cases to be analysed in an efficient, accurate and systematic way. The main challenge in this development is its multidisciplinary nature. It requires 3D geometry modelling, generation of several computational meshes, flow calculations, acoustic simulations and post-processing. It is a challenging task to ensure smooth and efficient operation of the whole system. In order to address these requirements the model of the scheme which has been proposed is illustrated in figure 4.1.

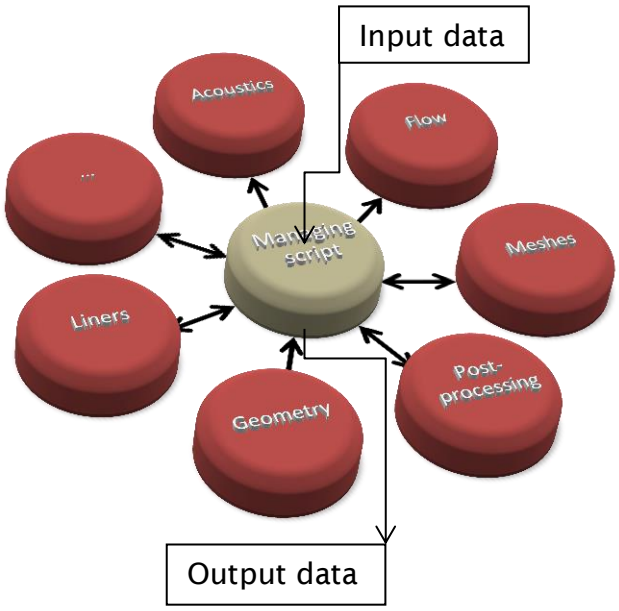

Figure 4.1: Organization of the proposed CAE scheme.

This is a modular framework which consists of simpler sub-elements (modules). The main assumptions are:

- The process is defined in the managing script (master script), which can be accessed and manipulated by any user with a fundamental programming knowledge.
- The modules are independent and separated. They are connected through the master script. Depending of the study purpose, different arrangements of the modules are possible.
- Problems, within the modules and sub-modules can be solved numerically or analytically and commercial or in-house codes can be accommodated.
- Input data is specified as required by the master script.
- Output data consists of multiple outputs from each module.

The Python programming language [144] [145] has been used, mainly because it is an interpreted and object-oriented language which makes it well suited for this development. Moreover, many Python open source scientific and graphics libraries are available which significantly reduces the programming effort, program testing and debugging.

4.2 The geometry module

Non-Uniform Rational B-Splines (NURBS) are used to perform the CAD modelling within the module. NURBS are commonly recognized technique for geometry definition [146]. The main reason for the popularity is its capability to deal simultaneously with mathematically described shapes such as spheres, conics, etc. as well as free-form shapes. NURBS curves and surfaces are defined by a number of control points. They can be either regularly or irregularly spaced. A representation of a NURBS surface is presented in figure 4.2. The curves and surfaces are defined by using piecewise rational function forms (polynomial ratios). A very important feature of NURBS geometry is its fully parametric character. The curves are parameterized by a single parameter, say u_g and surfaces by two parameters, say u_g and v_g. NURBS are easily implemented and widely used in Computer-Aided Design (CAD). The full definition of NURBS curves and surfaces is provided in Appendix A.1.

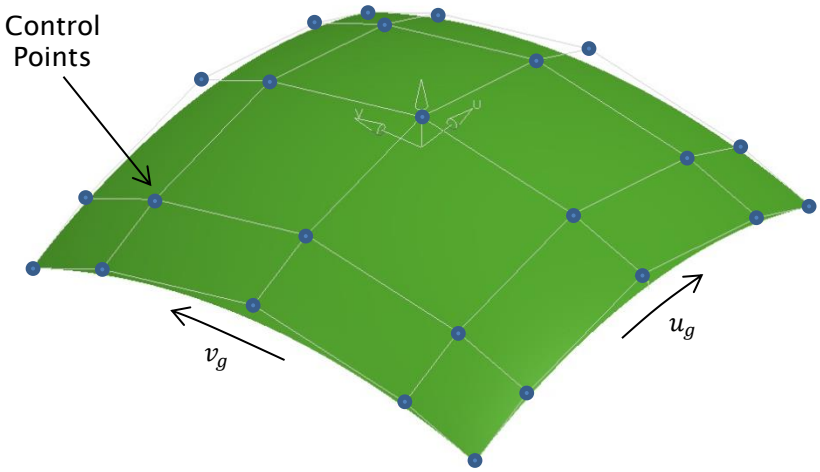

Figure 4.2: The parameterized NURBS surface.

All subroutines within the geometry module are written in the Python programming language. The geometry input data is defined by arrays of points which describe the profile of the intake cross-section at discrete azimuthal angles. An ASCII format is used. The aim of this module is to convert essential geometry data into fully parameterized geometry, i.e. curves and surfaces. A schematic diagram showing the structure of the module is presented in figure 4.3.

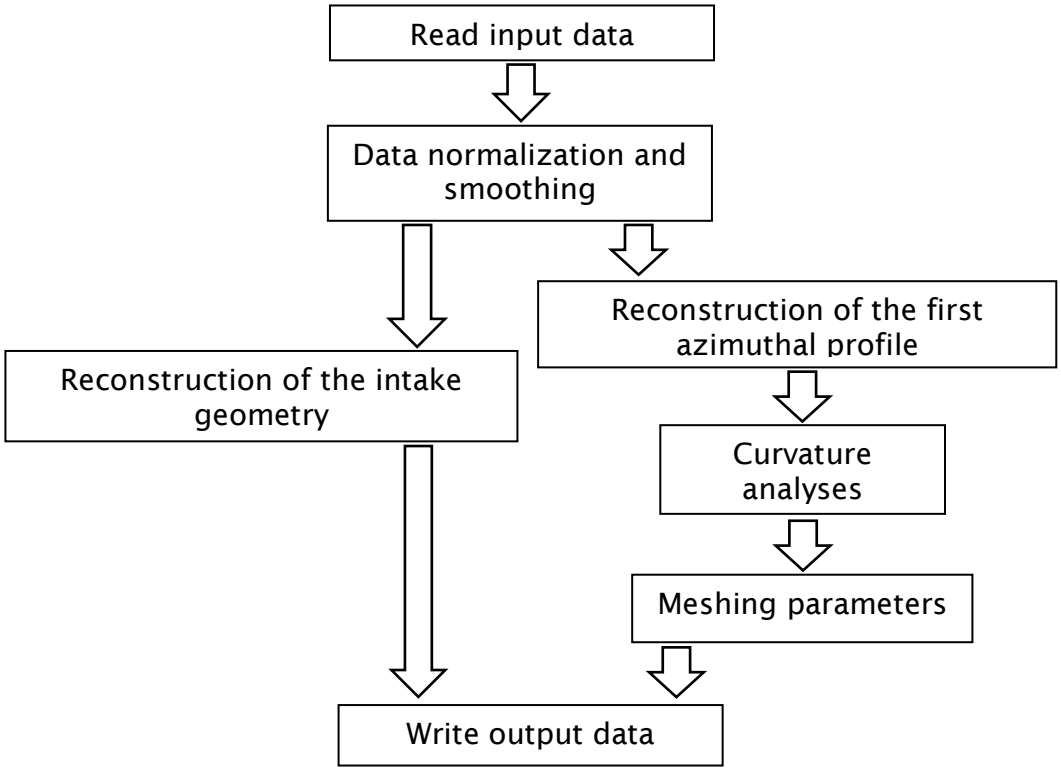

Figure 4.3: An organization scheme of the CAD module.

The input data consists of discrete points is read from a file. This is then smoothed and normalized. This is performed to filter out the effect of the wiggles in the data, which may occur as a result of small misalignment problems in the input data, and to ensure the same number of discrete points on each azimuthal profile (3D problems). The smoothing is achieved by a preliminary NURBS interpolation of the original point data with second order curves. Uniformly distributed discrete points are then extracted from these curves.

Once the data is smoothed and normalized the geometry is reconstructed. In the case of 2D axisymmetric models a NURBS curve interpolation is performed. The reconstruction of the 3D NURBS surfaces, i.e. spinner and intake, is more complex. Details are given in Appendix A.2. In the first step, an interpolation is performed to achieve the full set of azimuthal profiles (by default 3rd order NURBS curves are used). An example of the resulting azimuthal profiles defining the intake shape is shown in figure 4.4. The z-axis in the Cartesian system defines the shaft axis. Each azimuthal profile at non-dimensional azimuthal angle v_g is described by the non-dimensional longitudinal parameter u_g. The 3D NURBS intake surface is obtained by interpolating all the profiles (see Appendix A.2). The resulting surface generated from the profiles shown in figure 4.4 is illustrated in figure 4.5.

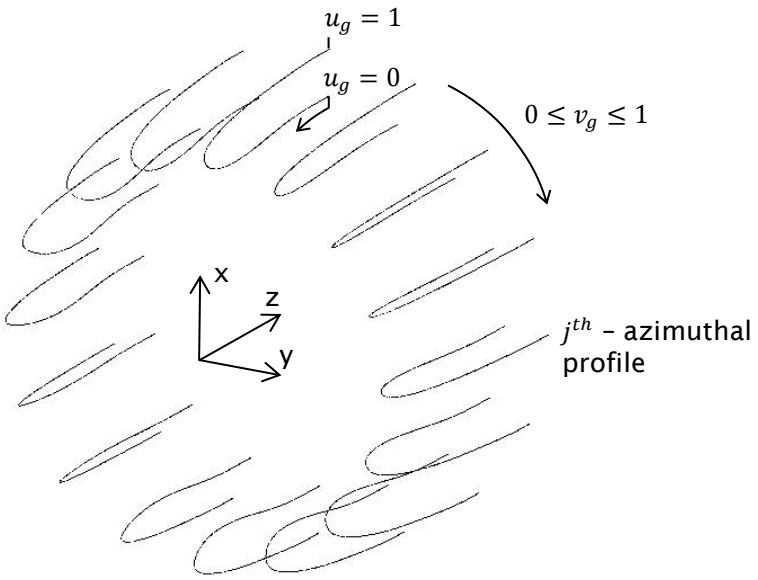

Figure 4.4: A skeleton of azimuthal profiles used for surface interpolation.

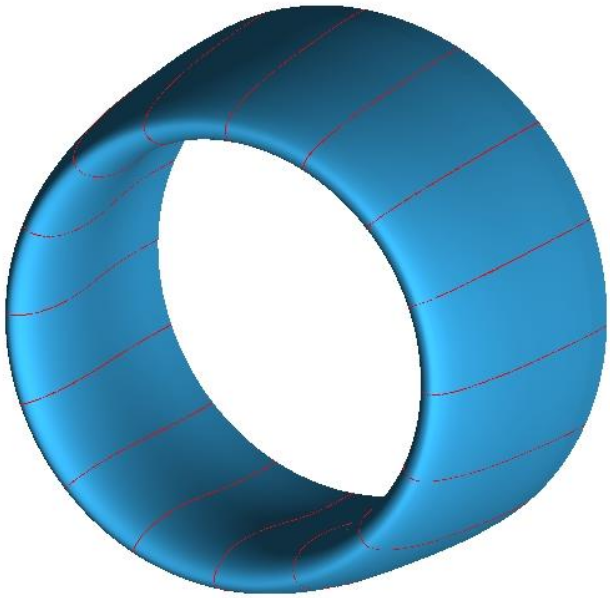

Figure 4.5: The resulting NURBS surface from the interpolation process.

It is important to note that in this approach the surface's shape depends on the number of the discrete points used. High resolution of discrete points is therefore desirable. This may lead, however, to unacceptable computational effort, when large problems are analysed.

In order to overcome the need to provide the large number of azimuthal profiles an alternative approach has also been implemented in which the reconstruction of 3D NURBS surface is achieved by using only four azimuthal profiles. This leads to significant reduction of the input data and size of the geometry file. Moreover, the geometry is easier to parameterize. The azimuthal profiles are provided on the vertical (XZ) and the horizontal (YZ) planes of the Cartesian coordinate system. To define the full model, some key assumptions have to be made. The model is defined axially on four azimuthal quadrants. Each quadrant is reconstructed by a single polynomial which is constrained, in general, to an elliptical shape. The quadrants are independent but continuity up to the first derivative is ensured between them (see Appendix A.3). The azimuthal profiles used for such a surface reconstruction are shown in figure 4.6 (a). The resulting surface is presented in figure 4.6 (b). In order to show the capability of this approach a free-form intake shape has been generated. It is important to note that the geometry is restricted to ellipse-like axial cross sections. Therefore, if one would like to obtain a completely free-form shape the approach with a large number of azimuthal profiles is necessary.

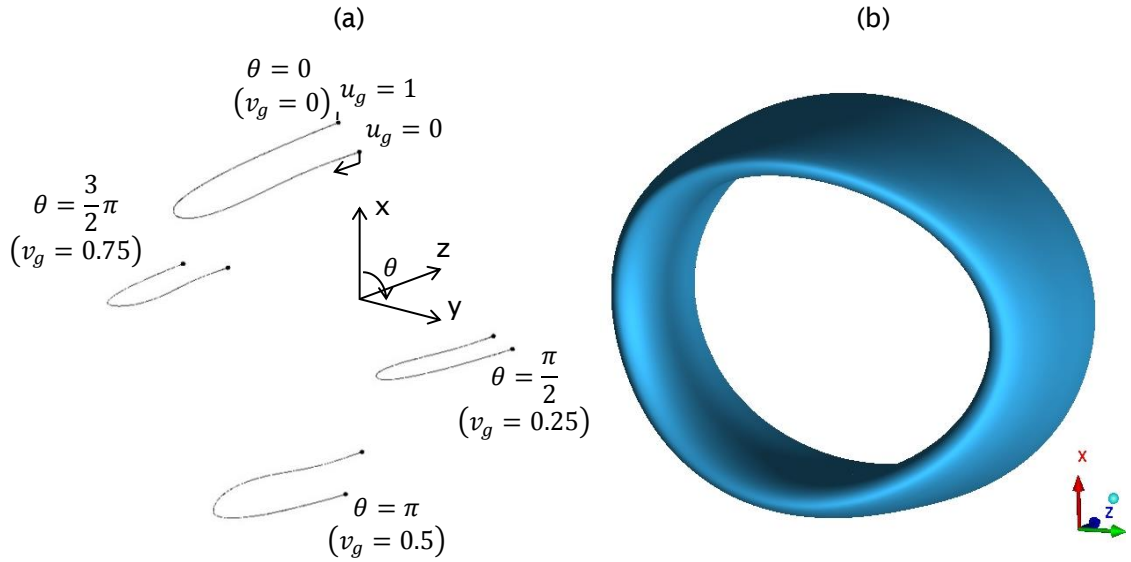

Figure 4.6: An example of the 3D freeform NURBS surface.

Finally the parameters defining the NURBS surface i.e. values of polynomial orders, knot vectors and control points are written into an output file which is passed further into the process.

In addition to the geometry, curvature information is also necessary in the meshing process. The distribution of the curvature over the surface could be obtained for the whole surface in its both directions. However, this would result in highly time consuming process. Instead, a search for local minima of radii of curvature is performed. The first azimuthal array of smoothed and normalized point data is approximated with a 3rd order NURBS curve. The polynomial order is chosen to ensure continuity of the second derivatives at the knot points. An approximation within a specified accuracy is performed (see Appendix A.2). The accuracy is set to 0.1% of the intake's mean radius. The minima of the radii of curvature and their locations are determined by applying simple calculus. This should be repeated for each azimuthal position (profile), for 3D models, in order to determine all extremes. It is, however, time consuming process. Therefore, simplified checks are performed over the azimuthal direction assuming that the general shape topology holds. The longitudinal locations of minima of the radii of curvature obtained in the full search for the first azimuthal profile are taken and used for the rest of profiles to verify if there is a lower radius of curvature at the specified locations. In this way the minima are determined for the whole surface. Results of the curvature analyses are saved at the end of the output CAD file as a comment.

4.3 Meshing module

This module is used to generate all of the necessary computational meshes. The following four types of mesh are constructed:

- CFD mesh for the mean flow calculations,
- Intermediate mesh used to interpolate mean flow data onto the acoustic mesh,
- CAA mesh for the acoustic computations,
- Post-Processing mesh to display the results.

This module is based on ICEM-CFD software [147]. All mesh models are constructed by using features implemented in this software. The organization of the module is presented in figure 4.7.

The geometry file created in the geometry module described in section 4.2 is supplied as an input file to the meshing module. It consists of the geometry and computed curvature information.

In the first step, additional geometry features necessary to generate an appropriate mesh type are created ("Creation of the geometry model" in figure 4.7). As in the geometry module, the geometry is based on a definition of points, curves, and surfaces (B-splines). The NURBS kernel from the geometry module is implemented here as well.

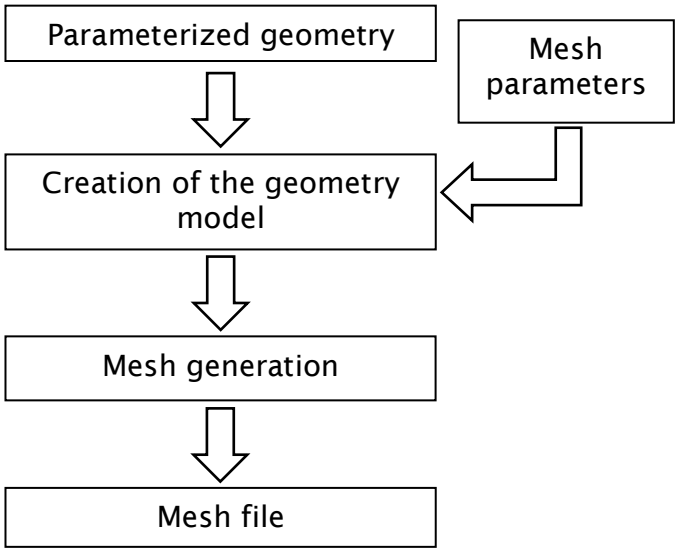

Figure 4.7: An organization scheme of the meshing module.

This ensures also the module's autonomy, which means that no communication is required between modules. All points, curves, and surfaces have their unique names, which are affiliated to appropriate boundary conditions for a given mesh type. Depending on the mesh type the names of the additional geometry features are different. An example of the geometry model used for generation of the flow mesh is presented in figure 4.8. In addition to the extra geometry features, 'volume indicators' (material points) have to be defined in order to determine volume meshes and their names. In the case of a model for the flow mesh presented in figure 4.8, only one volume 'indicator' is used. In other mesh types more volume zones may be necessary. For example, in the acoustic mesh, three volume zones have to be defined, i.e. "admission zone", "physical zone", and "buffer zone" as indicated in figure 3.5 of chapter 3. The size of the entire model and of the separate domains/zones is determined by the input parameters. The mesh resolution and its distribution are defined for each zone. The assumptions used are discussed in chapter 3 (see section 3.4.7).

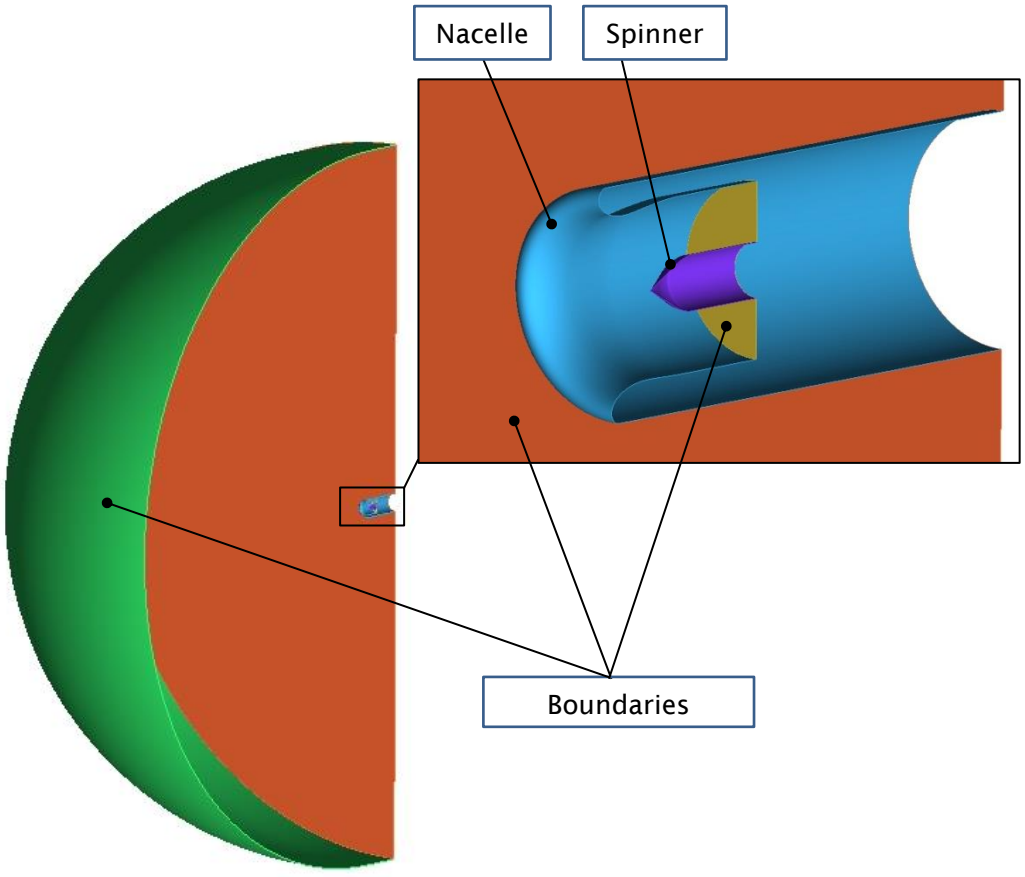

Figure 4.8: An example of the geometry model used for generation of the flow mesh.

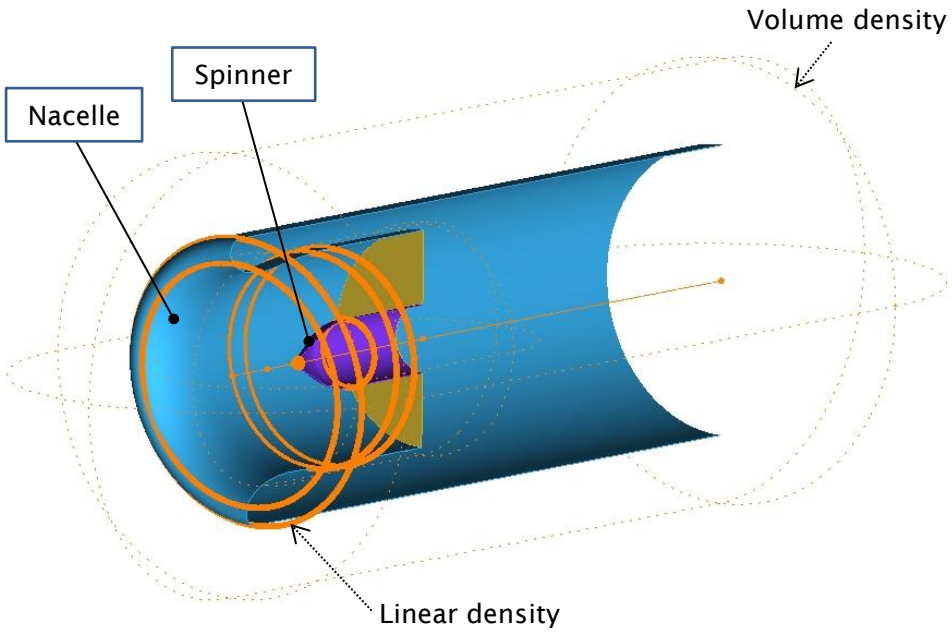

Figure 4.9: An example of density approach used in the 3D flow mesh.

The ICEM-CFD [147] mesh density approach is introduced in order to control efficiently mesh resolution and its distribution. Linear and volume densities are used. The former controls mesh size distribution on the model surfaces, i.e. the nacelle and spinner. These are related to local radii of curvatures determined in the geometry module. Volume densities are used to define the size of volume elements around and inside the intake. Depending of the mesh type slightly different density configurations are deployed. An example of the density configuration used to generate a 3D flow mesh is shown in figure 4.9.

Once the mesh data has been added to the geometry file the computational mesh is generated ('Mesh generation' in figure 4.7). The octree method implemented in ICEM-CFD is used [147]. The method utilizes spatial subdivision algorithm.

The final mesh is written to an appropriate output file, different formats are used depending of the mesh type.

4.4 The mean flow calculation (the flow module)

In this module the mean flow calculations for CAA simulations are performed. The organization of the module is shown in figure 4.10.

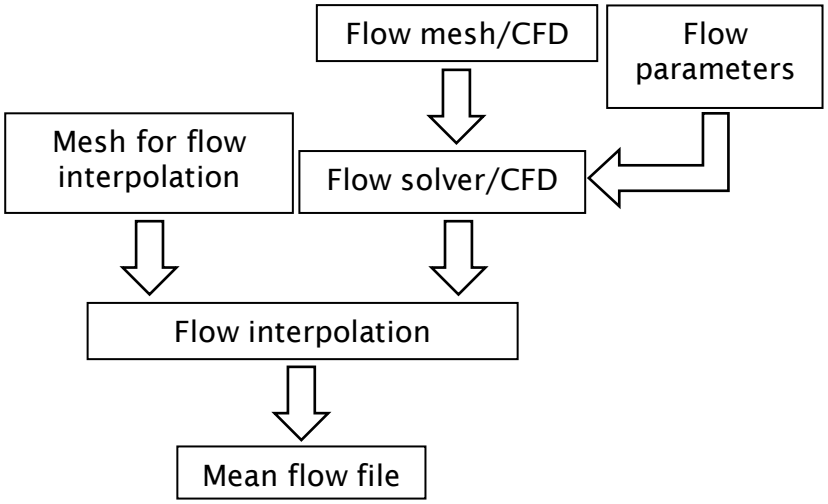

Figure 4.10: An organization scheme of the flow module.

All the operations are handled by a system of python scripts. Two commercially available CFD codes are used: ANSYS FLUENT [142] and MSC Actran TM – potential flow solver [93].

The necessary CFD mesh and flow parameters are provided to the flow solver. Three types of mean flow can be considered: irrotational inviscid potential flow, general Euler flow, and RANS flow. MSC Actran TM is used to obtain the velocity potential flow, whereas ANSYS FLUENT is used for the Euler and RANS flows. Description of the solvers, boundary conditions, and mesh requirements for each flow type is given in section 3.3.

Once the mean flow is obtained, it is interpolated onto an 'intermediate' spatial mesh, which is suitable for the Actran DGM solver. The iCFD utility, which is part of the MSC Actran software, is used. Details are given in section 3.4.8.

4.5 Computing the acoustics solution (the acoustic module)

This is the module where the acoustic solution is calculated. All of the operations are coded in Python programming language. Details of the CAA computation which is performed can be found in section 3.4. Actran DGM and the FWH utility in the MSC Actran software are used [72] [93]. The organization of the module is shown in figure 4.11.

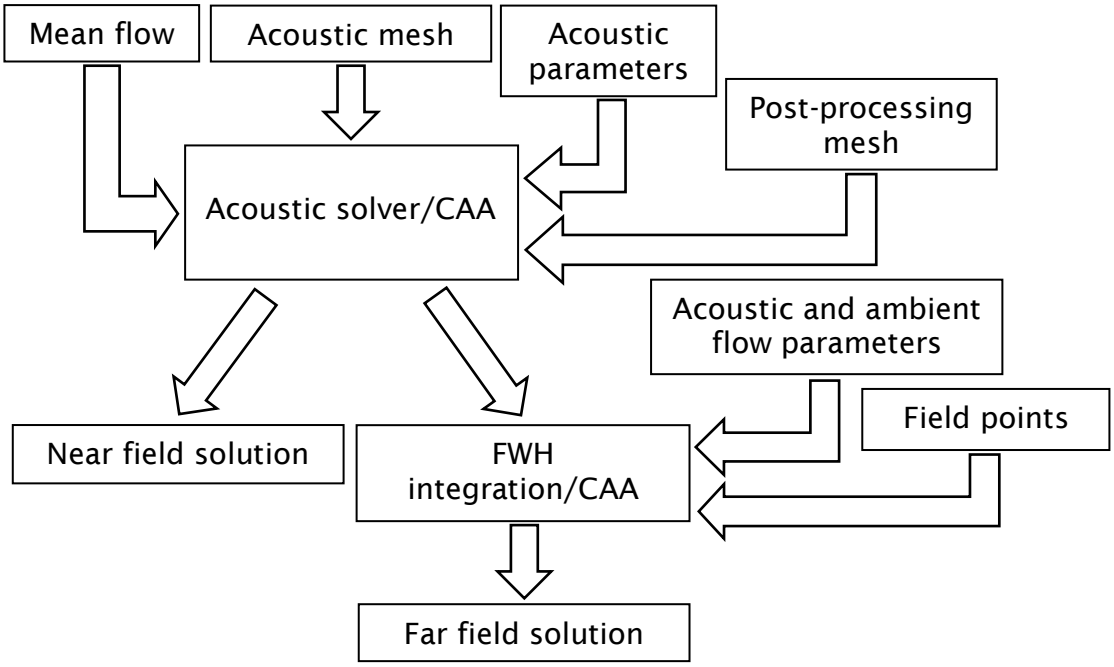

Figure 4.11: An organization scheme of the acoustic module.

The acoustic mesh and the acoustic parameters are provided to the module as input data. The mean flow necessary for the simulations is also supplied. Additionally, as an option, a post-processing mesh can be provided for the acoustic near field solution. The near field and the far-field acoustic calculations are performed separately as described in the section 3.4. The Ffowcs-Williams and Hawkings integration is used to reconstruct the far-field solution. The free field mean flow parameters and field points must be provided to this sub-module. The near field and far-field acoustic solutions are given as output from the module.

4.6 The post-processing module

All post-processing is performed in this module. The Python programming language is again used. Several methods are implemented. They utilize different tools, such as Tecplot [148], Actran VI [93], and Matplotlib library [149]. The module is still under development and many operations are carried out semi-manually at present.

4.7 An illustration of the whole process

An example of the sequence diagram illustrating the whole process is shown in figure 4.12.

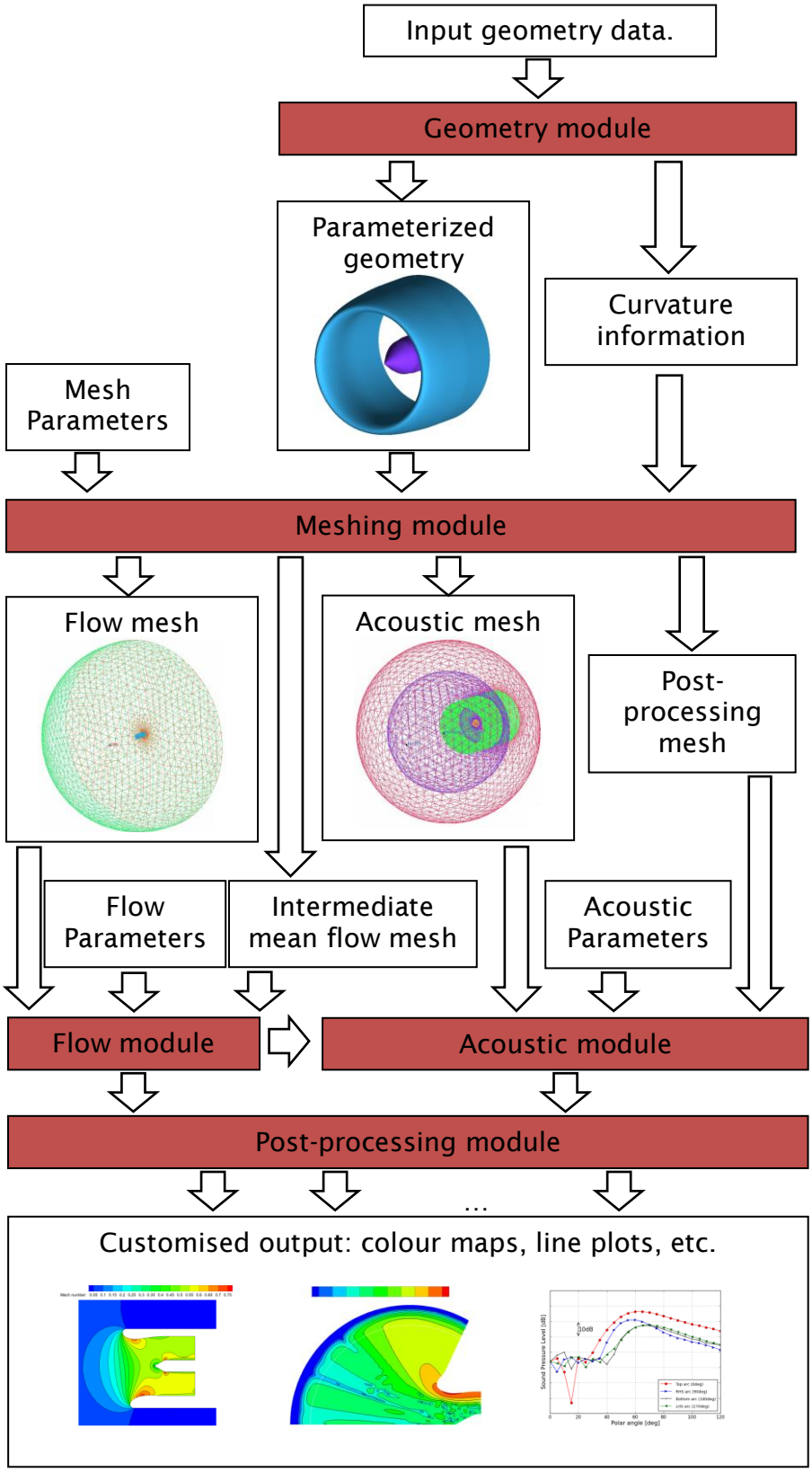

Figure 4.12: Flow diagram illustrating the whole process.

4.8 Observations and conclusions

A CAE platform has been developed for constructing and executing sequential mean flow and acoustic calculations for acoustic propagation and radiation from a turbofan intake.

The geometry module is based on an in-house development of the NURBS method.

The meshing module has been constructed by using the meshing kernel from a commercially available editor ICEM-CFD.

In the current implementation the flow module employs two different flow solvers.

The acoustic module has been developed to perform the acoustic simulations by using Actran DGM, a commercially available CAA programme which is based on a time domain DGM formulation for the linearized Euler equations.

The post-processing module is still under development.

5. Assessment and validation of the DGM for intake and exhaust problems

5.1 Introduction

In this chapter, the Discontinuous Galerkin Method (DGM) is benchmarked for acoustic propagation in turbofan intake and exhaust problems.

The objective of this chapter is to explore the accuracy and efficiency of the DG method for simulating intake and exhaust propagation and radiation at realistic frequencies and flow conditions.

5.2 Validation against analytical solutions: Sound radiation from a straight semi-infinite circular duct

The benchmark problem of Munt [150] is used as a reference case. The physical problem is presented in figure 5.1. A semi-infinite circular duct is formed by a zero thickness, impervious and rigid wall. The acoustic field is excited by a single incident mode travelling along the tube. The injected mode radiates through the unflanged duct termination. Uniform flow exists in the jet and the surrounding region. Two flow arrangements are considered, inflow (intake) and outflow (exhaust). In case of inflow, the jet and the external flow have the same velocity. For the outflow case the flows are still uniform but may have different velocities and physical properties. A vortex sheet is present when the flow velocities are different.

The flow in each region is determined by the density ρ_0, velocity $\boldsymbol{u}_0$ and speed of sound c_0. The acoustic field is defined in terms of the velocity potential ϕ. It satisfies the convected Helmholtz equation (Eq. 2.18). For the case of outflow the velocity potential and its gradient in the axial direction are discontinuous across the vortex sheet. Vortex shedding is expressed by means of the Kutta condition [151]. It states that the gradient of the radial displacement at the duct lip is equal to zero, which implies that: $\phi(R_0, z) = O\left(z^{3/2}\right) as\, z \to 0^+$. This ensures that velocity and pressure are finite at the duct lip.

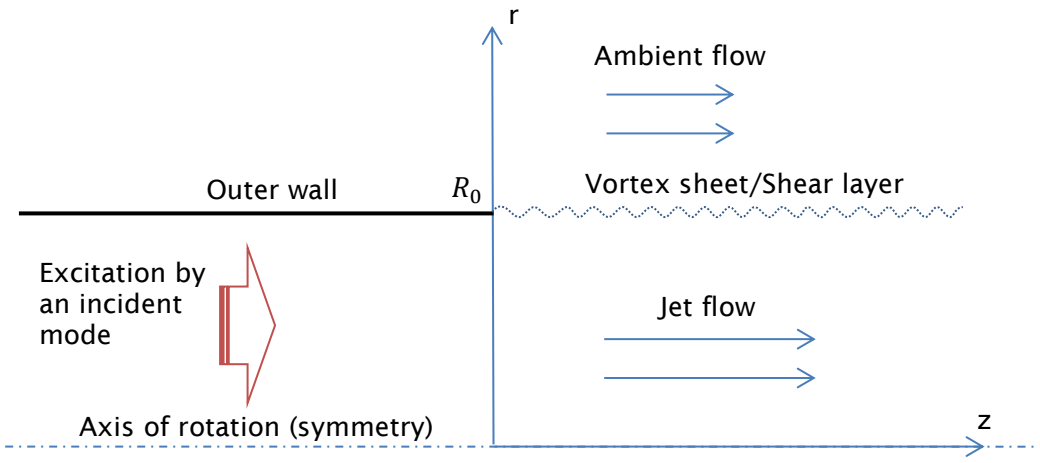

Figure 5.1: The Munt problem for outflow.

In the case of an inlet, the velocity potential and its gradients are continuous. This implies that, $\phi(R_0, z) = O\left(z^{1/2}\right) as\, z \to 0^+$. The pressure is singular at the duct lip. This problem can be solved using the Wiener-Hopf method [152]. An in-house code, GXMunt is used to compute such solutions. The theoretical background to this code is given by Gabard and Astley [153].

5.2.1 Axisymmetric model, no flow

5.2.1.1 The effect of domain size

Numerical experiments are performed to verify the influence of the computation domain size on accuracy and efficiency of the DG method in the absence of flow. A 2D axisymmetric model of a straight circular duct is used. The outer radius of the duct is R_0. Three model domains are considered: large (20x5R_0), medium (10x4R_0), and small (5x2R_0). They are illustrated in figure 5.2. In the numerical model the duct wall has a small thickness of approximately 0.05% of the duct radius. The mesh resolution is set to approximately 1–2 elements per free field wavelength. Further refinement at the duct lip is applied to ensure more accurate solution in this region. The calculations are performed for a single incident mode. A plane wave, with non-dimensional wave number kR_0 = 10, is generated. The details of the parameters used can be found in Appendix B.1.

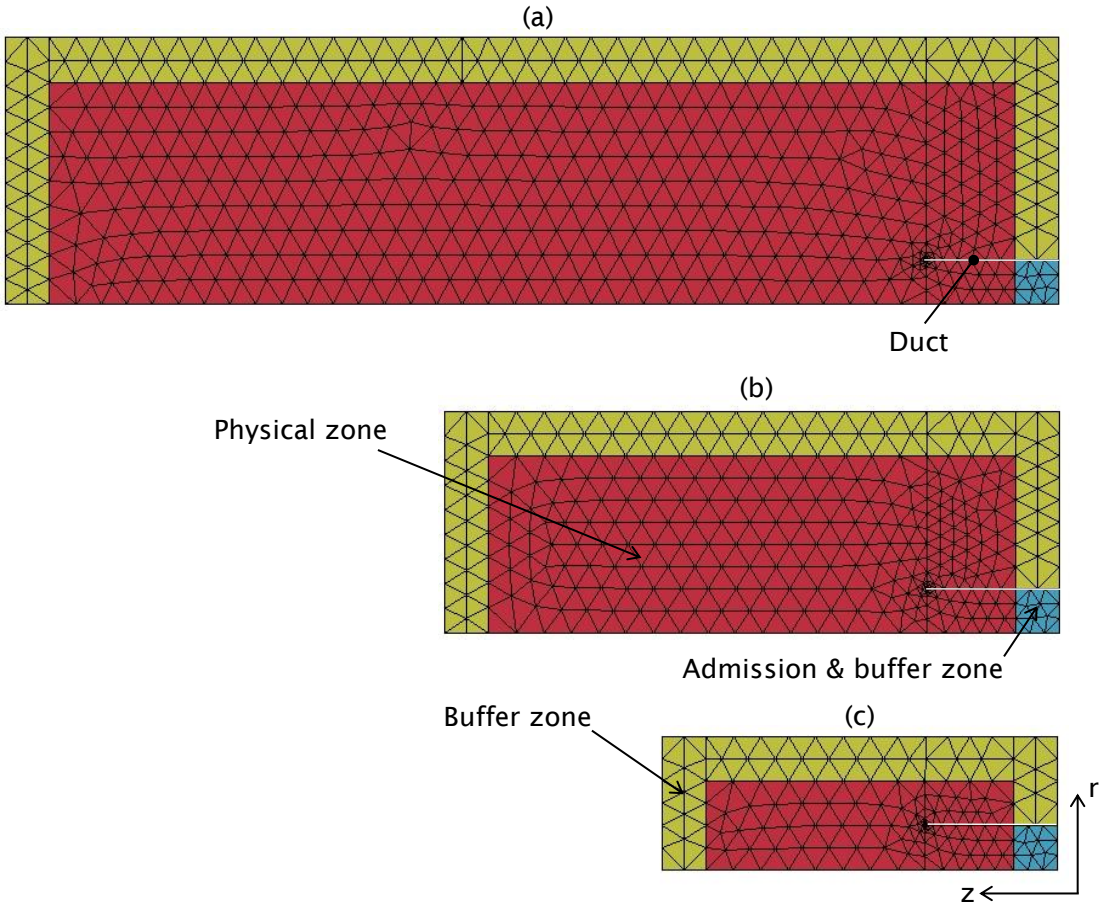

Figure 5.2: The meshes used for the sensitivity study of the computational domain size: (a) large (20x5R_0), (b) medium (10x4R_0), and (c) small (5x2R_0).

A comparison of computed and analytic SPL on a far-field arc is presented in figure 5.3. The polar angle is measured from the positive z axis. Good agreement to the analytical solution is observed for the three domains. The directivity lobes are well resolved. However, small discrepancies in SPL of approximately 0.5 to 1dB are observed. The largest domain shows slightly better accuracy in resolving these lobes. It is believed that less reflection from the buffer zone contaminates the solution. However, the largest domain provides a less accurate solution at a directivity of 90 degrees, where a difference of approximately 2dB is evident. In all cases, for the polar angles above 100 degrees some numerical oscillation is observed. The Ffowcs-Williams and Hawkings solution is obtained by using the free-space Green's function. Therefore, the solution may not be accurate in range of the polar angles where there is an interaction between the FWH surface and the geometry analysed.

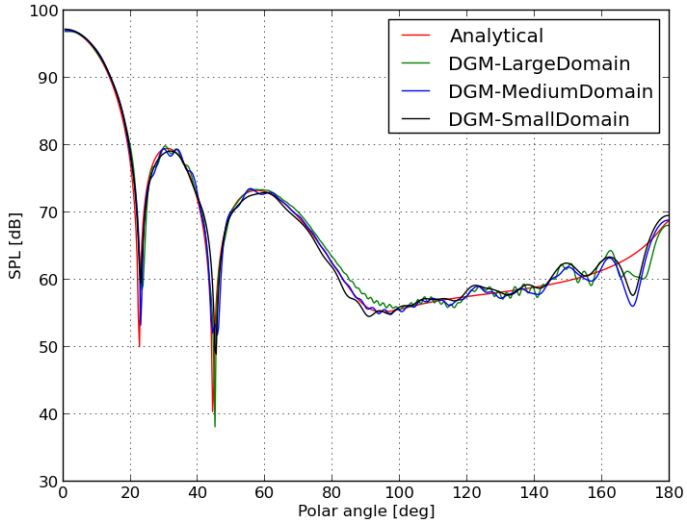

Figure 5.3: The far-field SPL directivity. Comparison between the DGM results for different sizes of the computational domain and the analytical solution, zero flow. A plane wave (mode (0,1)) with kR_0 = 10.

A significant difference in CPU time is observed for the different model sizes (see Table B.2 in Appendix B.1). The solution is integrated in the time domain, and the larger region of modelling results in more time steps since these are related to element size, and hence longer computational time. Additionally, when the larger model is used the number of degrees of freedom increases which slows down the calculations. The accuracy is not greatly affected by the domain size while the CPU time is highly dependent.

5.2.1.2 The effect of mesh resolution

The next set of calculations is performed in order to examine the convergence of the model with respect to element size. It is carried out for three different mesh refinements which are presented in figure 5.4. They are as follows: 1-2 elements per wavelength with the highest element order of 6 (figure 5.4 (a)), 4-5 elements per wavelength with the highest element order of 3 (figure 5.4 (b)), and 8-10 elements per wavelength with the highest element order of 2 (figure 5.4 (c)). The mesh resolution and domain size of the first coarse mesh correspond to the small computational domain model used in the previous study. Calculations are performed for a plane wave with kR_0 = 10. Details are showed in Appendix B.2.

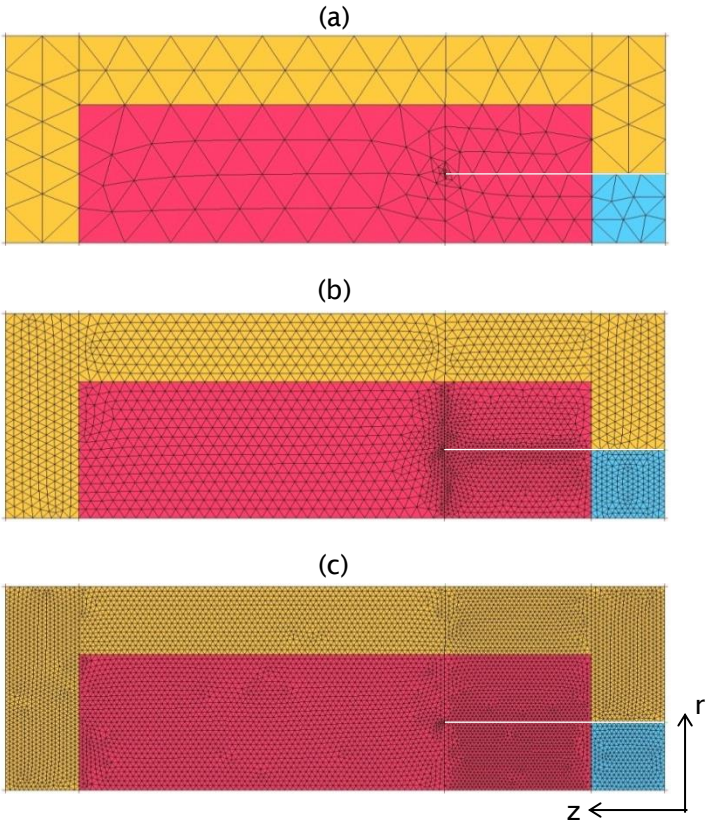

Figure 5.4: The meshes used for the mesh refinement study: (a) 1-2 elements per wavelength (the highest element order is 6), (b) 4-5 elements per wavelength (the highest element order is 3), and (c) 8-10 elements per wavelength (the highest element order is 2).

The SPL comparison in the far-field is shown in figure 5.5. It is plotted against the polar angle measured from the positive z axis. Good agreement to the analytical solution is achieved for all analysed mesh refinements. Some minor problems with the accuracy, similar to those reported in the previous section, are observed. The comparison clearly shows no influence of the mesh refinement on the accuracy. This is a significant outcome, showing that the automatic selection of polynomial order is correctly implemented (Eq. 2.34). It proves that unnecessary mesh over-refinement decreases dramatically efficiency, but not improving the accuracy.

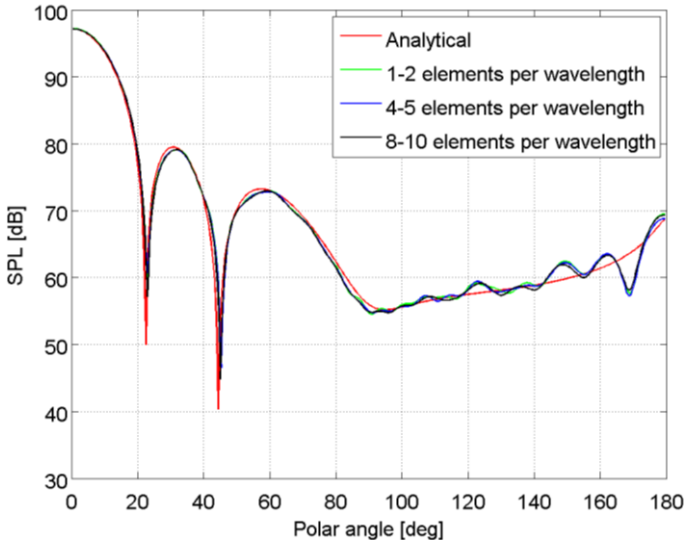

Figure 5.5: The far-field SPL directivity. Comparison between the DGM results for different mesh resolutions and the analytical solution, zero flow. A plane wave (mode (0,1)) with kR_0 = 10.

5.2.1.3 The effect of element order

The influence of element order on the accuracy and efficiency is studied. Two meshes are used: one with refined duct lip and second with uniformly sized elements. They are presented in figure 5.6 for three Helmholtz numbers, kR_0 = 10, 20, and 30. The polynomial order within each element is determined by Actran DGM based on the Helmholtz number and element size. The colour maps show the values of the element orders across the meshes; the left column corresponds to refined lip model, whereas the right column corresponds to the model with uniformly sized elements. The rows correspond to the three Helmholtz numbers. This gives the following average values of the number of wavelengths per element: 1 element per wavelength for kR_0=10, 0.5 elements per wavelength for kR_0=20, and 0.25 elements per wavelength for kR_0=30. The parameters used in these calculations are included in Appendix B.3.

Comparisons of computed and analytic SPL along a far-field arc are presented in figure 5.7. Reasonably good agreement (maximum difference is approximately 2dB) is achieved for an almost cut-off mode (8,1) with the non-dimensional wavenumber kR_0 =10 as shown in figure 5.7 (a). No influence of the grid refinement is observed in this case. This holds up to kR_0=20. The comparison for the mode (17,1) is presented in figure 5.7 (b).

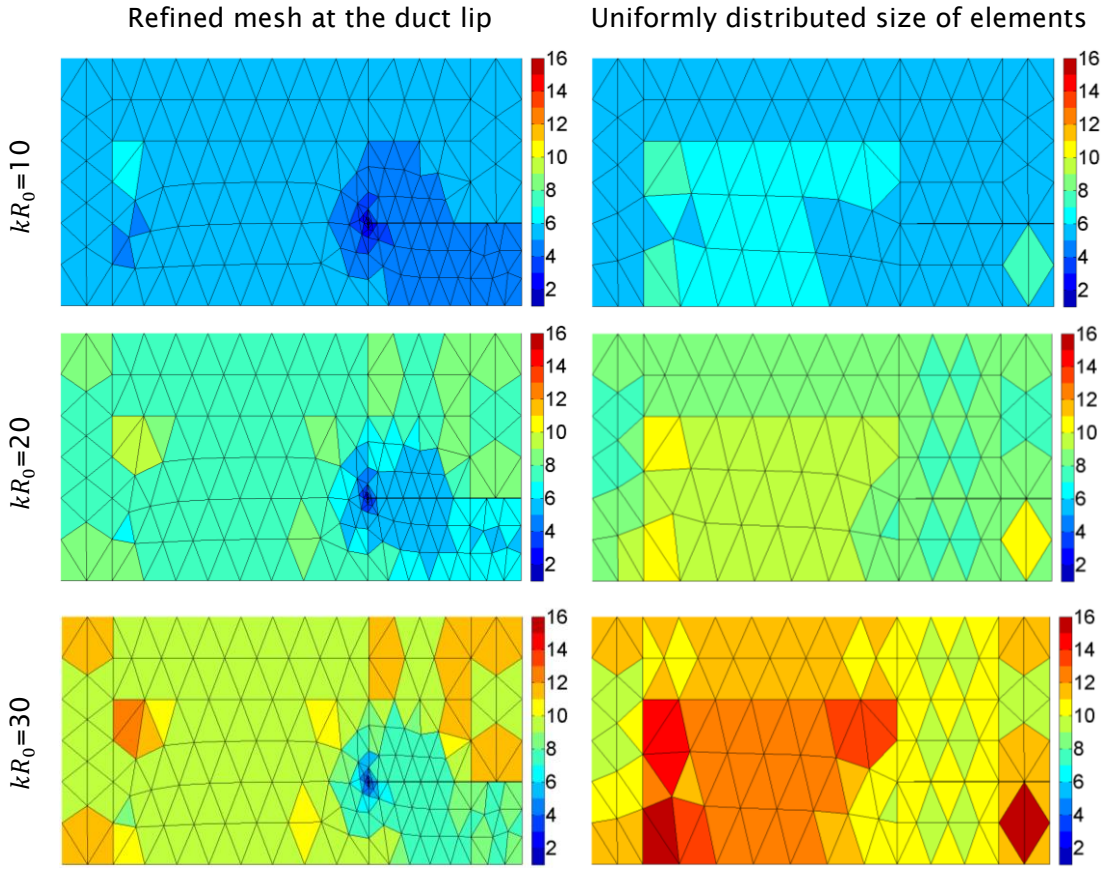

Figure 5.6: A distribution of selected element orders for two meshes used in the sensitivity study of elements orders on the DGM efficiency and accuracy.

In this case, however, some discrepancies are observed at low and high polar angles. Poor agreement is observed for the highest wavenumber kR_0=30. The results for modes (9,5) and (27,1) are presented in figure 5.7 (c) and (d), respectively. The amplitude of the principal lobe of the moderately cut-on mode (9,5) is predicted reasonably well, but the radiation lobes are less well resolved for small and moderate polar angles. Also, worse agreement is observed when a uniformly refined grid is used, as indicated by poor resolution and considerable error at a polar angle of around 80 degrees. In case of the almost cut-off mode (27,1), figure 5.7 (d), the mode shape is well recovered but the amplitude is underestimated by approximately 6dB. In general, the accuracy can be improved by using a finer mesh.

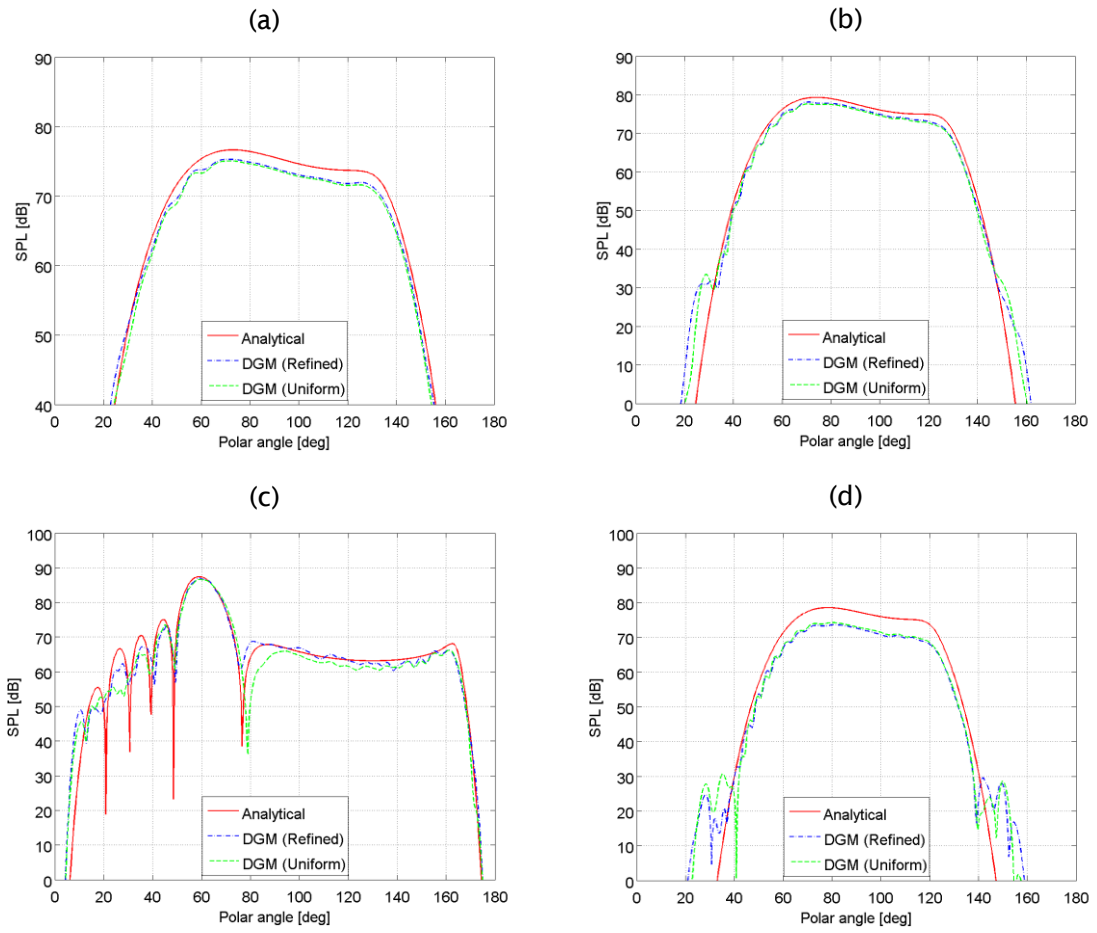

Figure 5.7: The far-field SPL directivity. Comparison between the DGM results for the two studied meshes: refined trailing edge, and uniform resolution and the analytical solutions, zero flow. (a) Mode (8,1), kR_0=10 (almost cut-off mode). (b) Mode (17,1), kR_0=20 (almost cut-off mode). (c) Mode (9,5), kR_0=30 (moderately cut-on mode). (d) Mode (27,1), kR_0=30 (almost cut-off mode).

The numerical experiment revealed dependency of the DGM accuracy on the element orders. Despite, already having showed advantages of using high order approximations, a very high order approximation may lead to locally inaccurate solution. It is shown that the mesh resolution of approximately 0.25 elements per wavelength, which results in elements orders between 13 and 15, leads to poor accuracy. Good meshing practice can be drawn from this study, namely the elements orders should not exceed a number of 8-9.

The study also showed that the refinement of sharp edges is not necessary as long as the global mesh resolution is sufficient.

5.2.2 3D model, zero flow

A parametric study of the mesh refinement for 3D DGM model of the Munt problem with zero flow is performed. The meshes are shown in figure

5.8. The first mesh is uniformly refined to 1 element per wavelength. The second is uniformly refined to 2 elements per wavelength. The last mesh, which is illustrated in figure 5.8 (c), is refined to 4 elements per wavelength in the duct region and to 1 element per wavelength elsewhere. The parameters used for the subsequent calculations are provided in Appendix B.4.

The DGM calculations are performed for a plane wave, moderately cut-on mode (5,4), and almost cut-off mode (17,1) separately on the same coarse mesh (figure 5.8 (a)), and for kR_0=20. The results of the three cases are illustrated in figure 5.9. Sound pressure levels are compared to the analytical solution on a far-field arc with the polar angle measured from the positive z axis. It is evident that the errors in these solutions increase with the azimuthal order. Reasonable agreement is achieved for a plane wave, but deteriorates at lower angles for the moderately cut-on mode (5,4), as illustrated in figure 5.9 (b). Moreover an unjustified fall of the SPL of approximately 13dB occurs at the angle of 100 degrees. In the case of the almost cut-off mode (17,1), figure 5.9 (c), the agreement in the middle range of the polar angles is fairly similar to that for the moderately cut-on mode, but deteriorates at the low and high polar angles, where the DGM solution does not correspond to the analytical solution.

In order to investigate the large discrepancies in the far-field SPL directivity between the DGM and analytical solutions we examine the near-field DGM solution for the incident mode (17,1) with kR_0=20. The near-field of the instantaneous pressure is presented in figure 5.10.

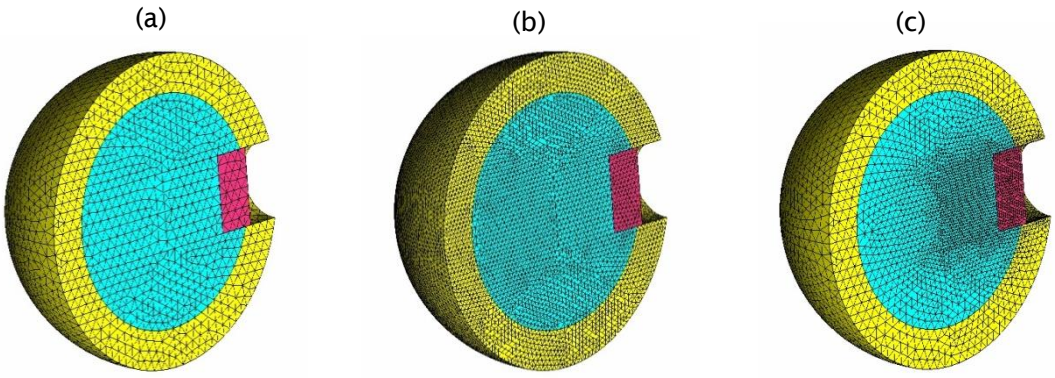

Figure 5.8: 3D meshes used for the Munt problem study, zero flow: (a) coarse mesh: 1 element per wavelength (element orders between 4 and 7), (b) uniformly refined mesh: 2 elements per wavelength (element orders between 3 and 5), and (c) refined duct only: 4 elements per wavelength – duct, 1 element per wavelength – elsewhere (element orders between 2 and 7).

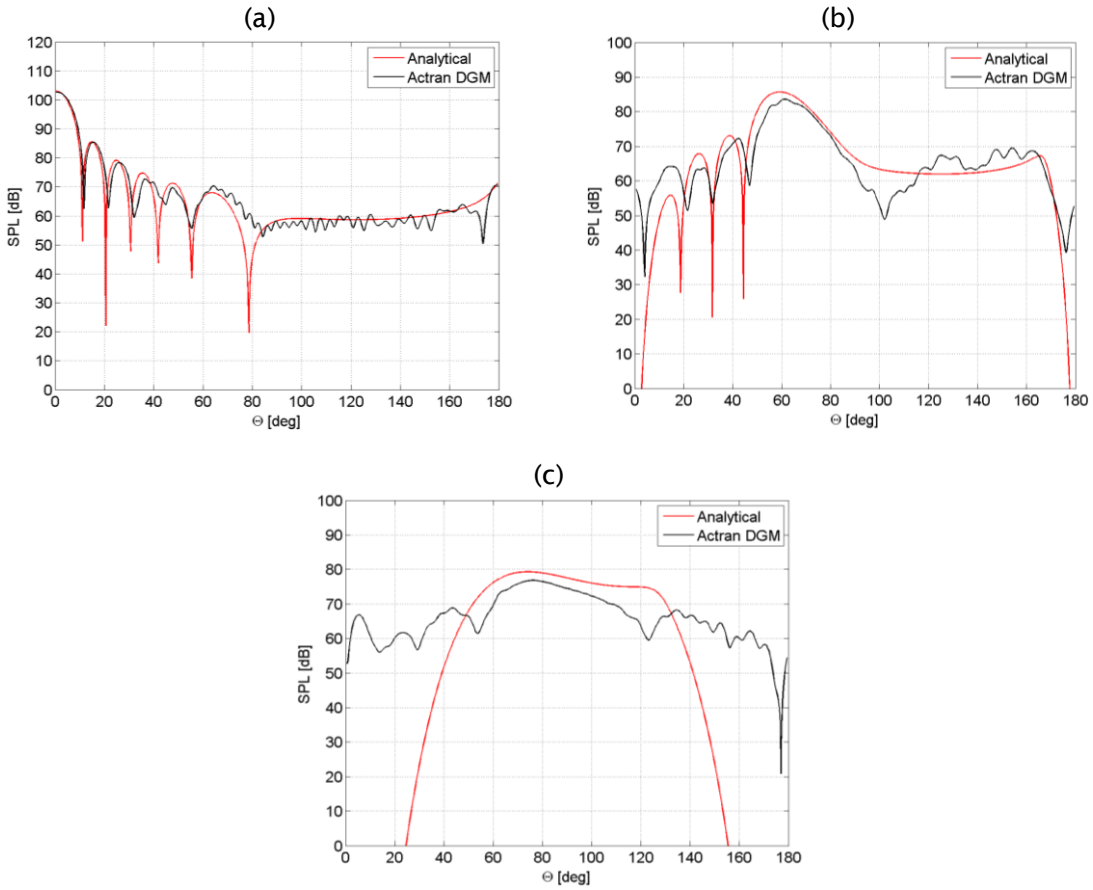

Figure 5.9: The far-field SPL directivity. Comparison between the 3D DGM results and the analytical solution, zero flow. The coarse mesh: 1 element per wavelength (Element orders between 4 and 7). A single incident mode with kR_0=20: (a) a plane wave (mode (0,1)), (b) mode (5,4), and (c) mode (17,1).

When contours of the instantaneous pressure field are plotted at uniform intervals over the full range of acoustic pressure the solution manifests the expected behaviour. However, when contours are plotted for a range of values closer to zero, figure 5.10 (b), some spurious scattered modes are evident at the centre of the duct. They are at approximately of 0.4 % of the pressure amplitude. Detailed studies have been conducted in order to verify whether the numerical solution has converged to a steady time-harmonic state by allowing longer simulation times. Moreover, the influence of element orders used for the spatial discretisation on the near field solution has been investigated. The results of the studies are not presented in this work. However, they confirmed that the solution reached the steady time-harmonic state. And there is no influence of the element orders on the near field solution.

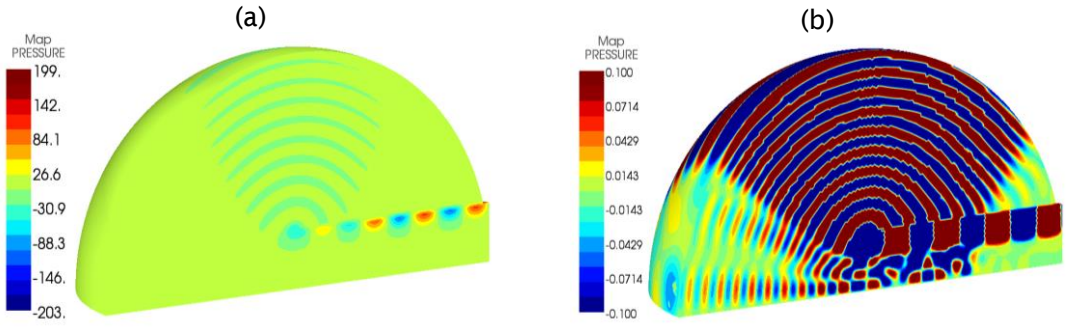

Figure 5.10: The near-field solution of the instantaneous pressure [Pa] for the incident mode (17,1) with kR_0=20, zero flow: (a) full scale, and (b) exaggerated scale.

The above behaviour appears to be related to the quadrature free formulation of the DGM, which is implemented in Actran DGM. This requires the elements edges and faces are straight and flat. The geometry of the duct is therefore approximated by a series of facets rather than being represented as a continuous cylindrical curve. This causes scattering of spinning modes, which can be understood in terms of Tyler & Sofrin scattering [12]. Defined as $m_{scattered} = nm + qV$, where m is azimuthal order, V is the number of element edges or faces, n=1,2,3…, and q is any integer. As a result, the total modal power is partly redistributed to scattered modes of other azimuthal orders. The generation mechanism of the spurious modes for an idealized case is illustrated in figure 5.11. In real applications, where the mesh size is not uniformly distributed, the spinning modes scatter randomly into a number of azimuthal and radial orders.

In order to confirm this hypothesis, propagation of a single incident mode through a finite length duct is investigated. The radius of the duct and rest of the parameters remain unchanged. The almost cut-off mode (17,1) with kR_0=20 is considered. 2D-axisymmetric and 3D models are studied.

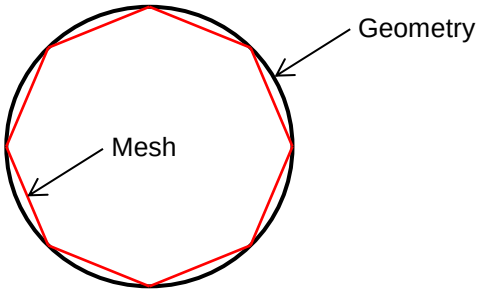

Figure 5.11: A mechanism of the spurious mesh-scattered modes generation.

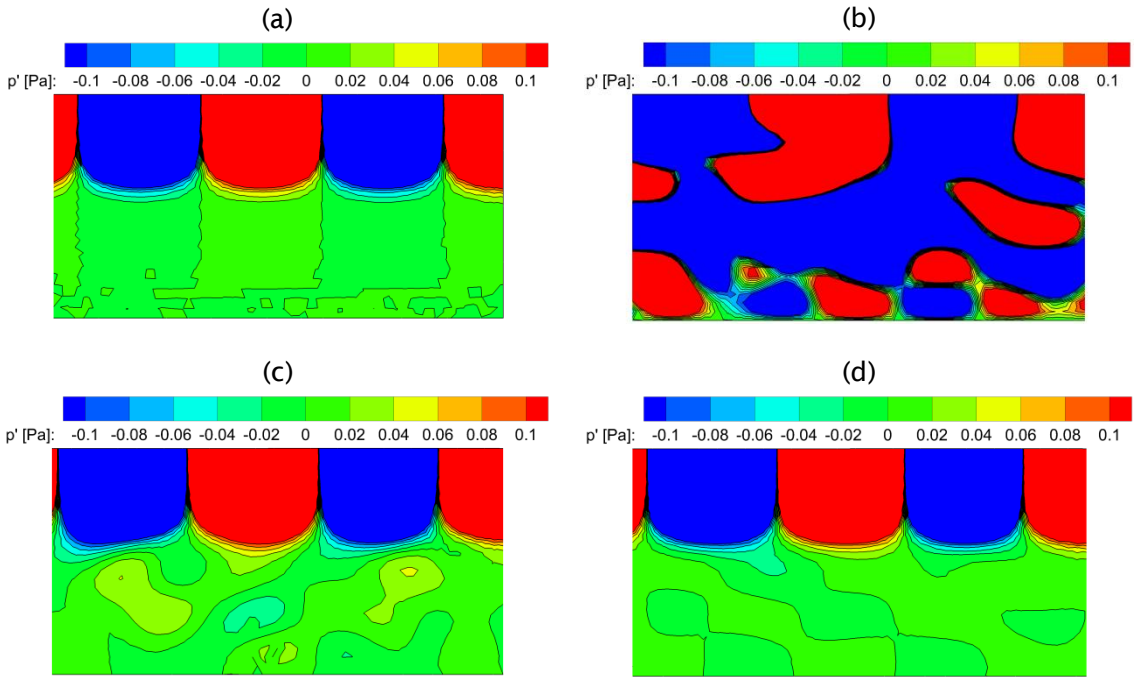

Figure 5.12: The near field solution of the instantaneous pressure [Pa] in the isolated duct for a single incident mode (17,1) with kR_0=20, zero flow, exaggerated scale to 1% of the mode amplitude: (a) 2D axisymmetric duct, (b) 3D duct, the wall refinement is 1 element per mode azimuthal order, (c) 3D duct, the wall refinement is 3 elements per mode azimuthal order, (d) 3D duct, the wall refinement is 14 elements per mode azimuthal order.

The colour maps of the instantaneous pressure are shown as figure 5.12. The contours of the instantaneous pressure field are plotted for a range of acoustic pressure corresponding to 1% of the mode amplitude. As expected, mesh scattering does not occur in the 2D-axisymmetric simulation. The colour map in figure 5.12 (a) reveals no evidence of the acoustic waves at the centre line of the duct. The spurious mesh-scattered azimuthal modes are however evident in the 3D simulations. This is shown in figures 5.12 (b), (c), and (d) for refinements of 1, 3, and 14 elements per mode azimuthal order, respectively. The scattered modes vanish gradually with increasing wall refinement.

The same behaviour can be reproduced in the 3D Munt solutions. The far field directivities from a mesh refinement study of the original 3D Munt problem are presented in figure 5.13 and compared to the analytical solution. Two incident modes are considered; a moderately cut-on mode (5,4), and an almost cut-off mode (17,1) for a wavenumber kR_0=20. The accuracy improves as the mesh is refined. Uniformly and locally refined in the vicinity of the curved wall meshes provide similar accuracy.

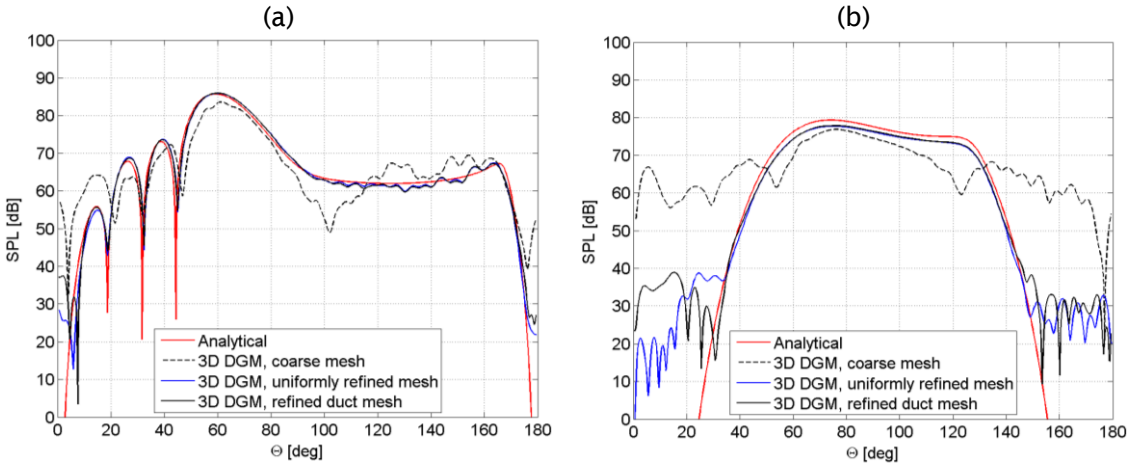

Figure 5.13: The far-field SPL directivity. Comparison between the 3D DGM results for different mesh refinements and the analytical solution, zero flow. A single incident mode with kR_0=20: (a) mode (5,4), (b) mode (17,1).

It is an important outcome confirming the necessity of mesh refinement at the curved wall but not requirement elsewhere. For the refined meshes the difference in dB between the peak value of the SPL and the numerical noise is about 40dB. This level of the numerical noise is acceptable from a practical point of view. One should note that the comparisons are made by using a logarithmic scale, where 20dB corresponds to change at one order of magnitude in the acoustic pressure.

A best practice for refining the mesh can be concluded from this study. It is found that, approximately 4 elements per azimuthal mode order at the wall and approximately 1 element per characteristic wavelength elsewhere (element orders between 2 and 7) gives reasonable solutions. This allows the full potential of the DG method to be realized in the coarser region. It is important to note that the size of the smallest element should be carefully selected as it determines the overall time step for the DGM simulations (see sections 2.7.3 and 3.4.6 for details).

5.2.3 The effect of mean flow

5.2.3.1 Uniform inflow

DGM simulations for uniform (constant) inflow are presented in this section. Mach numbers of 0.1, 0.4 and 0.6 are considered. The velocity in the duct and in the free stream is assumed to be the same. Results are presented for axisymmetric and 3D models.

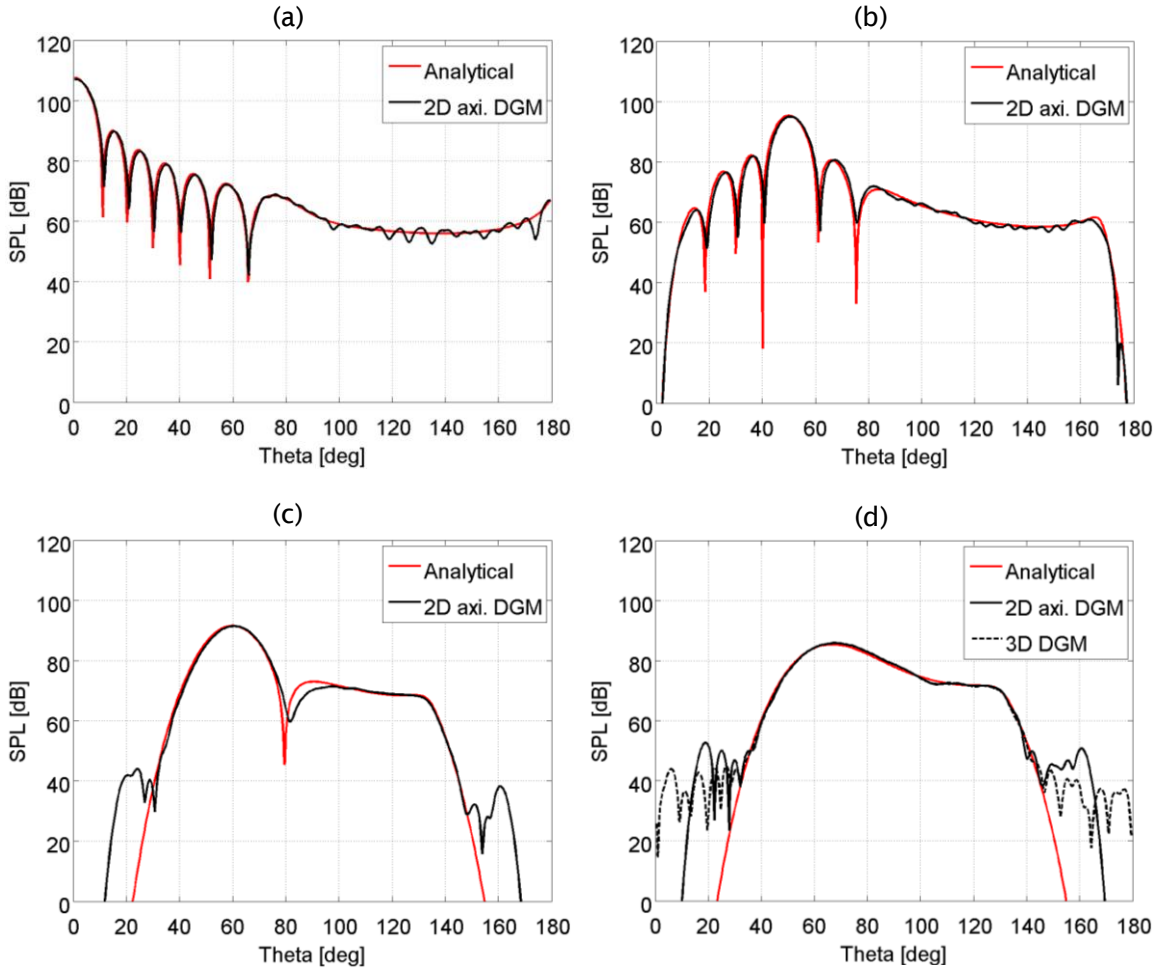

Figure 5.14: The far-field SPL directivity. Comparison between the DGM results and the analytical solution for a single incident mode with kR_0=20 propagating against a uniform inflow: (a) mode(0,1), Mach number of 0.4, (b) mode (5,4), Mach number of 0.6, (c) mode (17,1), Mach number of 0.6, and (d) mode (17,1), Mach number of 0.4.

The mesh refinement is realized according to the best practice identified in the previous section. Parameters (including information on the mesh refinement and element orders) used for the data presented here are given in Appendix B.5. The comparisons of the computed SPL with the analytical solution in the far-field for the case kR_0=20 are shown in figure 5.14 for modes (0,1), (5,4), and (17,1). Good agreement is observed for the plane wave for Mach number of 0.4 (figure 5.14 (a)). The oscillations at high polar angles, as reported previously, are a result of the FWH calculation. Good accuracy holds for moderately cut-on modes (5,4) and (17,1) for the Mach number of 0.6, figure 5.14 (b) and (c). However, for the higher azimuthal order mode (17,1) the decay at 80 degrees between radiation lobes is poorly resolved. This is a result of a slightly too coarse mesh used for calculation with a higher mean flow velocity (Mach number of 0.6). The study of the mean flow effects has been

performed for a single mesh. Therefore cases with higher mean flow velocity used higher order spatial approximation. The problem of inaccuracy when the element order is too high was already discussed in section 5.2.1.3. In case of the less cut-on mode (17,1) at Mach number of 0.4, figure 5.14 (d), the directivity is well represented for polar angles between 30 and 140 degrees. The numerical error noted previously in the case of zero flow is evident for low and high polar angles, but is approximately 40 dB below the peak values. Similar results are obtained for 2D axisymmetric and 3D models.

5.2.3.2 Uniform exhaust flow

A study analogous to the previous one is conducted for an exhaust flow in which the flows in the pipe and in the free field have the same velocity. Similarly as in the previous section, the mesh refinement is realized according to the best practice identified in section 5.2.2. Parameters (including information on the mesh refinement and element orders) for these computations are attached in Appendix B.5. Most of the conclusions from the inflow study hold. Additionally, it is found that the DGM properly models the vorticity shedding from the trailing edge of the duct as specified by the Kutta condition. This is shown in figure 5.15, where the numerical solution is compared to the analytical solution with Kutta condition 'on' and 'off' for kR_0=20, Mach number of 0.4, and for modes (5,4) and (17,1). The DGM solution matches well to the analytical solution with the Kutta condition imposed.

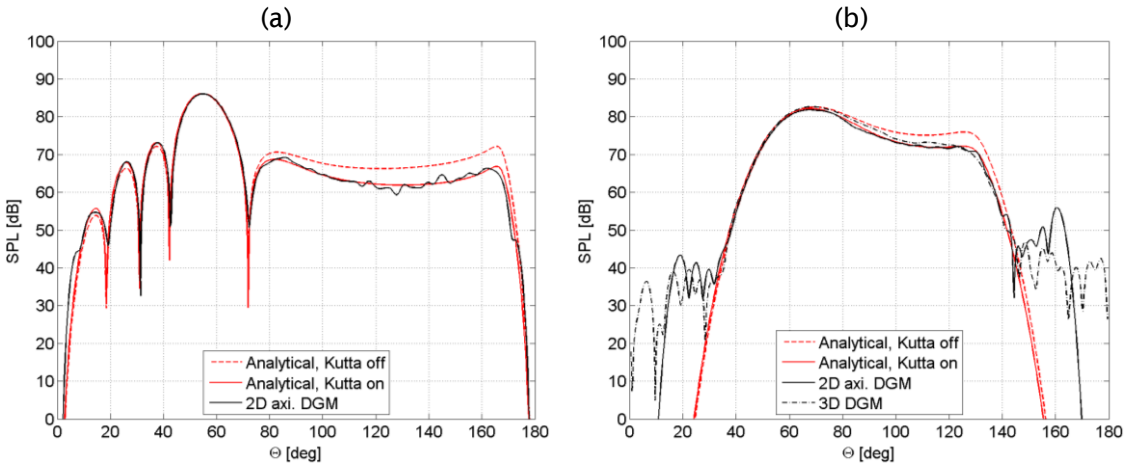

Figure 5.15: The far-field SPL directivity. Comparison between the DGM results and the analytical solution for a single incident mode with kR_0=20 propagating in a uniform outflow at Mach number of 0.4: (a) mode (5,4), (b) mode (17,1).

One may note that the DGM manifests similar accuracy levels for zero flow and uniform flow cases in both inflow and outflow configurations when sufficient mesh resolution is used. This is reasonable, since the acoustic perturbations are solved on top of the mean flow which is obtained independently prior to the acoustic computations. Moreover, when zero flow and uniform flow cases are considered the vector $\boldsymbol{G}$ in equation (2.12) is zero vector.

5.2.3.3 Inclusion of a shear layer and a mixing layer

In the numerical model a mixing layer of finite width can be included in the calculations. In case of the analytical model a shear layer is assumed, as described earlier, between the jet and the surrounding flow. A study of the numerical solution in the presence of a mixing layer is conducted. In order to generate the mixing layer a RANS solution (see section 3.3.4) is computed for the mean flow. The Mach number in jet flow is set to 0.4 and in free stream to 0.1. The resulting mean flow is shown in figure 5.16. The flow has a potential core and mixing layer. The potential core extends approximately 9 diameters along the axis.

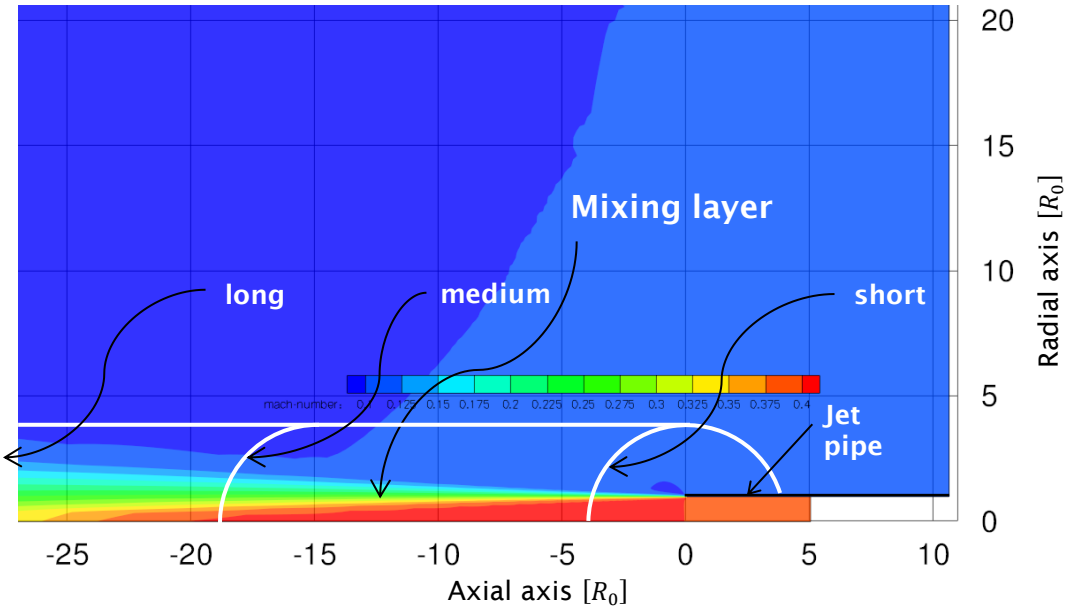

Figure 5.16: Non-uniform turbulent mean flow: Mach number of 0.4 in jet, and Mach number of 0.1 in free stream. Solid white lines indicate the extent of 'long', 'medium', and 'short' DGM domains.

The acoustic field is excited by a single incident mode. Three representative modes are considered, i.e. mode (0,1), mode (5,4), and mode (17,1) with kR_0=20. The mesh refinement is realized according to the best practice identified in section 5.2.2. Parameters (including information on the mesh refinement and element orders) used for these computations are attached in Appendix B.5 and in tables B.15 and B.16.

The calculations are performed for three lengths of the cylindrical computational domain: short, medium and long. The outer boundaries of the three domains are indicated in figure 5.16. They correspond to three axial extends of the mesh of: 4, 17, and 30 duct radii downstream of the exit.

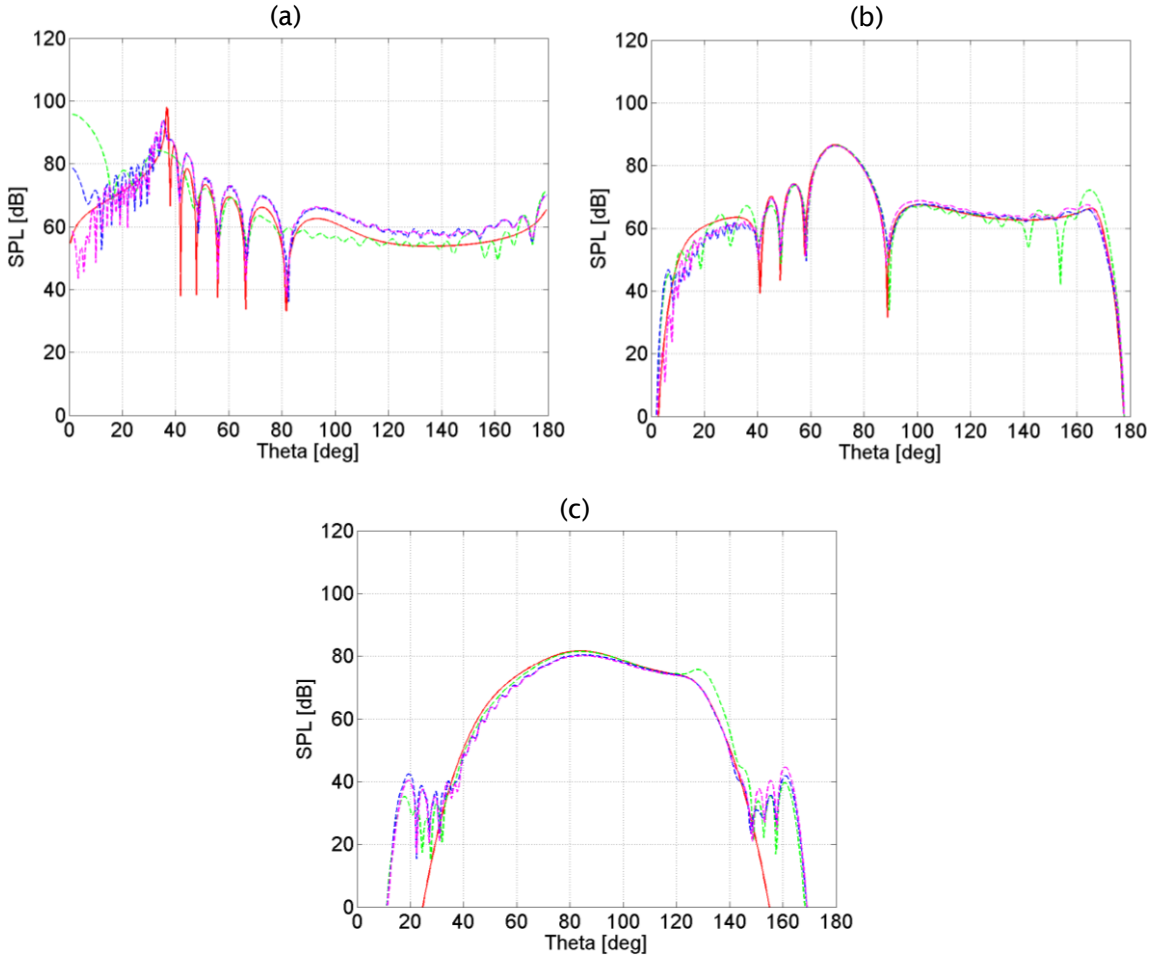

Figure 5.17: The far-field SPL directivity. Comparison between the DGM results and the analytical solution for a single incident mode with kR_0=20 propagating in a non-uniform outflow with mixing layer. Solid red line: analytical solution with Kutta condition 'on' and no mixing layer; dashed green line: 2D axisymmetric DGM solution for short domain (L = $4R_0$); dashed blue line: 2D axisymmetric DGM solution for medium domain (L = $17R_0$); and dashed pink line: 2D axisymmetric DGM solution for long domain (L = $30R_0$). (a) mode (0,1), (b) mode (5,4), and (c) mode (17,1).

The results are presented in figure 5.17. This shows far field directivities for modes (0,1), (5,4), and (17,1), respectively. The solutions converge to a close approximation of the analytical solution as the size of the domain increases. However, the analytical solution does not include the effect of the mixing layer therefore an exact correspondence is not expected. It is most evident for the plane wave, figure 5.17 (a), where the directivity pattern differs significantly from the pattern predicted analytically. Moreover, the cone of silence is not properly captured. This is manifested by an artificial radiation lobe at the centreline which can be seen in figure 5.17 (a) in the solutions for L = $4R_0$, and L = $17R_0$. In the case of the moderately cut-on mode (5,4), figure 5.17 (b) for the short domain, few artificial radiation lobes are evident for the polar angles up to 40 degrees. This is due to fact that the mean flow refraction effects are not properly modelled in not sufficiently long computational domains. An important portion of the jet and mixing region is cut-off. For the longer domains the cone of silence is better resolved as illustrated in figure 5.17 (a) by the solution for L = $30R_0$, and figure 5.17 (b) for the extended domains. In the case of the high spinning mode (17,1), figure 5.17 (c), the DGM solutions are similar for all three sizes of the physical domain. This is caused by fact that the mode (17,1) radiates nearly perpendicular to the longitudinal axis, and in this direction the domain's sizes remain unchanged. However, some unjustified rise in the SPL is observed for the short domain, which takes place at the polar angles of approximately 130 degrees. Moreover, strong oscillations are evident for the moderately cut-on mode at high polar angles for the short domain as can be seen in figure 5.17 (b).

5.3 Assessment of the DGM liner model: A cylindrical lined duct with a hard patch

In this section the DGM is applied to a lined duct problem. A straight circular duct with a uniform mean flow is considered. The extended Helmholtz resonator model with the Myers boundary condition is used to model lined surfaces (see section 2.7.6). The DGM results are compared to Actran TM [93] predictions in which a convected Helmholtz solution in the frequency domain (Eq. 2.18) is obtained by applying the finite element method [31] [36]. Actran TM is regarded, here, as a reference solution having been validated against analytical solutions for similar configurations [94].

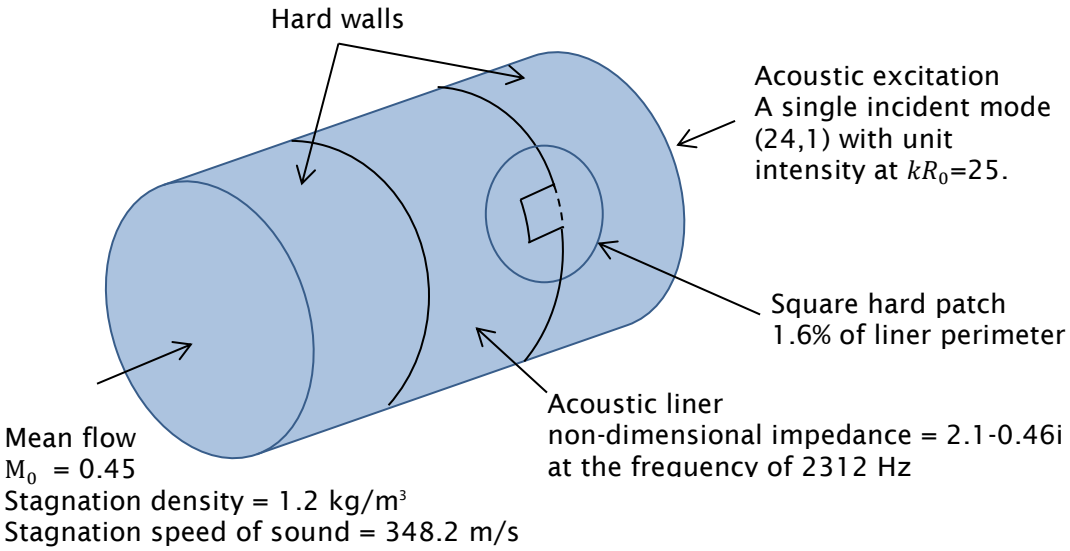

Figure 5.18: The physical model for the liner validation.

Acoustic propagation through a cylindrical duct of radius, R_0 = 0.635m is considered. An acoustic liner is placed in the middle section of the duct as shown in figure 5.18. Two cases are considered, one with a uniform liner and second one containing a hard patch. The lined section is 0.6 m long. The square hard patch has dimensions 0.06 by 0.06 m which is approximately 1.6% of the perimeter. The acoustic liner is defined by a non-dimensional impedance of 2.1–0.46i at the frequency of 2312 Hz. A single mode (24,1) with unit intensity is injected at the right hand side of the duct as shown in figure 5.18. The Helmholtz number for this problem is kR_0 = 25. A uniform flow is present with velocity corresponding to the Mach number of 0.45. The acoustic mode propagates against the flow (intake problem).

5.3.1 Uniform liner

The case with uniform liner is considered first. The DGM model is specified according to the description given in section 3.4. This consists of the three main components; admission zone, physical zone, and buffer zone. The computational mesh is defined to achieve optimal DGM performance and an appropriate resolution of the duct's outer wall. 6 elements per azimuthal mode order and 1 element per upstream wavelength are applied at the duct's wall and elsewhere, respectively. This is modelled as a 2D axisymmetric problem.

Acoustic pressure is measured along the duct wall. The SPL comparison to the Actran TM solution is presented in figure 5.19.

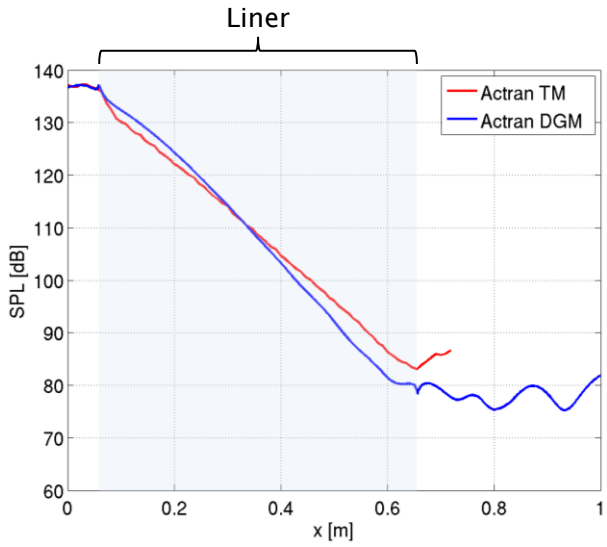

Figure 5.19: The SPL comparison between the DGM and Actran TM results along the duct wall – Uniform liner ($Z = \rho_0 c_0(2.1 - 0.46\mathrm{i})$ at 2312 Hz). A single incident mode (24,1) with kR_0 = 25 propagating against a uniform inflow with Mach number of 0.45.

Overall, the DGM solution agrees reasonably well with the Actran TM results. There are, however, some discrepancies in the predicted rate of attenuation. The slope of the attenuation in dB predicted by DGM is not linear. As a result of this the attenuation at the end of the liner is approximately 5dB lower than that predicted by Actran TM.

In order to deal with instabilities, which may occur along the lined surfaces when the Myers boundary condition is applied in the time domain (see section 2.4.2 for details), a spatial filter is applied to the convective term ($\boldsymbol{u}_0 \cdot \nabla \mathrm{p}'$) of the Myers boundary condition (Eq. 2.23) in the DGM code used in this work, as described in section 2.7.6. The discrepancies in the attenuation rate shown in figure 5.19 can therefore be attributed to the spatial filtering applied in the DGM, and to the assumption of constant impedance along the liner (Eq. 2.23). If the spatial filter is not applied to the convective term then an instability occurs at the beginning of the liner as can be seen in figure 5.20 (a) and zoomed-in figure (c). The near-field acoustic pressure solution is shown at the simulation time t_0 equal to 6 time periods. The instability grows rapidly with time leading to unstable solution. This behaviour agrees with that reported by Chevaugeon et al. [92]. The solution is stable at the same simulation time t_0 when the spatial filter is applied, as shown in figure 5.20 (b).

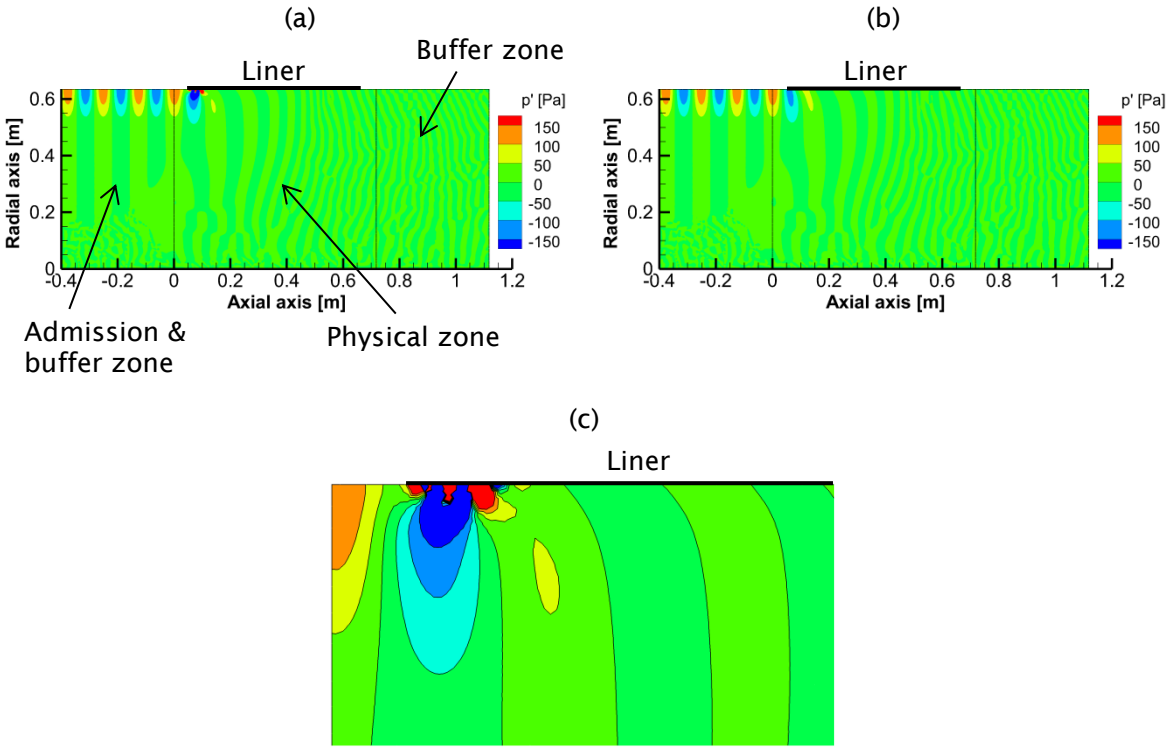

Figure 5.20: The near field solution of the instantaneous pressure [Pa] in the isolated duct with uniform liner ($Z = \rho_0 c_0(2.1 - 0.46\mathrm{i})$ at 2312 Hz) obtained at the simulation time t_0 equal to 6 time periods (the DGM solution is not coverged). A single incident mode (24,1) with kR_0 = 25 propagating against a uniform inflow with Mach number of 0.45. The spatial filter in the Myers boundary condition, (a) is deactivated, and (b) is working. (c) Zoomed-in view of the instability when the spatial filter is deactivated.

In the case of a generic turbofan intake at realistic frequencies and flow conditions which is considered in section 5.4.2 much larger discrepancies between Actran DGM and TM predictions were observed for lined intakes. Therefore, in order to investigate the issue further, the problem of inaccuracy has been reproduced for a straight unflanged cylindrical duct in the presence of uniform mean flow. Results of this investigation are included in Appendix C.

5.3.2 Influence of the hard patch

A study is conducted to assess the ability of the DG method to predict scattered modes and their influence on liner attenuation. The model is similar to one used in previous section. The mesh used in this study is shown in figure 5.21 (a). This is 3D unstructured mesh of tetrahedral elements constructed according to the description given in section 3.4.7. It is refined to 6 elements per azimuthal mode order at the duct wall and to 1 element per upstream wavelength elsewhere. The hard patch is further refined by using up to 15 elements per upstream wavelength.

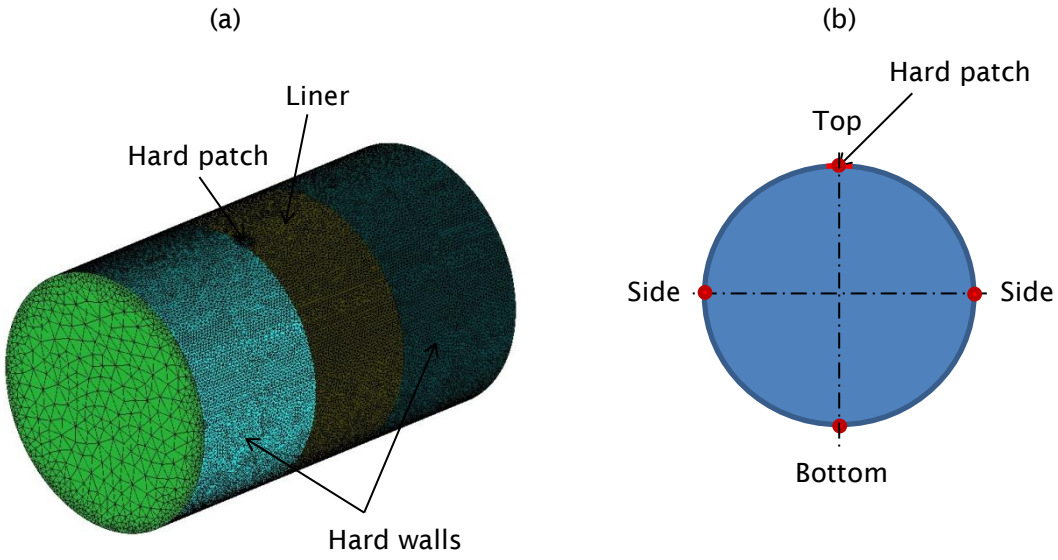

Figure 5.21: A study of the influence of the hard patch: (a) the computational mesh, (b) Front view of the duct – orientation of measurement arrays of points.

The sound pressure is recorded from the TM and DGM solutions at four axial arrays of points along the outer wall. Orientation of the arrays with respect to the duct is shown in figure 5.21 (b): 'Top' – the array of points is placed in the middle of the square hard patch, 'Bottom' – the array of points is placed below the hard patch on opposite duct wall, and 'Side' – the arrays of points are placed on both sides of the duct wall.

A comparison of computed values of SPL at the measurement arrays is shown in figure 5.22. The DGM results are compared to Actran TM solutions. The same conclusions hold as for the uniform liner case. Similar differences in the attenuation rate between Actran DGM and TM are achieved. Maximum discrepancies in the SPL are also at similar levels, i.e. approximately 5 dB. Additionally, strong standing waves are observed at the end of the liner. These are particularly noticeable at the top position, where the hard patch is placed, as shown in figure 5.22 (a). This is caused by spurious reflections from the buffer zone.

The DGM results clearly show that the buffer zone in this case is not fully effective. The efficiency of the buffer zone has been significantly improved for similar in-duct problems considered in chapter 6 by using three times thicker buffer zone with the optimal parameters given in section 2.7.4.2.

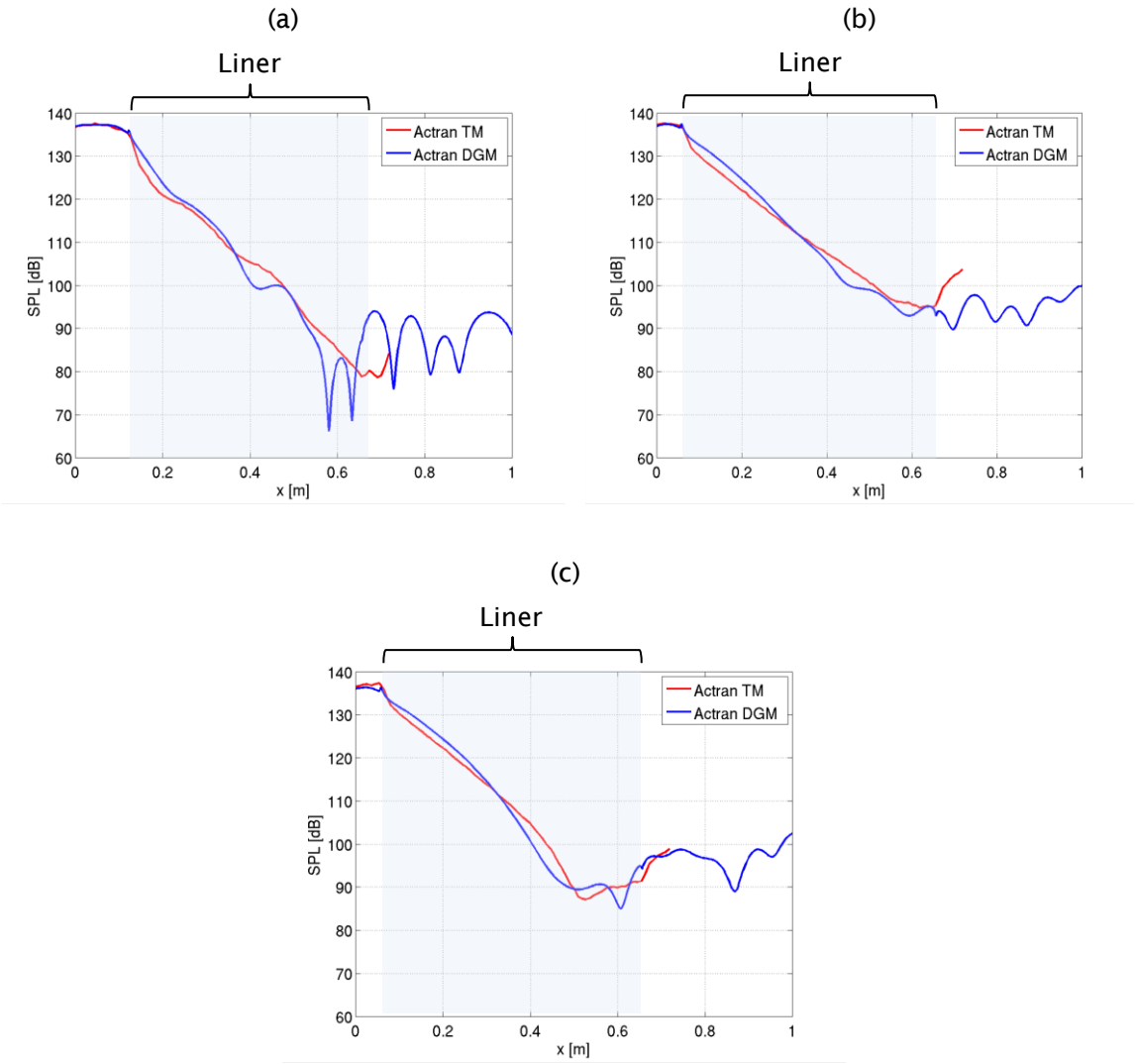

Figure 5.22: The SPL comparison between the DGM and Actran TM results along the duct wall. Non-uniform liner ($Z = \rho_0 c_0(2.1 - 0.46\mathrm{i})$ at 2312 Hz). A single incident mode (24,1) with kR_0 = 25 propagating against a uniform inflow with Mach number of 0.45. (a) Top – middle of the hard patch, (b) Bottom – opposite side to the hard patch, and (c) Side – a side to the hard patch.

5.4 Application to a generic, axisymmetric intake

The DG method is applied now to a generic turbofan intake at realistic frequencies and flow conditions. It is modelled as a 2D-axisymmetric problem. The DGM results are compared to Actran TM [93] (the Finite/Infinite Element (FE/IE) approach in the frequency domain) solutions. This approach is widely used for modelling of acoustic propagation and radiation from intakes [71], and has been validated against measured far-field data for similar configurations [154] [155]. A typical sideline engine condition at take-off is considered. This corresponds to the lateral full-power measurement point in certification process (see section 1.1).

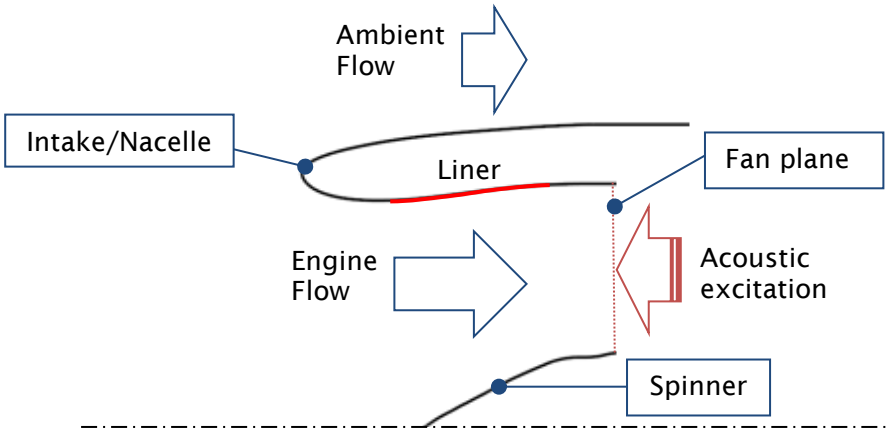

Figure 5.23: A physical model of a generic turbofan intake, cross-section through the shaft axis.

The geometry of the intake is defined by the profiles of the nacelle and the spinner. The model is illustrated in figure 5.23. It consists of two rigid surfaces, the spinner and the nacelle. The nacelle can be acoustically hard or acoustically treated. It is indicated during the study when the nacelle is treated. Two mean flow regimes are labelled as the engine and ambient flows. The modal acoustic excitation is applied at the fan plane, a plane in front of the real fan blades.

The flow and acoustic models which will be used are discussed in sections 3.3 and 3.4. Typical meshes have been shown in figures 3.4 (CFD) and 3.6 (CAA). Unstructured 2D meshes of triangular elements are used, refined as described in sections 3.3 and 3.4.

The numerical simulations are performed for a single incident mode (24,1) with unit intensity. Results are obtained for a frequency of 1300 Hz corresponding to kR_{fan} = 30. This is the blade passing frequency (BPF) for the generic problem. When a liner is present, a non-dimensional impedance of 2.06-0.02i is used. The values of total pressure and temperature at infinity are set to p_{tot} = 101562.86Pa and T_{tot} = 287.66K, respectively. Mach number contours for the mean flow used for the study are shown in figure 5.24. The Mach number in the ambient flow is set to 0.25. The Mach number at the fan plane is 0.56. The mean flow is computed by solving the velocity potential equation (see section 3.3.2 for details). The acoustic field is dependent of the whole mean flow. However, the flow in vicinity of the intake wall is most relevant, since most of the acoustic energy is transmitted close to the wall.

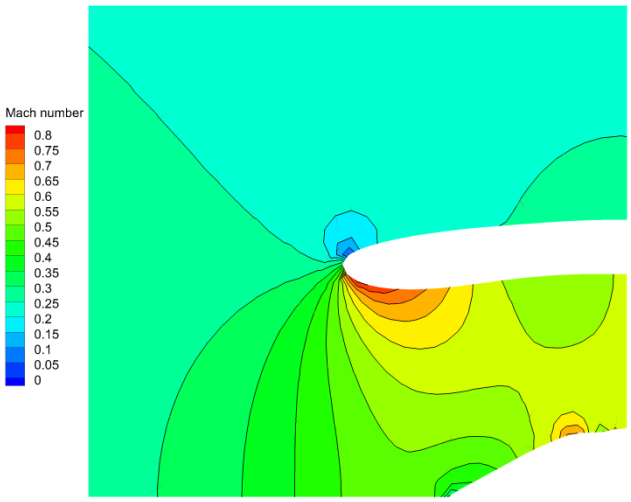

Figure 5.24: An example of the mean flow used for the validation of the DGM against the generic intake.

Additionally, high gradients are present in this region. The flow accelerates strongly from a stagnation point to high velocity at the throat and then decelerates as it approaches the fan plane. There are also high-velocity peaks regions close to the spinner, where the geometry changes rapidly.

5.4.1 The 2D axisymmetric solution: Actran TM.

As already mentioned, the Actran TM solution is regarded in this work as a reference solution. The main limitation of this method is its ability to deal only with sound propagation on non-rotational mean flows. The acoustic excitation is generated by analytical incident modes, which are injected at the fan plane.

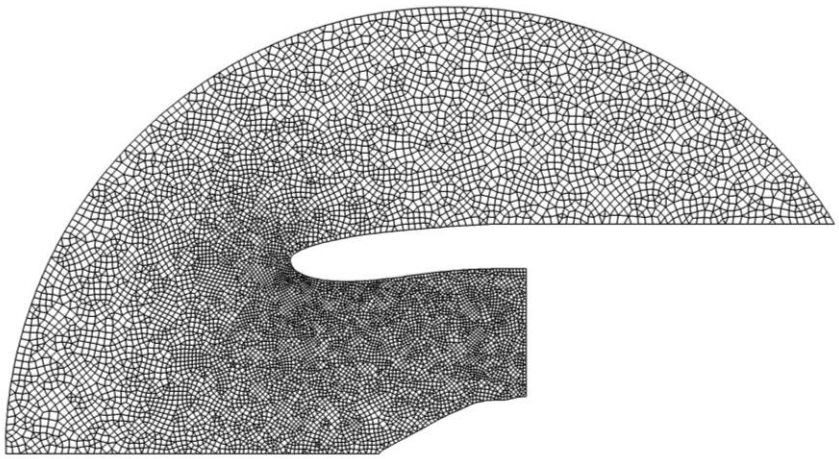

Figure 5.25: Actran TM mesh used for the study of noise propagation and radiation from a generic turbofan intake.

The minimum mesh resolution to ensure accurate results is 4 quadratic elements per wavelength including convective effects. The Actran TM mesh used in this study is shown in figure 5.25.

Results of Actran TM simulations for the generic intake in the absence of mean flow are shown in figure 5.26. Instantaneous pressure and the sound pressure level distributions are presented, in the left and right columns, respectively. As expected, most of the acoustic energy is transmitted through the outer part of the intake. In the case of the hard-walled intake, figures 5.26 (a) and (b), one radiation lobe is present with directivity of approximately 60 degrees measured from the forward axis. Results for the lined intake are shown in figures 5.26 (c) and (d).

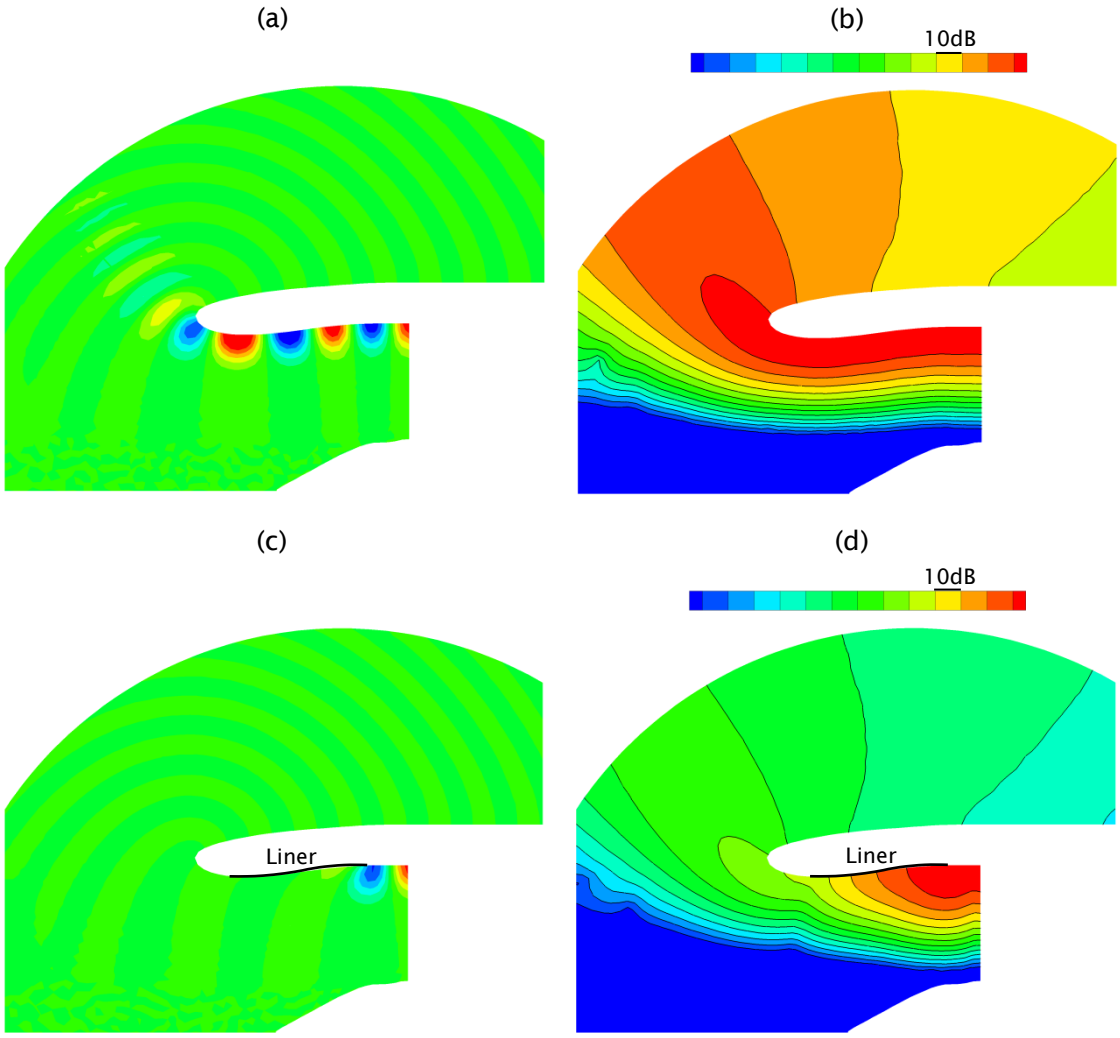

Figure 5.26: Near solution (Actran TM) for zero flow. A single incident mode (24,1) with kR_{fan} = 30. Hard walled intake: (a) instantaneous pressure [Pa], and (b) SPL [dB]. Lined ($Z = \rho_0 c_0(2.06 - 0.02\mathrm{i})$ at 1300 Hz) intake: (c) instantaneous pressure [Pa], and (d) SPL [dB].

Due to the liner presence, the solution is highly attenuated. 50dB attenuation is achieved at the end of liner. A similar directivity pattern is observed.

The corresponding results when flow is present are shown in figure 5.27. Instantaneous pressure and sound pressure level are illustrated in figures (a) and (b), respectively. The flow convective effects can clearly be seen in figure 5.27 (a) when comparing to the zero mean flow case. The wavelengths are much shorter and vary along the intake wall as the flow velocity changes. An amplification of 10dB to the SPL is observed in the vicinity of the throat as shown in figure 5.27 (b). Moreover, a complex acoustic pattern is visible inside the duct which is caused by scattering of the acoustic field by mean flow gradients and reflections from the throat.

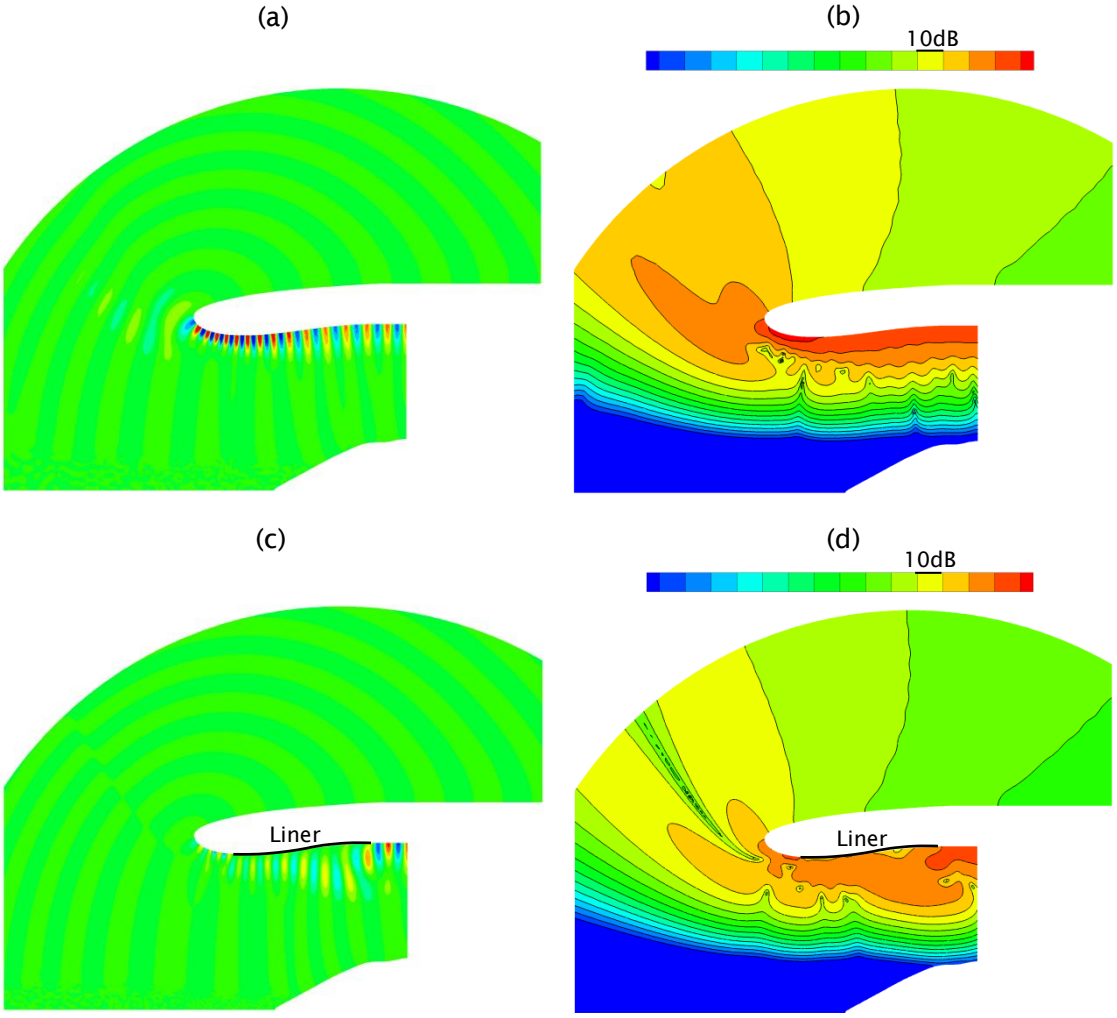

Figure 5.27: Near solution (Actran TM) for the mean flow case (Mach number of 0.25 in the ambient, and 0.56 at the fan plane). A single incident mode (24,1) with kR_{fan} = 30. Hard walled intake: (a) instantaneous pressure [Pa], and (b) SPL [dB]. Lined ($Z = \rho_0 c_0(2.06 - 0.02\mathrm{i})$ at 1300 Hz) intake: (c) instantaneous pressure [Pa], and (d) SPL [dB].

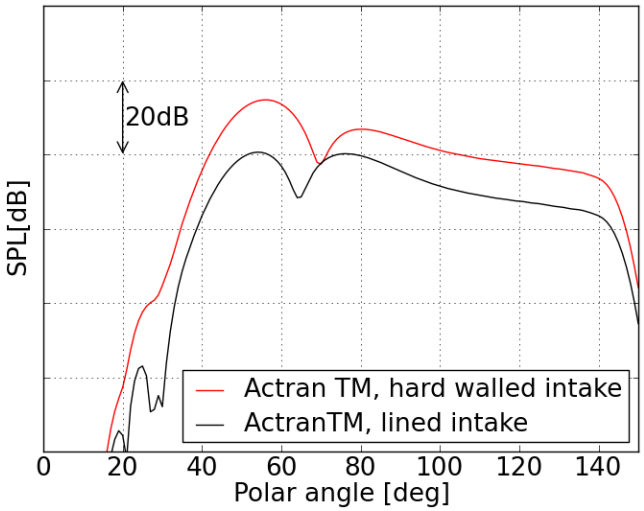

Figure 5.28: The far-field SPL directivity (Actran TM). Comparison between hard-walled and lined ($Z = \rho_0 c_0(2.06 - 0.02\mathrm{i})$ at 1300 Hz) intakes for the mean flow case (Mach number of 0.25 in the ambient, and 0.56 at the fan plane). A single incident mode (24,1) with kR_{fan} = 30.

The case with a liner is also considered. The resulting instantaneous pressure and SPL distributions are presented in figure 5.27 (c) and (d), respectively. The attenuation due to the liner is clearly visible and pressure contours are no longer orthogonal to the duct wall along the liner (see figure 5.27 (c)).

The directivity of the far field SPL for the hard-walled and lined cases are shown in figure 5.28 plotted against polar angle. The attenuation of sound due to the liner is clearly visible. The strength of the first radiation lobe is reduced by approximately 15dB. The second lobe is less attenuated, but its radiation angle is changed by approximately 5 degrees. As a result of the liner, the two directivity lobes have nearly the same amplitudes.

5.4.2 The 2D axisymmetric solution: Actran DGM.

The DGM calculations are now compared to the Actran TM results. The same set of simulations is carried out as presented and discussed in the previous section. The hard-walled & treated intake models for zero flow and typical sideline flow conditions are considered. The DGM mesh used in this study is shown in figure 5.29. It is optimised for the DGM simulation when mean flow is present. The element orders vary between 5 and 7 for the mean flow case, and between 4 and 5 for the zero flow case. The mesh along the nacelle is over refined in order to minimize mesh scattering (see section 5.2.2).

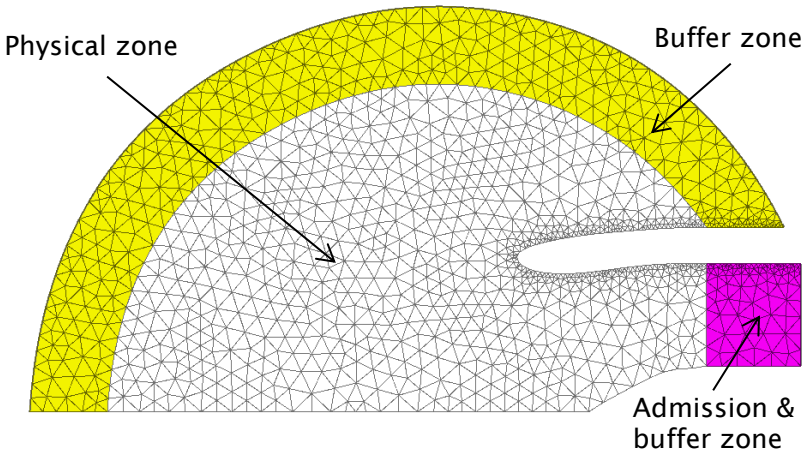

Figure 5.29: Actran DGM mesh used for the study of noise propagation and radiation from a generic turbofan intake.

5.4.2.1 Hard walled and lined intake for zero flow

The near field DGM solution for a hard-walled intake with zero mean flow is presented in figure 5.30. Good agreement to the relevant Actran TM solution (figure 5.26 (b)) can clearly be seen. Strong damping across the buffer zone is also observed, confirming that the buffer zone is working correctly. Some numerical contamination is evident in the region close to the centre line where acoustic pressure levels are low.

More detailed comparisons of the DGM results to the Actran TM solutions are shown in figure 5.31.

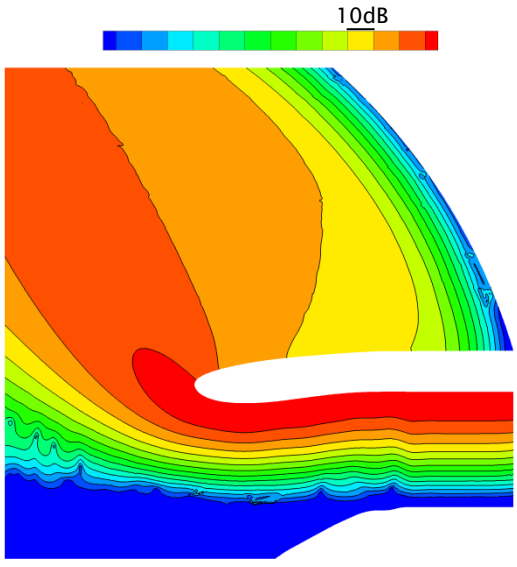

Figure 5.30: Near solution (Actran DGM) for hard walled intake with zero flow. The SPL for a single incident mode (24,1) with kR_{fan} = 30.

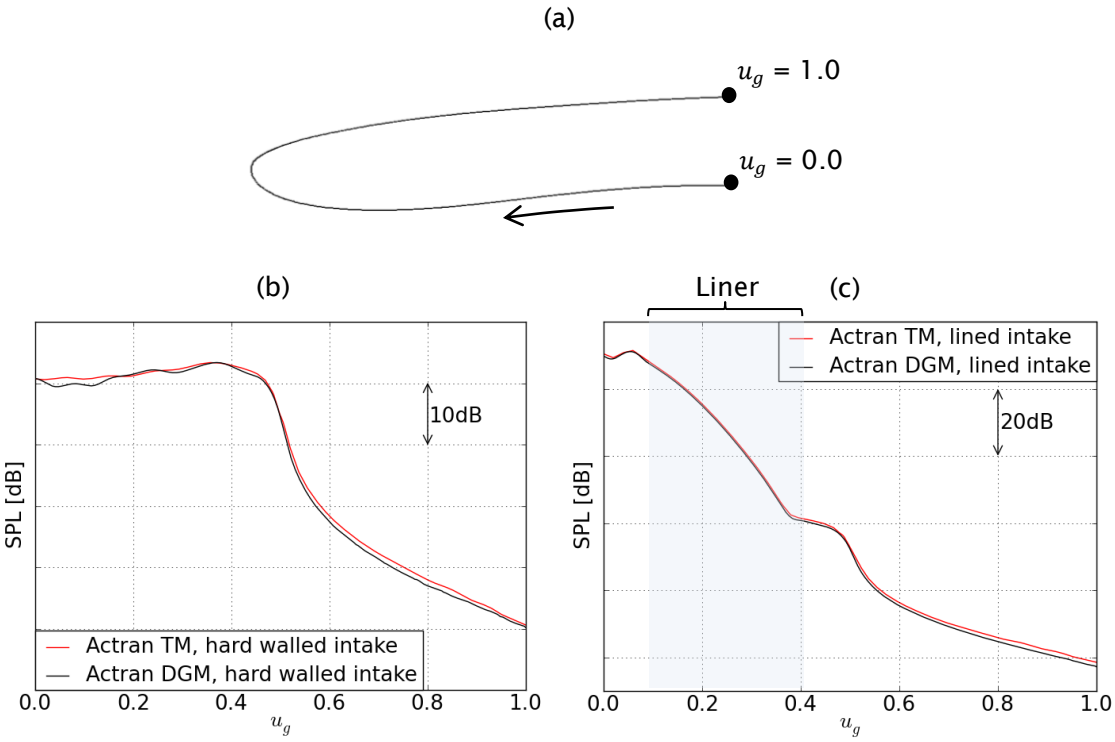

Figure 5.31: A comparison of SPL along the parameterized nacelle surface (a) between Actran DGM and TM solutions. Hard walled intake (figure (b)) and lined ($Z = \rho_0 c_0(2.06 - 0.02\mathbf{i}$) at 1300 Hz) intake (figure (c)) with zero mean flow for a single incident mode (24,1) with kR_{fan} = 30.

The variation of SPL along the nacelle wall for the hard walled and lined intakes is shown in figures 5.31 (b) and (c), respectively. The length of the nacelle wall is parameterized with a non-dimensional parameter u_g ranging from 0 to 1 as shown in figure 5.31 (a). In case of the hard walled intake (figure 5.31 (b)) slight amplification is observed from u_g = 0 to 0.4. This is caused by the area reduction of the intake duct. The attenuation due to the liner is clearly visible in the lined intake as shown in figure 5.31 (c). The tone amplitude is damped by 50 dB over the length of the liner (u_g ranging from 0.08 to 0.4). The attenuation rate is not constant due to the curved character of the intake wall. In both cases the DGM and TM solutions agree very well. The maximum discrepancies are approximately 1.5dB.

5.4.2.2 Hard walled intake with mean flow

A similar comparison has been made when mean flow is present. The same mean flow is used for the Actran DGM and Actran TM solutions. The mean flow contours are shown in figures 5.32 (a) and (b), respectively.

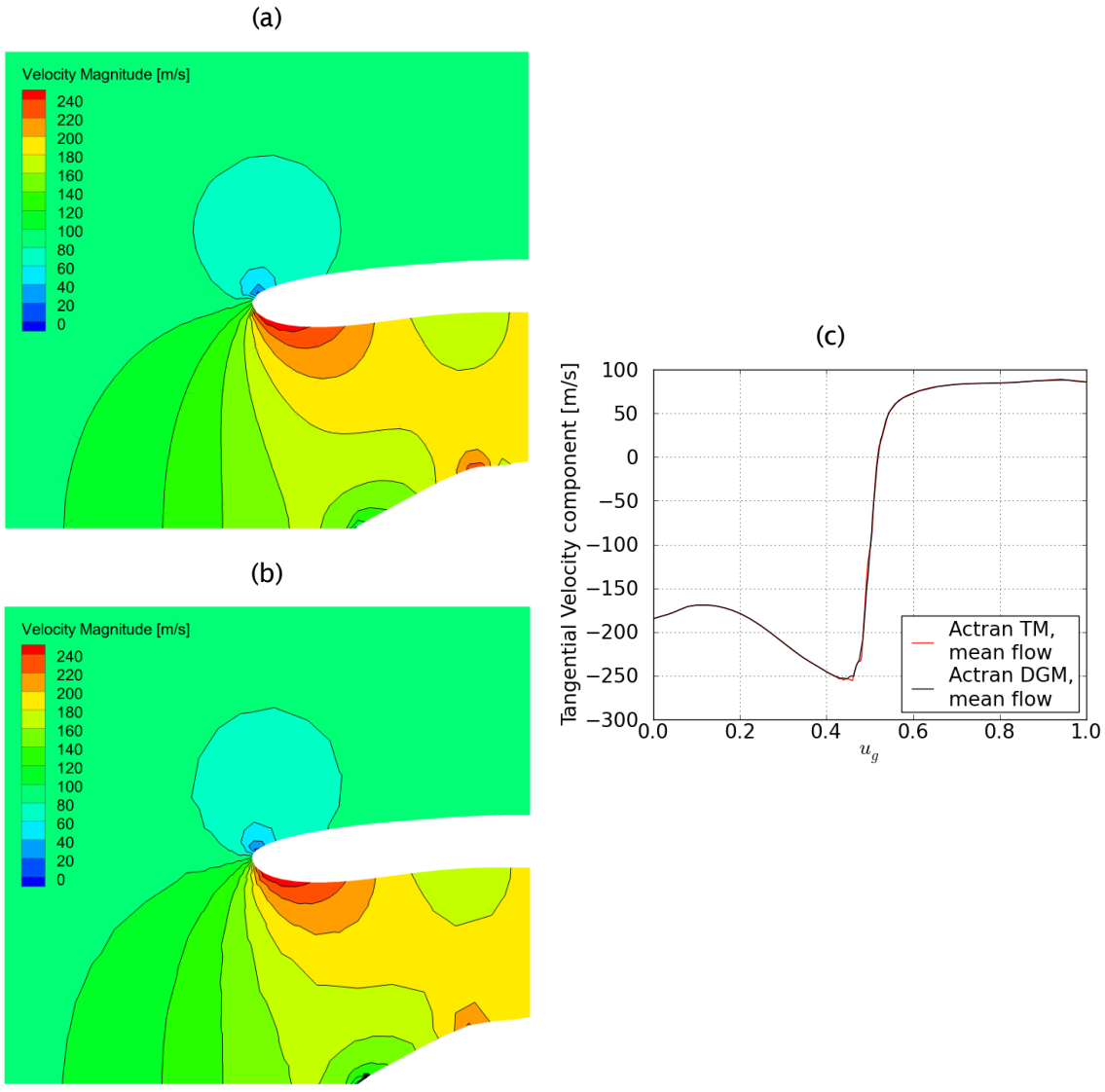

Figure 5.32: Comparison of the mean flows used by Actran TM and Actran DGM. (a) the mean flow map as represented by Actran TM mesh, (b) the mean flow map as represented by Actran DGM mesh, and (c) comparison of the tangential velocity component along the nacelle wall.

It is important to note, that these flow fields are interpolated on the CAA meshes for the DGM and TM simulations. Due to coarser mesh of the DG method, the flow isolines are slightly less smooth. The comparison of mean tangential flow velocity along the nacelle surface is shown in figure 5.32 (c). This shows clearly that the mean flows 'seen' by the DGM and TM acoustic solvers are very close to each other.

Results obtained by using Actran DGM and TM for the hard walled intake in the presence of mean flow are presented in figure 5.33. The variations of the SPL along the nacelle wall, figure (a), and in the far-field, figure (b), are shown. Very good agreement is achieved.

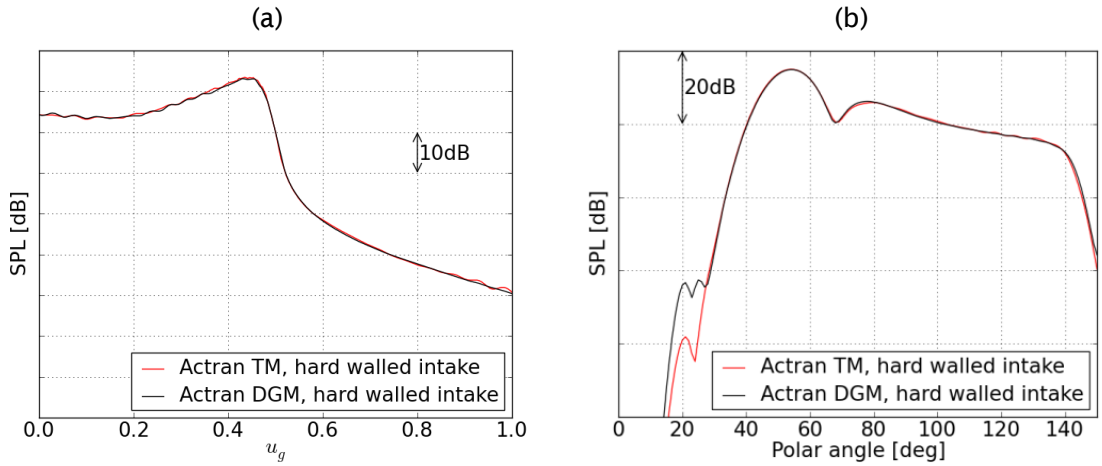

Figure 5.33: Comparison between Actran TM and DGM for hard walled intake with the mean flow (Mach number of 0.25 in the ambient, and 0.56 at the fan plane). A single incident mode (24,1) with kR_{fan} = 30. (a) The SPL along the nacelle wall. (b) The far-field SPL directivity.

To the scale shown no discrepancies are observed, except for some small difference in spurious numerical reflections at low polar angles in the far-field solution.

5.4.2.3 Lined intake with mean flow

In this section DGM is compared to Actran TM for a lined intake with non-uniform mean flow. Calculations are performed for two different implementations of the impedance boundary condition; the standard Myers boundary condition (slip boundary condition), and for a boundary layer with a small thickness δ_{bl} (no-slip boundary condition).

Firstly, DGM results are obtained for the Myers boundary condition. This can be regarded as a continuation of section 5.3 where the liner model was validated for a cylindrical duct with a uniform mean flow. The SPL comparisons between Actran TM and DGM along the nacelle wall and in the far field are presented in figures 5.34 (a) and (b), respectively. A discrepancy of 5 to 10 dB is observed along the lined surface. This increases to 20 dB at the end of the liner, and persists along the rest of the nacelle wall. The two solutions also differ significantly in the far field as shown in figure 5.34 (b). The peak values of the radiation lobes are under predicted by the DGM. The first by 13 dB; the second by over 20 dB. Moreover, a difference of 5 degrees in the directivity angle of the second radiation second lobe is observed.

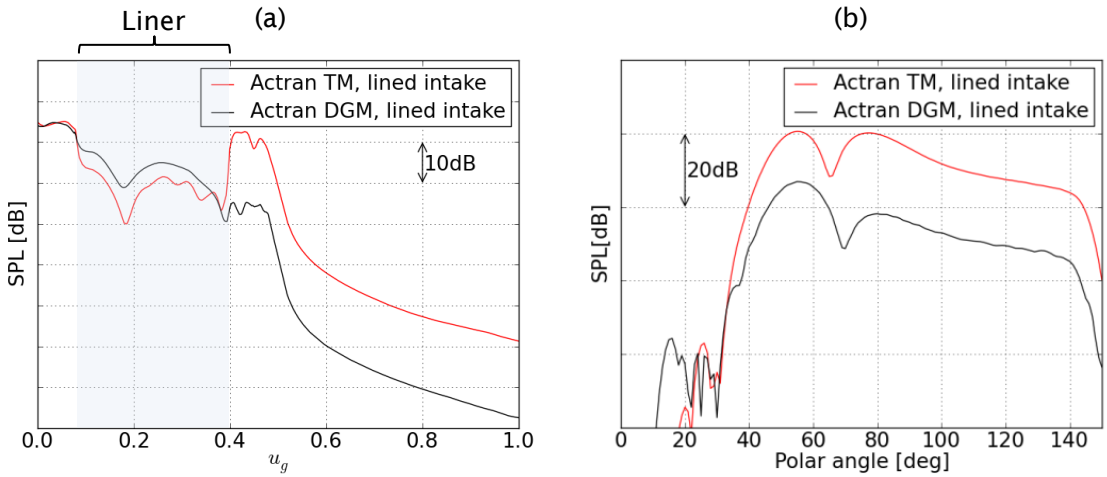

Figure 5.34: Comparison between Actran TM and DGM, both with Myers boundary condition, for lined ($Z = \rho_0 c_0(2.06 - 0.02\mathrm{i})$ at 1300 Hz) intake with the mean flow (Mach number of 0.25 in the ambient, and 0.56 at the fan plane). A single incident mode (24,1) with kR_{fan} = 30. (a) The SPL along the nacelle wall. (b) The far-field SPL directivity.

Clearly, the discrepancies observed for the realistic turbofan intake are much larger than those reported in section 5.3.1 for a straight cylindrical duct with a uniform mean flow.

As already discussed in section 5.3.1, in the DGM code used in this work, a spatial filter [92] is applied to the convective term ($\boldsymbol{u}_0 \cdot \nabla \mathrm{p}'$) of the Myers boundary condition (Eq. 2.23) to deal with instabilities which may occur along the lined surfaces. Moreover, the impedance in equation (2.23) is assumed to be constant over a liner. It is likely that the large discrepancies between Actran DGM and TM shown in figures 5.34 are caused by the spatial filtering applied in the DGM, and by the assumption of constant impedance along the liner. In order to verify the statement, this problem has been reproduced for a straight unflanged cylindrical duct in the presence of a uniform mean flow. The study has been performed for the mean flow Mach numbers of 0.25 and 0.56 which are corresponding to the Mach numbers in the ambient flow and at the fan plane of the generic intake problem, respectively. The rest of the aerodynamic and acoustic parameters used in the generic intake remained unchanged. The results of this study are included in Appendix C. Indeed, it has been confirmed that the discrepancies between Actran DGM and TM reported for lined intakes can be attributed to the Myers boundary condition currently implemented in Actran DGM. It has been shown that the spatial filtering may lead to inaccurate DGM solution. However, in the case of the faster mean flow, a stable DGM solution was not achieved when less stringent spatial filtering was applied.

Also, the accuracy of the liner model was not improved when a very fine mesh was used along the lined surface.

An alternative approach to the Myers boundary condition, in which an infinitely thin boundary layer is assumed, is to resolve the mean flow with a finite-thickness boundary layer (no-slip boundary condition). This requires a very fine mesh along the lined surfaces, which is a significant drawback. Nonetheless, for the purpose of this study the expected loss of efficiency due to a significant timestep reduction is accepted.

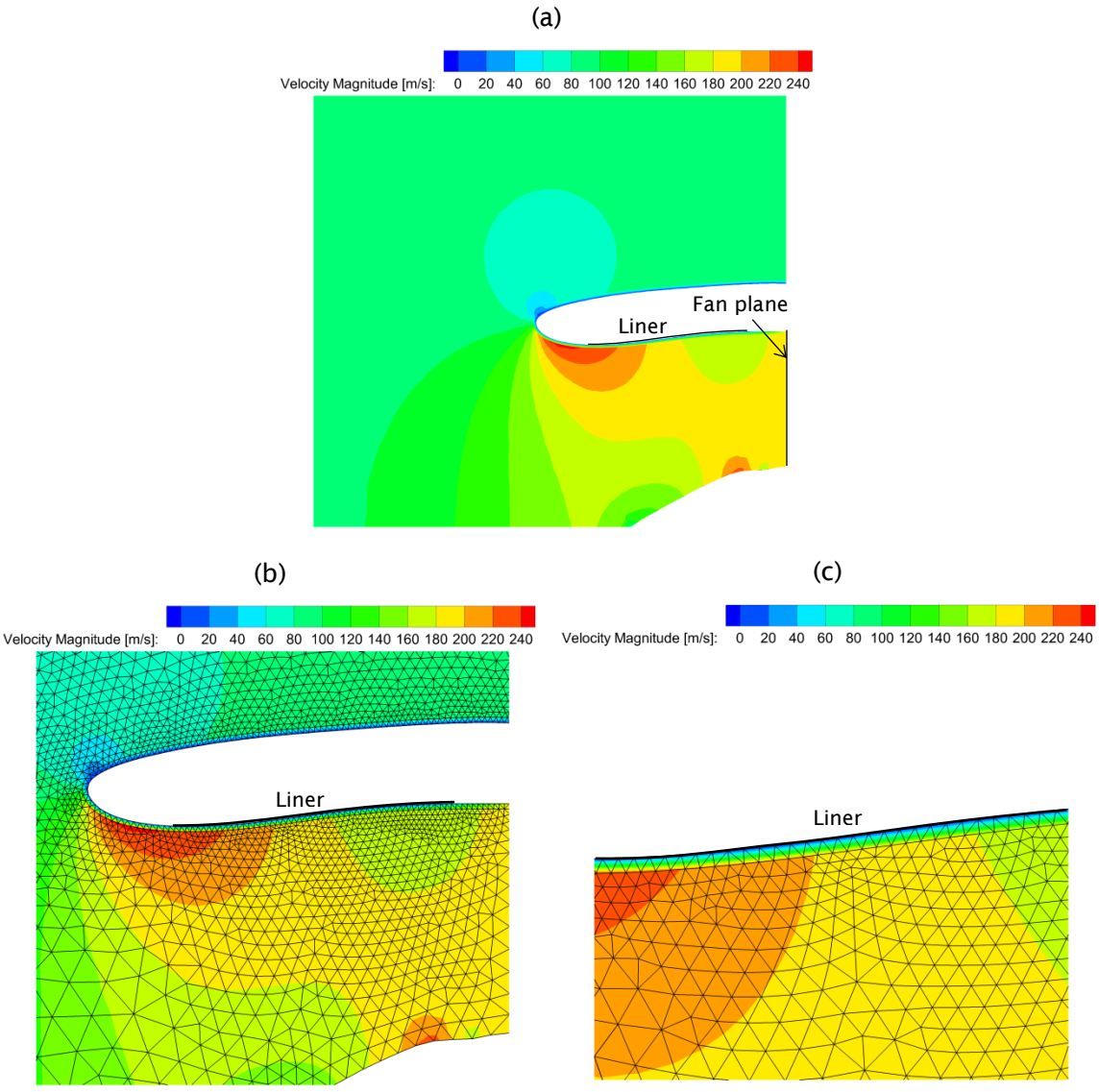

Figure 5.35: An example of the mean flow with a thin boundary layer used for the DGM simulations. (a) Contours of the velocity magnitude, (b) with the mesh on the nacelle, and (c) zoomed-in view of the mesh on the liner.

The mean flow obtained for a slip boundary condition, and used for the Myers boundary condition, is modified to accommodate a boundary layer with a small thickness. The boundary layer is simply created by setting zero velocity on mesh nodes lying on the nacelle. Interpolation within the first layer of acoustic elements then creates a boundary layer close to the wall. In the normal direction to the wall a uniform mean flow density and linear velocity profiles are assumed. The resulting mean flow is shown in figure 5.35 (a). A linear transition from a fully slip boundary condition to a fully no-slip boundary condition is applied between the fan plane and the beginning of the liner. This is performed to minimize a possible error due to a discontinuity between the slip boundary condition and the no-slip boundary condition at the fan plane which is the admission face of the DGM model (see section 3.4 for details). The boundary layer with constant thickness δ_{bl} along the nacelle is modelled by using one layer of uniformly distributed and sized linear elements. This means that the height of the first row of elements determines the boundary layer thickness δ_{bl}. An example of such mesh is illustrated in figure 5.35 (b) and zoomed-in figure (c).

A series of the DGM simulations for different boundary layer thicknesses was carried out. The timestep is proportional to minimum element size and hence boundary layer thickness. The boundary layer thickness δ_{bl} 0.25 percent of the fan radius requires a timestep which is half that used for the Myers boundary condition case. This gives a model which is approximately four times larger than the Myers model. DGM results are shown and compared to Actran TM in figure 5.36. It is important to note that the Actran TM results were obtained using the standard Myers boundary condition (slip boundary condition).

In general, a better agreement to Actran TM is achieved when the Myers boundary condition is replaced with a small but finite boundary layer in the DGM simulations. The effect of the boundary layer thickness and the transition from a fully slip to a fully no-slip boundary condition can be seen in figure 5.36 (a) where the SPL is plotted along the nacelle surface (u_g ranging from 0 to 0.08). The inclusion of the boundary layer thickness of 1.6 percent of the fan radius introduces a difference of approximately 10 dB in the SPL at the beginning of the liner when compared to the Actran TM solution. It is less pronounced for the boundary layer thickness of 0.25 percent.

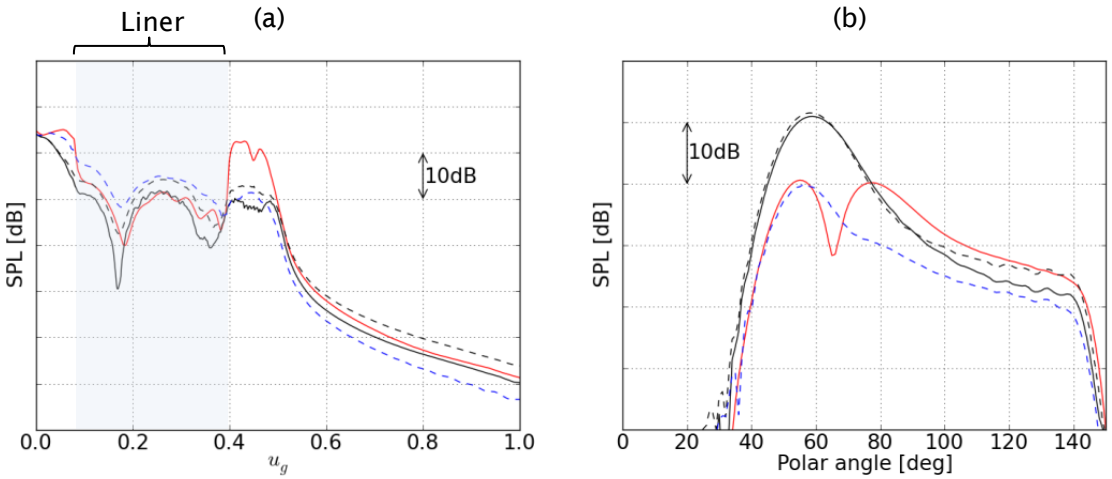

Figure 5.36: The SPL comparisons between Actran TM with Myers boundary condition (red) and Actran DGM with different thicknesses of the boundary layer: $\delta_{bl} = 1.6\%\, R_{fan}$ (black), and $\delta_{bl} = 0.25\%\, R_{fan}$ (blue). Dashed lines: DGM solutions obtained with all mean gradients of the mean flow removed. (a) The SPL along the nacelle wall. (b) The far-field SPL directivity.

Some agreement between Actran DGM, with the boundary layer thickness of 1.6 percent, and Actran TM is achieved along the liner. The maximum discrepancy is approximately 10 dB. At the end of the liner the sudden increase in the SPL predicted by Actran TM is not predicted by the DGM. However, the agreement along the external part of the nacelle (u_g ranging from 0.5 to 1) is fairly good. In the far field the DGM with the boundary layer thickness of 1.6 percent provides significantly different directivity pattern than Actran TM, one radiation lobe instead of two radiation lobes predicted by Actran TM (figure 5.36 (b)). The peak values differ significantly. The maximum discrepancy is approximately 10 dB.

In order to simulate more closely the Myers condition, DGM simulations with a much thinner boundary layer thickness were conducted. The DGM simulations with the boundary layer thickness of 0.25 percent, however, resulted in Kelvin-Helmholtz instabilities [156] along the refined/thinner boundary layers. These were suppressed by removing the mean flow gradients from the original equations (the vector $\boldsymbol{G}$ in equation (2.12) is zero vector). It has been shown by Tester et al. [157] that this is an effective technique to eliminate such instabilities for exhaust nozzle problems. The influence of the mean flow gradients on sound absorption by the lined surface can be seen in figure 5.36 where DGM results for the case of a boundary layer thickness of 1.6 percent of the fan radius are shown with, and without the mean flow gradient suppression. A nearly constant increase in the SPL of approximately 4-

5 dB along the nacelle surface is visible in figure 5.36 (a). In the far field, as shown in figure 5.36 (b), the solutions match well for polar angles up to 90 degrees. Above this angle the solutions are no longer consistent. A maximum difference of 4 dB is observed for the polar angle of 140 degrees.

For the boundary layer thickness 0.25 percent of the fan radius a fairly good consistency with Actran TM solution along the liner is observed, however the DGM over predicts the SPL by approximately 4-5 dB, assuming that the solution predicted by Actran TM is correct. The sudden increase in the SPL predicted by Actran TM at the end of the liner is also not captured by the DGM solution. On the external surface of the nacelle the DGM with the thin boundary layer under predicts the SPL by 5 dB. A similar radiation pattern to that reported for the thick boundary layer (1.6 percent of the fan radius) is observed for the thin boundary layer (0.25 percent of the fan radius) as shown in figure 5.36 (b). However, a significant reduction (10 dB) in the peak value of the radiation lobe is observed for the thin boundary layer. This confirms the important role of the boundary layer thickness on sound absorption by liner as reported by Gabard [101]. Moreover, for the case of the thin boundary layer good match to Actran TM in terms of the far-field SPL directivity is observed for the polar angles up to 60 degrees (figure 5.36 (b)). Further conclusions cannot be drawn as the DGM solution does not include effects due to the mean flow gradients which may have a significant impact on sound absorption for a thin boundary layer where the gradients are expected to be large.

5.5 Application to a 3D non-axisymmetric intake

In this section the DG method is applied to a 3D non-axisymmetric intake at realistic frequencies and flow conditions. The objective is to test the scheme developed for automated 3D CAA noise simulations (see chapter 4).

The physical model is illustrated in figure 5.37. The geometry of the intake is defined by the profiles of the nacelle and the spinner. The flow Mach number is set to 0.55 at the fan plane. In the free field the fluid is at rest. The mean flow is computed as a compressible Euler flow by using the Fluent solver (see section 3.3.3 for details). The total pressure and temperature are set to, p_{tot} = 101.3 kPa, and T_{tot} = 288 K, respectively.

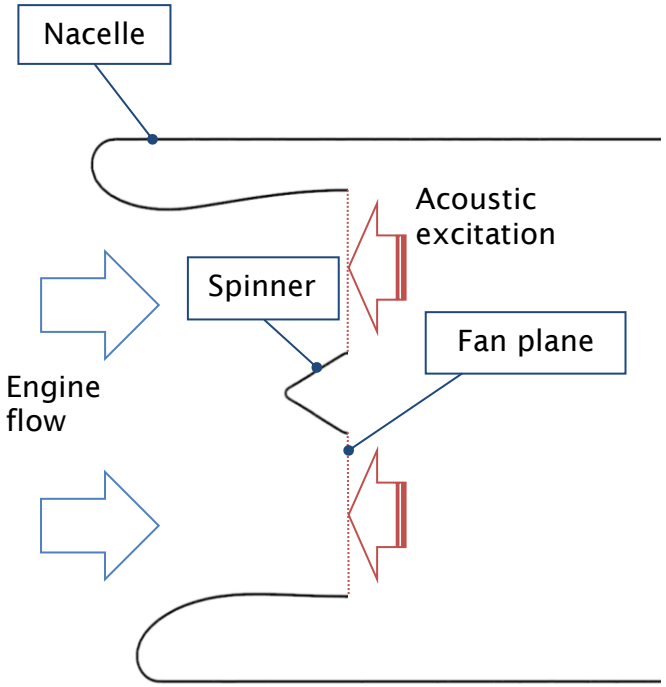

Figure 5.37: A physical model of 3D, non-axisymmetric intake, a vertical cross-section through the shaft axis.

The resulting flow pattern is shown in figure 5.38. It is a typical flow field with a high velocity region in the throat and low velocity in the diffuser part. As a result of a sharp corner, which connects the cone shaped spinner with a cylindrical extension, a local inaccuracy at the end of spinner is observed, which extends up to the outflow plane of the CFD model.

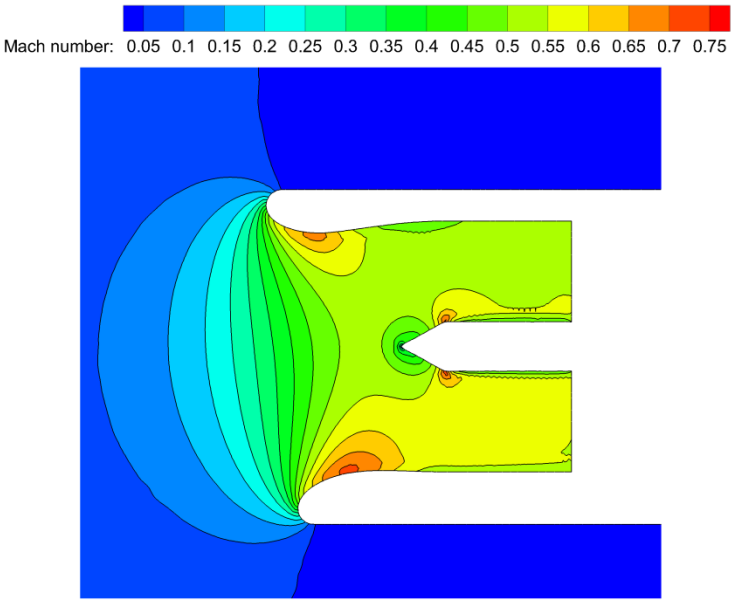

Figure 5.38: The mean flow used for 3D non-axisymmetric intake CAA simulations. Mach number distribution on a vertical cut-plane crossing the engine shaft axis.

This part of the flow solution does not, however, affect the rest of the CFD solution and CAA simulations.

The CAA simulations are performed for separate incident modes with unit intensity. It is carried out according to the methodology described in section 3.4. Solutions are obtained for modes (24,1) and (24,2) (corresponding to the BPF), and for mode (12,1) (corresponding to one half of the BPF). The geometry reconstruction, mesh generation, mean flow calculation and acoustic simulations are performed by using the CAE scheme described in chapter 4. The hard-walled cases are only considered.

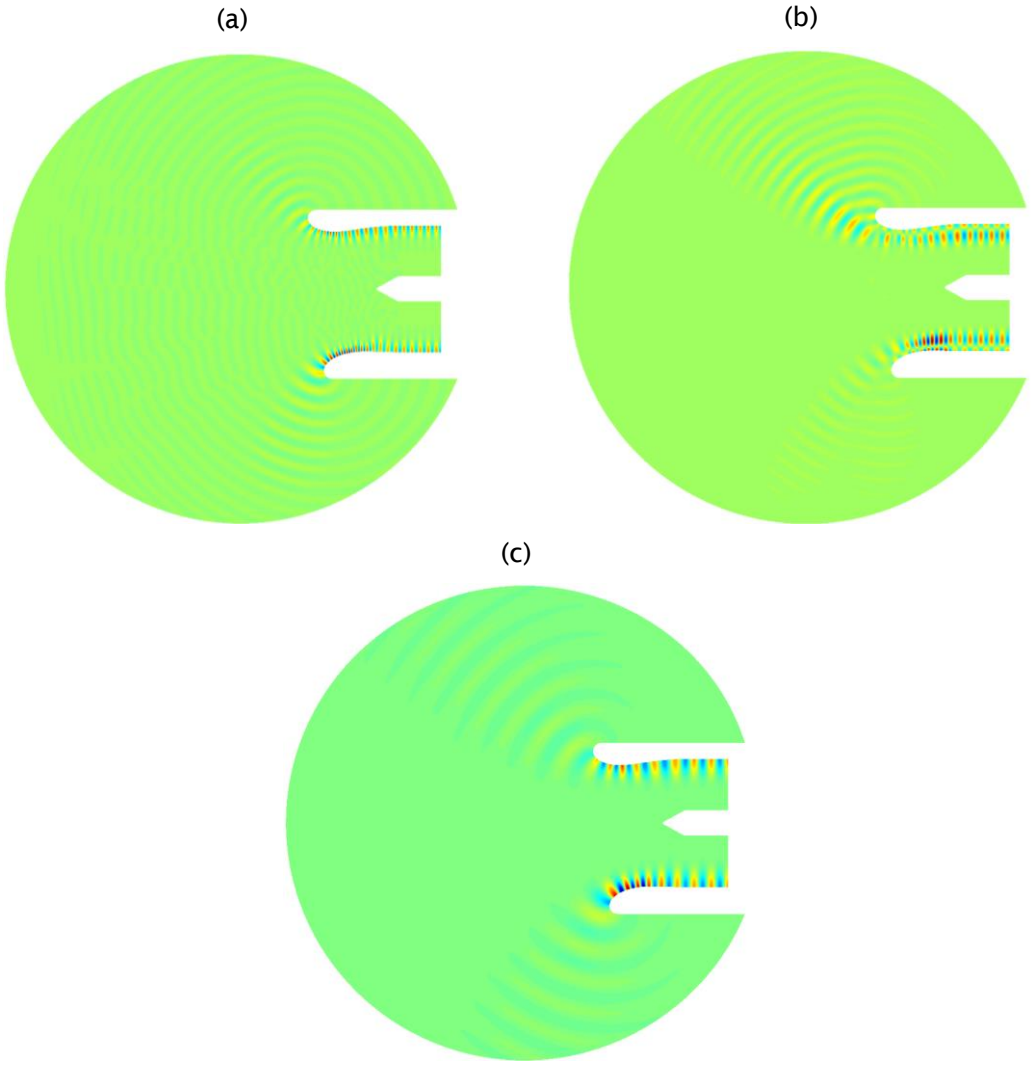

Figure 5.39: The instantaneous pressure at the vertical plane of the model. Mach number at fan plane = 0.55, zero mean flow in the ambient.
(a) Mode (24,1) – 1BPF, (b) Mode (24,2) – 1BPF, and (c) Mode (12,1) – 0.5BPF.

The near-field acoustic solutions are presented in figure 5.39. The instantaneous acoustic pressure distribution is shown for each mode. The results are presented on the vertical plane of the model crossing the engine shaft axis. Due to the non-axisymmetric geometry and the mean flow, the regions above and below the intake differ considerably. Stronger sound amplitude is observed in the region of high velocity at the bottom of the throat. The radiation angle is also different. In the case of mode (24,2) two radiation lobes are observed (figure 5.39 (b)).

The SPL directivities in the far-field for all three modes are shown in figure 5.40. The solutions are reconstructed at the four azimuthal planes, labelled as: top, right, bottom, left. The diagram showing the planes with respect to the fan is shown in figure 5.40 (a) viewed when facing the inlet.

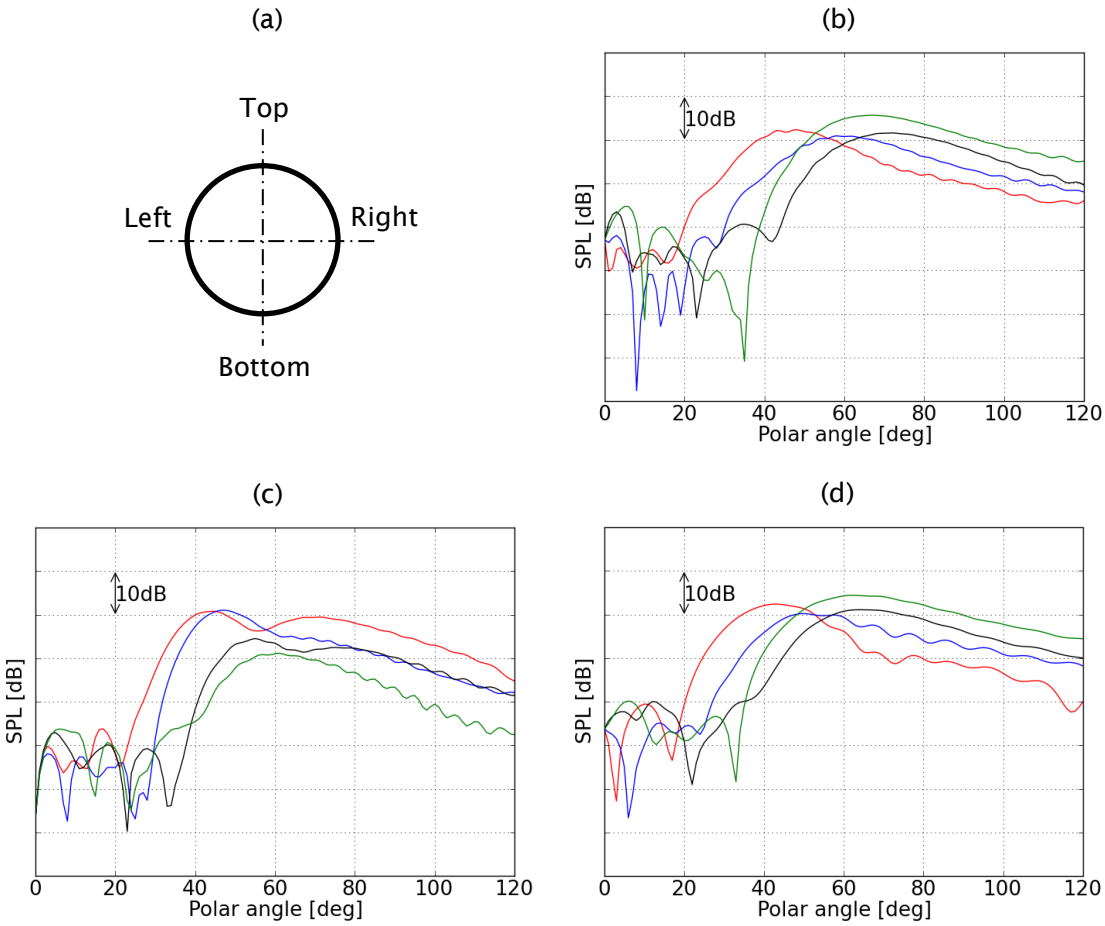

Figure 5.40: The CAA directivity plot lines. (a) Orientation of azimuthal arcs with respect to the fan as seen when facing the inlet. Solid red line: Top arc (0deg); solid blue line: Right arc (90deg); solid black line: Bottom arc (180deg) and solid green line: Left arc (270deg). (b) Mode (24,1) – 1BPF, (c) Mode (24,2) – 1BPF, and (d) Mode (12,1) – 0.5BPF.

The results show the non-axisymmetric character of the far-field solution. The mesh scattering, already discussed, is evident for low polar angles. It is kept at a low level (25 dB below the peak value) by sufficient mesh refinement at the wall. The solutions for all three modes in a band of polar angles between 20 and 120 degrees are fully converged. For all three modes, differences in the radiation directivity between the top, bottom, and sides are evident. The sound is radiated upwards at a lower polar angle than downwards. The shift is approximately 20 degrees for modes (24,1) and (12,1) and approximately 17 degrees for mode (24,2). Also, a difference in amplitude is observed between the top and bottom arcs for all modes analysed. It is most pronounced for the mode (24,2), where a difference of 6 dB is observed. There is a shift of approximately 5 – 10 degrees in the directivity between left and right arcs for modes (24,1) and (12,1). The modes radiate more outward (higher polar angle) at the left hand side. It holds for the mode (24,2), although the shift in the radiation angle is larger. In addition to the differences in the directivity, the amplitude differs between the left and right arcs. It is larger at left hand side for the modes (24,1) and (12,1), whereas for mode (24,2) it is the opposite. Moreover, in a case of the mode (24,2), the second radiation lobe is nearly not visible on the right-hand side, and not visible at all on the left-hand side.

These results are of particular interest, since no analytical solution is available. A more detailed study of the shielding and distortion effects on noise propagation and radiation from non-axisymmetric 3D intakes is presented in chapter 7.

5.6 Computational Performance

A performance study has been undertaken by using the data collected from the computations presented in this chapter. The majority of cases were executed on a dual processor workstation (with a total of 8 cores), a clock rate of 3.06 GHz, 96 GB of RAM memory, and running on the Linux Red Hat Enterprise 5.7, operating system.

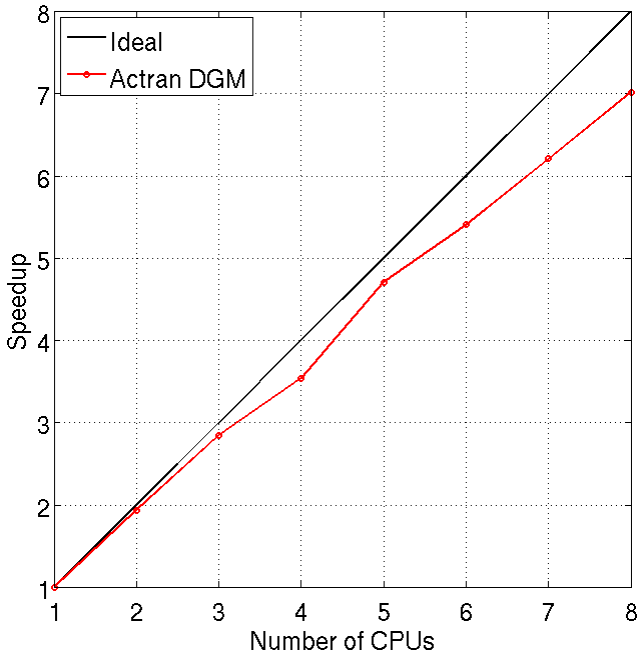

Figure 5.41: Speedup of Actran DGM.

Actran DGM manifests a very good parallel speedup. This is defined as the ratio of the runtime on a single processor to the runtime on multiple processors. It is nearly ideal, as presented in figure 5.41. Due to slightly unbalanced distributions of the number of degrees of freedom over the CPUs the speedup is a bit disturbed. The results confirm the DG method to be well suited for parallel calculations. Similar conclusions have been obtained in other applications [44] [51] [52], which covered much larger numbers of CPUs, e.g. Leneveu et al. [52] reported speedup factor of 12 for 16 CPUs.

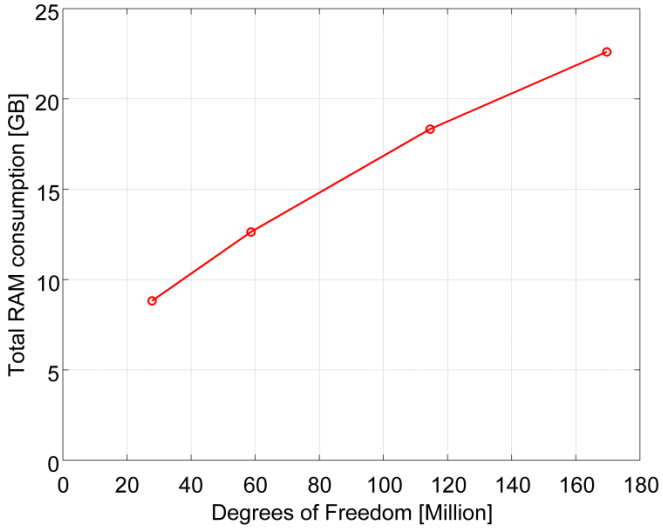

Figure 5.42: Memory consumption against the number of degrees of freedom.

The variation of RAM consumption with problem size is presented in figure 5.42. RAM consumption is moderate and varies almost linearly with the number of degrees of freedom. For a very large case of approximately 170 million of degrees of freedom, the DGM uses 23GB of RAM memory. The results are in line with what was reported by Leneveu et al. [52].

5.7 Summary and Conclusions

An assessment of the Discontinuous Galerkin Method for noise propagation and radiation from intake and exhaust systems of a turbofan engine has been presented. Actran DGM, which is a commercial implementation of this method, has been used.

Firstly, DGM solutions were compared to analytical solutions for idealized intake and exhaust problems. In general, this demonstrated a good correspondence between DGM and analytical solutions. The flow and no flow cases demonstrated a similar degree of accuracy. It was also shown that the DGM correctly resolves vorticity shedding in the exhaust case as represented in the Kutta condition. Best practice guidelines have been identified in relation to the computational domain sizes, mesh refinements, elements orders, and other parameters.

The DGM has also been compared to another numerical approach (Actran TM) for a generic turbofan intake at realistic frequencies and flow conditions. Good agreement has been demonstrated for axisymmetric hard walled turbofan intake problems. This holds when the intake is acoustically treated for zero flow cases.

Special attention has been paid to lined intakes in the presence of mean flow. It has been found that the implementation of the Myers boundary condition in Actran DGM leads to non-physical solutions in time-domain CAA simulations. A study with a small but finite boundary layer thickness has shown that the boundary layer thickness has a significant impact on the DGM solution. However, instabilities have occurred for thin boundary layers which have been suppressed by removing all mean flow gradients. In general, a better agreement to Actran TM for lined intakes has been observed when a small boundary layer thickness has been included in the DGM modelling.

Finally, it has been shown that the DGM is computationally efficient for CAA of 3D turbofan nacelles, and scaling well with the number of processors. The low RAM memory consumption of the scheme has been confirmed.

6. CFD/CAA coupling for 3D fan stage tone noise prediction

6.1 Introduction

In this chapter a CFD/CAA coupling interface is proposed for fan stage tonal noise propagation and radiation from a turbofan engine. Typical turbofan architecture is considered, similar to the physical problem illustrated and discussed in chapter 3.

The objective of this chapter is to provide a description of a new methodology for coupling a Computational Fluid Dynamics (CFD) simulation with a Computational Aero-Acoustics (CAA) method for 3D fan tone noise predictions. The process is based on existing computer methods for the CFD and CAA, i.e. the Rolls-Royce proprietary CFD code HYDRA [158] and Actran DGM [72]. HYDRA can perform non-linear analysis, whereas Actran DGM is a linear solver with good capabilities to predict noise radiation. Combining these two schemes provides a powerful tool to deal with arbitrary 3D nacelles shapes and flows. In order to couple the sources predicted by the CFD method with the CAA prediction for the acoustic propagation, the solutions are matched at a certain region. One way to achieve this is by using the mode matching techniques [159]. It is, however, difficult to apply this technique to ducts with arbitrary flows since acoustic waves do not exist individually for non-uniform flows. Moreover, it is not directly applicable in connection with linearized CAA methods when non-linear effects are present as a result of high-amplitude tones at high fan speeds. The non-linear effects can be included within a linear CAA model by applying analytical model proposed by Morfey and Fisher [160], further extended by Fisher et al. [161] and McAlpine et al. [162] [163]. This approach is, however, limited to axisymmetric problems. Another way, which allows full 3D matching, is to include the non-linear effects implicitly by adjusting the linear source. It can be achieved by adjusting a modal source to obtain the linearized CAA solution which is “equivalent” to the CFD solution over a matching region where the non-linear effects are less important, e.g. at some axial distance upstream from the fan. This is the approach which will be demonstrated in this chapter.

6.2 Methodology

In the proposed approach the fan tonal noise generation, propagation and radiation are predicted by coupling the CFD and CAA methods. The process is shown in details in figure 6.1.

Firstly, the source CFD is calculated for the fan stage to obtain the flow perturbations (noise sources). The model illustrated in figure 6.1 (a) consists of: the inner part of the intake duct (upstream of the fan), the bypass duct (downstream of the OGV), and the fan blades and OGVs. The Reynolds-Averaged Navier–Stokes (RANS) equations are solved by applying the finite volume method (see section 6.2.1.1). A rotating frame is used for the fan and a stationary frame for the OGV. A mixing plane is used between the two regions.

Secondly, the in-duct CAA calculations are carried out. The model is illustrated in figure 6.1 (b). The in-duct acoustic field is obtained by a superposition of the solutions for single incident modes. All cut-on and a few cut-off modes are included. The solutions are obtained by solving the linearized Euler equations using the discontinuous Galerkin method. The model corresponds to inner part of the intake duct and bypass duct used in the CFD modelling. The incident modes are defined at the fan and OGV planes. The walls are modelled as hard walls. Buffer zones are applied at the duct terminations to minimalize reflections. See section 6.2.2.1 for further details.

Thirdly, the CFD and the in-duct CAA solutions are matched in regions where the non-linear effects can be considered less important. The source modes at the fan and OGV planes are calculated for the radiation CAA model so that the CAA and CFD solutions ‘match’ in the overlapping region. Any non-linear effects in the CFD source region are included in the CAA radiation problem by adjustment of the modal source. The matching regions are indicated in figures 6.1 (a) and (b). See section 6.2.3 for further details.

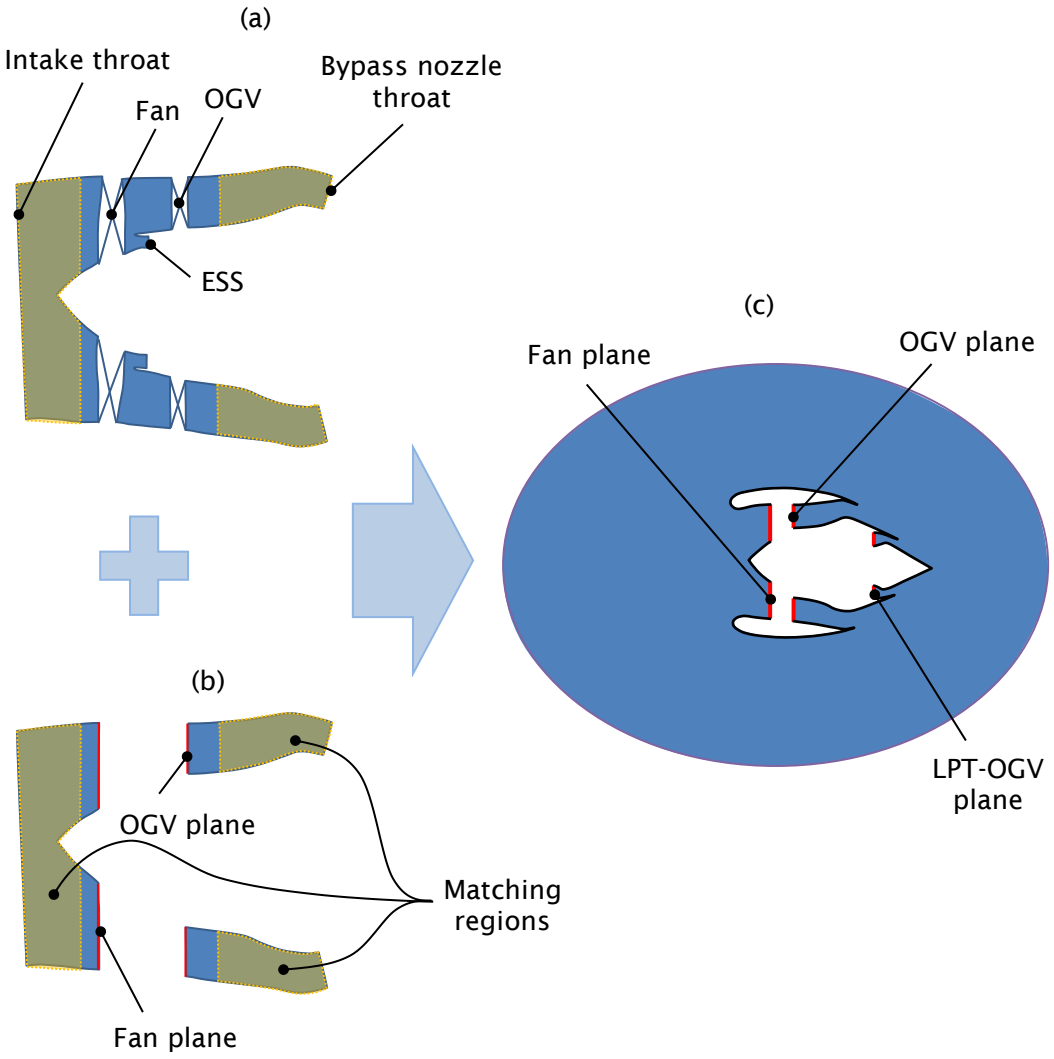

Figure 6.1: The process of the numerical modelling. (a) CFD model for determining the source flow, (b) CAA model for in-duct calculations, (c) CAA model for radiation analyses.

Finally, the CAA radiation analysis is conducted by using the matched equivalent source. Here, the full nacelle geometry is included as shown in figure 6.1 (c). As for the in-duct CAA calculation, the sound field in the computational domain is computed by solving linearized Euler equations applying discontinuous Galerkin method. The outer termination of the model is a non-reflecting boundary, which is also the case for the fan, OGV and Low Pressure Turbine Outlet Guide Vanes (LPT-OGV) planes. The nacelle boundary condition can be modelled as a hard wall or as a combination of hard and acoustically treated walls. The source modes determined in the matching process are applied to the fan and OGV planes. This is further discussed in section 6.2.2.2.

6.2.1 The Computational Fluid Dynamics modelling

6.2.1.1 The source flow

The noise source is obtained by solving the Reynolds-Averaged Navier–Stokes equations. The computation was performed by the Rolls-Royce Noise Department by using the HYDRA in-house aerothermal code [158]. The non-linear effects, which are particularly important for high fan speeds, are included in the CFD solution. The CFD simulation is highly demanding in terms of CPU time and memory requirements. Therefore the size of the CFD domain has to be reduced to the minimum required for the model. A sketch of the CFD model is shown in figure 6.2. The model consists of: the spinner, fan blades, Engine Section Stators (ESS), splitter, OGV, bypass duct, and inner surface of the intake. The computational domain at the inlet is extended to introduce a damping zone in which the unsteady perturbations decay to avoid spurious reflections. On the right-hand side of the outlet guide vanes, the bypass duct is also extended and ended with a damping zone. A mixing plane is used as an interface between the solutions in the rotating (rotor) and stationary (stator) frames. It is placed between the fan blades and OGV above the splitter. Additionally, in the case of non-axisymmetric intake a sliding mesh interface is used to connect the physically rotating part of the model with the upstream part. The boundary conditions on the surfaces are modelled as adiabatic and rigid walls.

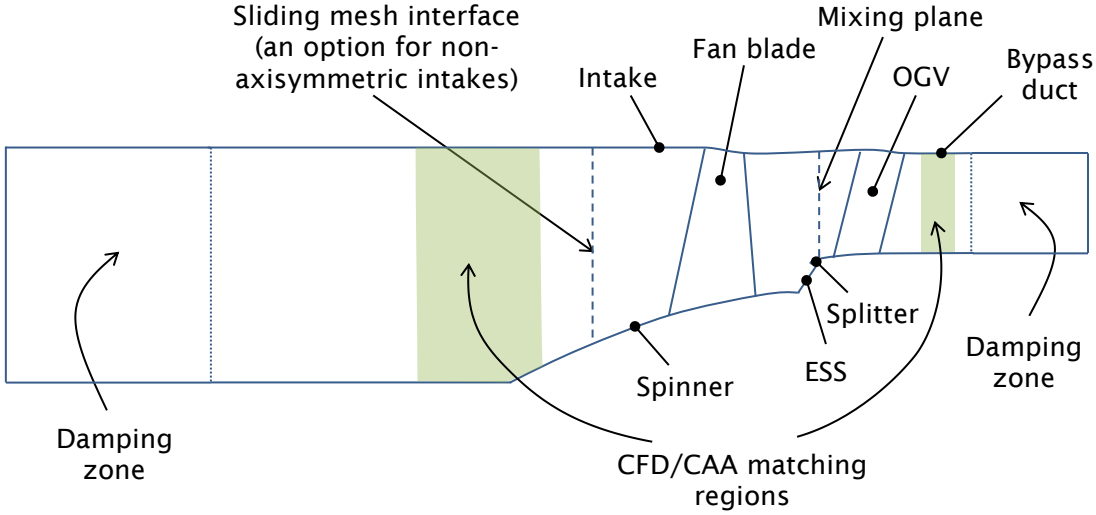

Figure 6.2: Hydra steady-state CFD model for determining the fan stage flow source.

The flow is set by using the inlet and outlet boundary conditions to match the required fan stage operating point. In case of an axisymmetric intake, RANS equations with the Spalart-Allmaras turbulence model [164] are solved as steady-state in the rotating reference frame attached to the fan. It can be performed for the whole annular sector or a sector containing an arbitrary number of fan blades. However the latter (reduced model) results in missing azimuthal Fourier components in the solution. Unsteady RANS, which covers the whole annular sector, is necessary for non-axisymmetric problems and in cases where variations in blade stagger angles are important. Hexahedral meshes for the flow computations are obtained by using Rolls-Royce mesh generator PADRAM [165]. In order to achieve the required high accuracy very fine meshes are necessary. In the current approach the mesh refinement of more than 20 mesh points per wavelength is used which results in a typical mesh size of approximately four million of elements per blade passage. The convergence is accelerated by applying a multi-grid algorithm [166].

The resulting flow maps on the matching regions are post-processed and used as input data for the CFD/CAA matching.

6.2.1.2 Time averaged flow (mean flow)

In theory, the flow could be gained from the source calculation, however, it is challenging in many respects, particularly due to the lack of some geometry features in the CAA models, e.g. fan blades. Moreover, this flow would be only applicable for the in-duct CAA. Therefore, in the proposed approach the mean flow is calculated independently to the source flow.

The mean flow for the in-duct CAA is obtained by running either a potential or Euler solver. The underpinning physics are similar in both cases, however obvious differences exist. The potential flow is obtained by solving the velocity potential equation for an irrotational compressible flow. The Euler flow is obtained by solving a full set of Euler equations. A generic numerical model is presented in figure 6.3.

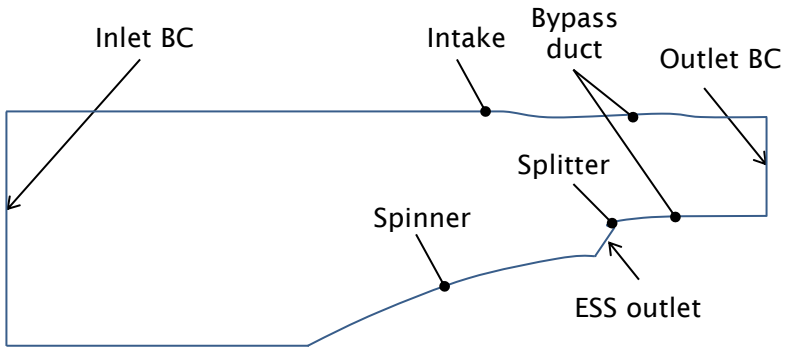

Figure 6.3: A generic CFD model for in-duct mean flow calculation.

One may note that the model does not include fan blades and some other geometric features. This simplification is justified, since these features are not present in the CAA simulations and have little effect on the flow in the matching region. The walls are assumed to be adiabatic and rigid with slip boundary conditions. The inlet and outlet conditions are set to ensure a given mass flow rate. In the potential method the velocity potential and velocity vector are applied at inlet and outlet, respectively, whereas, in the Euler approach total pressure and total temperature are set at the inlet and static pressure is imposed at the outlet. The mesh type, its resolution and interpolation order are the same for both approaches.

6.2.2 The Computational Aero-Acoustics modelling

6.2.2.1 In-duct calculations

The in-duct acoustic field is obtained for each incident mode applied at a nominal fan plane at a given frequency by solving the linearized Euler equations for acoustic perturbations propagating on the mean flow. The numerical model consist of three main zones; admission, physical and buffer. The model for the matching is shown in figure 6.4. While the two dimensional axisymmetric model is shown, 3D models can also be used. The acoustic excitation is provided by analytical modes applied at the fan plane through the admission zone. The physical zone is a computational domain where the LEE equations are solved. The walls are rigid boundaries. Buffer zones are added at both ends of the duct. A 1-D Characteristic NRBC is applied at the end of the buffer zones to damp any persistent incident waves. The thickness of the buffer zone is based on an axial upstream wavelength. A thickness of two to six wavelengths is used.

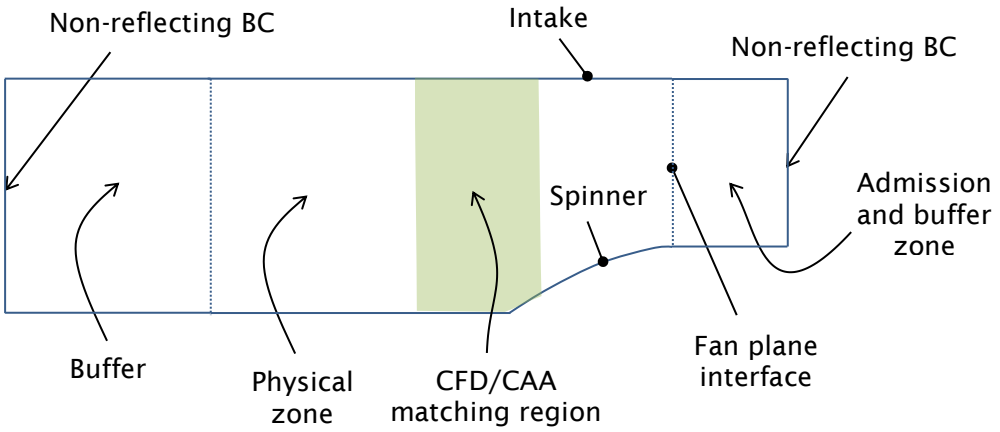

Figure 6.4: In-duct CAA model for the CFD/CAA matching in the forward arc.

The mesh refinement is also defined with reference to the characteristic wavelength (usually 1 – 2 elements per upstream wavelength). In addition, further refinement is necessary at the walls to ensure minimum mesh scattering. This leads to element orders between 2 and 7.

6.2.2.2 Radiation simulations

The radiation CAA simulations are performed according to the methodology described in chapter 3, section 3.4.

6.2.3 CFD/CAA matching

In this section the matching of the in-duct CAA solutions to the CFD source flow is described. By matching the CFD and the CAA solutions in a region where the non-linear effects are less important, equivalent source modes on the fan plane in the CAA model can be determined which take into account non-linear attenuation close to the fan. The matching is performed for the acoustic pressure only, which minimises the influence of vorticity convected by the mean flow. The model assumes no reflections therefore no separation is performed between out- and in-coming waves. The following function is minimized to estimate unknown coefficients by applying a least squares fit in the matching regions.

$$\sum_i \left| \mathrm{p}_{CFD}(\boldsymbol{x_i}, \omega) - \sum_{m,\mu} L_{c^{\omega}_{m,\mu}} \tilde{\mathrm{p}}^{\omega}_{m,\mu}(\boldsymbol{x_i}) \right|^2, \tag{6.1}$$

where $p_{CFD}(\boldsymbol{x},\omega)$ and $\tilde{p}^{\omega}_{m,\mu}(\boldsymbol{x})$ are, respectively, the CFD and in-duct CAA predicted complex pressure amplitudes in the matching region for a given frequency. The in-duct CAA sound field is obtained for the acoustic excitation provided by a set of azimuthal (m) and radial (μ) order modes applied at the fan plane. $L_{c^{\omega}_{m,\mu}}$ are unknown coefficients. The CAA modal sources on the fan plane, which ensure minimum error to the CFD solution in the matching region, are found by multiplying the amplitudes of the sources used for the in-duct CAA by the coefficients determined in the matching process.

6.2.3.1 Axisymmetric intake - matching in the forward-arc at high fan speeds

The CFD/CAA matching is applied in this thesis to noise radiation into the forward-arc through the intake. Rotor alone blade passing tones (BPF tones) and buzz-saw tones are considered.

The CFD and CAA results in the matching region are given in two different coordinate systems, i.e. rotating (CFD) and stationary (CAA). The relationship between the frames is shown in figure 6.5. They have a common origin and z axis. The angular velocity of the rotating frame (fan) is defined by Ω. The theta angles in both systems are related according to $\theta = \theta'' + \Omega t$.

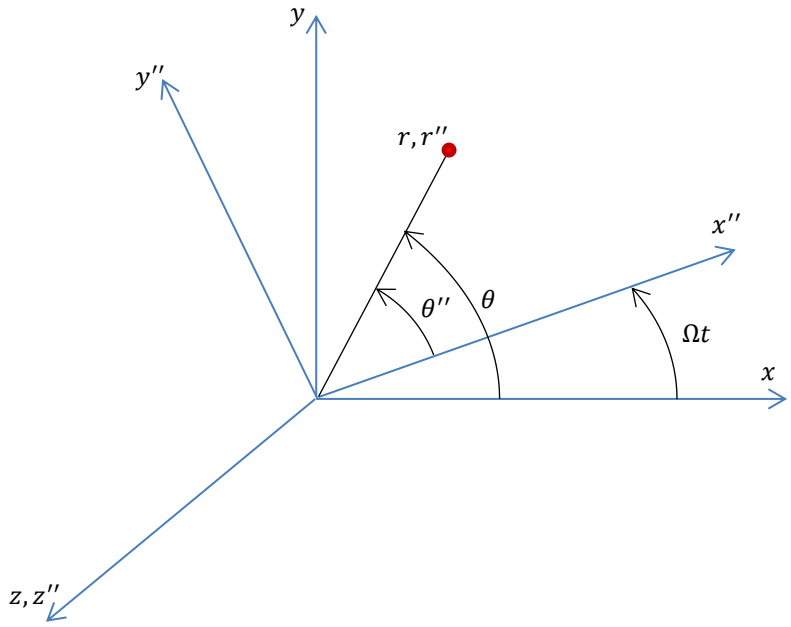

Figure 6.5: Coordinate systems. Stationary: r, θ, z. Rotating: r'', θ'', z''.

The steady CFD solution is given in the rotating reference frame as $\mathrm{p}''(r,\theta'',z)$ assuming that it covers the full annular range, where θ'' is an azimuthal angle. It can be defined as a sum of azimuthal components

$$\mathrm{p}''(r,\theta'',z) = \sum_{m=-\infty}^{\infty} \mathrm{p}''_m(r,z)e^{-im\theta''}, \tag{6.2}$$

where

$$\mathrm{p}''_m(r,z) = \frac{1}{2\pi}\int_0^{2\pi} \mathrm{p}''(r,\theta'',z)e^{im\theta''}d\theta''. \tag{6.3}$$

The CFD solution for the rotor alone tones and buzz-saw tones can be written in the stationary frame for azimuthal modes, $m = -\infty$ to $+\infty$ as

$$\mathrm{p}(r,\theta,z,t) = \mathrm{p}''(r,\theta-\Omega t,z) = \sum_{m=-\infty}^{\infty} \mathrm{p}''_m(r,z)e^{-im(\theta-\Omega t)}. \tag{6.4}$$

This can be further split into steady and unsteady components

$$\mathrm{p}(r,\theta,z,t) = \mathrm{p}''_{m=0} + \sum_{\substack{m=-\infty \\ m\neq 0}}^{\infty} \mathrm{p}''_m(r,z)e^{-im(\theta-\Omega t)}. \tag{6.5}$$

This indicates that each azimuthal component contributes only at angular frequency $\omega = m\Omega$, which corresponds to harmonics of the shaft frequency (engine order).

The in-duct CAA simulations are carried out for each engine order separately. The resulting acoustic field for a single engine order is given by

$$\mathrm{p}^{\omega}_m(r,\theta,z,t) = Re\left\{\sum_{\mu=1}^{\infty} {L_c}^{\omega}_{m,\mu}\tilde{\mathrm{p}}^{\omega}_{m,\mu}(r,z)e^{-im(\theta-\Omega t)}\right\}, \tag{6.6}$$

where $\tilde{\mathrm{p}}^{\omega}_{m,\mu}(r,z)$ is the Fourier component and ${L_c}^{\omega}_{m,\mu}$ are the unknown coefficients.

The CFD and CAA solutions are matched for each engine order m. The residuals are defined as follows

$$\delta \mathrm{p}_m(r,\theta,z,t) = Re\left\{\left(\mathrm{p}'_m(r,z) - \sum_{\mu=1}^{\infty} L_{c}{}^{\omega}_{m,\mu}\tilde{\mathrm{p}}^{\omega}_{m,\mu}(r,z)\right)e^{-im(\theta-\Omega t)}\right\}. \tag{6.7}$$

The coefficients $L_{c}{}^{\omega}_{m,\mu}$ are found by minimizing the following function

$$S\left(L_{c}{}^{\omega}_{m,1},\dots,L_{c}{}^{\omega}_{m,M}\right) = \sum_{i,j}\left|\mathrm{p}'_m(r_i,z_j) - \sum_{\mu=1}^{M} L_{c}{}^{\omega}_{m,\mu}\tilde{\mathrm{p}}^{\omega}_{m,\mu}(r_i,z_j)\right|^2. \tag{6.8}$$

with respect to the unknown complex-valued coefficients $L_{c}{}^{\omega}_{m,\mu}$. The minimization is performed over a region(s), defined by its radial and axial coordinates. The standard least squares method is applied on discrete points $\{r_i, z_j\}$. The function has its minimum for each radial mode when

$$\frac{\partial S\left(L_{c}{}^{\omega}_{m,1},\dots,L_{c}{}^{\omega}_{m,M}\right)}{\partial L_{c}{}^{\omega}_{m,\mu}} = 0. \tag{6.9}$$

This leads to system of linear equations with unknown matching coefficients

$$[A]_{MxM}\begin{bmatrix} L_{c}{}^{\omega}_{m,1} \\ \dots \\ L_{c}{}^{\omega}_{m,k} \\ \dots \\ L_{c}{}^{\omega}_{m,M} \end{bmatrix}_M = [B]_M, \tag{6.10}$$

where

$$A_{l,k} = \sum_{i,j}\tilde{\mathrm{p}}^{\omega}_{m,l}(r_i,z_j)\tilde{\mathrm{p}}^{\omega}_{m,k}{}^{*}(r_i,z_j),$$

and

$$B_k = \sum_{i,j}\mathrm{p}'_m(r_i,z_j)\tilde{\mathrm{p}}^{\omega}_{m,k}{}^{*}(r_i,z_j).$$

The maximum number of radial modes considered in the matching process M is set usually to all cut-on plus few cut-off modes.

6.3 Automated CFD/CAA coupling

The CAE scheme described in chapter 4 has been developed to allow the automated CFD/CAA coupling discussed in this chapter. The process is conducted by the managing script according to the description given in section 4.1. It is worth noting that the source flow CFD is performed externally and results are provided in the input file as a data on the matching points. The input file contains all necessary information for the coupling interface.

Following tasks are performed to obtain the final radiation CAA solution from the source flow CFD solution:

- Geometry reconstruction for in-duct simulations;
- Generation of meshes for in-duct mean flow and in-duct CAA analyses;
- In-duct mean flow calculation;
- In-duct CAA simulations for each engine order and mode separately;
- Matching of the in-duct CAA solutions to the acoustic pressure field predicted by the source flow CFD over the mesh of matching points according to equation 6.8;
- Sources for the radiation CAA are determined by the modal coefficients $L_{c^{\omega}_{m,\mu}}$ obtained from equations 6.10;
- Geometry reconstruction for radiation simulations;
- Generation of meshes for radiation mean flow and acoustic calculations;
- Mean flow calculation for radiation CAA;
- Radiation CAA simulation for the sources determined in the matching process;
- Post-processing of the results.

6.4 Benchmarking calculations

6.4.1 Validation for a 'mimic' of CFD

In the first approach, the mode matching scheme is validated for a 'mimic' of the source flow CFD ('CFD input') in which Actran TM is used to simulate the input from the CFD source. An axisymmetric generic turbofan intake is considered. The model is presented in figure 6.6 (a). The fan plane (admission plane for the CAA simulations) and the throat plane are indicated by dotted lines. The mean flow used in this study is shown in figure 6.6 (b). It

is obtained by solving the velocity potential equation for an irrotational compressible flow (see section 3.3.2). The flow at the fan plane has a Mach number of 0.55. In the external region the Mach number is 0.25. The total pressure and total temperature are set to 101563 Pa and 288 K, respectively. The mimic of the source flow CFD is obtained for a known set of incident modes at the fan plane by executing a different CAA tool, Actran TM [93]. In both Actran TM and Actran DGM, the acoustic excitation is realized by analytical modes applied to the fan plane. Therefore, the source used in Actran TM should be recovered in the CFD/CAA matching process. The error is easily assessed, since the original source is known. This allows checking, not only of the error in the matching region, but also of the overall precision in determining the CAA sources.

6.4.1.1 Parametric studies of the matching accuracy

In this section the accuracy and efficiency of the matching are examined. This is performed for zero mean flow and for a mean flow with a Mach number of 0.55 at the fan place (figure 6.6 (b)). The 'CFD input' is obtained for a single incident mode (12,1) with unit amplitude 1+0i Pa for the Helmholtz number kR_{fan} = 28. The following matching parameters are considered.

The number of points along a single matching rake: The matching for zero mean flow on a single matching rake (an array of points) placed at the fan plane has been studied.

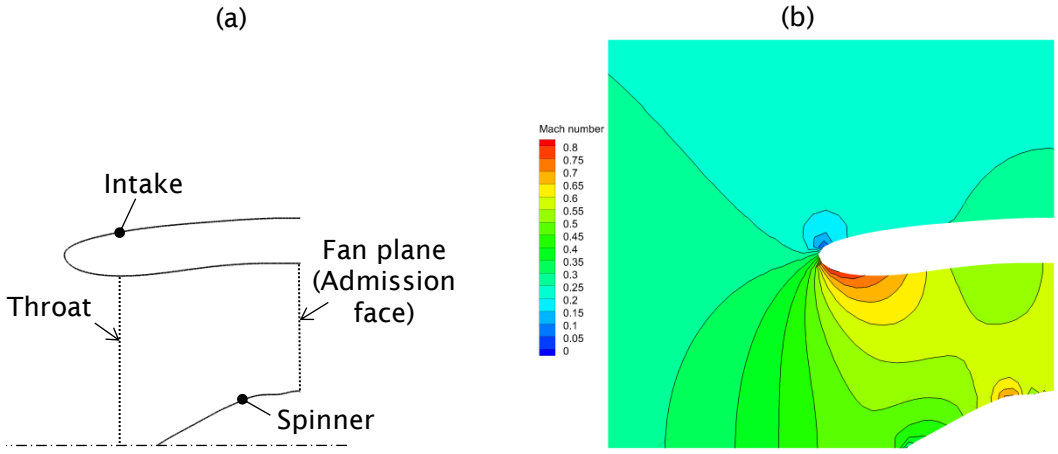

Figure 6.6: A generic turbofan intake. (a) The geometry; (b) The mean flow.

Results not presented in this work indicate clearly that the number of points just above the maximum radial order involved in the problem is sufficient. Despite a further increase in the number of points the matching errors (i.e. amplitude and phase) remained unchanged.

The number of radial modes used on the fan plane: In this case the matching is performed at the throat plane for the mean flow corresponding to the Mach number of 0.55 at the fan plane. The amplitude error at a level of approximately 2.5% and phase error slightly above 0.04 radians is observed, respectively, see figures 6.7 (a) and (b). The errors are constant until all cut-on modes are included, and then up to three additional cut-off modes. The amplitude error starts to increase when further fan modes are included increasing rapidly as radial order μ exceeds 10. In the case of the phase error, it reduces slightly for the radial orders 10 and 11, and decreases further for the higher orders. It is evident that the system of linear equations in the matching process is ill-conditioned when too many cut-off radial orders are included. This is due to the fact that the cut-off modes decay rapidly and are not detected by the matching process.

The effect of a single matching rake position and the number of matching rakes: Studies are presented for the flow case. All cut-on radial orders are included in the matching process. Firstly, the position of a single rake is examined. The rake is moved from the throat plane towards the fan plane. Secondly, the number of rakes is considered by adding additional rakes to an initial rake placed at the intake throat; a single rake is added at each position, moving towards the fan plane. The axial stations for both tests are the same. The results of the amplitude and phase errors of the estimated CAA source are presented in figures 6.8 (a) and (b), respectively. In both plots, the top horizontal axis represents the number of matching rakes, whereas the bottom one shows the axial position of a matching rake. In general, the accuracy improves when a single matching rake moves, or new rakes are added, towards the fan plane (position 0.0 in figure 6.8). In the case of an increasing number of matching rakes, the errors are more stable and reveal consistent decreasing tendency. However, in the vicinity of the throat (position -1.0 in figure 6.8) some rapid change occurs in the amplitude error, which is amplified when a single rake is considered.

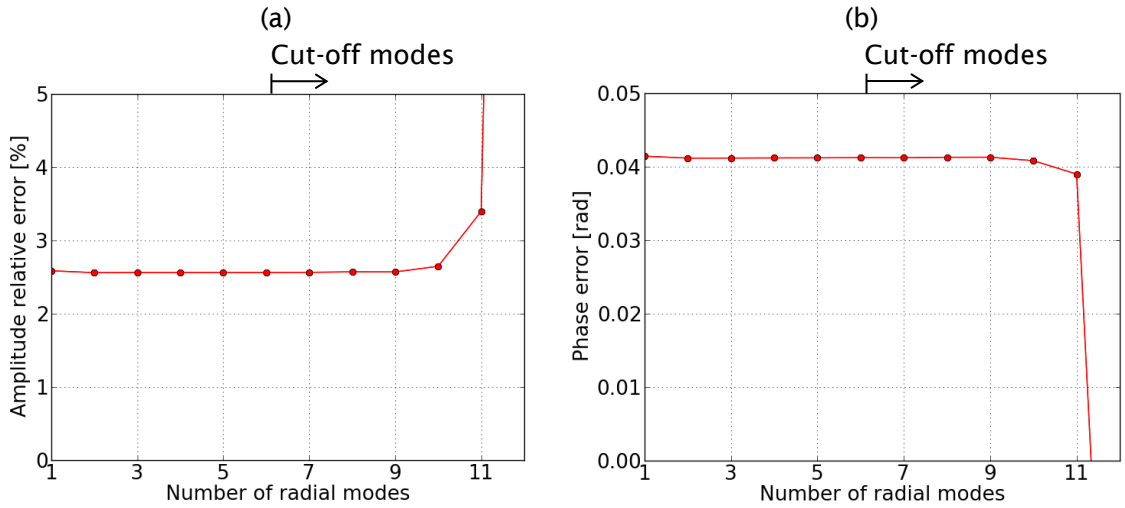

Figure 6.7: Amplitude relative error (a) and phase error (b) of the estimated CAA source versus number of radial orders included in the matching. The mimic of the CFD is obtained for a single incident mode (12,1) for kR_{fan} = 28. The matching is performed on a single rake at the throat.

It is believed that strong mean flow gradients, which take place in this region, cause the unsettled behaviour of the error. The phase error indicates that one rake provides better matching accuracy. The improvement with respect to the multi-rakes matching is not constant along the intakes axial axis. It oscillates around 0.01 radians. The higher phase error in the case of the multi-rake matching is a result of different behaviour of dispersion errors inherent to the numerical schemes used to obtain the mimic of the source flow and the in-duct CAA solutions.

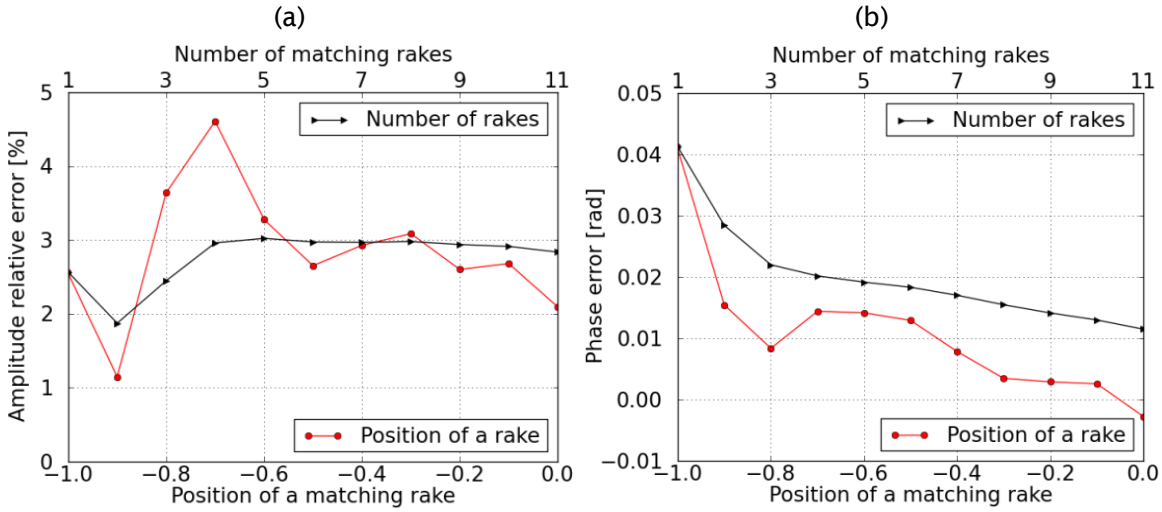

Figure 6.8: Amplitude relative error (a) and phase error (b) of the estimated CAA source for different positions of the matching rake (red dots and solid red line) and the number of the matching rakes (black triangles and solid black line). The mimic of the CFD source flow is obtained for a single incident mode (12,1) and kR_{fan} = 28.

The rapid decay of the phase error which is observed in the vicinity of the throat can be also explained by strong mean flow gradients occurring in this region.

6.4.1.2 Comparison of in-duct acoustic pressure

In order to investigate further the accuracy of the matching the mimic of the CFD and matched in-duct CAA solutions are compared. This comparison is made for the non-dimensional Helmholtz number kR_{fan} = 30. The intake geometry and the mean flow are the same as those used in the previous section. Two of the CFD solution are considered. In the first case the solution is obtained for an excitation realized by a single incident mode (24,1) with unit amplitude 1+0i Pa. In the second case it is obtained for an excitation realized by three incident modes (24,1), (24,2) and (24,3) with amplitudes equal to 1+0i Pa; 0.5+0.0i Pa and 0.1+0.75i Pa, respectively. The matching is conducted on a single matching rake placed at the intake throat and all cut-on modes, i.e. (24,1); (24,2) and (24,3) are included.

The SPL colour maps corresponding to the mimics of the CFD obtained for the excitation realized by a single incident mode (24,1), and the excitation realized by three incident modes (24,1), (24,2) and (24,3) are shown in figures 6.9 (a) and (b), respectively. Good agreement between the mimic of the CFD and matched in-duct CAA in the whole computational domain is achieved for both excitation cases as can be seen when comparing figures 6.9 (c) and (a), and figures 6.9 (d) and (b), respectively. Important acoustic features are well captured, including physical scattering in the radial direction as a result of the non-uniform mean flow. However, evidence of spurious reflections in the buffer zone is observed in the DGM solution (figures 6.9 (c) and (d)). In order to alleviate this problem, three times thicker buffer zone with the optimal parameters given in section 2.7.4.2 is used to perform the in-duct CAA computations presented later in this thesis. A significant difference between the mimic of the CFD and matched in-duct CAA solutions is evident at the fan plane for the multimodal excitation case. This is due to the last radial mode (24,3) which is cut-on at the fan plane but becomes evanescent (exponentially decaying) when travelling upstream. Therefore, the mode is not detected by the matching process on the matching rake and finally not predicted as a source.

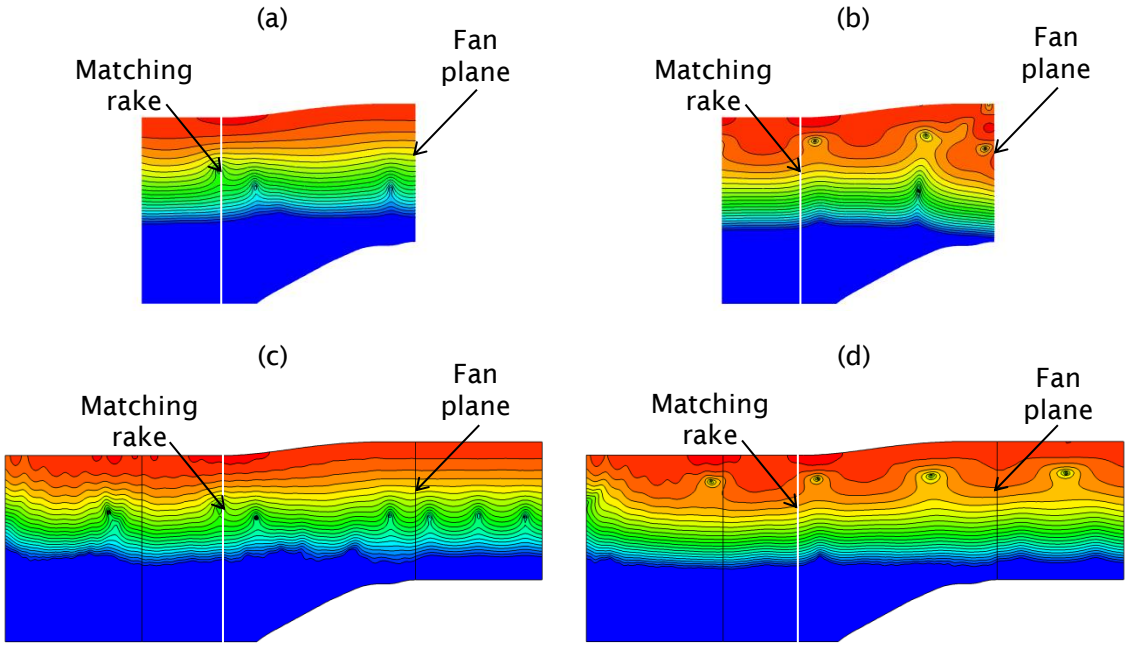

Figure 6.9: The in-duct SPL comparison. The mimic of the CFD solution obtained: (a) for a single incident mode (24,1) with unit amplitude 1+0i, and (b) for modes (24,1), (24,2) and (24,3) with amplitudes equal to 1+0i, 0.5+0.0i and 0.1+0.75i, respectively. Both for kR_{fan} = 30. The resulting matched CAA in-duct solutions obtained by matching to the mimic of the CFD solution obtained: (c) for a single incident mode (24,1), and (d) for modes (24,1), (24,2) and (24,3).

The SPL comparisons along the matching rake are shown in figure 6.10. Here, the good agreement between the mimic of the CFD and matched in-duct CAA is confirmed for both excitation cases.

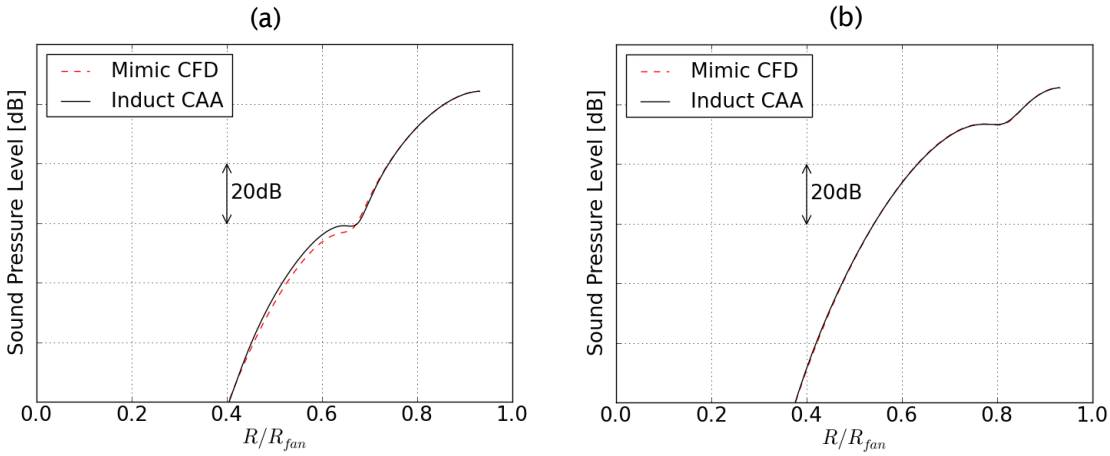

Figure 6.10: The SPL comparison along the matching rake, mimic of the CFD against matched in-duct CAA. The mimic of the CFD solution is obtained (a) for a single incident mode (24,1) with unit amplitude 1+0i, and (b) for modes (24,1), (24,2) and (24,3) with amplitudes equal to 1+0i, 0.5+0.0i and 0.1+0.75i, respectively. Both for kR_{fan} = 30.

However, in the case of the 'CFD input' excited by a single incident mode (24,1) some disagreement of approximately 3-4 dB is observed for the middle radii (figure 6.10 (a)).

6.4.1.3 Comparison of radiated acoustic pressure

The radiation CAA analyses are carried out for the sources determined in the matching process discussed in the previous section. The same generic intake geometry is used. The mean flow is set to the Mach number of 0.55 at the fan plane. The ambient mean flow is uniform and corresponds to the flight Mach number of 0.25. Two sets of the incident modes (sources) are used for the radiation CAA analyses: one determined for the 'CFD input' obtained for a single incident mode excitation, and the second determined for the 'CFD input' obtained for multimodal excitation. The comparison of the modal sources used to obtain the 'CFD input' and the sources determined in the matching process is shown in Table 6.1. Examining the determined sources, one should notice that for the case of matching to the mimic of the CFD excited by three incident modes the determined source mode (24,3) does not correspond to the equivalent incident mode used originally to obtain the mimic of the CFD. This is, as already reported, due to the fact that the incident mode (24,3) becomes evanescent before reaching the matching face. As a result, it is not found in the matching process and therefore not reconstructed as a source for the radiation CAA.

Table 6.1. The comparison of the modal sources used for the 'CFD input' and the sources determined in the matching process.

	Sources used for the mimic of the CFD			Determined sources		
Mimic of the CFD excited by a single incident mode	(24,1) 1+0i			(24,1) 0.9815+0.0011i	(24,2) 0.0037+0.0015i	(24,3) 0.0029-0.0100i
Mimic of the CFD excited by three incident modes	(24,1) 1+0i	(24,2) 0.5+0.0i	(24,3) 0.1+0.75i	(24,1) 0.9824+0.0006i	(24,2) 0.4143+0.0102i	(24,3) 0.0078-0.0171i

The SPL comparisons in the far-field between the mimic of the CFD and the radiation CAA are presented in figures 6.11 (a) and (b). These show the cases when the mimic of the CFD contains one and three incident modes, respectively.

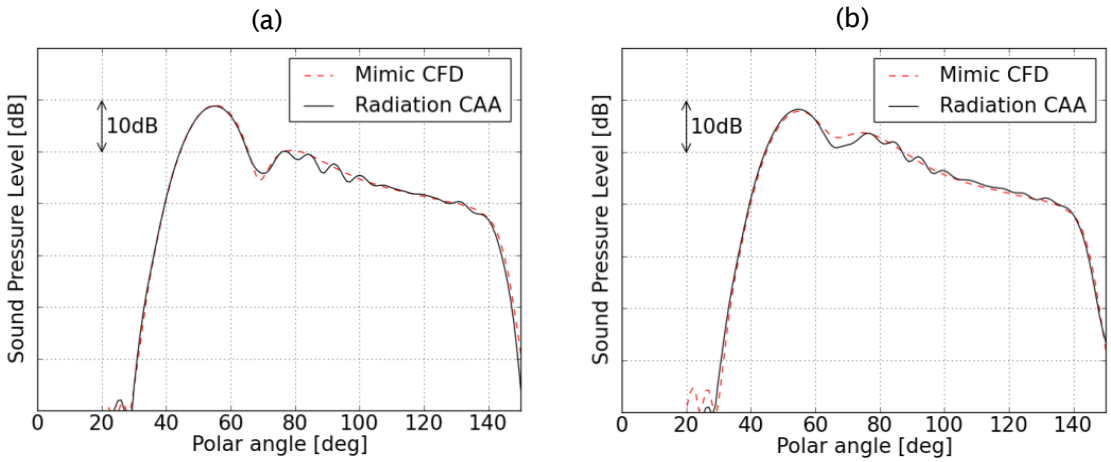

Figure 6.11: The SPL comparisons in the far-field between the mimic of the CFD and radiation CAA. The mimic of the CFD solution is obtained (a) for a single incident mode (24,1) with unit amplitude 1+0i and (b) for the modes (24,1), (24,2) and (24,3) with amplitudes equal to 1+0i, 0.5+0.0i and 0.1+0.75i, respectively. Both for kR_{fan} = 30.

The SPL is plotted in the forward-arc at a radius of $40R_{fan}$; the polar angle ranges from 0 to 150 degrees. Very good agreement is achieved, however some small discrepancies are observed for both cases. Numerical oscillations are evident in the DGM solution of approximately 1-2 dB in range of the polar angles between 75 and 140 degrees. These oscillations are caused by spurious reflections from the buffer zone. Additionally, the decay between the radiation lobes at the angle of 70 degrees seems to be slightly worse resolved by Actran DGM (Radiation CAA). This may suggest that the mesh resolution or selected element orders are not fully optimal.

6.4.2 Validation against rig test data

The validation is performed for 1/3-scale model fan rig which was tested at the AneCom AeroTest GmbH anechoic facility [167] within EC 7th Framework Programme OPENAIR [168]. The intake rig model is shown in figure 6.12. This is an axisymmetric intake which is defined by the spinner and by a section of the nacelle. The fan plane and matching rakes are indicated by dashed lines. Two matching rakes are considered, both are placed in the vicinity of the intake throat in order to include non-linear effects implicitly.

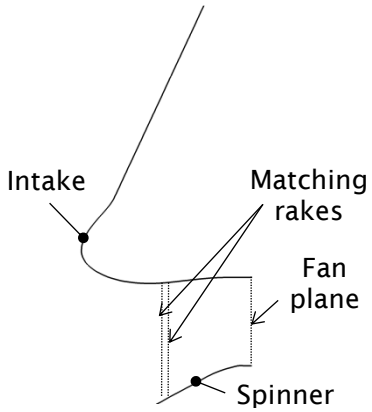

Figure 6.12: Intake rig geometry.

The matching rake '0' is placed slightly closer to the fan plane, whereas the matching rake '1' is placed on the side closer to the throat. In this case the matching is performed for the proper source flow CFD. The CFD model is described in section 6.2.1.1. The inlet total pressure and total temperature of the flow are equal to 101202 Pa and 288 K, respectively. The Mach number at the fan plane is set to ensure the same mass flow rate as achieved in the source flow CFD calculation. The estimated value is 0.54. A comparison of the mean flow velocity along the matching rake '1' obtained from the steady component of the source flow CFD and the mean flow independently computed for the CAA simulations is shown in figure 6.13. The agreement is fairly good. One must note that the models and methods used in each case are considerably different (see sections 6.2.1.1 and 6.2.1.2 for details).

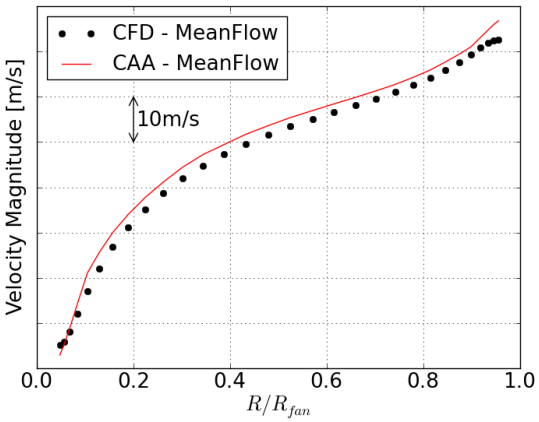

Figure 6.13: The mean flow velocity comparison along the matching rake '1' between the source CFD and the in-duct CAA.

6.4.2.1 In-duct CAA

The matching is performed for the rotor-alone tone noise component (see section 1.2.1). The analyses are carried out for a single engine order 20, which corresponds to the blade passing frequency. The shaft speed is equal to 7680 rpm. For this fan speed one radial mode is cut on for m = 20, i.e. (20,1). Two sets of the source flow input are considered, the first one corresponds to a one-blade-passage CFD solution and the second to a four-blade-passages CFD simulation. The SPL comparison along the matching rake '1' for engine order 20 is shown in figure 6.14. As expected, the results differ slightly due to a variation in blade stagger angle introduced in the model for four blade passages CFD (in order to generate buzz-saw noise tones). The difference is around 1-2dB over the relevant range of radii. Some differences in the mode shape are also observed. The numerical contamination at low radii is somewhat lower for the case of the four-blade-passages CFD.

A series of matching tests were conducted for the CFD data corresponding to one and four blade passages. The following matching configurations are considered: matching on a single rake, either on the matching rake '0' or '1', matching on the two matching rakes simultaneously, matching including only cut-on modes, and matching including all cut-on modes plus one cut-off mode. The least square fitting errors are estimated on the matching rakes. The relative errors on the acoustic pressure $\sum_i \|p_{CAA,i} - p_{CFD,i}\|^2 / \sum_i \|p_{CFD,i}\|^2$ are presented in Table 6.2. In the case of four blade passages a better fit is achieved.

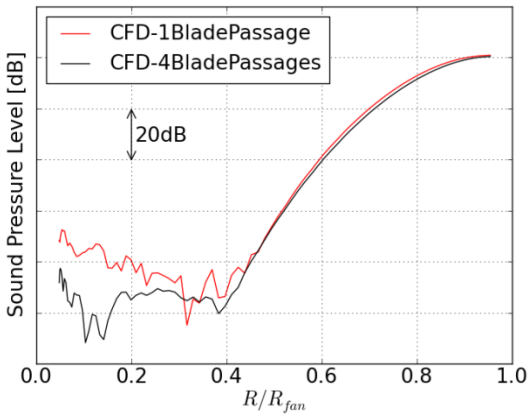

Figure 6.14: The SPL comparison between the one blade passage CFD and four blade passages CFD at matching rake '1', EO = 20 (1BPF).

The relative matching error is less than half of that for the one blade passage CFD. The estimated errors clearly show that a small change in the position of a single matching rake has little impact on the matching accuracy. A significant improvement, nearly one order of magnitude, is achieved when the matching on a single rake, either '0' or '1', is performed with an additional cut-off mode included. An increase in the error is observed when the matching is conducted on the two matching rakes simultaneously. This is a rather unexpected result. The error is approximately three times higher compared to the equivalent errors for the matching on a single rake. In this case adding an additional cut-off mode in the matching process also improves the accuracy, but on a much lower scale.

Table 6.2. Relative matching errors on the matching rakes.

Matching configuration	Relative error on rake '0'	Relative error on rake '1'
1 blade passage CFD: Matching on a single rake '0' – All cut-on modes included.		4.684E-03
4 blade passages CFD: Matching on a single rake '0' – All cut-on modes included.	2.278E-03	
4 blade passages CFD: Matching on a single rake '0' – All cut-on modes plus one cut-off mode included.	0.266E-03	
4 blade passages CFD: Matching on a single rake '1' – All cut-on modes included.		2.259E-03
4 blade passages CFD: Matching on a single rake '1' – All cut-on modes plus one cut-off mode included.		0.273E-03
4 blade passages CFD: Matching on rakes '0' and '1' – All cut-on modes included.	7.024E-03	7.600E-03
4 blade passages CFD: Matching on rakes '0' and '1' – All cut-on modes plus one cut-off mode included.	5.876E-03	6.736E-03

In order to better understand the matching errors displayed in Table 6.2 the SPL comparisons along the matching rakes are made. The first one, for one blade passage CFD is shown in figure 6.15. Good agreement is achieved. The discrepancies of approximately 2dB for the relevant radii are observed.

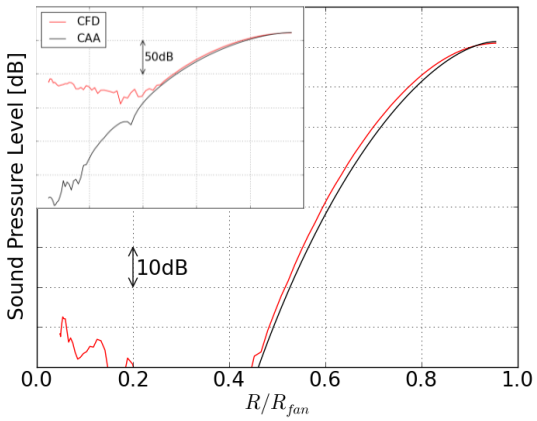

Figure 6.15: The SPL comparison between the one blade passage CFD and in-duct matched CAA on the matching rake '1'. EO = 20 (1BPF).

This corresponds to the differences between the two types of the CFD input data used in this work. A large gap between the matched CAA and CFD is evident at low radii where levels are low and poorly resolved. Nonetheless, the dynamic range of the CFD solution is around 75dB, which is acceptable in the context of CAA applications.

The following four SPL comparisons along the matching rakes for the four-blade-passage CFD are shown in figure 6.16. In the case of matching conducted for all cut-on modes (figures 6.16 (a) and (c)) the maximum disagreement between the CFD and matched in-duct CAA is approximately 2-3dB. A slightly better agreement is observed when a single cut-off mode is added in the matching process (figures 6.16 (b) and (d)). These SPL comparisons confirm the behaviour of the matching errors displayed in Table 6.2. However, the improvement in the matching accuracy due to adding a single cut-off mode in the matching process is less pronounced in the SPL comparisons. A similar set of the SPL comparisons to the one discussed in the previous paragraph is shown in figure 6.17. In this case the matching is performed on the two matching rakes simultaneously. Two matching variations are considered: one with all cut-on modes included in the matching process and second with an additional cut-off mode included. The former corresponds to the left column of figure 6.17, whereas the latter corresponds to the right column of the same figure.

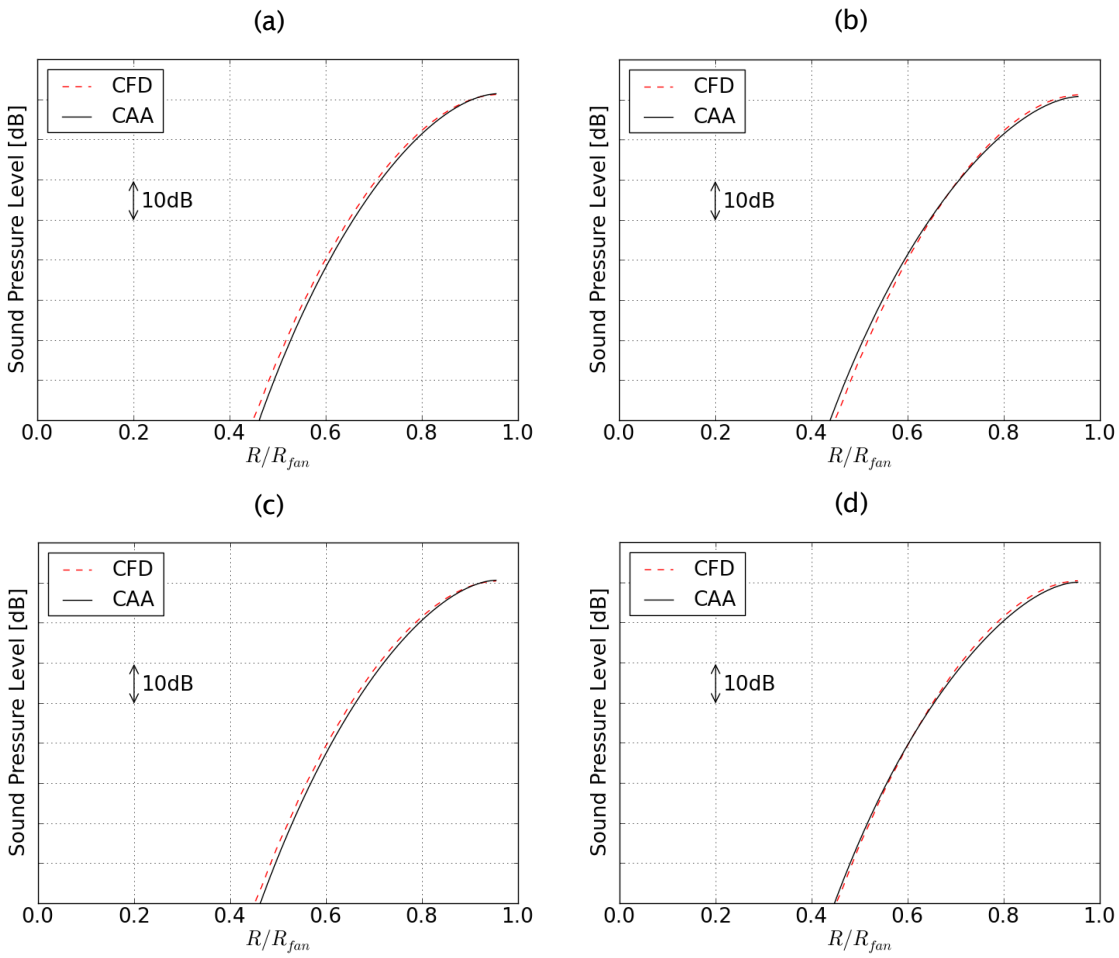

Figure 6.16: The comparisons of the SPL along the matching rakes between the four blade passages source flow CFD and matched in-duct CAA. The matching is performed: (a) on the matching rake '0' – all cut-on modes included, (b) on the matching rake '0' – all cut-on modes plus one cut-off mode included, (c) on the matching rake '1' – all cut-on modes included, and (d) on the matching rake '1' – all cut-on modes plus one cut-off mode included.

The rows are for matching rake '0' (top row) and matching rake '1' (bottom row), respectively. In this case the consistency with the errors shown in Table 6.2 is not that well maintained as it was for the matching on a single matching rake. A large decrease in the matching accuracy is suggested by the values of the relative errors (Table 6.2) achieved for the matching performed on the two matching rakes simultaneously. This is, however, not confirmed by the SPL comparisons shown in figures 6.17 (a) and (c) which suggest fairly similar accuracy to the one reported for the matching using a single matching rake (figures 6.16 (a) and (c)). Moreover, the relative errors indicate slight improvement when a cut-off mode is added in the matching process, whereas the SPL comparisons show clearly worsening of the matching accuracy, figures 6.17 (b) and (d).

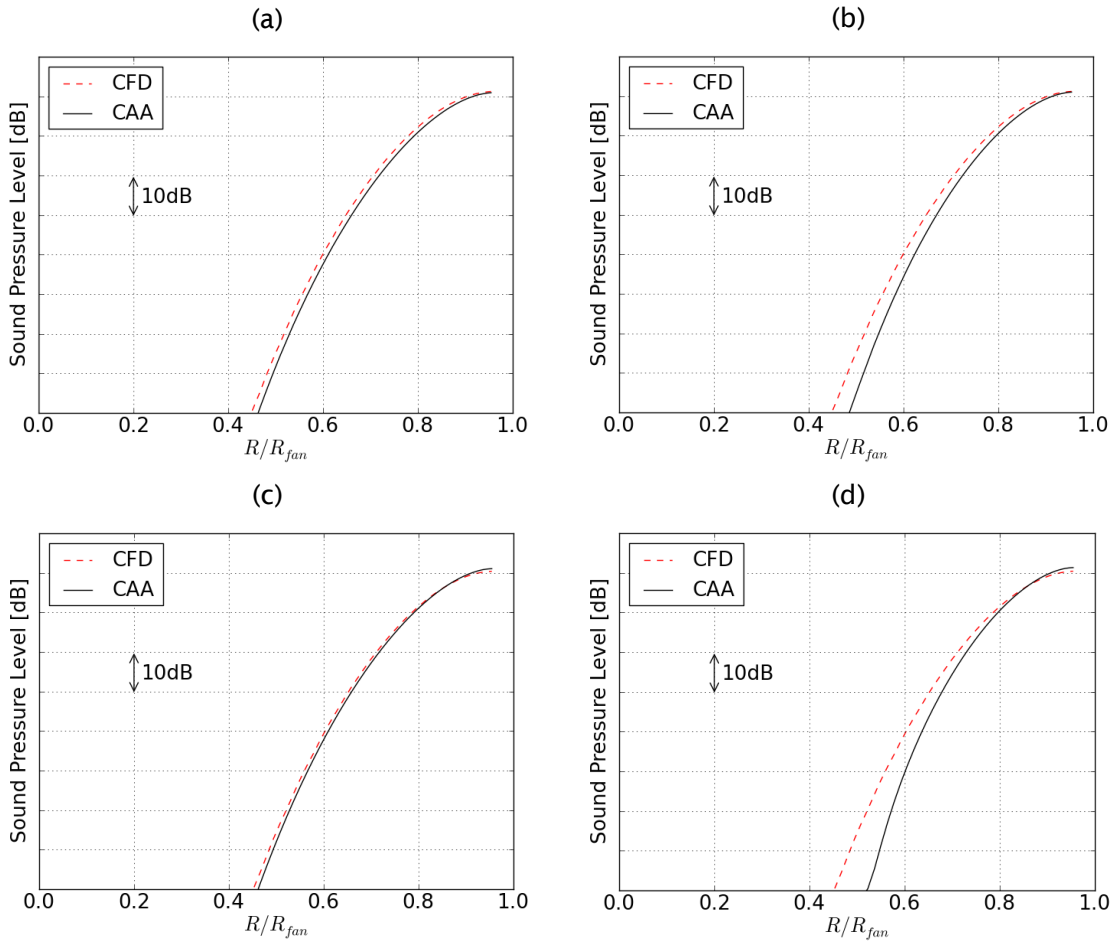

Figure 6.17: The comparisons of the SPL along the matching rakes between the four blade passages source flow CFD and matched in-duct CAA. The matching is performed on the two matching rakes simultaneously. The following SPL comparisons are shown (a) on the matching rake '0' – all cut-on modes, (b) on the matching rake '0' – all cut-on modes plus one cut-off mode, (c) on the matching rake '1' – all cut-on modes, and (d) on the matching rake '1' – all cut-on modes plus one cut-off mode.

6.4.2.2 Radiation CAA

The radiation CAA simulations are carried out for the rotor-alone tone source determined in the matching process for engine order 20 as described in the previous section. The matching has been performed on the matching rake '1' for all cut-on modes included.

The mean flow used for the radiation CAA simulations is shown in figure 6.18 (a). The flow parameters, i.e. total pressure, total temperature and the Mach number at the fan plane are the same as those used for the in-duct CAA analyses (section 6.4.2.1). The flow accelerates strongly from rest to the high flow velocity at the intake highlight.

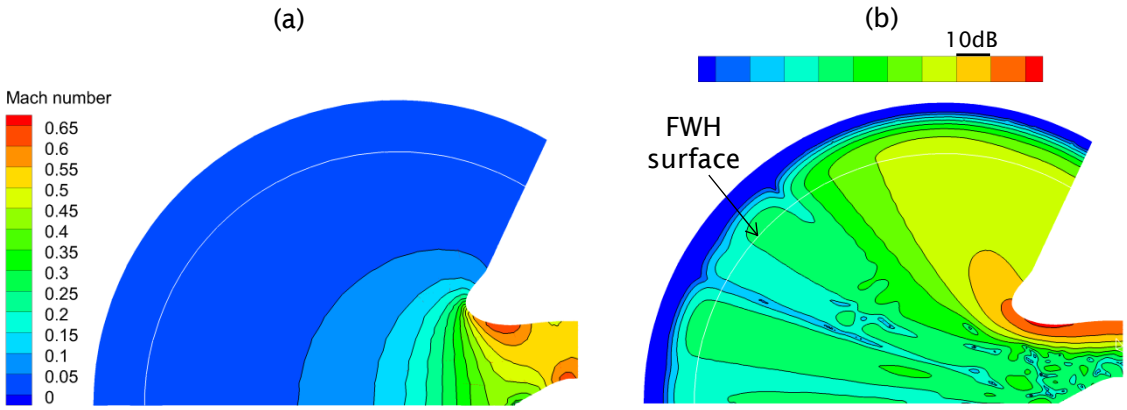

Figure 6.18: (a) The mean flow used for the radiation CAA simulations. The Mach number at the fan plane is set to 0.54 and to zero in the ambient. (b) The radiation CAA solution in the near-field, SPL [dB]. The CFD/CAA matching is achieved for the rotor-alone tone at EO = 20 (1BPF).

Inside the intake duct there are two high speed regions: one at the throat and second at the spinner where its shape transforms to a cylinder. The latter velocity peak has a negligible impact on the acoustic field, since most of the acoustic energy is transmitted along the outer wall of the intake duct. As already stated, a fairly good agreement between the steady component of the source flow CFD and the mean flow computed for the CAA along the matching rake '1' has been achieved (see figure 6.13).

The resulting SPL in the near-field is shown in figure 6.18 (b). A single radiation lobe can be seen. Amplification in the SPL of approximately 2.5dB is observed in vicinity of the outer wall at the throat location. This is due to the mean flow acceleration and narrowing of the intakes duct cross section area. Some spurious mesh-scattered modes are present in the centre region of the model (see section 5.2.2). The FWH surface used for the far-field reconstruction is also indicated in figure 6.18 (b). The solution outside of the FWH surface is strongly damped which is to be expected, since it is the buffer zone.

The instantaneous pressure on the fan plane and on the matching plane of '1' is shown in figure 6.19. An axisymmetric solution is achieved. It is an expected result, since the geometry and the mean flow are axisymmetric. The instantaneous pressure maps clearly show that the injected mode (20,1) as shown in figure 6.19 (a) is correctly solved, and its shape is well preserved in the matching plane as shown in figure 6.19 (b).

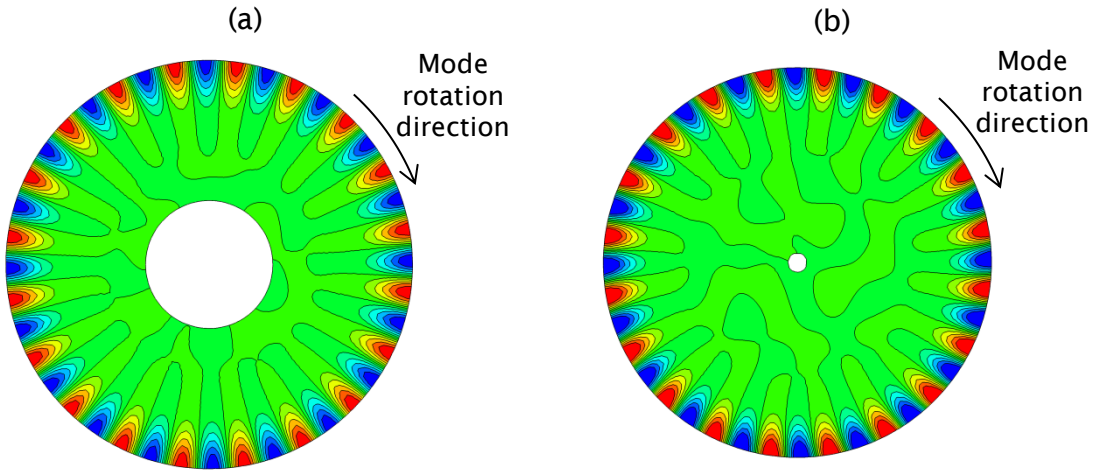

Figure 6.19: The instantaneous pressure on the traverse cut planes, (a) The fan plane and (b) the matching plane at '1'. The CFD/CAA matching is achieved for the rotor-alone tone at EO = 20 (1BPF).

The SPL in the far-field is shown and compared to the experimental data in figure 6.20. It is calculated on a forward arc with radius of approximately $40R_{fan}$. The polar angle ranges from 0 to 120 degrees in increments of 5 degrees. Good agreement between the 2D axisymmetric and 3D radiation CAA models is observed. A discrepancy of approximately 2-3 dB can be seen for the polar angles above 20 degrees. In the 3D solution numerical noise due to the mesh-scattered modes is observed for the polar angles below 20 degrees. Very good agreement between the experimental data and the radiation CAA results is achieved in terms of the directivity shape over the entire range of the polar angles. The observed pressure amplitudes agree worse. A maximum discrepancy of approximately 10-15dB is observed for the high polar angles. For the rest of the polar angles the discrepancy varies between 5 and 8dB.

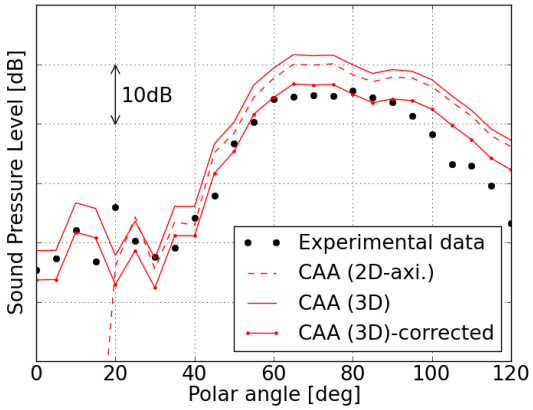

Figure 6.20: The comparison of the far-field directivity of the SPL between the experimental data and the radiation CAA on a forward arc of radius $40R_{fan}$. The CFD/CAA matching is achieved for the rotor-alone tone at EO = 20 (1BPF).

In order to identify the origin of the inconsistency, the SPL comparison inside the intake duct along the wall has also been made[7]. It has been found that the SPL is over-predicted of approximately 5dB at the throat location by the CFD/CAA coupling approach when compared to the experimental data. After correcting the CAA results by 5dB much better agreement between the CAA and experimental data has been achieved, as can be seen in figure 6.20. Nonetheless, considerable discrepancies can still be found at the high polar angles. In the proposed CFD/CAA integration approach the non-linear effects have not been included in the CAA models, although they are implicitly included in the region downstream of the CFD matching rake. However, in the case of hard-walled intake, which is considered here, the sound pressure level remains at a high level along the whole intake as shown in figure 6.18 (b). The discrepancies between the CAA and experimental data may therefore be attributable to the absence of non-linear effects in the CAA part of the solution. This approach is, however, expected to give better accuracy for lined cases. While the discrepancies, at the high polar angles, can be attributed to small differences between the numerical and experimental setup. Namely, that there was an acoustic cavity with bulk-reacting sound absorbing material located on the outer side wall of the rig in the experimental setup which was not included in the CAA simulations.

6.4.3 Demonstration for buzz-saw noise

In this section the CFD/CAA integration is demonstrated for selected buzz-saw noise tones. This calculation is performed for the axisymmetric rig intake model presented in figure 6.12 and discussed in section 6.4.2. The mean flow and the rest of the parameters also remain unchanged. The matching is carried out on a single matching rake '1'. The SPL comparisons between the CFD and matched in-duct CAA along the matching rake are shown in figure 6.21 for engine orders: 5, 10, 15, and 25, respectively. As expected the mode shape and its peak value change significantly when moving towards the higher engine orders. Good agreement is achieved for all analysed engine orders. However, a slight decay in the accuracy is observed for the higher engine orders (see figures 6.21 (c) and (d)).

[7] The comparison is not included due to confidentiality protection.

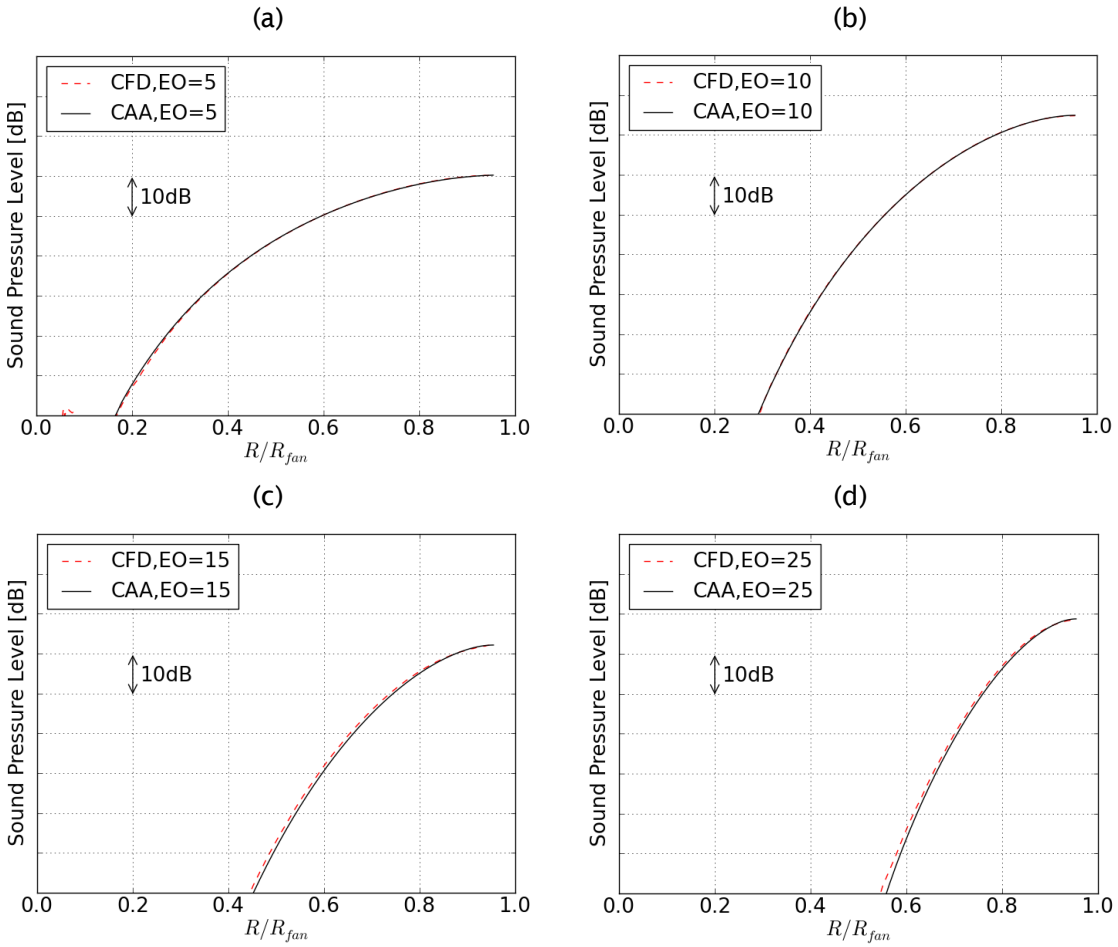

Figure 6.21: The comparisons of the SPL along the matching rake '1' between the source flow CFD and matched in-duct CAA for buzz-saw noise tones (a) EO = 5, (b) EO = 10, (c) EO = 15, and (d) EO = 25.

It is believed that the small mismatch is a result of differences in the mean flow between the CFD and the CAA which are more important for high frequencies as the wavelength become-progressively shorter.

Radiation CAA simulations are conducted for the sources determined in the matching process. The far-field directivities of the SPL on a forward arc for the rotor alone tone and buzz-saw noise tones are shown in figure 6.22. The rotor alone tone (BPF tone) is the most evident noise component. The buzz-saw tone corresponding to the engine order 10 is also contributing considerably. In some ranges of the polar angles the difference is less than 10dB. This is an important outcome confirming the significance of the buzz-saw noise in the overall noise level in the far-field. Additionally, as reported already, the numerical noise due to the mesh scattering is evident for low polar angles. No measured data is available for validating these results.

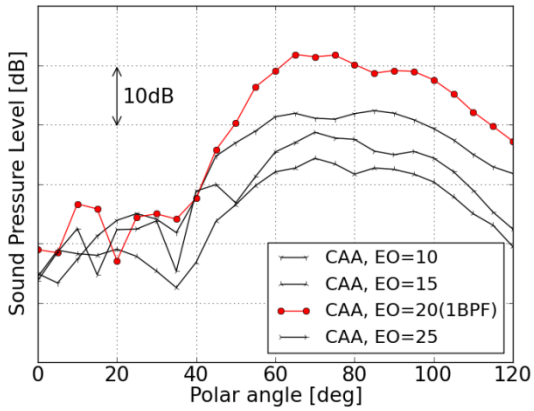

Figure 6.22: The far-field directivities of the SPL on a forward arc for the rig intake. The CFD/CAA matching is achieved for the rotor-alone tone (EO = 20), and buzz-saw noise tones (EO = 10, 15, and 25).

6.5 Summary and Conclusions

An approach for integrating Computational Fluid Dynamics (CFD) and Computational Aero-Acoustics (CAA) to predict the fan stage tonal noise propagation and radiation from a turbofan intake has been proposed and developed. The CFD and the CAA solutions are matched in a region where non-linear effects can be considered less important and the source modes for the CAA model are determined. The modal source is then used for the radiation CAA to obtain the acoustic solution.

Firstly, the matching technique has been validated for an artificial CFD input. The artificial data has been obtained by using other linearized frequency domain CAA method. The preliminary validation has been performed for a generic 2D axisymmetric intake. Several parameters defining the matching process, such as the position and the number of matching rakes, the number of discrete points in each matching rake, and the number of cut-off modes included in the matching process, have been examined. The technique has proved successful, although it has been performed for an artificial CFD input.

In the next stage, the CFD/CAA coupling has been compared to rig test data. In this case, the source CFD was obtained by solving the Reynolds-Averaged Navier-Stokes equations in a frame fixed to the fan. The matching has been performed for the rotor-alone tone component. Good agreement on matching rakes has been achieved. Maximum discrepancy observed between the CFD and in-duct CAA was slightly above 1dB. Minor discrepancies between

the 2D axisymmetric and 3D models have been reported in the far-field solution, approximately 2-3dB. Finally, the SPL in the far-field has been compared to the experimental data. Here, the observed discrepancies were higher, about 10-15dB for high polar angles and about 5-8dB in the peak value. It has been found that the SPL is over-predicted of approximately 5dB at the throat location by the CFD/CAA coupling approach when compared to the experimental data. It can be inferred that for hard walled intakes, where the SPL remains at high levels along the intake wall, non-linear effects may play an important role along the whole length of the intake, and may have a considerable impact on the far-field solution. Correcting the far-field CAA solution by the induct discrepancies a much better agreement to the far field experimental data is achieved, with maximum difference of approximately 2-3 dB in the peak value.

Finally, a demonstration of the method for the buzz-saw noise has been performed. Good agreement along the matching rake has been achieved, particularly for lower engine orders. In the far field a typical character of the buzz-saw noise tones in relation to the rotor alone tone has been confirmed.

7. 3D intake shape and mean flow effects on sound propagation

7.1 Introduction

The problem considered in this chapter is that of noise propagation and radiation from 3D non-axisymmetric turbofan intakes. Numerical studies are conducted for rotor-alone tone at the blade passing frequency. The effects of geometry, mean flow distortion and static versus flight conditions on the sound field are examined.

The sound transmission through ducts with varying shapes has been widely studied using analytical and numerical approaches. The method of multiple-scales has been developed for hard-walled and lined straight ducts with slowly varying cross-sections both with and without mean flow [169] [170] [171]. An analytical approach which allows for curved (three-dimensional bends) hard-walled and lined circular cross-section ducts in the absence of mean flow has been also proposed [172] [173]. Brambley and Peake [174] applied asymptotic multiple-scales analysis to investigate sound propagation through curved hard-walled and lined ducts with smoothly varying wall radii along the duct in the presence of a non-uniform mean flow. Another analytical approach has been proposed by McAlpine et al. [175] to evaluate sound radiation from a flanged inclined duct with zero mean flow. On the other hand, the numerical methods have been used to perform studies of sound propagation and radiation from non-axisymmetric turbofan intakes. Hamilton and Astley [176] applied the time-domain finite/infinite element method to predict the acoustic propagation in a non-axisymmetric intake in the presence of irrotational mean flows. A similar intake problem has also been investigated numerically by Park et al. [43] using the high-order finite difference scheme (DRP) to solve the linearized Euler equations. The Kirchhoff integral method has been applied to compute the far-field directivity. Schoenwald et al. [46] studied the influence of the scarfing angle of a turbofan intake and the mean flow angle of attack on the sound field. This was also performed by means of a DRP scheme applied to solve the linearized Euler equations. In order to obtain

the far-field solution the Ffowcs Williams-Hawkings (FWH) formulation was used.

The purpose of this chapter is to explore sound propagation and radiation from turbofan intakes to understand the effects of complex 3D shapes and mean flows on the sound field at realistic frequencies. The numerical studies will be performed by means of the DGM approach. However, a semi-analytical method and the frequency-domain finite/infinite element method will be used for a simplified intake problem to validate the DGM approach for sound propagation through distorted flows, and to investigate the impact of the mean flow distortion on sound absorption by liners.

7.2 Geometry effect, zero flow

The geometry effect on the sound field is examined for the case of zero flow. This is performed for a non-axisymmetric intake rig and three simplified variants of this geometry.

The non-axisymmetric intake rig is shown in figure 7.1. Its shape corresponds to 1/3-scale model fan rig which was considered within the EC 5th Framework Programme SILENCE(R) [177].

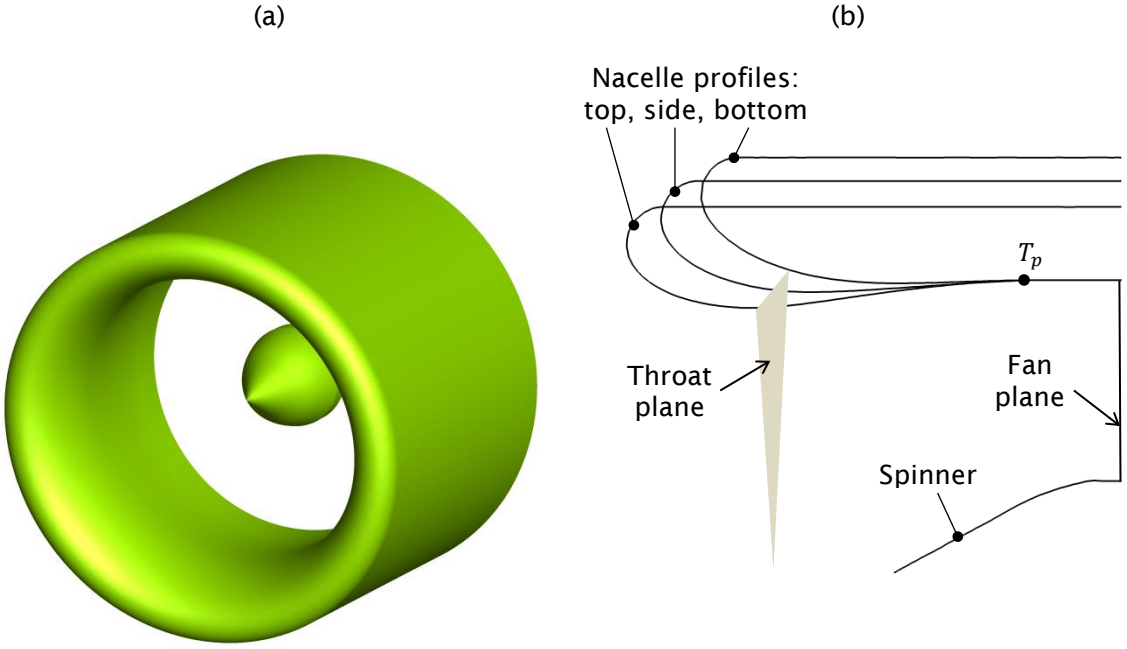

Figure 7.1: A non-axisymmetric intake rig: (a) rendered nacelle and spinner surfaces, (b) main azimuthal profiles, T_p is the transition point from an axisymmetric to a non-axisymmetric part of the nacelle.

The spinner has an axisymmetric shape. Unlike for the axisymmetric intake rig discussed in section 6.4.2, the external part of the nacelle is modelled as a cylinder. It has a negligible impact on the far-field directivity for the considered static rig condition since there is no external flow. The fan and throat planes are indicated in figure 7.1 (b). Three azimuthal profiles defining the nacelle surface are also shown. The vertical plane cutting through the centre line of the model is simultaneously a symmetry plane of this model. Therefore the side azimuthal profile is the same for both sides of the model. The shape of the nacelle between the fan plane and point T_p, which is indicated in figure 7.1 (b), is axisymmetric. In this study we focus our attention on the two main features describing the shape of the nacelle, i.e. the scarfing angle (inclined lip) and the droop effect (vertical displacement of the lip).

In order to better understand the influence of the scarfing angle and the droop effect on the sound field, simplified variants of the non-axisymmetric reference intake rig were produced. These are shown in figure 7.2. The first variant, which is shown in figure 7.2 (a), is an axisymmetric intake created by revolution of the side profile of the reference intake presented in figure 7.1. The other two variants, shown in figures 7.2 (b) and (c), are further simplifications to achieve idealized scarfed and drooped intakes, respectively. The axisymmetric spinner from the reference intake is used for all variants. The inclination angle of the idealized scarfed intake is set to the value of that measured for the reference intake, i.e. 6 degrees. This is also the case for the vertical displacement to obtain the idealized drooped intake which is around 8 percent of the fan radius. The 3D intake shapes are recovered from three azimuthal profiles located at the main azimuthal stations as described in section 4.2.

The DGM model is generated as described in chapter 3 (see respective sections). Model creation and execution is carried out automatically by using the CAE scheme described in chapter 4. The computational meshes which are used are refined to approximately one element per free field wavelength and to four elements per maximum mode azimuthal order over the nacelle surface. This gives element orders in the range 2 to 7. The modal source corresponding to a rotor-alone BPF tone determined in the CFD-CAA matching process for the axisymmetric intake rig is applied at the fan plane (see section 6.4.2.1).

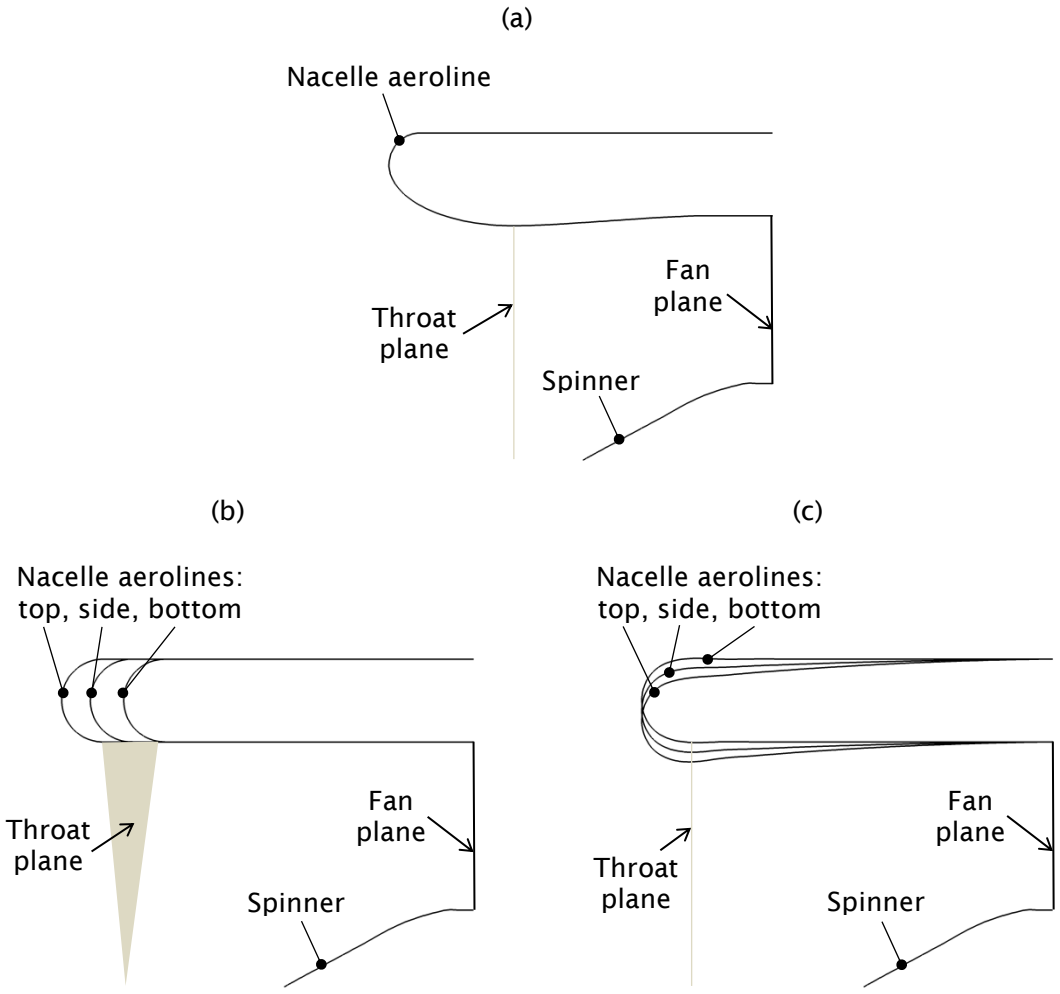

Figure 7.2: Simplified intake geometries used for the study of intake shape effects on the sound field: (a) axisymmetric version of the reference intake, (b) scarfed intake, (c) drooped intake.

To ensure a similar mode cut-on ratio[9] for the zero flow case the shaft speed is increased to 9360 rpm and the cut-on ratio of 0.888 is obtained. The total pressure and total temperature of air are taken as 101.2 kPa and 288 K, respectively, for all computations.

7.2.1 In-duct propagation

In this section we focus on propagation and scattering of the incident mode (20,1) along the 3D intake duct before it radiates from the open end. In figure 7.3 the sound pressure level distribution on the fan plane is shown for all intakes considered.

[9] The cut-on ratio is defined as the ratio of the cut-on frequency to the frequency of the source. For the values below one the mode is propagating (cut-on), whereas for the values above one the mode is evanescent (cut-off).

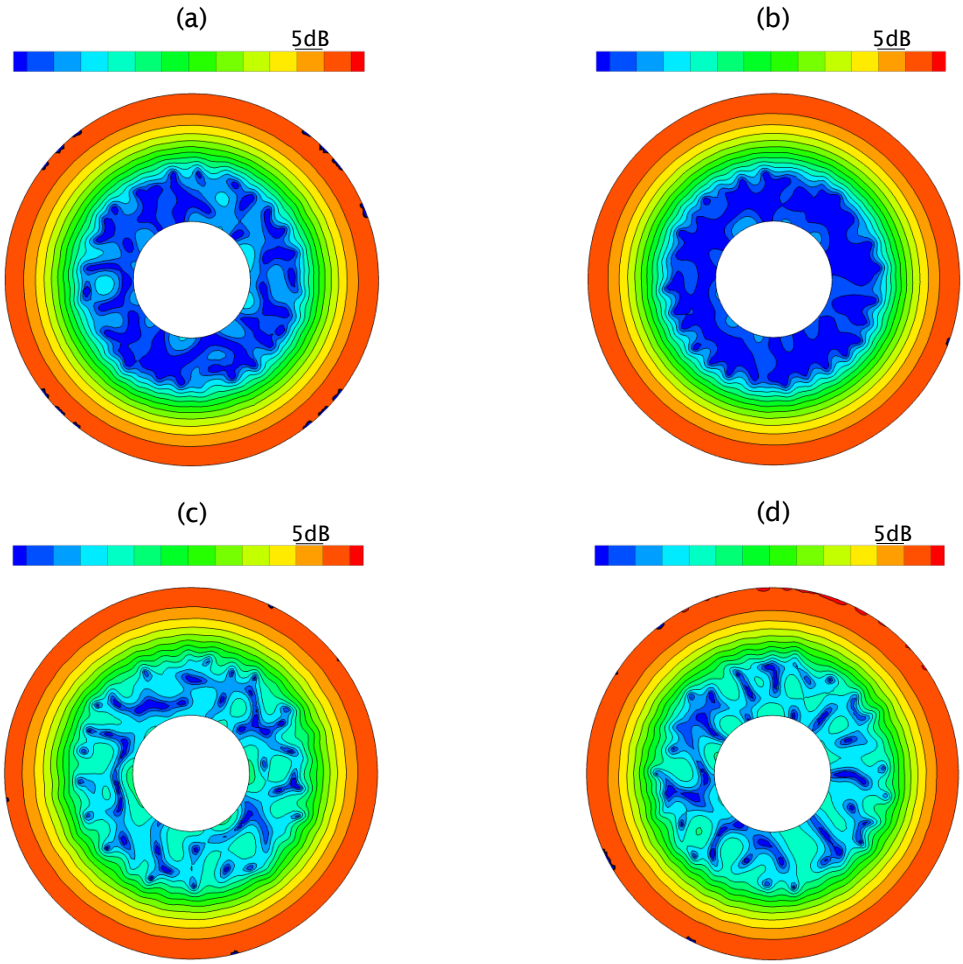

Figure 7.3: SPL distribution on the fan plane for a single incident mode (20,1) with zero mean flow: (a) the reference intake, (b) axisymmetric version of the reference intake, (c) scarfed intake, (d) drooped intake.

The distribution is similar for all the cases, as expected, since it is a face where the source is applied. Comparison to the analytical solution (not included) has confirmed that the incident mode is correctly recovered at the fan plane for all the cases. Small variations in the pressure field due to mesh scattering are evident close to the spinner (see section 5.2.2). Additionally, small over prediction spots exist near the outer casing for the idealized drooped intake shown in figure 7.3 (d). These are caused by interpolation errors in the post-processing.

The instantaneous pressure fields on the throat plane for all four intakes are shown in figure 7.4. The throat location and its shape are illustrated for each intake in figures 7.1 and 7.2. A non-axisymmetric distribution of the pressure is observed for the non-axisymmetric intakes (including a small variation in azimuthal wavelengths).

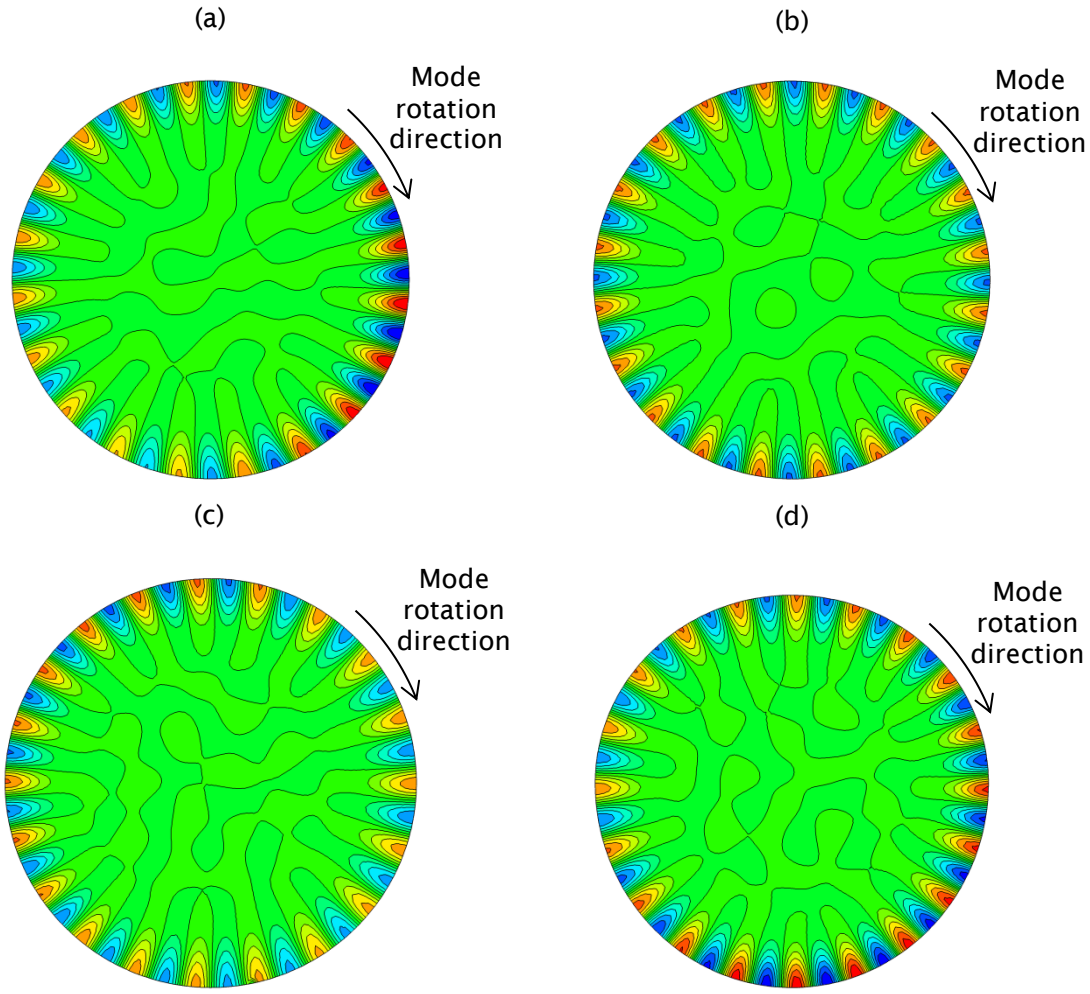

Figure 7.4: Instantaneous pressure on the throat plane with zero mean flow: (a) reference intake, (b) axisymmetric version of the reference intake, (c) scarfed intake, and (d) drooped intake.

The SPL variation along the outer edge of the throat is approximately 3.5 dB for the reference intake (figure 7.4 (a)), 2.5dB for the idealized drooped intake (figure 7.4 (d)), and approximately 2dB for the idealized scarfed intake (figure 7.4 (c)). A single region of amplified acoustic pressure is present in the three cases. It is located on the right-hand side of the reference intake (the observer is standing in front of the intake). While for the idealized drooped intake the amplified region is much wider, covering more than half of the throat perimeter and it extends through an angle of approximately 40 degrees towards the bottom of the intake when compared to the reference intake. In the case of the idealized scarfed intake the amplified region is less visible as expected. The distribution of the instantaneous pressure at the throat plane is axisymmetric for the axisymmetric intake (figures 7.4 (b)).

As a first step to understanding how the incident field is scattered due to the intake geometry we now perform the Fourier decomposition of the acoustic field in frequency and azimuthal order. If the pressure is periodic in time with period of T each Fourier component $\tilde{p}_m$ is defined as follows,

$$\tilde{p}_m(r,z,\omega) = \frac{1}{2\pi T}\int_0^{2\pi}\int_0^T p'(r,z,\theta,t)e^{im\theta - i\omega t}dt\,d\theta, \tag{7.1}$$

where m is the azimuthal order and ω is the angular frequency. This is computed on a cross-section perpendicular to the axis and located at the last axial station, towards the throat, where the geometry of the reference intake (point T_p in figure 7.1) is still axisymmetric. The axial location of the cross-section is approximately a quarter of the fan radius upstream from the fan plane. The geometry of each intake up to this cross-section is the same.

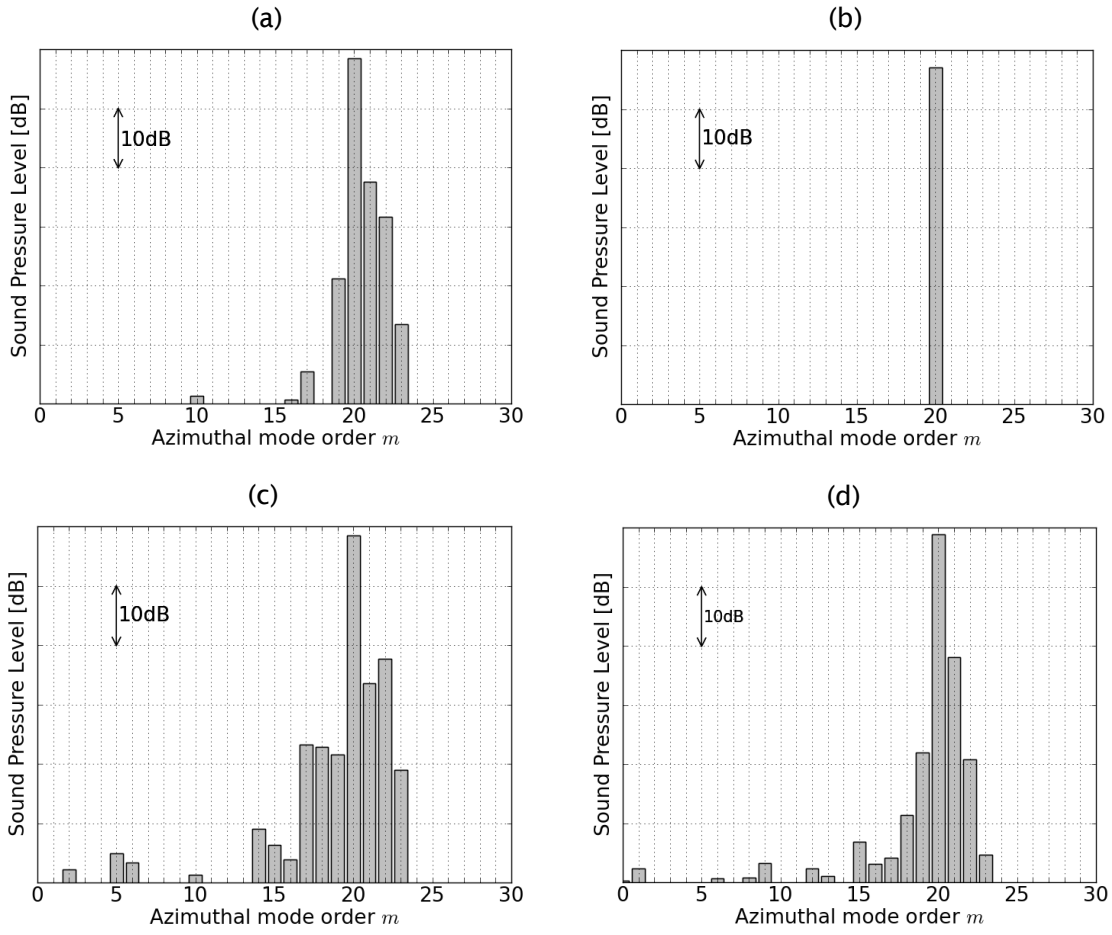

Figure 7.5: The SPL against azimuthal orders on the last axisymmetric cross-section of the reference intake at the frequency corresponding to the BPF: (a) the reference intake, (b) axisymmetric version of the reference intake, (c) scarfed intake, (d) drooped intake.

The Fourier decomposition is performed at the outer wall on a large number of uniformly distributed discrete points (1000). There is a small offset between the points and the wall to ensure minimum error from the wall approximated by straight elements. Results of the SPL as a function of azimuthal order are shown in figure 7.5. For all the cases (as expected) the acoustic field on the cross-section is dominated by the mode (20,1), which is the source mode. This is most relevant for the axisymmetric intake (figure 7.5 (b)). For the non-axisymmetric intakes adjacent modes exist (figures 7.5 (a), (c) and (d)). Since the duct is axisymmetric up to the plane where it is sampled any scattering due to the geometry must be due to back scattering from geometric effects upstream of the plane. The fact that the additional azimuthal orders are observed for the non-axisymmetric intakes clearly indicates that the waves propagating in a varying shape duct create a complex acoustic field. Indeed, it can lead to the amplification of the acoustic pressure amplitude in some range of the azimuthal angles as shown in figures 7.4 (a), (c) and (d).

7.2.2 Streamlines of the acoustic energy flux

The intake shapes effects on sound propagation and radiation are further illustrated by 3D streamlines of the acoustic energy flux. These are obtained as parametric curves $\boldsymbol{C} = \boldsymbol{C}(s)$, where s is the distance along the streamline. Hence, the tangent to the streamline can be defined as follows,

$$\frac{d\boldsymbol{C}(s)}{ds} = \frac{\bar{\boldsymbol{I}}(\boldsymbol{x})}{|\bar{\boldsymbol{I}}(\boldsymbol{x})|}, \tag{7.2}$$

where $\bar{\boldsymbol{I}}(\boldsymbol{x})$ is the acoustic intensity vector computed from the DGM solution. For the zero mean flow it is given by $\bar{\boldsymbol{I}}(\boldsymbol{x}) = \frac{1}{2}\mathrm{Re}\{\tilde{p}\tilde{\boldsymbol{v}}^*\}$, where $\tilde{p}$ is the complex amplitude of the acoustic pressure, and $\tilde{\boldsymbol{v}}^*$ is the conjugate of the complex amplitude vector of the acoustic velocity vector.

The 3D DGM solution is provided on a unstructured, tetrahedral post-processing mesh, refined to approximately 7 linear elements per free-field wavelength (see section 3.4.7). The streamlines are generated in Tecplot [148] according to the equation (7.2). In this case 18 seed points uniformly distributed at the outer edge of the fan plane are used. The streamlines are coloured by the magnitude of the acoustic intensity vector.

3D streamlines for the four configurations considered in this study are shown in figure 7.6. The streamlines are illustrated in two views as seen when facing the inlet: 3D perspective view (left-hand side column) and the front view (right-hand side column). In general, the streamlines of the acoustic intensity form a helical pattern for all intakes. In the case of the reference intake the streamlines are strongly concentrated at some azimuthal angles as can be seen in figures 7.6 (a.1) and (a.2). This is caused by the complex 3D shape of the intake, i.e. the droop effect and scarf angle. The pattern clearly indicates focussing of the acoustic energy inside the intake. The streamlines outside of the intake maintain the characteristic pattern in the azimuthal direction. In this case, the majority of the sound power is radiated downwards as shown in figure 7.6 (a.2). In the case of the axisymmetric intake the streamlines are uniformly distributed in the azimuthal direction (figures 7.6 (b.1) and (b.2)). In the case of the idealized scarfed and drooped intakes, the directivity patterns are clearly affected by the non-axisymmetric features of the intake geometry. However, in both cases the resulting pattern is different. In the scarfed intake the streamlines are uniformly distributed until the throat plane (figures 7.6 (c.1) and (c.2)) which is consistent with the instantaneous pressure distribution shown in figure 7.4 (c). The impact of the scarf angle (diffraction by the intake geometry) can be seen in figure 7.6 (c.2). The sound power radiated toward the bottom right-hand side of the intake is approximately twice that radiated upwards.

(a.1) (a.2)

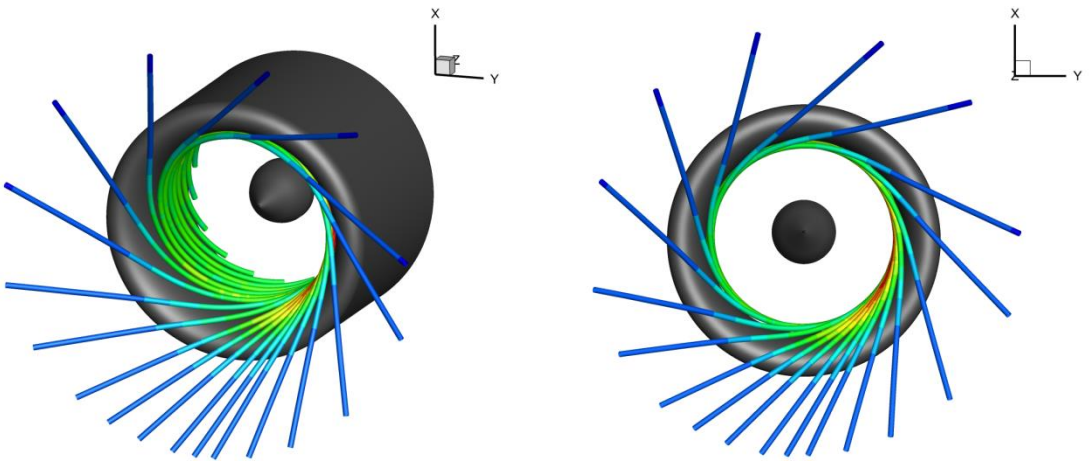

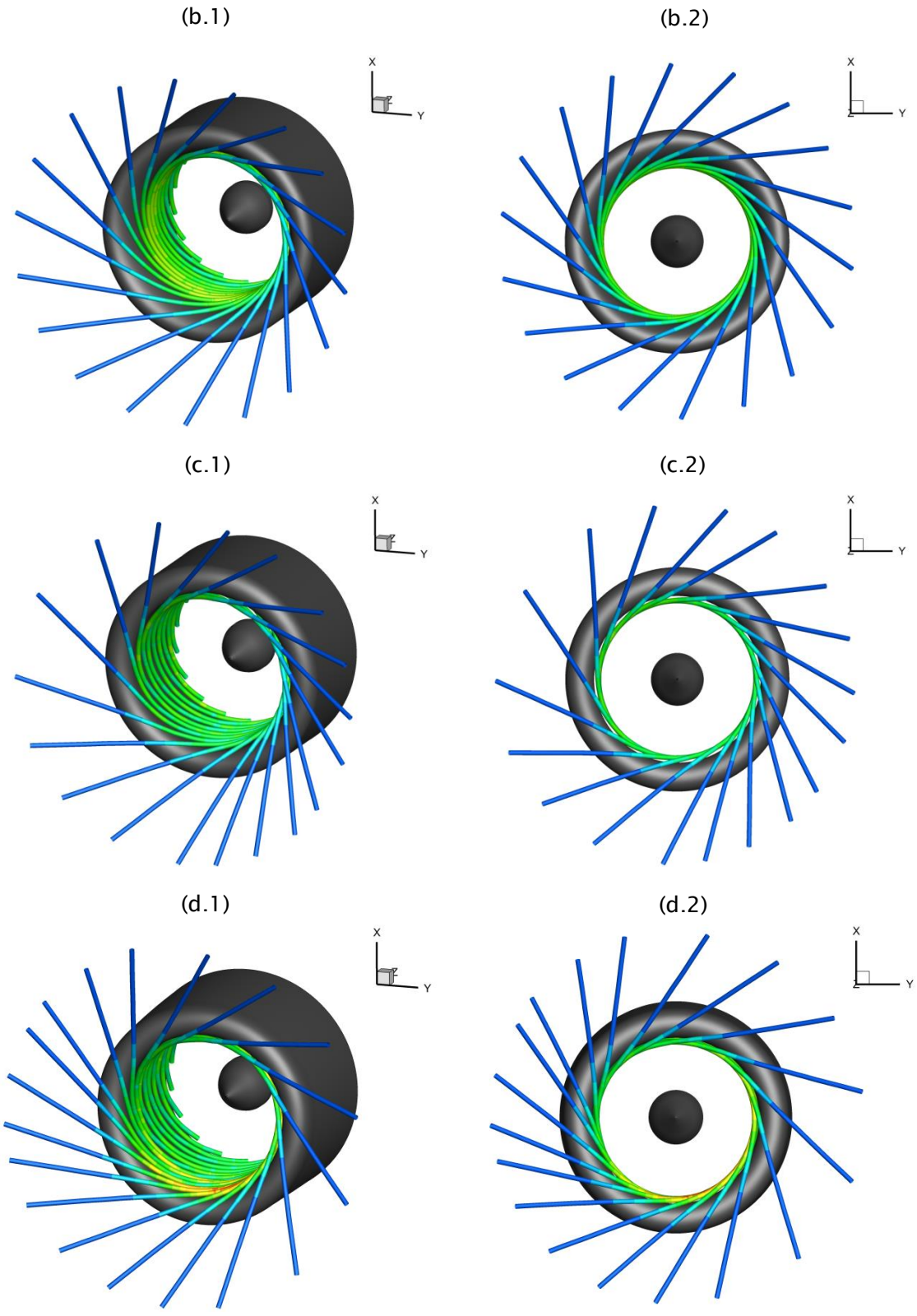

Figure 7.6: The 3D streamlines of the acoustic energy flux for zero mean flow: (a) the non-axisymmetric intake rig (the reference intake), (b) axisymmetric version of the reference intake, (c) scarfed intake, (d) drooped intake. Left-hand side column: Perspective view. Right-hand side column: Front view when facing the inlet.

For the idealized drooped intake (figures 7.6 (d.1) and (d.2)) we see a similar focussing of the energy flux, as for the reference intake. However, the radiation pattern is different. The azimuthal distribution of the acoustic energy is more uniform, with most of the energy radiated toward top left-hand side of the intake.

7.2.3 Far-field directivity

We now consider the effect of the intake geometry on the far-field directivity. The far-field solution is calculated from a Ffowcs Williams-Hawkings (FWH) surface at the outer boundary of the DGM physical zone (see section 3.4.4). The observation points (field points) are uniformly distributed on a parametric far-field spherical surface. High resolution is used, below 0.5 degrees in each direction. The surface maps a sphere centred one fan radius upstream of the fan plane and of radius equal to 40 fan radii. It covers the full range of the azimuthal angles, and extends 120 degrees in the polar angles from the forward shaft axis. The surface is illustrated in figure 7.7.

The far-field directivity of the SPL for all the intakes considered is shown in figure 7.8. The SPL is plotted, on dB-scale, on the unwrapped parametric surface described above.

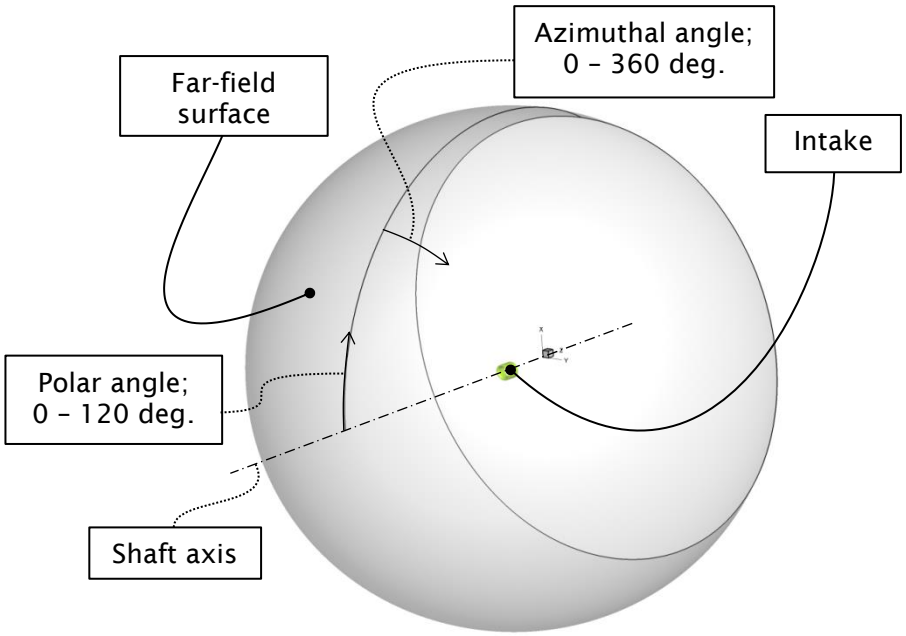

Figure 7.7: 3D parametric surface, a sphere with a radius equal to $40R_{fan}$, used for the reconstruction of the far-field solution.

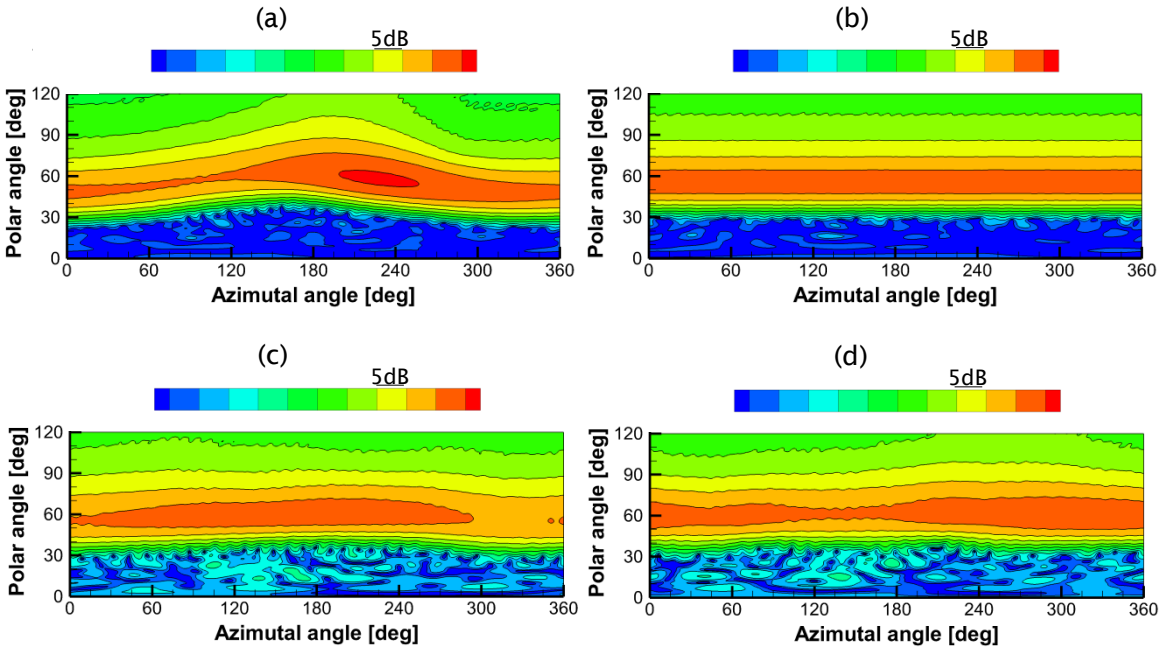

Figure 7.8: The far-field directivity of the SPL for a single incident mode (20,1) with zero mean flow on a sphere of radius $40R_{fan}$: (a) the reference intake, (b) axisymmetric version of the reference intake, (c) scarfed intake, (d) drooped intake.

The solution for the reference intake (figure 7.8 (a)) shows the greatest variation. The peak value of SPL is located at the azimuthal angle of 225 degrees. This corresponds to the lower left-hand side of the intake. The maximum peak-to-peak difference in the azimuthal direction is 5dB. Moreover, the location of the peak value varies in the polar direction for different azimuthal angles. The maximum difference observed between bottom and top sides is 16 degrees. The sound radiates at highest polar angle in the downward direction. This far-field directivity confirms the conclusions drawn based on the acoustic intensity pattern, namely that sound waves are bent (diffracted) due to the droop effect and scarf angle of the intake. For the axisymmetric intake (figure 7.8 (b)) an axisymmetric distribution of the SPL is obtained. The idealized scarfed and drooped intakes show comparable levels of variation of the SPL (3 to 4.5dB) and polar directivity (4 to 5 degrees) in the azimuthal direction. However, the peak value for each case is located at different azimuthal angle. In the case of the scarfed intake, slightly higher sound pressure level is observed at the bottom right-hand side of the intake, whereas for the drooped intake the maximum SPL is located at the top left-hand side of the intake.

7.3 Flow distortion effects

In this section, we take into account the effect of the flow distortion. Firstly, we focus our attention on a uniform annular duct with distorted parallel flow, and then on the non-axisymmetric intake rig.

7.3.1 Uniform duct with flow distortion

We consider the effect of mean flow distortion on noise propagation in a straight annular duct illustrated in figure 7.9. The ratio of inner to outer radii is b/R_0 = 0.3. A single mode (24,1) is incident at the duct entrance and propagates against the mean flow. The Helmholtz number for this problem is kR_0 = 27. Parallel steady isentropic compressible mean flow is assumed. At each axial station the mean flow varies azimuthally so that

$$M(\theta, z) = M_0(1 + \epsilon(z)cos\theta), \tag{7.3}$$

where M_0 is the mean value of the Mach number, and θ is the azimuthal angle in the cylindrical coordinate system. The distortion parameter ϵ varies along the length of the duct taking values of zero at each end. The variation of $\epsilon(z)$ in the axial direction is shown in figure 7.10. The mean value of the Mach number is 0.6, and the total pressure and total temperature of air are set to 101.5 kPa and 288 K, respectively.

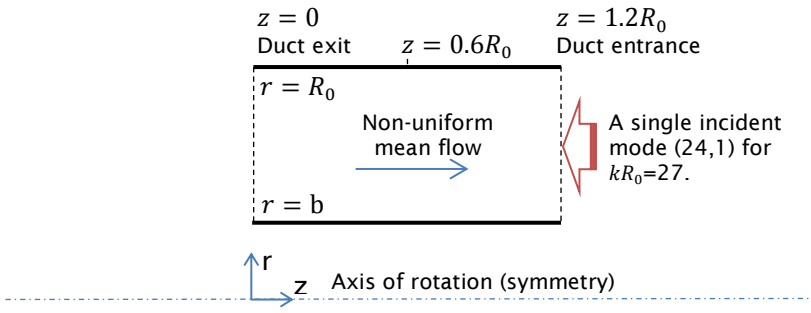

Figure 7.9: A physical problem of noise propagation through a straight annular duct in the presence of a non-uniform mean flow.

The flow distortion parameter reaches a maximum value of 0.1 in the middle section of the duct. It is important to note that the distribution of the parameter along the axial axis corresponds to that of a real turbofan intake rig operating at sideline engine condition.

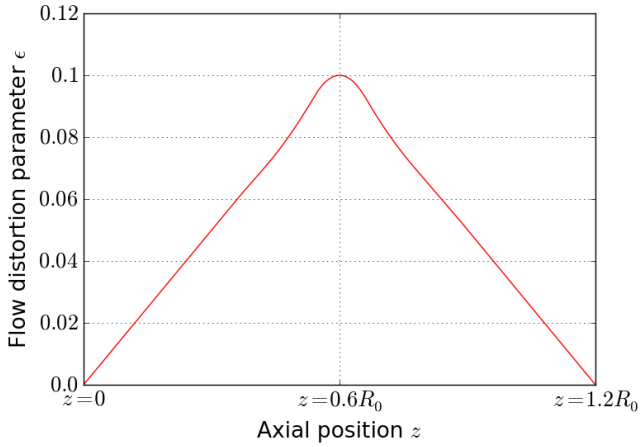

Figure 7.10: The axial distribution of the mean flow distortion parameter ϵ.

7.3.1.1 Mean flow distortion effect on the sound field

Firstly, we consider the hard-walled case. The sound field in the duct is calculated by using Actran DGM. Admission and buffer zones are added to both ends of the duct. The computational mesh is refined to approximately one element per upstream wavelength. Further mesh refinement is applied in the near-wall regions to ensure at least four elements per source mode azimuthal order (see section 5.2.2). This gives element orders between 3 and 9. The resulting sound fields at the duct entrance (z = $1.2R_0$), at the mid-section of the duct (z = $0.6R_0$), and at the duct exit (z = 0.0) are shown in figure 7.11. The SPL distribution at z = $1.2R_0$ is axisymmetric as shown in figure 7.11 (a). There is no distortion in the mean flow at this axial station. At z = $0.6R_0$ significant scattering has occurred as shown in figure 7.11 (b). The maximum SPL difference in the azimuthal direction along the outer wall of the duct is approximately 5dB. The SPL distribution at z = 0.0 clearly shows the cumulative impact of the flow distortion although the distortion parameter has decreased to zero (figure 7.11 (c)). The maximum SPL difference in the azimuthal direction along the outer wall of the duct is approximately 15dB.

To better understand the scattered sound fields shown in figure 7.11 a Fourier decomposition is performed in the azimuthal direction at the outer radius of the duct. The DGM azimuthal components in dB as a function of the azimuthal order are compared to a semi-analytical solution [127] and to results obtained by using Actran TM applied to the same configuration. This comparison is shown in figure 7.12.

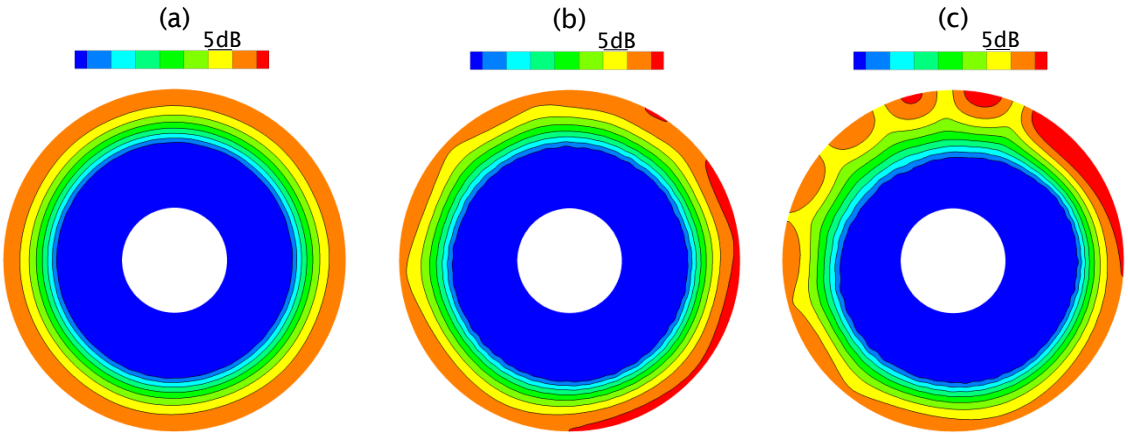

Figure 7.11: The SPL distribution – hard-walled duct: (a) on the cross-section at the duct entrance ($z = 1.2R_0$), (b) on the cross-section in the middle of the duct ($z = 0.6R_0$), and (c) on the cross-section at the duct exit ($z = 0.0$).

The SPL results obtained from the DGM agree reasonable well with those obtained from the semi-analytical solution and Actran TM. Some discrepancies can be seen between the Actran DGM and Actran TM solutions at the duct entrance for azimuthal orders above the source azimuthal order (figures 7.12 (a)). It is likely that the error is due to spurious scattering of the source mode as a result of slightly insufficient mesh resolution in the azimuthal direction used for both acoustic meshes. These discrepancies are, however, at least 20 dB below the SPL of the dominant azimuthal orders. In general, a qualitative agreement is observed between the two numerical schemes and the semi-analytical solution. The maximum amplitude difference in the SPL of individual modes is approximately 7 dB for the Actran TM solution. In the case of the DGM solution, the agreement is slightly worse. The differences up to 20 dB in the SPL are visible for the azimuthal orders adjacent to the source azimuthal order, i.e. 24 (figure 7.12 (b)). Despite the differences for particular azimuthal orders the general character of the acoustic solution is well captured both by the DGM and TM computations.

The sound field which is initially represented by a dominant single acoustic mode (24,1), as shown in figure 7.12 (a), is scattered into a sound field represented by many azimuthal components at the duct exit, as can be seen in figure 7.12 (c). This is caused entirely by mean flow distortion since the geometry in this case is uniform.

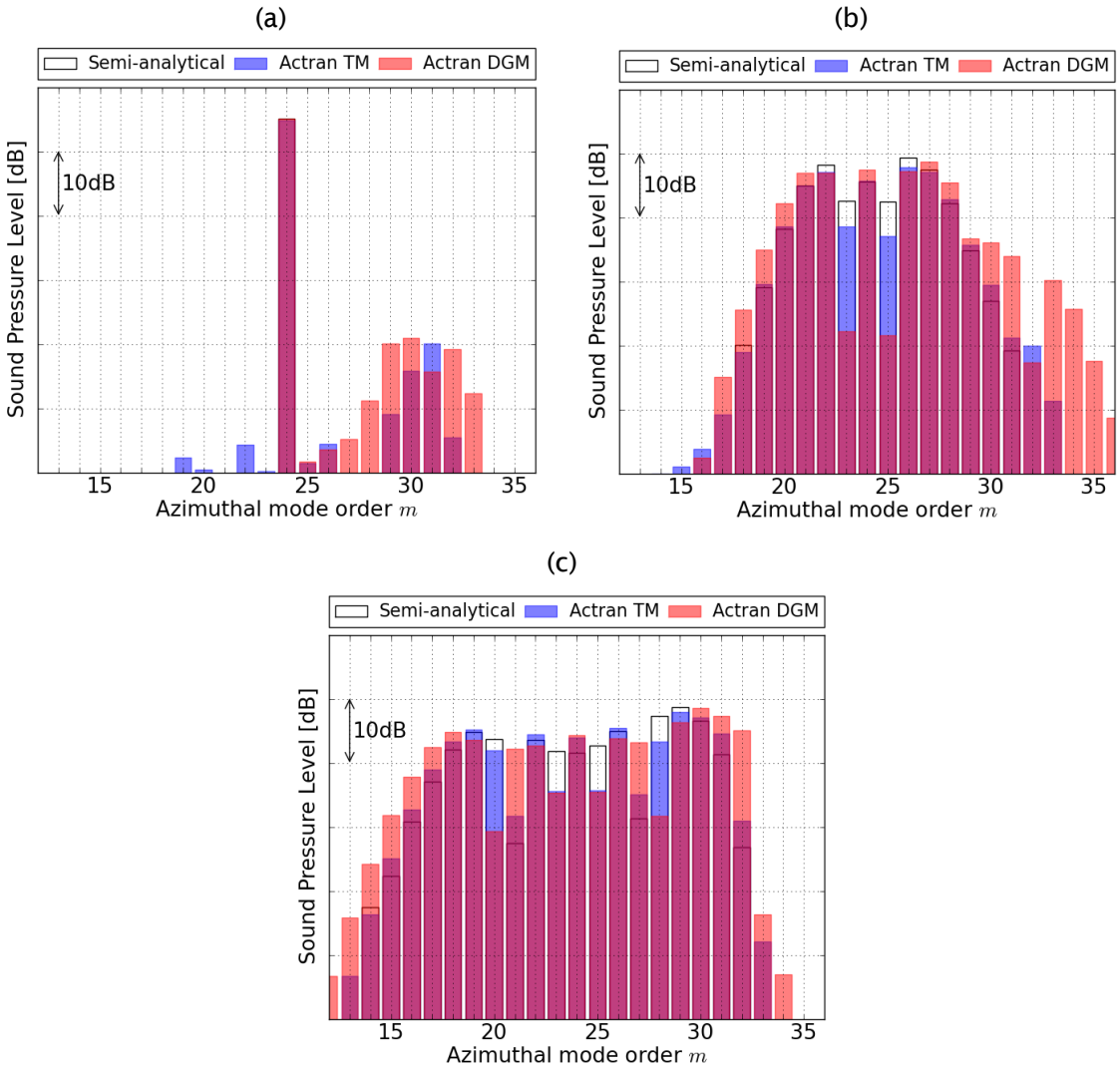

Figure 7.12: The SPL against azimuthal orders – hard-walled duct: (a) on the cross-section at the duct entrance ($z = 1.2R_0$), (b) on the cross-section in the middle of the duct ($z = 0.6R_0$), and (c) on the cross-section at the duct exit ($z = 0.0$).

7.3.1.2 The mean flow distortion effect on the sound attenuation by a liner

The effect of mean flow distortion on the sound attenuation by a liner in the idealized straight duct of figure 7.9 is now investigated. The outer wall of the duct is assumed to be lined with a non-dimensional impedance of 2.6 - 1.265i for the frequency of 3480Hz. The sound field is computed in this case by using Actran TM only (the liner model in Actran DGM is not sufficiently accurate to be used for this case). The duct shown in figure 7.9 is extended by 10 percent of its outer radius at both ends to accommodate hard-walled segments which are required by the mode-matching boundary condition in Actran TM. The length of the lined part of the duct is the same as the length of

the hard-walled duct considered in the previous section. The same mean flow distortion is used. The mean flow in the hard-walled segments is assumed to be uniform. The minimum mesh resolution is taken to be 7 linear elements per upstream wavelength. The SPL distributions at the entrance to the duct, the middle section, and the exit are shown in figure 7.13. The acoustic field is nearly axisymmetric on the duct entrance (figure 7.13 (a)). At the centre and exit of the duct strongly non-axisymmetric distributions of the SPL are evident. In the middle section the maximum SPL difference around the circumference is approximately 7dB (figure 7.13 (b)), whereas at the duct exit the maximum difference is approximately 30dB as shown in figure 7.13 (c). In both cases the mean SPL is heavily attenuated by the liner. The influence of the flow distortion on the sound attenuation by liner can be clearly seen.

The variation of the attenuation rate can be explained physically by refraction due to the mean flow velocity gradients. As a result of the refraction the direction of the waves changes, which causes the significant difference in sound absorption at the lined outer surface. It is instinctive to decompose the acoustic field over the lined outer surface of the duct into lower and higher azimuthal components in the azimuthal direction at the duct entrance, middle section, and duct exit. This is done by using equation (7.1). A comparison of resulting distribution of azimuthal components is made between the cases with a uniform mean flow (of Mach number 0.6) and the distorted mean flow given by the axial distribution of the flow distortion parameter shown in figure 7.10. The comparison for each cross-section is shown in figure 7.14.

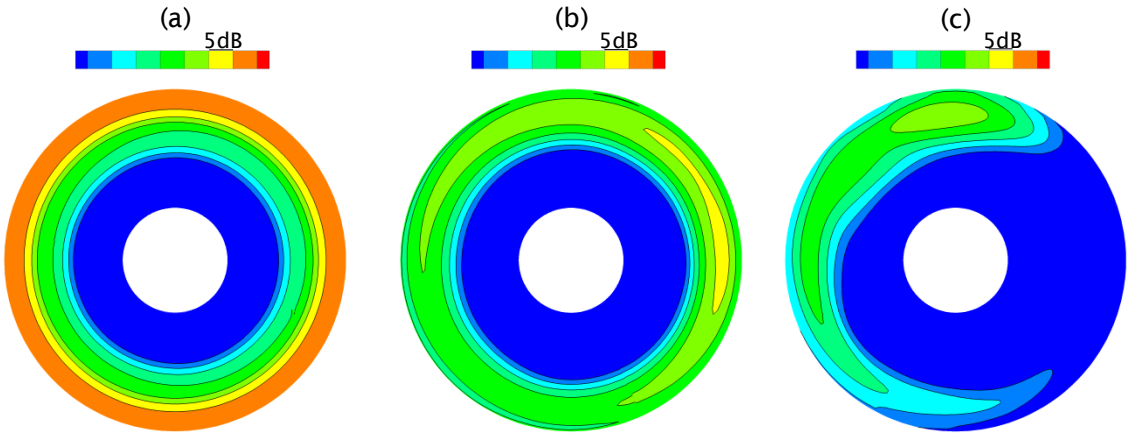

Figure 7.13: The SPL distribution – lined ($Z = \rho_0 c_0(2.6 - 1.265\mathrm{i})$ at 3480 Hz) duct: (a) on the cross-section at the duct entrance ($z = 1.2R_0$), (b) on the cross-section in the middle of the duct ($z = 0.6R_0$), and (c) on the cross-section at the duct exit ($z = 0.0$).

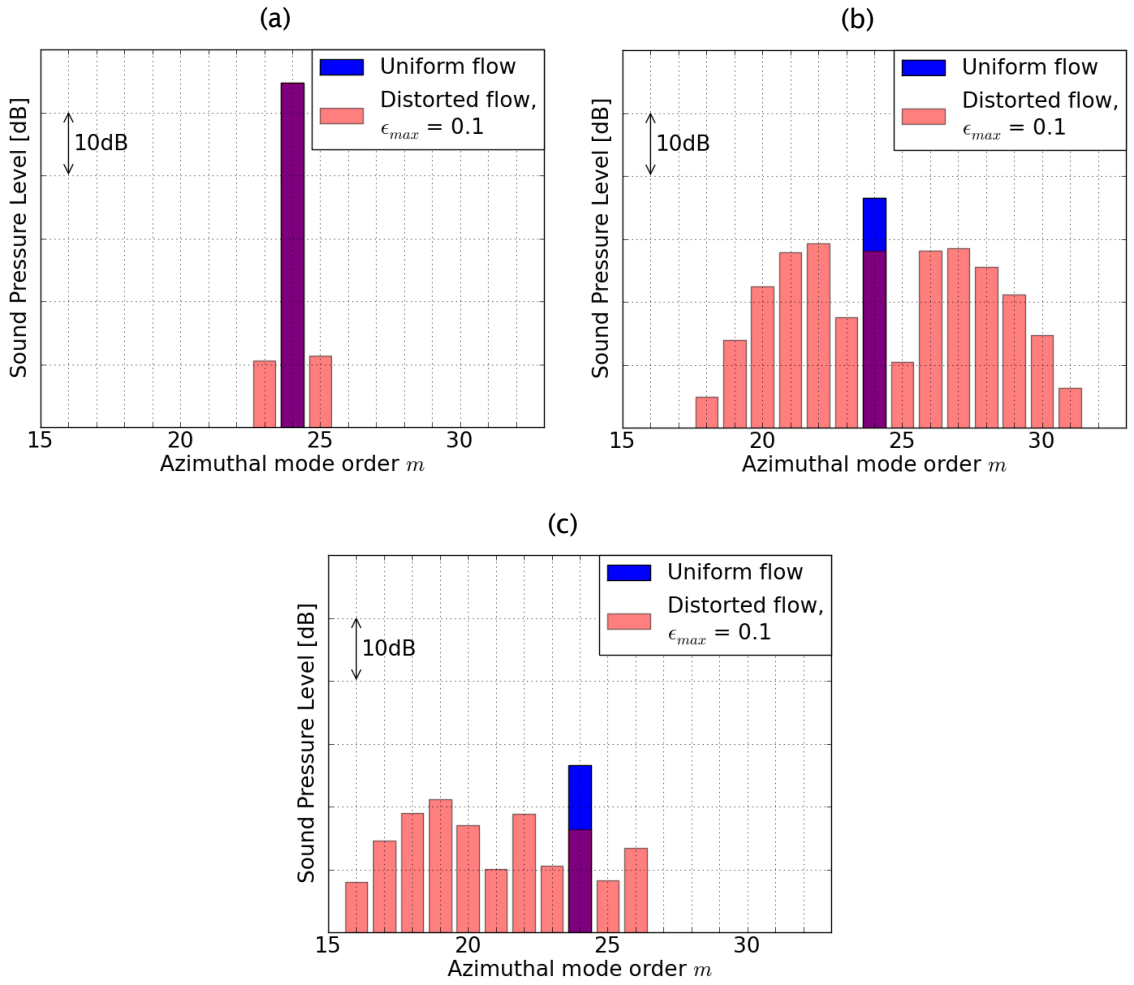

Figure 7.14: The SPL against azimuthal orders – lined ($Z = \rho_0 c_0(2.6 - 1.265\mathrm{i})$ at 3480 Hz) duct: (a) on the cross-section at the duct entrance ($z = 1.2R_0$), (b) on the cross-section in the middle of the duct ($z = 0.6R_0$), and (c) on the cross-section at the duct exit ($z = 0.0$).

As in the case of the hard-walled duct, the source mode (24,1) scatters to adjacent azimuthal components due to the flow distortion. For the case of the distorted flow a small level of scattering occurs directly at the duct entrance as shown in figure 7.14 (a) which is due to reflection or back scattering, or to numerical error at the impedance discontinuity (hard-to-lined surface transition) since the mean flow is uniform up to this cross-section. The effect is 40 dB below the SPL of the source mode, therefore can be neglected. In the middle sector of the duct the incident mode scatters nearly symmetrically to lower and higher azimuthal orders, and the amplitudes of all modes are damped nearly uniformly by the liner as can be seen in figure 7.14 (b). From figure 7.14 (c), we can conclude that in the second half of the duct the components with higher azimuthal orders are more strongly damped than those of lower azimuthal orders.

To assess the impact of the mean flow distortion on the sound power absorption by liner the axial power at sections along the duct is computed. Morfey's formula [178] presented in Appendix D is used. This definition assumes homentropic and irrotational mean flow therefore a small amount of vorticity which is present in the mean flow defined by equation (7.3) is not included in the power calculations. The modal power at both ends of the numerical model is evaluated by using the modal expansion in non-distorted hard walled sections [93]. The distribution of sound power level (PWL) along the axis of the duct is shown in figure 7.15. The PWL comparison between the cases with uniform and non-uniform mean flows shows clearly that the sound energy is more strongly absorbed by the liner for the case with uniform mean flow. The different absorption behaviour is observed from the middle section of the duct up to the duct exit where a maximum difference of 3.5 dB is reached. In addition, the modal power evaluated at both ends of the Actran TM model is consistent with the values calculated at each section. A difference of approximately 0.7dB is observed between the PWL computed by using the Morfey's expression and the modal expansion. This is due to the fact that the modal acoustic intensity which is used to compute the modal power is measured in the direction of the propagating mode, whereas the intensity computed by using Morfey's expression is evaluated in the axial direction of the duct.

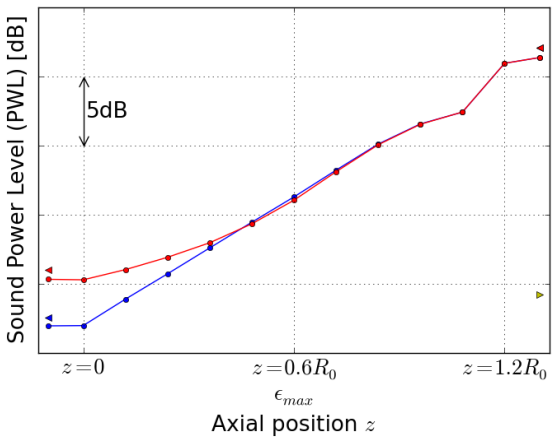

Figure 7.15: The sound power level (PWL) distribution along lined ($\boldsymbol{Z = \rho_0 c_0(2.6 - 1.265i)}$ at 3480 Hz) duct. The mean flow distortion effect. Solid blue line with dots: Uniform flow, Morfey's expression (axial direction); solid red line with dots: distorted flow ($\boldsymbol{\epsilon_{max}}$= 0.1), Morfey's expression (axial direction); solid blue left-pointing triangle: uniform flow, total modal power; solid red left-pointing triangle: distorted flow ($\boldsymbol{\epsilon_{max}}$= 0.1), total modal power; solid yellow right-pointing triangle: total reflected modal power.

7.3.2 The effect of flow distortion in a non-axisymmetric intake rig

In this section we investigate the effect of mean flow distortion and the impact of the source mode axial propagation angle (mode angle) θ_{mode}[10] on the sound field in the static non-axisymmetric intake rig which was used as a reference intake for the geometry effect study (section 7.2). The intake is shown in figure 7.1. Its shape has been designed to ensure a mean flow distribution inside the intake duct which reproduces the flow in a real engine intake during the take-off flight condition.

CAA simulations are conducted by using Actran DGM. The mesh is refined to approximately one element per wavelength in the free field, and to four elements per maximum mode azimuthal order over the intake surface. This gives element orders in the range 2 to 7. The modal excitation is that obtained in the matching process for the intake rig described in section 6.4.2.1. A single mode (20,1) is incident at the fan plane with the axial propagation angle of 62.5 degrees (cut-on ratio 0.888).

The impact of the source mode angle at the fan plane on sound propagation and radiation is assessed by varying the frequency of the incident mode. The amplitude and phase remain unchanged. The axial propagation angle varies from 51.2 degrees (cut-on ratio 0.78) at a shaft speed of 8715 rpm to the angle of 71.6 degrees (cut-on ratio 0.95) at a shaft speed of 7157 rpm. It is worth noting that the angle of 90 degrees (cut-on ratio 1) corresponds to the transition from a propagating to an evanescent mode, and zero to a plane wave (cut-on ratio 0).

The mean flow used for the study is an isentropic compressible flow computed by solving the Euler equations (see section 3.3.3). The flow on the fan plane is set to Mach number of 0.54. The ambient flow is zero. The total pressure and total temperature are equal to 101.2 kPa and 288.2 K, respectively. The Mach number distribution on a vertical cut-plane through the shaft axis is shown in figure 7.16 (a). The cross-section where the flow distortion parameter reaches its maximum value is marked by a black line. The maximum value at the outer surface is 0.11.

---

[10] θ_{mode} is the axial propagation angle (mode angle), for the case of uniform mean flow it is defined as $\sin\theta_{mode} = \mp\frac{k_r}{k_0}\sqrt{1-M^2}$, where k_r is a radial wave number.

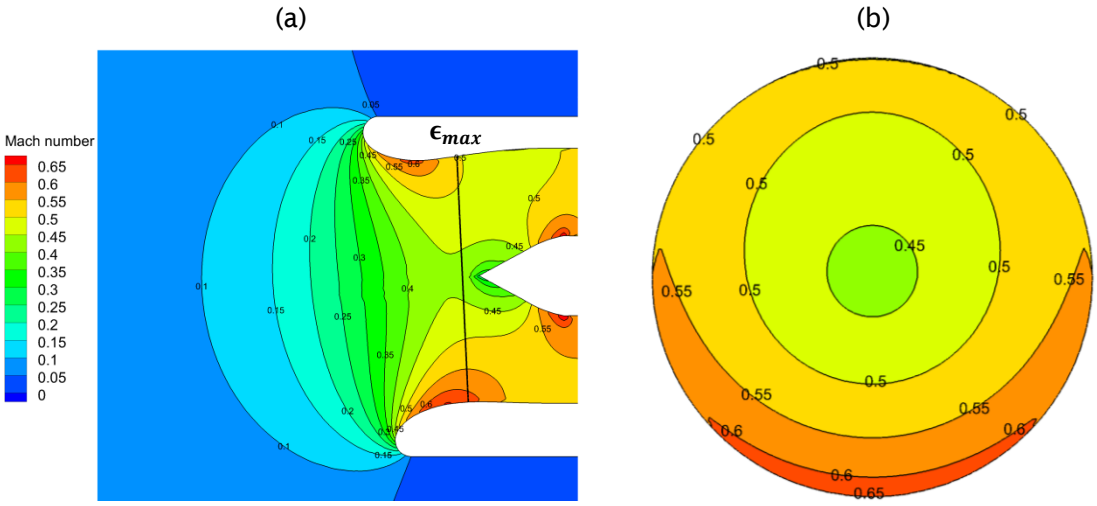

Figure 7.16: Mean flow contours for the non-axisymmetric intake rig: (a) on the vertical cut-plane (symmetry plane) of the model, (b) on the cross-section where the flow distortion is greatest.

The Mach number distribution on the cross-section where the flow distortion is greatest is shown in figure 7.16 (b). The orientation in the 3D space of the cross-section is determined with respect to the general shape of the intake. The level of flow distortion is comparable to that assumed for the mean flow in the straight duct case discussed in section 7.3.1.

7.3.2.1 In-duct propagation

Propagation of the incident mode (20,1) along the non-axisymmetric intake rig (figure 7.1) in the presence of the non-uniform mean flow has been computed for varying mode angles at the fan plane. The following angles are examined θ_{mode} = 51.2, 62.5, 71.6 degrees (cut-on ratios 0.78, 0.888, and 0.95, respectively). The resulting SPL distributions on the throat plane are shown in figure 7.17. Similar concentrations of the SPL in the azimuthal direction to those observed for the zero flow are visible here. The effect of the source mode angle on the SPL distribution inside the intake is significant. We observe that the region of amplified SPL changes its azimuthal position when the mode angle is varied. The width of this region also varies. Again we observe some spurious pressure fluctuations in the centre of the intake due to the mesh scattering. These are at least 40 dB below the peak values, and will be ignored in our considerations.

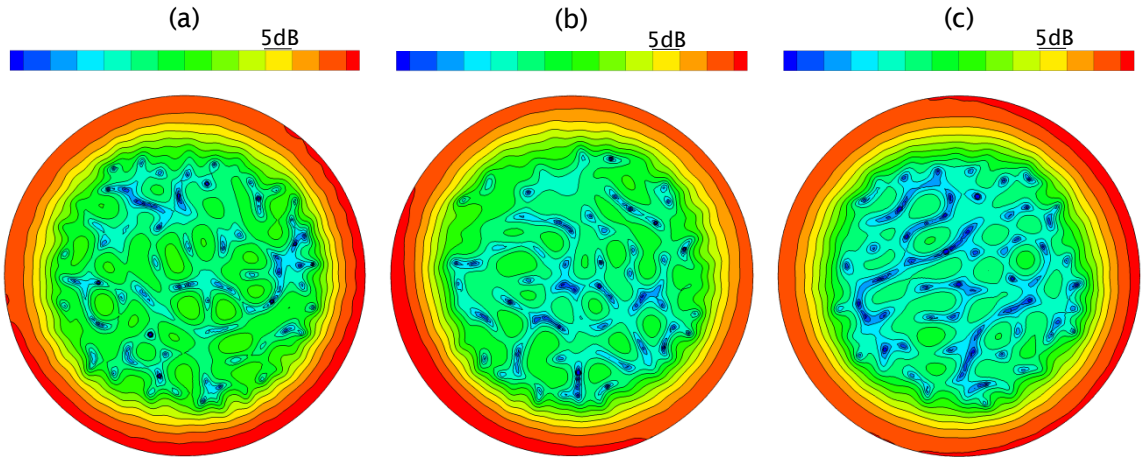

Figure 7.17: The SPL distribution on the throat plane for varying source mode angles θ_{mode} (a) 51.2°, (b) 62.5°, and (c) 71.6°.

A Fourier decomposition of the acoustic field into azimuthal components has been made according to equation (7.1). This is performed on a cross-section perpendicular to the axis and located at the axial station farthest from the fan at which the internal geometry of the intake is still axisymmetric. The SPL as a function of azimuthal component on the outer edge of the cross-section for all source mode angles θ_{mode} is shown in figure 7.18. Clearly, the incident mode (20,1) scatters to adjacent azimuthal orders. Similar behaviour was observed for zero flow cases as discussed in section 7.2.1. However, when the mean flow is present the scattering is much stronger and starts just upstream of the fan plane because of the non-axisymmetric flow. The SPL of the modes scattered to the lower azimuthal orders seems to be not affected by the variation of the mode angle (figure 7.18 (a), (b), and (c)). The influence of the source mode angle on scattering to the higher azimuthal orders is however noticeable. In view of this, the stronger concentration of the SPL on the throat which can be seen in figure 7.17 (b) for $\theta_{mode} = 62.5°$ can be explained by the stronger scattering to the higher adjacent azimuthal orders as shown in figure 7.18 (b). For the highest propagation angle considered, i.e. $\theta_{mode} = 71.6°$ (cut-on ratio 0.95) less of the higher orders is visible as shown in figure 7.18 (c) which may be due to the fact that the higher order azimuthal modes are evanescent modes. Interestingly, an increase of 4dB in the SPL of the dominant mode (20,1) occurs for the highest propagation angle. This can also be explained by the fact that for $\theta_{mode} = 71.6°$ the incident mode (20,1) is closer to the transition from a propagating to an evanescent mode.

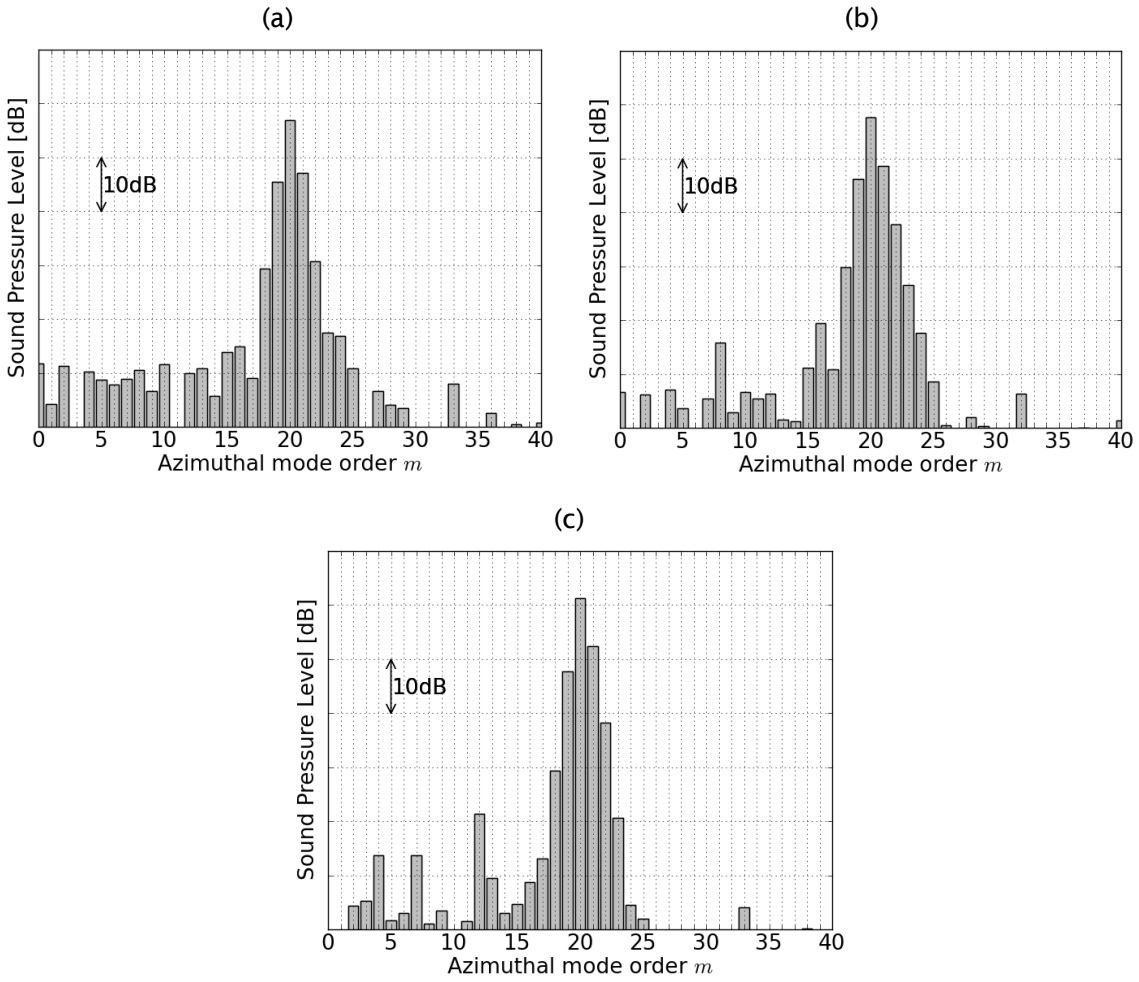

Figure 7.18: The SPL as a function of the azimuthal order on the outer edge of the last transverse axisymmetric cross-section towards the throat of the non-axisymmetric intake rig for varying the source mode angle θ_{mode}= (a) 51.2°, (b) 62.5°, and (c) 71.6°.

7.3.2.2 Streamlines of the acoustic intensity

The 3D tracing of the acoustic intensity streamlines is performed to investigate the effect of the mean flow distortion and of the source mode angle on the energy flux. When the mean flow is present the expression for the acoustic intensity is more complex. The definition of the acoustic intensity for homentropic and irrotational flows is given in Appendix D. This has been implemented for the 3D DGM solution on an unstructured, tetrahedral post-processing mesh refined to approximately 7 linear elements per wavelength (see section 3.4.7). The streamlines are generated by a post-processing tool in Tecplot [148] according to Eq. (7.2). 18 seed points uniformly distributed at the outer edge of the fan plane are used. The streamlines are coloured by the magnitude of the acoustic intensity vector.

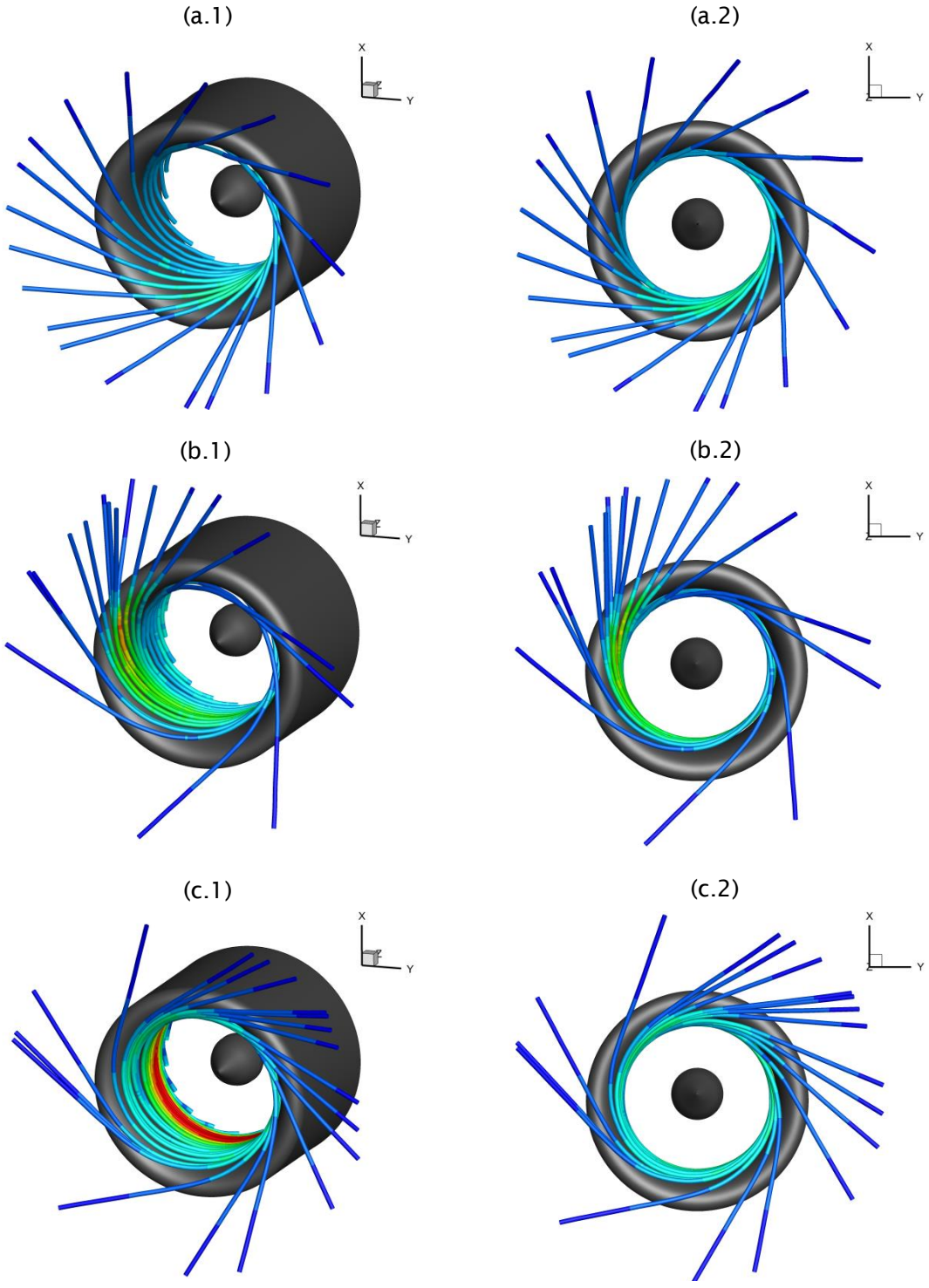

Figure 7.19: The 3D streamlines of the acoustic energy flux for varying source mode angle θ_{mode} (a) 51.2°; (b) 62.5°; (c) 71.6°. Figures a.1, b.1, c.1: Perspective view. Figures a.2, b.2, c.2: Front view when facing the inlet.

The resulting 3D distribution of the intensity streamlines for the source mode angles of θ_{mode}= 51.2, 62.5, and 71.6 degrees, respectively, are depicted in figure 7.19 (3D perspective view – left-hand side column, front view – right-hand side column). It is worth mentioning that the mode angles correspond to

the angles at which the streamlines project from the seed points on the fan plane.

We consider first the effect of mean flow distortion by comparing the streamlines for the non-axisymmetric intake rig, with and without the mean flow (figures 7.19 (b.1) and (b.2) with figures 7.6 (a.1) and (a.2), respectively). In both cases the streamlines leave the fan plane at the same angle, which has been ensured by increasing the source frequency for the zero flow case to achieve the same source mode angle of θ_{mode}= 62.5 degrees (cut-on ratio 0.888). The refraction effect bends the streamlines due to the complex 3D mean flow. As a result, different behaviour of the streamlines of the acoustic energy flux is observed in the presence of flow. For the mean flow case, most of the sound power is radiated upwards, whereas for zero flow case most of the sound is radiated downwards. Furthermore when the mean flow is present, the radiated sound power is more focused in specific azimuthal regions.

The effect of varying the source mode angle on sound propagation and radiation in the presence of mean flow can be seen in figure 7.19, which plots the streamlines of the acoustic intensity for varying the source mode angles θ_{mode}(cut-on ratio) at the fan plane. The distributions of the streamlines reveal significant differences in the sound power distribution in the intake and in the free field. The concentration of the sound power in the azimuthal direction increases with increasing source mode angle. Moreover, the region of higher sound power moves clockwise (the direction of rotation of the source mode) for higher mode angles. This is consistent with the results for the in-duct propagation analysis discussed in the previous section (7.3.2.1). For the source mode angle of 51.2 degrees the majority of the sound power is radiated towards top left-hand side of the intake. For the mode angle θ_{mode}= 62.5 degrees the sound power is mainly radiated upwards with some slight deviation towards right-hand side. In the case of the highest mode angle (θ_{mode}= 71.6 degrees) the majority of the sound power is radiated towards the right-hand side. Moreover, for this highest mode angle evanescent waves appear to be present inside the intake upstream of the fan plane as indicated in figure 7.19 (c.1) by a concentration of the acoustic energy streamlines (red coloured streamlines) which decay rapidly upstream of the fan. An additional view of the 3D streamlines for the case θ_{mode}= 71.6 degrees is illustrated in figure 7.20.

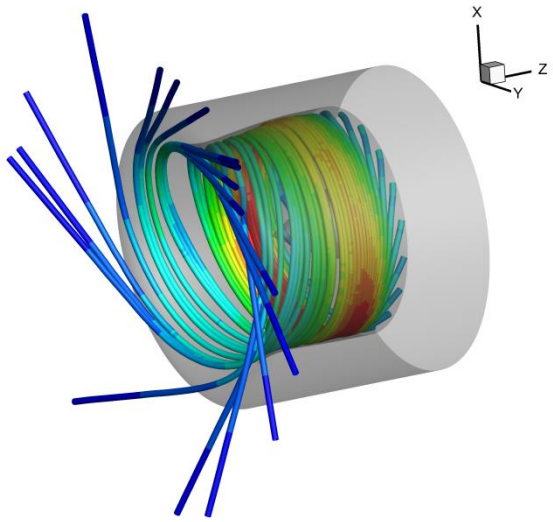

Figure 7.20: The 3D streamlines of the acoustic energy flux inside the intake duct for the source mode angle θ_{mode} = 71.6° (cut-on ratio 0.95).

This illustrates more clearly the distribution of the streamlines inside the intake and confirms that the incident mode appears to 'cut-off' a small distance upstream of the fan plane (the streamlines are perpendicular to the shaft axis and the magnitude of the acoustic intensity increases rapidly). Nonetheless, it can be seen that there is still some amount of the incident energy which is transmitted further upstream. This is due to the fact that the source mode scatters to other cut-on (propagating) and cut-off (evanescent) modes as shown in figure 7.18 (c). The cut-off modes can also carry the acoustic energy if there is more than one such mode present.

7.3.2.3 Far-field directivity

The influence of the source mode angle on the far-field directivity is examined in this section. The far-field solution is obtained using the Ffowcs Williams-Hawkings (FWH) method described in section 3.4.4. The solution is mapped onto the observation points (field points) as defined in section 7.2.3 covering the full range of the azimuthal angles, and polar angles up to 120 degrees from the forward axis.

The far-field directivities for the three source mode angles are displayed in figure 7.21. The SPL for each source mode angle is plotted as a function of the azimuthal and polar angles, on dB-scale. The conclusions drawn from the in-duct and near-field solutions discussed in the previous two sections hold here.

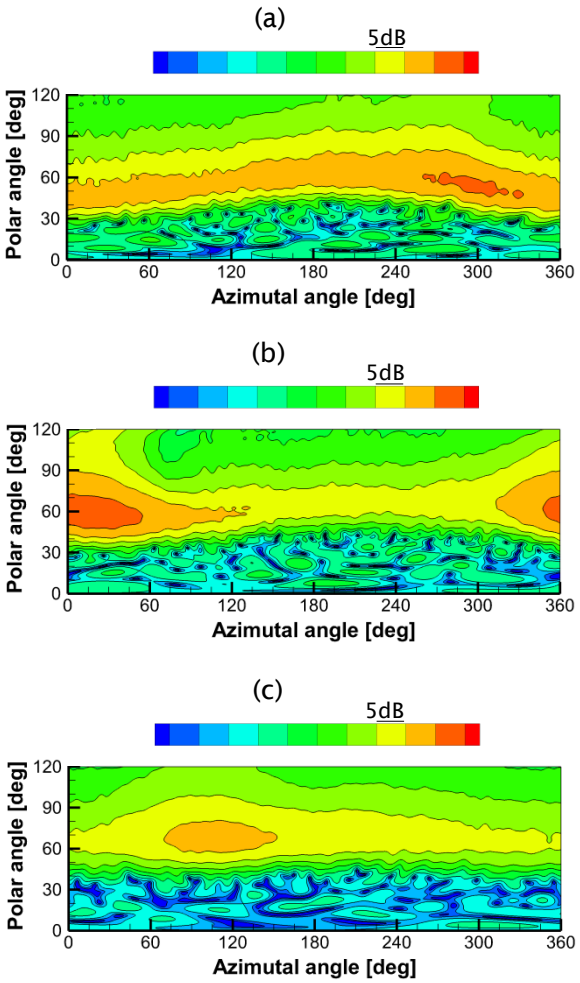

Figure 7.21: The far-field directivity of the SPL for varying the source mode angle θ_{mode} (a) 51.2°, (b) 62.5°, and (c) 71.6°.

When comparing the far-field solutions shown in figure 7.21 for different mode angles one can clearly see a greater directivity of the SPL in the azimuthal direction for higher angles. The maximum SPL difference in the azimuthal direction varies between the cases. It is 5dB for θ_{mode}= 51.2 degrees (figure 7.21 (a)), 10dB for θ_{mode}= 62.5 degrees (figure 7.21 (b)), and 7dB for θ_{mode}= 71.6 degrees (figure 7.21 (c)). The location of the SPL peak value moves from 300 degrees (top left-hand side of the intake) for the lower mode angle through 20 degrees (upwards direction) for the middle mode angle to 110 degrees (right-hand side of the intake) for the higher mode angle. The radiation angle in the polar direction increases with increasing the source mode angle, which is indeed to be expected. However, the polar location of the SPL peak region varies in the azimuthal direction. This is due to the scarfing angle of the nacelle (figure 7.1). For the lower source mode angle (θ_{mode}= 51.2 degrees) case the maximum polar angle difference observed between bottom

and top sides of the intake is 17 degrees. The sound radiates at highest polar angle in the downward direction. In the case of the middle value of the mode angle (θ_{mode}= 62.5 degrees) the maximum difference in the polar directivity is 20 degrees, however the minimum and maximum are located at different azimuthal angles. The former is located at 30 degrees, and the latter at 217 degrees. Nonetheless, the difference in the azimuthal direction of approximately 180 degrees is maintained. This is not the case for the higher source mode angle (θ_{mode}= 71.6 degrees) where the polar directivity is nearly constant over the whole range of the azimuthal angles. The polar directivity behaviour confirms the presence of evanescent modes inside the intake duct for the higher source mode angle. Moreover, for all source mode angles the SPL peak region is wider in the polar direction towards the higher polar angles at the azimuthal location where the SPL reaches its maximum value.

7.4 Flight effect

In this section the influence of the mean flow distortion is assessed for a flight intake. The non-axisymmetric intake rig used in the previous sections has been designed to account for the flight effect but the aerolines were adjusted for the static external flow. In this study we aim to investigate the flight effect for a non-axisymmetric flight intake in the presence of an external free stream flow. The flight intake is shown in figure 7.22. The nacelle and spinner surfaces are shown in figure 7.22 (a), and the main azimuthal profiles defining the nacelle surface are displayed in figure 7.22 (b). The fan and throat planes are indicated in figure 7.22 (b). The vertical plane cutting through the centre line of the model is a symmetry plane of this model. Therefore the side azimuthal profile is the same for both sides of the model. As in the case of the non-axisymmetric static rig, the geometry is axisymmetric between the fan plane and an axial station some distance along the axial axis. The intake's shape including the external aerolines has been optimised to maximize engine performance. The geometry features discussed in section 7.2, i.e. scarfing angle and droop, can be identified in the geometry.

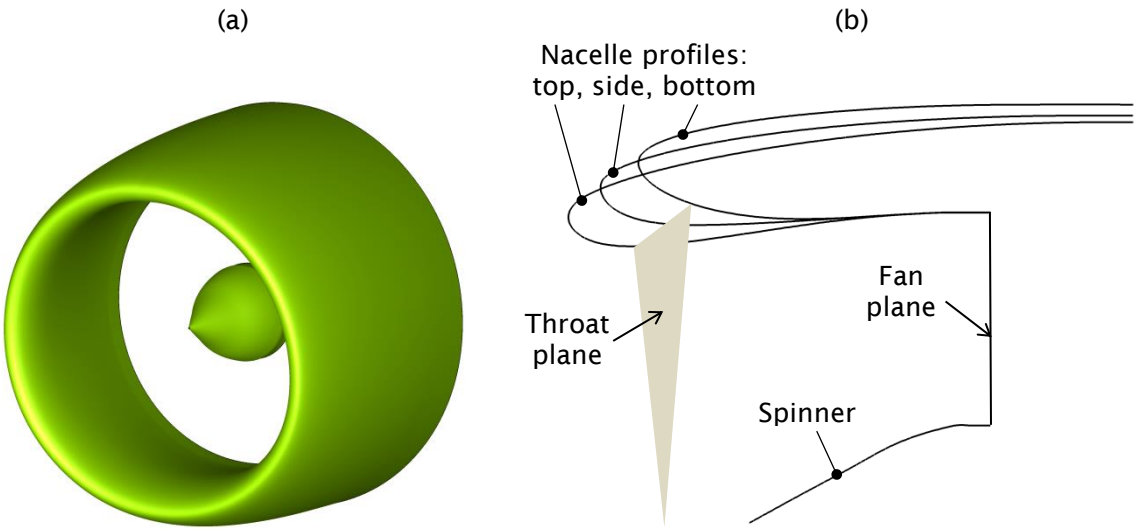

Figure 7.22: A flight non-axisymmetric intake: (a) rendered nacelle and spinner surfaces, (b) main azimuthal profiles.

The CAA calculations have been performed by using Actran DGM (see chapter 3) implemented in the CAE scheme described in chapter 4. The DGM mesh is refined to approximately one element per upstream wavelength with further refinement to four elements per maximum mode azimuthal order involved in the problem over the intake surface to minimize the mesh scattering (see section 5.2.2). This gives element orders between 2 and 7. In this case, due to numerical instabilities induced by strong mean flow gradients in the vicinity of the mean flow stagnation region, a coarse mesh is used in the near-wall region of the intake lip. This has succeeded in damping these numerical instabilities but required a manual intervention to correct the mean flow velocity vector on a small number of mesh nodes in this region. In addition, the terms associated with the mean flow gradients in the linearized Euler equation used by Actran DGM (see section 2.2.2) are removed to avoid instabilities in other regions. This has been shown by Tester et al. [157] to be a reasonably accurate technique which can be used to deal with the Kelvin-Helmholtz instabilities for exhaust nozzle problems. In the case of intake problems the mean flow gradients are lower. Therefore we can conclude that this approach will give at least a similar level of accuracy.

As in the case of the non-axisymmetric intake rig the modal excitation consists of a single BPF incident mode (20,1) with the mode angle of 62.5 degrees (cut-on ratio 0.888) for the shaft speed of 7680 rpm (excitation frequency of 2560 Hz).

An isentropic compressible flow computed by solving the Euler equations (see section 3.3.3) is used. The flow parameters are similar to those used in section 7.3.2. The Mach number at the fan plane is 0.54 and the total pressure and total temperature are, respectively, 101.2 kPa and 288.2 K. A free-stream flow with the Mach number of 0.25 is assumed in the external domain, and the free-stream flow is inclined at an angle of 7 degrees to the shaft axis. The Mach number distribution on a vertical cut-plane through the shaft axis is shown in figure 7.23 (a). The mean flow is shown by contours of Mach number and by means of streamlines. The location of the stagnation points on the bottom and top azimuthal profiles are clearly visible. The pattern of the streamlines also confirms the mean flow quality. A transverse cross-section at which the flow distortion parameter ϵ reaches its maximum value is marked by a black line in figure 7.23 (a). The maximum value is approximately 0.12. The Mach number distribution on the cross-section is shown in figure 7.23 (b). The maximum value of the flow distortion parameter and its distribution inside the intake duct are therefore comparable though a little greater than those observed for the non-axisymmetric intake rig (section 7.3.2). This confirms that the non-axisymmetric intake rig reproduces reasonably well the mean flow distortion in the flight intake at an incidence angle of around 7 degrees.

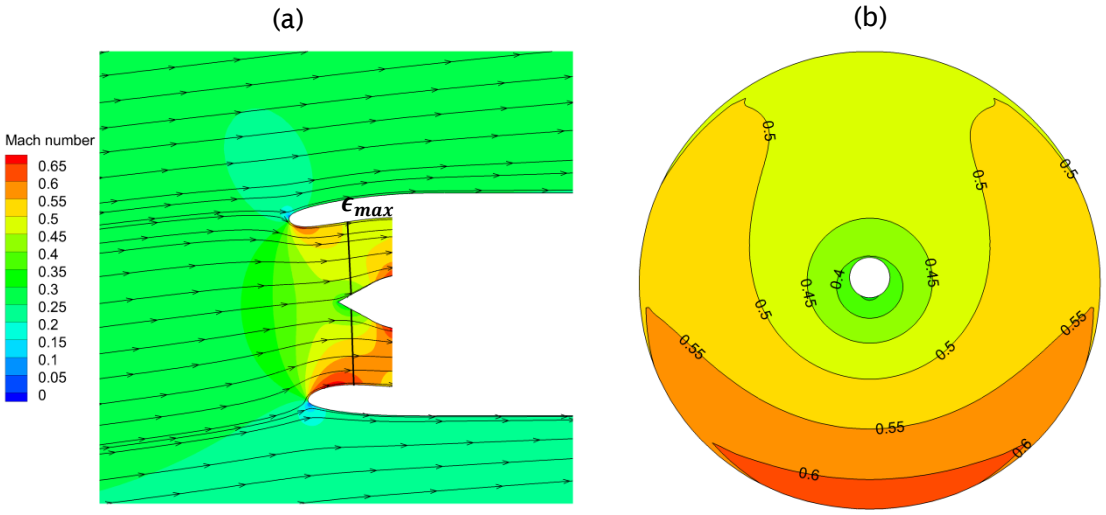

Figure 7.23: Steady flow distortion in the non-axisymmetric flight intake. The Mach number distribution: (a) on a vertical cut-plane (symmetry plane) of the model, (b) on the cross-section where the flow distortion parameter reaches its maximum value.

7.4.1 Near-field solution

We first examine the effect of flow distortion on the near-field acoustic solution. The SPL pattern on the throat plane is shown in figure 7.24. This confirms what was observed in the previous sections, namely that the geometry and the mean flow distortion have a crucial role in shaping the sound field. The SPL pattern is broadly similar to that of the static non-axisymmetric intake rig (see section 7.3.2) for the same mode angle (θ_{mode}= 62.5 degrees). In this case, however, unlike in the static rig, two regions of amplified SPL are visible. The first region is located on the bottom of the throat plane covering over half of its perimeter with the peak on its left-hand side. The second region is located on the top left-hand side of the throat plane and it covers a quarter of the perimeter. The maximum SPL differences between the peaks and the minimum decay, which is visible on the top right-hand side of the throat, are 23 and 18 dB, respectively. Once again some spurious fluctuations are present in the centre of the throat plane due to the mesh scattering (see section 5.2.2). The error level is again low (at least 40 dB below the peak values).

The streamlines of acoustic intensity for the flight intake, coloured by the magnitude of the acoustic intensity vector, are shown in figure 7.25. They were generated as described in section 7.3.2.2. As for the static rig, a large amount of the sound power is radiated upwards as can be seen in figure 7.25 (a). However, in this case, a considerable portion of the power is radiated also towards the lower right-hand side of the intake.

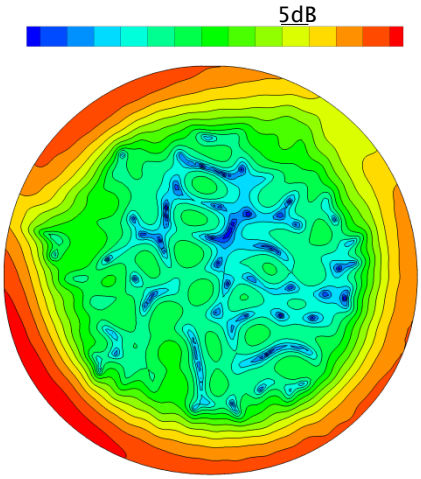

Figure 7.24: The SPL distribution on the throat plane. The flight non-axisymmetric intake with the mean flow.

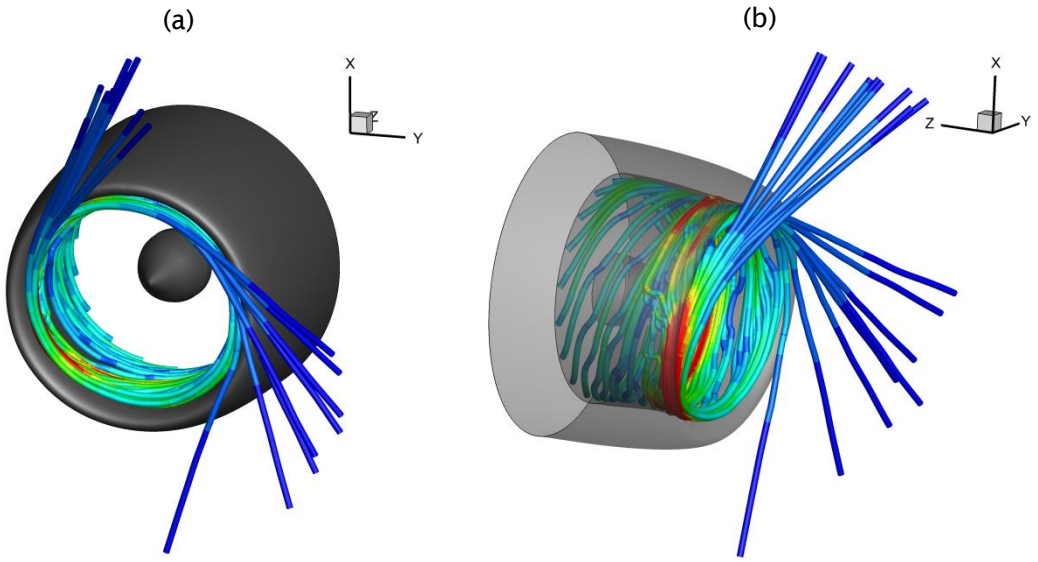

Figure 7.25: The 3D streamlines of the acoustic energy flux for the flight non-axisymmetric intake with the mean flow: (a) perspective view, (b) View inside the intake.

This is consistent with a concentration of the acoustic energy streamlines (red coloured streamlines) in the vicinity of the intake highlight on its lower left-hand side as shown in figure 7.25 (b). The distribution of the streamlines in this region is similar to that observed in the non-axisymmetric intake rig upstream of the fan plane for θ_{mode} = 71.6 degrees (see figure 7.20). However, in this case the pattern is less regular which is perhaps attributable to the lack of terms associated with the mean flow gradients in the current solution. Nonetheless, the general pattern of the streamlines indicates that some evanescent modes occur in this region. As already mentioned in section 7.3.2.2 a group of evanescent modes can carry the acoustic energy.

7.4.2 Far-field directivity

The far-field solution is obtained by using a Ffowcs Williams-Hawkings (FWH) surface as described in section 3.4.4. The solution is mapped onto the field points, as defined in section 7.2.3, for the full range of the azimuthal angles, and for the polar angles extending 120 degrees from the forward axis.

The far-field directivity of the SPL is shown in figure 7.26. The radiation pattern is displayed as function of the azimuthal and polar angles.

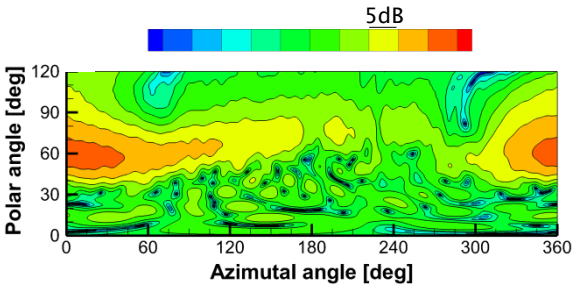

Figure 7.26: The far-field directivity of the SPL for the flight non-axisymmetric intake with the mean flow.

The far-field radiation pattern is fairly similar to that of the non-axisymmetric intake static rig (see section 7.3.2) for the corresponding mode angle (θ_{mode}= 62.5 degrees). The SPL peak is located at a similar azimuthal angle of 15 degrees, which is close to the upward direction. A higher concentration of the SPL in the azimuthal direction is observed. The maximum variation in SPL is 17 dB. One can also see a larger variation in the polar radiation angle which is a result of convective effect of the free-stream mean flow. The sound radiates at a higher polar angle in the downward direction. The difference is approximately 7-8 degrees when comparing to the static rig.

7.5 Summary and Conclusions

Numerical studies have been performed for rotor-alone tones at the blade passing frequency to investigate the effects of nacelle geometry, mean flow distortion and flight effect on the sound field.

Firstly, the effects of a complex 3D nacelle shape and scarfing angle on the sound field has been examined in the absence of mean flow by using the DGM approach. These studies have been conducted for a static rig configuration. It has been shown that any non-axisymmetric shape leads to scattering of an incident source mode into adjacent azimuthal components and as a consequence generates a non-axisymmetric acoustic field in the duct and in the free field. The different effect of scarfing and droop on the radiated sound field has been confirmed.

Special attention has been paid to evaluating the impact of mean flow distortion on the sound field. The DGM has been validated against a semi-analytical and a frequency domain finite element approach for a straight duct with a parallel distorted mean flow. In addition, the impact of the mean flow

distortion on sound absorption by liner has been investigated. Refraction due to the mean flow distortion has been found to play a major role in shaping the sound field inside and outside the nacelle. It has been shown that liner performance can be significantly affected by the mean flow distortion.

Finally, the effect of flight rather than static test condition has been studied by using the DGM approach. The results confirm that the directivity pattern of the sound field is strongly influenced by steady mean flow distortion inside the intake. While the convective effects of the free-stream mean flow have a minor impact on the directivity of sound in the far-field.

8. Summary, conclusions and outlook

8.1 Summary and conclusions

Firstly, the discontinuous Galerkin method was validated against several benchmark cases corresponding to the turbofan nacelle acoustics. The following properties of the method were considered; accuracy of the scheme; impedance modelling capabilities; applicability for realistic axisymmetric and 3D non-axisymmetric turbofan intake problems, and finally overall efficiency. The DGM clearly manifests high accuracy for zero flow and flow cases in both inflow and outflow configurations. Validation of the impedance model implemented in the current development of the DG method confirmed already reported issues with the Ingard/Myers boundary layer condition in the time domain. A study with a small but finite boundary layer thickness has also been conducted and it has been shown that the boundary layer thickness has a significant impact on the DGM solution. Benchmarking of the DGM for realistic intake problems has shown that the approach can be successfully applied for axisymmetric and 3D non-axisymmetric hard walled problems at realistic frequencies and mean flows. Although with some guidelines regarding mesh resolution on curved walls to minimize mesh scattering and buffer zone settings to avoid spurious reflections. In term of efficiency the DGM manifests clear advantage over direct solvers when applied in parallel computations.

Secondly, novel hybrid CFD/CAA approach for modelling 3D fan stage tone noise was proposed and developed. Two widely known CFD and CAA methods are coupled in order to utilize their features in a most optimal manner. The coupling interface was validated for rotor alone tones and buzz-saw noise against experimental data and other numerical method. Additionally, demonstration for 3D non-axisymmetric intake was carried out and good results were also obtained. The results presented in this work clearly show advantages of using such approach for full 3D modelling of the turbofan nacelle acoustic.

Finally, the numerical studies have been performed for rotor-alone tones at the blade passing frequency to investigate the effects of nacelle geometry, and mean flow distortion on the sound field. It has been shown that the nacelle

shape and refraction due to the mean flow distortion play an important role in shaping the sound field inside and outside the nacelle. Furthermore, it has been found that liner performance can be significantly affected by the mean flow distortion. In addition, a study with free stream included (flight effect) has confirmed that the directivity pattern of the sound field is strongly influenced by steady mean flow distortion inside the intake while the convective effects of the free-stream mean flow are less important.

A scheme for automated 3D CAA noise radiation calculations for turbofan intakes has been developed and is briefly described in this thesis.

8.2 Outlook

Discontinuous Galerkin Method

The impedance modelling is the main problem of the current implementation of the DG method. This is particularly important issue with respect to turbofan nacelle acoustics, since it usually includes acoustic liners. The impedance boundary condition is highly challenging from the mathematical point of view as described to some extent in chapter 2. The main difficulty is the mean flow boundary layer, which has to be included in the acoustic model. In the current work it was realized by the Myers boundary condition. It has been shown to be ill-posed and numerically unstable in the time domain. Therefore the boundary condition has to be modified or reinvented. Recently, new boundary condition, which is modification of the Myers boundary condition, has been proposed by Brambley [99]. This has been shown for a straight cylindrical duct with thin boundary layers. Another very interesting research of the hydrodynamic stability of the shear layer over the liner model has been performed by Rienstra and Darau [100]. Recently, Gabard [101] compared these two new boundary conditions to standard Myers boundary condition and validated against an exact solution for the case of the reflection of a plane wave by a lined plane surface.

In the considered DGM development the non-reflecting boundary condition is realized by 1D characteristics complemented with the buffer zone. This has been shown to be sufficiently accurate approach, however for some applications the buffer zone has to be extended to ensure minimum spurious reflections. As a result the mesh size increases considerably, particularly for

3D problems. A perfectly matched layer absorbing boundary condition would be more efficient approach, and in theory reflection-less [124] [179] [180]. This could be a good direction to further develop the absorbing boundary condition. However, the full implementation of the PML boundary condition in the time domain introduces more complexity to the DGM scheme, and may lead to instabilities [122]. Therefore further investigation is necessary.

The quadrature free formulation of the DGM is currently implemented in the whole computation domain. Therefore the geometry is represented by straight edges and flat facets elements. In order to ensure minimum mesh scattering, mesh refinement is necessary in vicinity of the wall boundary conditions. This leads to locally small elements and in consequence to significant reduction of the timestep in the time integration. This could be addressed by applying a quadrature formulation of the DGM [181] [182] over curved walls. However, the quadrature formulation of the DGM is computationally demanding, therefore the high computational performance of the quadrature-free DGM would drop down slightly.

The graphics processing units (GPUs) have recently evolved to general purpose computing devices. They are cheap and very powerful for multithreaded computations. The DG method, due to its discontinuity property, is unusually suited for implementation on the GPUs [53] [54] [55].

CFD/CAA coupling for 3D fan stage tone noise prediction

In the current development of the coupling interface, the matching is realized as an axisymmetric problem. Nonetheless, under some assumptions, the determined sources can be used for the full 3D radiation study of the fan tonal noise. In order to make this method more complete, it should be complemented with an option for full 3D matching including matching at lined surfaces. Also, it should be tested in bypass ducts with arbitrary mean flows. Moreover, the matching should be validated for a full range of engine orders and different types of fan noise.

3D intake shape and mean flow effects on the sound field

The numerical study of intake geometry and steady flow distortion effects on the sound field has provided encouraging results. The effects of steady flow distortion on intake fan noise should be further investigated, particularly for

lined cases to further investigate influence of the mean flow distortion on liner performance. The investigation could be extended for a wide range of fan speeds and performed for different types of fan noise. Furthermore, the numerical results should be validated against available experimental data.

Appendices

A Non-Uniform Rational B-Spline (NURBS) method

A.1 Curve and surface definition

A parameterized curve defined by p^{th} degree polynomials is given by [146]

$$\boldsymbol{C}(u_g) = \frac{\sum_{i=0}^{n} B_{i,p}(u_g) w_i \boldsymbol{P}_i}{\sum_{i=0}^{n} B_{i,p}(u_g) w_i}, \tag{A.1}$$

where u_g is a non-dimensional parameter in range of 0 to 1, $B_{i,p}$ is i^{th} basis function of order p, w_i is i^{th} weight, and $\boldsymbol{P}_i$ is i^{th} control point.

The B-spline basis functions are defined on the following knot vector $U = \left\{0, \dots, 0, u_{g_{p+1}}, \dots, u_{g_{mu_g-p-1}}, 1, \dots, 1\right\}$, where, $mu_g = n + p + 1$.

The mathematical properties of the NURBS curve imply the following geometrical features:

- Start and end of the curve agree with the corresponding control points, i.e. $\boldsymbol{C}(0.0) = \boldsymbol{P}_0$; $\boldsymbol{C}(1.0) = \boldsymbol{P}_n$;
- The curve is defined by the control points and weights. Its shape can be modified in the 3D space by repositioning the control points and/or changing weights;
- The curve is infinitely differentiable at its sections between the knot points and $p - k$ differentiable at any knot point, where k is the knot multiplicity;
- A change in position of a control point, $\boldsymbol{P}_i$ and/or its weight, w_i results in curve transformation, only in part between knot points at u_{g_i} and $u_{g_{i+p+1}}$.

A parameterized surface approximated by p^{th} degree polynomials in direction u_g, and by q^{th} degree polynomials in direction v_g is given by [146]

$$\boldsymbol{S}(u_g, v_g) = \frac{\sum_{i=0}^{n} \sum_{j=0}^{m} B_{i,p}(u_g) B_{j,q}(v_g) w_{i,j} \boldsymbol{P}_{i,j}}{\sum_{i=0}^{n} \sum_{j=0}^{m} B_{i,p}(u_g) B_{j,q}(v_g) w_{i,j}}, \tag{A.2}$$

where u_g, v_g are the non-dimensional parameters in both surface's directions. They range from 0 to 1. $B_{i,p}, B_{j,q}$ are i^{th} and j^{th} basis functions of orders p and q, respectively. $w_{i,j}$ are i^{th} and j^{th} weights, and $\boldsymbol{P}_{i,j}$ are i^{th}, j^{th} control points.

The B-spline basis functions are defined in both direction on the following knot vectors: $U = \left\{0, \dots, 0, u_{g_{p+1}}, \dots, u_{g_{mu_g-p-1}}, 1, \dots, 1\right\}$, and $V = \left\{0, \dots, 0, v_{g_{q+1}}, \dots, v_{g_{mv_g-q-1}}, 1, \dots, 1\right\}$, where $mu_g = n + p + 1$, and $mv_g = m + q + 1$, respectively.

This implies the following geometric properties:

- Control points at the surface corners determine simultaneously these corners, i.e. $\boldsymbol{S}(0.0{,}00) = \boldsymbol{P}_{0,0}$, $\boldsymbol{S}(1.0{,}0.0) = \boldsymbol{P}_{n,0}$, $\boldsymbol{S}(0.0{,}1.0) = \boldsymbol{P}_{0,m}$, $\boldsymbol{S}(1.0{,}1.0) = \boldsymbol{P}_{n,m}$;
- The surface is defined by the control points and weights. Its shape can be modified by repositioning the control points and/or by variation of the weights;
- The surface is infinitely differentiable in both directions within sectors defined by the skeleton polygons. It is $p - k$ and $q - k$ times differentiable along any sector's edges, where k is the knot multiplicity.

A.2 Curve and surface fitting

Interpolation or approximation can be applied for fitting the NURBS curve or surface to data provided on a number of discrete points.

In the interpolation the input data is accurately represented by the geometry. The curve or surface passes through the discrete points. This may, however, lead to wiggled geometry solution. Therefore, additional conditions can be imposed at the control points, e.g. derivatives. An example of the interpolation for a curve is presented in figure A.1.

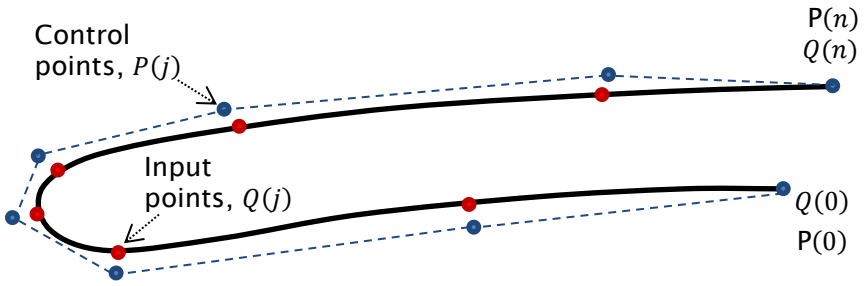

Figure A.1: An example of the NURBS curve interpolation to discrete points.

The NURBS curve is interpolated globally to the data of discrete points $\boldsymbol{Q} = \{\boldsymbol{Q}_0, \dots, \boldsymbol{Q}_i, \dots, \boldsymbol{Q}_n\}$. The curve is defined by the control points $\boldsymbol{P} = \{\boldsymbol{P}_0, \dots, \boldsymbol{P}_i, \dots, \boldsymbol{P}_n\}$, knot vector $\boldsymbol{U}$ and polynomials degree p. In the proposed approach, the weights are set to unity. A vector of the non-dimensional parameters u_g is determined according to the input data $\boldsymbol{Q}$. It is given by $\boldsymbol{u_g} = \left\{u_{g_0}, \dots, u_{g_n}\right\}$. The curve at each data point is defined as follows

$$\boldsymbol{Q}_k = \boldsymbol{C}\left(u_{g_k}\right) = \sum_{i=0}^{n} B_{i,p}\left(u_{g_k}\right)\boldsymbol{P}_i. \tag{A.3}$$

A system of (n+1) linear equations is obtained for the entire input data. It is solved to find the control points $\boldsymbol{P}$. The complete NURBS curve in now defined. The derivative constraints can be imposed by adding extra control points, which yields additional equations in the linear system.

The NURBS surface is interpolated globally to (n+1) x (m+1) matrix of the data points $\boldsymbol{Q}$. The surface is defined by the control points, knot vectors and the polynomial degrees in the both directions. Two vectors of the non-dimensional parameters u_g, v_g are defined according to the input data $\boldsymbol{Q}$. They are as follows; $\boldsymbol{u}_g = \left\{u_{g_0}, \dots, u_{g_n}\right\}$, and $\boldsymbol{v}_g = \left\{v_0, \dots, v_{g_m}\right\}$. The surface passes through each data point, which yields

$$\boldsymbol{Q}_{k,l} = \boldsymbol{S}\left(u_{g_k}, v_{g_l}\right) = \sum_{i=0}^{n}\sum_{j=0}^{m} B_{i,p}\left(u_{g_k}\right) B_{j,q}\left(v_{g_l}\right)\boldsymbol{P}_{i,j}. \tag{A.4}$$

This can be recasted to:

$$\boldsymbol{Q}_{k,l} = \boldsymbol{S}\left(u_{g_k}, v_{g_l}\right) = \sum_{i=0}^{n} B_{i,p}\left(u_{g_k}\right)\left(\sum_{j=0}^{m} B_{j,q}\left(v_{g_l}\right)\boldsymbol{P}_{i,j}\right) = \sum_{i=0}^{n} B_{i,p}\left(u_{g_k}\right)\boldsymbol{C}_{i,l}. \qquad \text{(A.5)}$$

One may note, that it is equivalent to curve interpolation in both surface's directions, i.e. u_g, and v_g. This yields m+1 sets of n+1 linear equations in one direction and n+1 sets of m+1 linear equations in the second direction. In u_g direction, the set of linear equations is formulated for each v_g-isoparametric curve l as follows:

$$\boldsymbol{B}\boldsymbol{C}_l = \boldsymbol{Q}_l, \qquad \text{(A.6)}$$

where

$$\boldsymbol{B} = \begin{bmatrix} B_{0,p}\left(u_{g_0}\right) & \cdots & B_{n,p}\left(u_{g_0}\right) \\ \vdots & \ddots & \vdots \\ B_{0,p}\left(u_{g_n}\right) & \cdots & B_{n,p}\left(u_{g_n}\right) \end{bmatrix}_{n,n},$$

$$\boldsymbol{Q}_l = \begin{bmatrix} Q_{0,l} \\ \vdots \\ Q_{n,l} \end{bmatrix}_n,$$

$$\boldsymbol{C}_l = \begin{bmatrix} C_{0,l} \\ \vdots \\ C_{n,l} \end{bmatrix}_n.$$

Once matrix $\boldsymbol{C}$ is determined, the control points $\boldsymbol{P}$ can be found by solving the second array of the linear systems. This is achieved by interpolating each u_g-isoparametric curve k in direction v_g;

$$\boldsymbol{B}\boldsymbol{P}_k = \boldsymbol{C}_k, \qquad \text{(A.7)}$$

where

$$\boldsymbol{B} = \begin{bmatrix} B_{0,q}\left(v_{g_0}\right) & \cdots & B_{m,q}\left(v_{g_0}\right) \\ \vdots & \ddots & \vdots \\ B_{0,q}\left(v_{g_m}\right) & \cdots & B_{m,q}\left(v_{g_m}\right) \end{bmatrix}_{m,m},$$

$$\boldsymbol{C}_k = \begin{bmatrix} C_{k,0} \\ \vdots \\ C_{k,m} \end{bmatrix}_m ,$$

$$\boldsymbol{P}_k = \begin{bmatrix} P_{k,0} \\ \vdots \\ P_{k,m} \end{bmatrix}_m .$$

The NURBS surface is now defined. The derivative constraints can be imposed by adding extra arrays of control points in considered regions. This, however, yields additional equations in the linear systems.

In the approximation the input data is not precisely represented by the geometry. It does not necessarily pass through the input points. An example is presented in figure A.2. This is an advantage of the method, since the data is inherently smoothed. A fitting error is controlled by the number of the NURBS control points and their distribution. Similarly to the interpolation, additional constraints can be imposed at the control points.

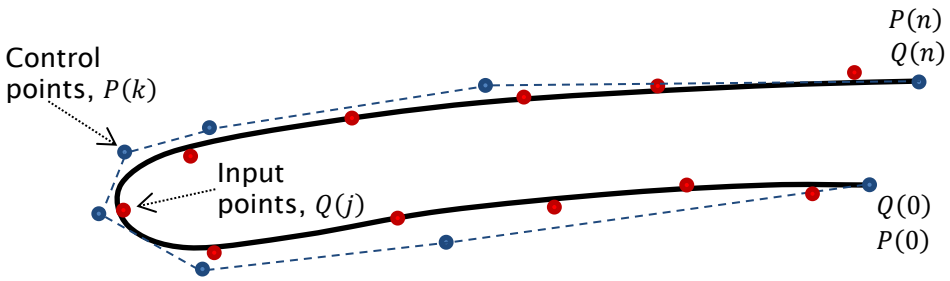

Figure A.2: An example of the NURBS curve approximation to discrete points.

The process is slightly more complex. However, many similarities to the interpolation exist. The end data points agree with the corresponding end control points; all weights are set to unity and the parameter vectors are pre-computed from the input data. In the proposed approach the data is approximated by applying the least squares method. The following functions are minimalized for curve and surface, equations A.8 and A.9, respectively.

$$\sum_{k=1}^{nd-1} \left| \boldsymbol{Q}_k - \sum_{i=0}^{n} B_{i,p}\left(u_{g_k}\right) \boldsymbol{P}_i \right|^2 , \tag{A.8}$$

and

$$\sum_{k=1}^{nd-1}\sum_{l=1}^{md-1}\left|\boldsymbol{Q}_{k,l}-\sum_{i=0}^{n}\sum_{j=0}^{m}B_{i,p}\left(u_{g_k}\right)B_{j,q}\left(v_{g_l}\right)\boldsymbol{P}_{i,j}\right|^2, \tag{A.9}$$

where

$\boldsymbol{u_g}$ and $\boldsymbol{v_g}$ are the pre-computed parameter vectors, both in range between 0 and 1,

$\boldsymbol{Q}$ are the input data points, (nd+1) x (md+1),

B are appropriate basis functions of order p or q, respectively

$\boldsymbol{P}$ are the control points, (n+1) x (m+1).

Knowing, that the end points of a curve or corner points of a surface agree with the corresponding control points, the equations A.8 and A.9 can be slightly reduced. This is achieved by implementing a new variable $\boldsymbol{D}$ defined by

$$\boldsymbol{D}_k=\boldsymbol{Q}_k-B_{0,p}\left(u_{g_k}\right)\boldsymbol{Q}_0-B_{n,p}\left(u_{g_k}\right)\boldsymbol{Q}_n,$$

and in the case of the surface,

$$\begin{aligned}\boldsymbol{D}_{k,l}=\boldsymbol{Q}_{k,l}&-B_{0,p}\left(u_{g_k}\right)B_{0,q}\left(v_{g_l}\right)\boldsymbol{Q}_{0,0}-B_{n,p}\left(u_{g_k}\right)B_{0,q}\left(v_{g_l}\right)\boldsymbol{Q}_{n,0}\\&-B_{0,p}\left(u_{g_k}\right)B_{m,q}\left(v_{g_l}\right)\boldsymbol{Q}_{0,m}-B_{n,p}\left(u_{g_k}\right)B_{m,q}\left(v_{g_l}\right)\boldsymbol{Q}_{n,m}.\end{aligned}$$

The sum of deviation squares for a curve and surface is given by

$$S_{curve}=\sum_{k=1}^{nd-1}\left|\boldsymbol{D}_k-\sum_{i=1}^{n-1}B_{i,p}\left(u_{g_k}\right)\boldsymbol{P}_i\right|^2, \tag{A.10}$$

and

$$S_{surface}=\sum_{k=1}^{nd-1}\sum_{l=1}^{md-1}\left|\boldsymbol{D}_{k,l}-\sum_{i=1}^{n-1}\sum_{j=1}^{m-1}B_{i,p}\left(u_{g_k}\right)B_{j,q}\left(v_{g_l}\right)\boldsymbol{P}_{i,j}\right|^2. \tag{A.11}$$

The functions A.10 and A.11 are having their minima when their derivatives with respect to control points $\boldsymbol{P}$ are equal to zero. As already mentioned, a surface can be reconstructed by series of curve interpolation to the input data for iso-parametric curves in both directions. This applies also for the

approximation. Therefore, in this work, the least squares fitting approach is used only with respect to the curve approximation. The derivative of the equation A.10 with respect to the k^{th} control point is given by

$$\frac{\partial S_{curve}}{\partial \boldsymbol{P}_k} = \sum_{k=1}^{nd-1} \left(-2\boldsymbol{D}_k B_{k,p}\left(u_{g_k}\right) + 2B_{k,p}\left(u_{g_k}\right) \sum_{i=1}^{n-1} B_{i,p}\left(u_{g_k}\right) \boldsymbol{P}_i \right) = 0. \tag{A.12}$$

The vector of n-1 unknown control points is found by solving the set of n-1 linear equations, defined as follows,

$$(\boldsymbol{B}^T \boldsymbol{B})\boldsymbol{P} = \boldsymbol{D}, \tag{A.13}$$

where,

$$B = \begin{bmatrix} B_{1,p}\left(u_{g_1}\right) & \cdots & B_{n-1,p}\left(u_{g_1}\right) \\ \vdots & \ddots & \vdots \\ B_{1,p}\left(u_{g_{nd-1}}\right) & \cdots & B_{n-1,p}\left(u_{g_{nd-1}}\right) \end{bmatrix}_{nd-1,n-1},$$

$$\boldsymbol{D} = \begin{bmatrix} B_{1,p}\left(u_{g_1}\right)\boldsymbol{D}_1 + \cdots + B_{1,p}\left(u_{g_{nd-1}}\right)\boldsymbol{D}_{nd-1} \\ \vdots \\ B_{n-1,p}\left(u_{g_1}\right)\boldsymbol{D}_1 + \cdots + B_{n-1,p}\left(u_{g_{nd-1}}\right)\boldsymbol{D}_{nd-1} \end{bmatrix}_{n-1},$$

$$\boldsymbol{P} = \begin{bmatrix} \boldsymbol{P}_1 \\ \vdots \\ \boldsymbol{P}_{n-1} \end{bmatrix}_{\mathrm{n-1}}.$$

The curve is now approximated. Additional constrains, if necessary, are imposed to the control points.

The approximation to a specified accuracy is an extension of the least squares fit described above. In this approach maximum fitting error determined for a surface is given by,

$$\max_{\substack{0 \le k \le n \\ 0 \le l \le m}} \left| \boldsymbol{Q}_{k,l} - \boldsymbol{S}\left(u_{g_k}, v_{g_l}\right) \right|. \tag{A.14}$$

The process starts with smallest possible number of control points, i.e. $n = p$, $m = q$, where p and q are polynomial orders in both surface's directions. The maximum error is checked, if it is higher than requested additional control

point is added in the considered direction. This is looped till the requested accuracy is met.

A.3 The reconstruction of 3D NURBS surface from 4 azimuthal profiles

In the first step, the data at each azimuthal station is interpolated according to description given in Appendix A.2.

Once the control points at the four stations are found, the azimuthal direction of the surface is reconstructed at each j^{th} longitudinal station. This is presented in figure A.3. In fact, it is a projection of the surface's cross section at the j^{th} station on to the XY plane of the Cartesian coordinate system. It is worth to note that a displacement of any control point, $P'(i,j)$ in the axial direction does not change the projection on to the XY plane. The j^{th} projection is performed for the four quadrants. A single third order polynomial is used for each quadrant. By adding two fill control points with appropriate weights into each quadrant an analytical solution to ellipse can be found. The positions of the control points are fixed by a non-dimensional parameter delta. The weights of the control points lying on XZ and YZ planes are equal to unity. Each azimuthal profile is independent; therefore an axial position can vary between the profiles. To ensure the continuity of the first derivative between the quadrats the control points are grouped into four groups, $Gr(0,j), Gr(1,j), Gr(2,j)\ and\ Gr(3,j)$. Each group contains three control points. The continuity is achieved by their affiliation to just one straight line. The axial position of the each group is determined by the positions of the origin control points, $P(0,j), P(1,j), P(2,j) and\ P(3,j)$. The rotation of groups, 0 and 2 in the X axis is determined by angle coming from axial positions of control points, $P(1,j)$ and $P(3,j)$. Analogously, the rotation of groups, 1 and 3 in the Y axis is determined by angle coming from axial positions of control points, $P(0,j)$ and $P(2,j)$. The azimuthal knot vector is set to ensure that the knot points lay only on the XZ and XY planes.

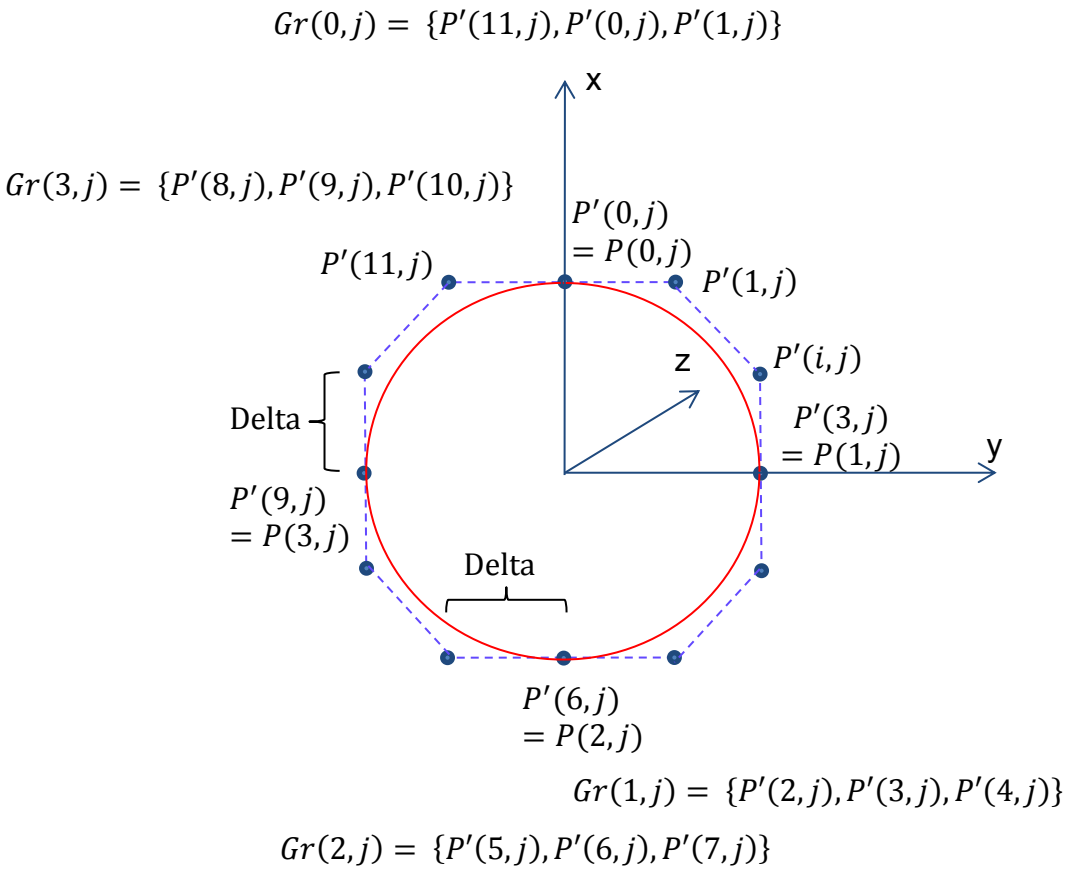

Figure A.3: A projection on the XY plane of the surface cross section at j^{th} station in the longitudinal direction.

B Parameters used in the validation of the DG method

B.1 The effect of domain size

Table B.1. The effect of domain size – operating conditions.

Conditions	Helmholtz Number **k**	Flow	Modes	Physical Domain Size/number of elements	Buffer zone Thickness	Element Size	Element Order Max/Min	Degrees of Freedom
Run – 1	**10**	**0.0**	**(0,1)**	**5x2R / 386**	**1.59λ**	**~1-2 el./λ**	**6/1**	**49 612**
Run – 2	**10**	**0.0**	**(0,1)**	**10x4R / 757**	**1.59λ**	**~1-2 el./λ**	**6/1**	**118 212**
Run – 3	**10**	**0.0**	**(0,1)**	**20x5R / 1255**	**1.59λ**	**~1-2 el./λ**	**6/1**	**216 128**

Table B.2. The effect of domain size – convergence information.

Conditions	Helmholtz Number **k**	Modes	Real Time / number of iterations	Time Step	CPU Time	CPU Time per iteration
			s/iterations	s	m' s''	s
Run – 1	**10**	**(0,1) Well cut-on**	**0.026193 / 3 266**	**8.02000e-06**	**1' 25"**	**0.026026**
Run – 2	**10**	**(0,1) Well cut-on**	**0.042310 / 4 029**	**1.05013e-05**	**3' 21"**	**0.034996**
Run – 3	**10**	**(0,1) Well cut-on**	**0.080156 / 7 633**	**1.05013e-05**	**10' 48"**	**0.084895**

B.2 The effect of mesh resolution

Table B.3. The effect of mesh resolution – operating conditions.

Conditions	Helmholtz Number **k**	Flow	Modes	Physical Domain Size/number of elements	Buffer zone Thickness	Element Size	Element Order Max/Min	Degrees of Freedom
Run – 1	**10**	**0.0**	**(0,1)**	**5x2R / 386**	**1.59λ**	**~1-2 el./λ**	**6/1**	**49 612**
Run – 5	**10**	**0.0**	**(0,1)**	**5x2R / 5099**	**1.59λ**	**~4-5 el./λ**	**3/1**	**156 040**
Run – 6	**10**	**0.0**	**(0,1)**	**5x2R / 14445**	**1.59λ**	**~8-10 el./λ**	**2/1**	**412 056**

Table B.4. The effect of mesh resolution – convergence information.

Conditions	Helmholtz Number **k**	Modes	Real Time / number of iterations	Time Step	CPU Time	CPU Time per iteration
			s/iterations	s	m' s''	s
Run – 1	**10**	**(0,1) Well cut-on**	**0.026193 / 3 266**	**8.02000e-06**	**1' 25"**	**0.026026**
Run – 5	**10**	**(0,1) Well cut-on**	**0.026826 / 1 950**	**1.37569e-05**	**6' 02"**	**0.185641**
Run – 6	**10**	**(0,1) Well cut-on**	**0.027422 / 1 683**	**1.62935e-05**	**20' 37"**	**0.734997**

B.3 The effect of element order

Table B.5. The effect of element order – operating conditions.

Mesh with refined lip:								
Conditions	Helmholtz Number **k**	Flow	Modes	Physical Domain Size/number of elements	Buffer zone Thickness	Element Size	Element Order Max/Min	Degrees of Freedom
Run – 1	**10**	**0.0**	**(0,1)**	**5x2R / 386**	**1.59λ**	**~1-2 el./λ**	**6/1**	49 612
Run – 8	**10**	**0.0**	**(3,2)**	**5x2R / 386**	**1.59λ**	**~1-2 el./λ**	**6/1**	49 612
Run – 9	**10**	**0.0**	**(8,1)**	**5x2R / 386**	**1.59λ**	**~1-2 el./λ**	**6/1**	49 612
Run – 16	**20**	**0.0**	**(0,1)**	**5x2R / 386**	**3.23λ**	**~0.5-1 el./λ**	**9/1**	112 020
Run – 17	**20**	**0.0**	**(5,4)**	**5x2R / 386**	**3.23λ**	**~0.5-1 el./λ**	**9/1**	112 020
Run – 18	**20**	**0.0**	**(17,1)**	**5x2R / 386**	**3.23λ**	**~0.5-1 el./λ**	**9/1**	112 020
Run – 19	**30**	**0.0**	**(0,1)**	**5x2R / 386**	**4.76λ**	**~0.3-0.7 el./λ**	**12/2**	212 012
Run – 20	**30**	**0.0**	**(9,5)**	**5x2R / 386**	**4.76λ**	**~0.3-0.7 el./λ**	**12/2**	212 012
Run – 21	**30**	**0.0**	**(27,1)**	**5x2R / 386**	**4.76λ**	**~0.3-0.7 el./λ**	**12/2**	212 012
Mesh with uniformly sized elements:								
Conditions	Helmholtz Number **k**	Flow	Modes	Physical Domain Size/number of elements	Buffer zone Thickness	Element Size	Element Order Max/Min	Degrees of Freedom
Run – 22	**10**	**0.0**	**(0,1)**	**5x2R / 238**	**1.59λ**	**~1 el./λ**	**7/5**	39 952

Run – 23	**10**	**0.0**	**(3,2)**	**5x2R / 238**	**1.59λ**	**~1 el./λ**	**7/5**	39 952
Run – 24	**10**	**0.0**	**(8,1)**	**5x2R / 238**	**1.59λ**	**~1 el./λ**	**7/5**	39 952
Run – 25	**20**	**0.0**	**(0,1)**	**5x2R / 238**	**3.23λ**	**~0.5 el./λ**	**10/7**	110 244
Run – 26	**20**	**0.0**	**(5,4)**	**5x2R / 238**	**3.23λ**	**~0.5 el./λ**	**10/7**	110 244
Run – 27	**20**	**0.0**	**(17,1)**	**5x2R / 238**	**3.23λ**	**~0.5 el./λ**	**10/7**	110 244
Run – 28	**30**	**0.0**	**(0,1)**	**5x2R / 238**	**4.76λ**	**~0.25 el./λ**	**15/9**	223 308
Run – 29	**30**	**0.0**	**(9,5)**	**5x2R / 238**	**4.76λ**	**~0.25 el./λ**	**15/9**	223 308
Run – 30	**30**	**0.0**	**(27,1)**	**5x2R / 238**	**4.76λ**	**~0.25 el./λ**	**15/9**	223 308

Table B.6. The effect of element order – convergence information.

Mesh with refined lip:						
Conditions	Helmholtz Number **k**	Modes	Real Time / number of iterations	Time Step	CPU Time	CPU Time per iteration
			s/iterations	s	m' s''	s
Run – 1	**10**	**(0,1)** Well cut-on	**0.026193 / 3 266**	**8.02000e-06**	**1' 25"**	**0.026026**
Run – 8	**10**	**(3,2)** Moderately cut-on	**0.037724 / 5 250**	**7.18559e-06**	**2' 13"**	**0.025333**
Run – 9	**10**	**(8,1)** Almost cut-off	**0.043229 / 6 636**	**6.51427e-06**	**2' 45"**	**0.024864**
Run – 16	**20**	**(0,1)** Well cut-on	**0.025266 / 3 892**	**6.49187e-06**	**2' 26"**	**0.037513**
Run – 17	**20**	**(5,4)** Moderately cut-	**0.031746 / 5 744**	**5.52678e-06**	**3' 23"**	**0.035341**

		on				
Run – 18	**20**	**(17,1)** Almost cut-off	**0.040227 / 8 226**	**4.89018e-06**	**5' 14"**	**0.038172**
Run – 19	**30**	**(0,1)** Well cut-on	**0.025286 / 5 100**	**4.95795e-06**	**5' 18"**	**0.062353**
Run – 20	**30**	**(9,5)** Moderately cut-on	**0.031461 / 7 905**	**3.97995e-06**	**7' 43"**	**0.058571**
Run – 21	**30**	**(27,1)** Almost cut-off	**0.050072 / 14 042**	**3.56587e-06**	**13' 05"**	**0.055904**
Mesh with uniformly sized elements:						
Conditions	Helmholtz Number **k**	Modes	Real Time / number of iterations	Time Step	CPU Time	CPU Time per iteration
			s/iterations	s	m' s''	s
Run – 22	**10**	**(0,1)** Well cut-on	**0.028321 / 555**	**5.10295e-05**	**0' 10"**	**0.018018**
Run – 23	**10**	**(3,2)** Moderately cut-on	**0.031638 / 692**	**4.57204e-05**	**0' 13"**	**0.018786**
Run – 24	**10**	**(8,1)** Almost cut-off	**0.045096 / 1088**	**4.14489e-05**	**0' 20"**	**0.018382**
Run – 25	**20**	**(0,1)** Well cut-on	**0.025466 / 990**	**2.57228e-05**	**0' 32"**	**0.032323**
Run – 26	**20**	**(5,4)** Moderately cut-on	**0.027330 / 1 248**	**2.18988e-05**	**0' 49"**	**0.039263**
Run – 27	**20**	**(17,1)** Almost cut-off	**0.035265 / 1 820**	**1.93764e-05**	**1' 04"**	**0.035165**
Run – 28	**30**	**(0,1)** Well cut-on	**0.024570 / 1 479**	**1.66128e-05**	**1' 27"**	**0.058824**
Run – 29	**30**	**(9,5)** Moderately cut-	**0.025498 /**	**1.33358e-05**	**2' 02"**	**0.063808**

		on	**1 912**			
Run – 30	**30**	**(27,1) Almost cut-off**	**0.040684 / 3 405**	**1.19483e-05**	**3' 27"**	**0.060793**

B.4 3D model, zero flow

Table B.7. 3D model, zero flow – operating conditions.

Conditions	Helmholtz Number **k**	Flow	Modes	Physical Domain Size/number of elements	Buffer zone Thickness	Element Size	Element Order Max/Min, mean	Degrees of Freedom
Run – 09	**20**	**0.0**	**(5,4)**	**3R / 131 311**	**3.23λ**	**~1 el./λ**	**7/4, 5.13**	**27 813 376**
Run – 10	**20**	**0.0**	**(5,4)**	**3R / 936 279**	**3.23λ**	**~2 el./λ**	**5/3, 3.84**	**114 542 896**
Run – 11	**20**	**0.0**	**(5,4)**	**3R / 479 185**	**3.23λ**	**~4 el./λ – duct ~1 el./λ – elsewhere**	**7/2, 3.77**	**58 675 960**
Run – 12	**20**	**0.0**	**(17,1)**	**3R / 479 185**	**3.23λ**	**~4 el./λ – duct ~1 el./λ – elsewhere**	**7/2, 3.77**	**58 675 960**
Run – 13	**20**	**0.0**	**(17,1)**	**3R / 543 076**	**3.23λ 6.46λ - admission zone**	**~4 el./λ – duct ~1 el./λ – elsewhere**	**7/2, 3.68**	**63 499 872**

Table B.8. 3D model, zero flow – convergence information.

Conditions	Helmholtz Number **kR**	Modes	Real Time / number of iterations	Time Step	CPU Time	CPU Time per iteration
			s/iterations	s		s
Run – 09	**20**	**(5,4) Moderately cut-on**	**0.031356 / 3762**	**8.33485e-06**	**2h 42m 37s**	**2.5**
Run – 10	**20**	**(5,4) Moderately cut-on**	**0.030722 / 5070**	**6.06075e-06**	**18h 43m 16s**	**11**

Run – 11	**20**	**(5,4) Moderately cut-on**	**0.030628 / 4732**	**6.47397e-06**	**8h 45m 21s**	**6**
Run – 12	**20**	**(17,1) Almost cut-off**	**0.037795 / 5838**	**6.47397e-06**	**10h 59m 51s**	**6.5**
Run – 13	**20**	**(17,1) Almost cut-off**	**0.038367 / 6525**	**5.88005e-06**	**19h 11m 09s**	**8**

B.5 The effects of the mean flow

Table B.9. The effects of the mean flow. 3D model, Uniform steady flow – Operating conditions.

Conditions	Helmholtz Number **kR**	Flow	Modes	Physical Domain Size/number of elements	Buffer zone Thickness	Element Size	Element Order Max/Min, mean	Degrees of Freedom
Uniform Inflow	20 (1083Hz)	0.1	(17,1)	3R / 374215	3.23λ	~4 el./mode at duct wall ~1 el./λ – elsewhere	7/3, 4.24	57 082 044
Uniform Inflow	20 (1083Hz)	0.4	(17,1)	3R / 374215	3.23λ	~4 el./mode at duct wall ~1 el./λ – elsewhere	9/3, 5.37	96 835 016
Uniform Inflow	20 (1083Hz)	0.6	(17,1)	3R / 374215	3.23λ	~4 el./mode at duct wall ~1 el./λ – elsewhere	13/4, 6.80	169 656 988
Uniform Outflow	20 (1083Hz)	0.1	(17,1)	3R / 374215	3.23λ	~4 el./mode at duct wall ~1 el./λ – elsewhere	7/3, 4.24	57 082 044

Uniform Outflow	20 (1083Hz)	0.4	(17,1)	3R / 374215	3.23λ	~4 el./mode at duct wall ~1 el./λ – elsewhere	9/3, 5.37	96 835 016
Uniform Outflow	20 (1083Hz)	0.6	(17,1)	3R / 374215	3.23λ	~4 el./mode at duct wall ~1 el./λ – elsewhere	13/4, 6.80	169 656 988

Table B.10. The effects of the mean flow. 3D model, Uniform steady flow – Convergence information.

Conditions	Helmholtz Number **kR**	Modes	Real Time / number of iterations	Time Step	CPU Time	CPU Time per iteration
			s/iterations	s		s
Uniform Inflow, Mn = 0.1	20 (1083Hz)	(17,1) Almost cut-off	0.037883 / 6047	6.26469e-06	Re-run	~6
Uniform Inflow, Mn = 0.4	20 (1083Hz)	(17,1) Almost cut-off	0.037396 / 10712	3.49105e-06	1d 10h 15m 18s	~11
Uniform Inflow, Mn = 0.6	20 (1083Hz)	(17,1) Almost cut-off	0.042772 / 20460	2.09054e-06	6d 20h 55m 54s	~29
Uniform outflow, Mn = 0.1	20 (1083Hz)	(17,1) Almost cut-off	0.035959 / 5740	6.26469e-06	09h 33m 58s	~6
Uniform outflow, Mn = 0.4	20 (1083Hz)	(17,1) Almost cut-off	0.029681 / 8502	3.49105e-06	1d 03h 13m 22s	~12
Uniform outflow, Mn = 0.6	20 (1083Hz)	(17,1) Almost cut-off	0.032010 / 15312	2.09054e-06	5d 03h 02m 17s	~29

Table B.11. The effects of the mean flow. 2D model, Uniform steady inflow – Operating conditions.

Conditions	Helmholtz Number **k**	Flow	Modes	Physical Domain Size/number of elements	Buffer zone Thickness	Element Size	Element Order Max/Min, mean	Degrees of Freedom
Uniform Inflow	20 (1083Hz)	0.1	(0,1)	3R / 2022	3.23λ	~4 el./mode at duct wall ~1 el./λ – elsewhere	6/3, 3.90	251 308
Uniform Inflow	20 (1083Hz)	0.1	(5,4)	3R / 2022	3.23λ	~4 el./mode at duct wall ~1 el./λ – elsewhere	6/3, 3.90	251 308
Uniform Inflow	20 (1083Hz)	0.1	(17,1)	3R / 2022	3.23λ	~4 el./mode at duct wall ~1 el./λ – elsewhere	6/3, 3.90	251 308
Uniform Inflow	20 (1083Hz)	0.4	(0,1)	3R / 2022	3.23λ	~4 el./mode at duct wall ~1 el./λ – elsewhere	7/3, 4.82	395 396
Uniform Inflow	20 (1083Hz)	0.4	(5,4)	3R / 2022	3.23λ	~4 el./mode at duct wall ~1 el./λ – elsewhere	7/3, 4.82	395 396

Uniform Inflow	20 (1083Hz)	0.4	(17,1)	3R / 2022	3.23λ	~4 el./mode at duct wall ~1 el./λ – elsewhere	7/3, 4.82	395 396
Uniform Inflow	20 (1083Hz)	0.6	(0,1)	3R / 2022	3.23λ	~4 el./mode at duct wall ~1 el./λ – elsewhere	9/4, 6.05	669 764
Uniform Inflow	20 (1083Hz)	0.6	(5,4)	3R / 2022	3.23λ	~4 el./mode at duct wall ~1 el./λ – elsewhere	9/4, 6.05	669 764
Uniform Inflow	20 (1083Hz)	0.6	(17,1)	3R / 2022	3.23λ	~4 el./mode at duct wall ~1 el./λ – elsewhere	9/4, 6.05	669 764

Table B.12. The effects of the mean flow. 2D model, Uniform steady inflow – Convergence information.

Conditions	Helmholtz Number **kR**	Modes	Real Time / number of iterations	Time Step	CPU Time	CPU Time per iteration
			s/iterations	s		s
Uniform Inflow, Mn = 0.1	20 (1083Hz)	(0,1) Well cut-on	0.021375 / 1673	1.27766e-05	03m 59s	< 1
Uniform Inflow, Mn = 0.1	20 (1083Hz)	(5,4) Moderately cut-on	0.030108 / 2768	1.08772e-05	06m 03s	< 1
Uniform Inflow, Mn = 0.1	20 (1083Hz)	(17,1) Almost cut-off	0.037766 / 3924	9.62432e-06	09m 33s	< 1

Uniform Inflow, Mn = 0.4	20 (1083Hz)	(0,1) Well cut-on	0.028187 / 4082	6.9053e-06	11m 11s	< 1
Uniform Inflow, Mn = 0.4	20 (1083Hz)	(5,4) Moderately cut-on	0.035802 / 6090	5.87876e-06	16m 48s	< 1
Uniform Inflow, Mn = 0.4	20 (1083Hz)	(17,1) Almost cut-off	0.037582 / 7225	5.20161e-06	18m 50s	< 1
Uniform Inflow, Mn = 0.6	20 (1083Hz)	(0,1) Well cut-on	0.040115 / 9020	4.44733e-06	30m 57s	< 1
Uniform Inflow, Mn = 0.6	20 (1083Hz)	(5,4) Moderately cut-on	0.044980 / 11880	3.78619e-06	41m 20s	< 1
Uniform Inflow, Mn = 0.6	20 (1083Hz)	(17,1) Almost cut-off	0.042693 / 12744	3.35008e-06	42m 36s	< 1

Table B.13. The effects of the mean flow. 2D model, Uniform steady outflow – Operating conditions.

Conditions	Helmholtz Number **kR**	Flow	Modes	Physical Domain Size/number of elements	Buffer zone Thickness	Element Size	Element Order Max/Min, mean	Degrees of Freedom
Uniform Outflow	20 (1083Hz)	0.1	(0,1)	3R / 2022	3.23λ	~4 el./mode at duct wall ~1 el./λ – elsewhere	6/3, 3.90	251 308
Uniform Outflow	20 (1083Hz)	0.1	(5,4)	3R / 2022	3.23λ	~4 el./mode at duct wall ~1 el./λ – elsewhere	6/3, 3.90	251 308
Uniform Outflow	20 (1083Hz)	0.1	(17,1)	3R / 2022	3.23λ	~4 el./mode at duct wall ~1 el./λ – elsewhere	6/3, 3.90	251 308

Uniform Outflow	20 (1083Hz)	0.4	(0,1)	3R / 2022	3.23λ	~4 el./mode at duct wall ~1 el./λ – elsewhere	7/3, 4.82	395 396
Uniform Outflow Order = 13	*20 (1083Hz)*	*0.4*	*(0,1)*	*3R / 2022*	*3.23λ*	*~4 el./mode at duct wall ~1 el./λ – elsewhere*	*13/13, 13*	*3 996 160*
Uniform Outflow	20 (1083Hz)	0.4	(5,4)	3R / 2022	3.23λ	~4 el./mode at duct wall ~1 el./λ – elsewhere	7/3, 4.82	395 396
Uniform Outflow	20 (1083Hz)	0.4	(17,1)	3R / 2022	3.23λ	~4 el./mode at duct wall ~1 el./λ – elsewhere	7/3, 4.82	395 396
Uniform Outflow	20 (1083Hz)	0.6	(0,1)	3R / 2022	3.23λ	~4 el./mode at duct wall ~1 el./λ – elsewhere	9/4, 6.05	669 764
Uniform Outflow Order = 13	*20 (1083Hz)*	*0.6*	*(0,1)*	*3R / 2022*	*3.23λ*	*~4 el./mode at duct wall ~1 el./λ – elsewhere*	*13/4, 10.98*	*2 982 284*
Uniform Outflow	20 (1083Hz)	0.6	(5,4)	3R / 2022	3.23λ	~4 el./mode at duct wall ~1 el./λ – elsewhere	9/4, 6.05	669 764

Uniform Outflow	20 (1083Hz)	0.6	(17,1)	3R / 2022	3.23λ	~4 el./mode at duct wall ~1 el./λ – elsewhere	9/4, 6.05	669 764

Table B.14. The effects of the mean flow. 2D model, Uniform steady outflow – Convergence information.

Conditions	Helmholtz Number **kR**	Modes	Real Time / number of iterations	Time Step	CPU Time	CPU Time per iteration
			s/iterations	s		s
Uniform Outflow, Mn = 0.1	20 (1083Hz)	(0,1) Well cut-on	0.017887 / 1400	1.27766e-05	03m 16s	< 1
Uniform Outflow, Mn = 0.1	20 (1083Hz)	(5,4) Moderately cut-on	0.028281 / 2600	1.08772e-05	05m 53s	< 1
Uniform Outflow, Mn = 0.1	20 (1083Hz)	(17,1) Almost cut-off	0.036033 / 3744	9.62432e-06	09m 05s	< 1
Uniform Outflow, Mn = 0.4	20 (1083Hz)	(0,1) Well cut-on	0.014183 / 2054	6.9053e-06	05m 45s	< 1
Uniform Outflow, Mn = 0.4 Order = 13	20 (1083Hz)	(0,1) Well cut-on	0.013697 / 11400	1.20152e-06	02h 58m 59s	~1
Uniform Outflow, Mn = 0.4	20 (1083Hz)	(5,4) Moderately cut-on	0.027689 / 4710	5.87876e-06	12m 24s	< 1
Uniform Outflow, Mn = 0.4	20 (1083Hz)	(17,1) Almost cut-off	0.029712 / 5712	5.20161e-06	18m 56s	< 1
Uniform Outflow, Mn = 0.6	20 (1083Hz)	(0,1) Well cut-on	0.019212 / 4320	4.44733e-06	15m 14s	< 1

Uniform Outflow, Mn = 0.6 Order = 13	20 (1083Hz)	(0,1) Well cut-on	0.016401 / 14499	1.1312e-06	02h 59m 12s	~1
Uniform Outflow, Mn = 0.6	20 (1083Hz)	(5,4) Moderately cut-on	0.029532 / 7800	3.78619e-06	26m 08s	< 1
Uniform Outflow, Mn = 0.6	20 (1083Hz)	(17,1) Almost cut-off	0.031930 / 9531	3.35008e-06	32m 52s	< 1

Table B.15. The effects of the mean flow. 2D model, Non Uniform turbulent outflow – Operating conditions.

Conditions	Helmholtz Number **kR**	Flow	Modes	Physical Domain Size/number of elements	Buffer zone Thickness	Element Size	Element Order Max/Min, mean	Degrees of Freedom
Standard size of physical domain								
Non-Uniform Outflow	20 (1083Hz)	0.4-jet 0.1 amb.	**(0,1)**	**3R / 2022**	**3.23λ**	**~4 el./mode at duct wall ~1 el./λ – elsewhere**	**7/3, 4.2035**	**297868**
Non-Uniform Outflow	20 (1083Hz)	0.4-jet 0.1 amb.	**(5,4)**	**3R / 2022**	**3.23λ**	**~4 el./mode at duct wall ~1 el./λ – elsewhere**	**7/3, 4.2035**	**297868**
Non-Uniform Outflow	20 (1083Hz)	0.4-jet 0.1 amb.	**(17,1)**	**3R / 2022**	**3.23λ**	**~4 el./mode at duct wall ~1 el./λ – elsewhere**	**7/3, 4.2035**	**297868**

B Parameters used in the validation of the DG method

13 x longer physical domain								
Non-Uniform Outflow	20 (1083Hz)	0.4-jet 0.1 amb.	(0,1)	3R L=13R/ 4645	3.23λ	~4 el./mode at duct wall ~1 el./λ – elsewhere	7/3, 4.5529	821772
Non-Uniform Outflow	20 (1083Hz)	0.4-jet 0.1 amb.	(5,4)	3R L=13R/ 4645	3.23λ	~4 el./mode at duct wall ~1 el./λ – elsewhere	7/3, 4.5529	821772
Non-Uniform Outflow	20 (1083Hz)	0.4-jet 0.1 amb.	(17,1)	3R L=13R/ 4645	3.23λ	~4 el./mode at duct wall ~1 el./λ – elsewhere	7/3, 4.5529	821772
26 x longer physical domain								
Non-Uniform Outflow	20 (1083Hz)	0.4-jet 0.1 amb.	(0,1)	3R L=26R/ 7151	3.23λ	~4 el./mode at duct wall ~1 el./λ – elsewhere	7/3, 4.6245	1301136
Non-Uniform Outflow	20 (1083Hz)	0.4-jet 0.1 amb.	(5,4)	3R L=26R/ 7151	3.23λ	~4 el./mode at duct wall ~1 el./λ – elsewhere	7/3, 4.6245	1301136
Non-Uniform Outflow	20 (1083Hz)	0.4-jet 0.1 amb.	(17,1)	3R L=26R/ 7151	3.23λ	~4 el./mode at duct wall ~1 el./λ – elsewhere	7/3, 4.6245	1301136

Table B.16. The effects of the mean flow. 2D model, Non Uniform turbulent outflow – Convergence information.

Conditions	Helmholtz Number **kR**	Modes	Real Time / number of iterations	Time Step	CPU Time	CPU Time per iteration
			s/iterations	s		s
Standard size of physical domain						
Non-Uniform Outflow, Mn = 0.4 / 0.1	20 (1083Hz)	(0,1) Well cut-on	0.015807 / 2124	7.44187e-06	06m 05s	<1
Non-Uniform Outflow, Mn = 0.4 / 0.1	20 (1083Hz)	(5,4) Moderately cut-on	0.040978 / 6468	6.33556e-06	17m 03s	<1
Non-Uniform Outflow, Mn = 0.4 / 0.1	20 (1083Hz)	(17,1) Almost cut-off	0.046640 / 8320	5.60580e-06	23m 01s	<1
13 x longer physical domain						
Non-Uniform Outflow, Mn = 0.4 / 0.1	20 (1083Hz)	(0,1) Well cut-on	0.054551 / 6776	8.05066e-06	01h 27m 23s	<1
Non-Uniform Outflow, Mn = 0.4 / 0.1	20 (1083Hz)	(5,4) Moderately cut-on	0.039293 / 5733	6.85385e-06	39m 50s	<1
Non-Uniform Outflow, Mn = 0.4 / 0.1	20 (1083Hz)	(0,1) Well cut-on	0.054551 / 6776	8.05066e-06	01h 27m 23s	<1

B Parameters used in the validation of the DG method

26 x longer physical domain						
Non-Uniform Outflow, Mn = 0.4 / 0.1	20 (1083Hz)	(0,1) Well cut-on	0.079896 / 9440	8.46352e-06	02h 24m 10s	<1
Non-Uniform Outflow, Mn = 0.4 / 0.1	20 (1083Hz)	(5,4) Moderately cut-on	0.081017 / 11244	7.20533e-06	02h 20m 25s	<1
Non-Uniform Outflow, Mn = 0.4 / 0.1	20 (1083Hz)	(17,1) Almost cut-off	0.222603 / 34916	6.37538e-06	06h 45m 15s	<1

C A further investigation of inaccurate impedance modelling in the time domain

The problem of the inaccuracy of the liner model implemented in Actran DGM reported in sections 5.3.1 and 5.4.2.3 is further investigated for a straight unflanged cylindrical duct in the presence of a uniform mean flow. This is performed to verify the hypothesis that the Myers boundary condition is the main issue in the current implementation of the liner model. The simplification of the model is made to eliminate influence of the wall curvature and the mean flow non-uniformity. The physical problem is illustrated in figure C.1. The duct has negligible thickness. The outer radius of the duct corresponds to that of the generic intake at the fan plane described in section 5.4. The acoustic field is excited by a single incident mode travelling along the duct against the mean flow. The liner is placed in the middle section of the duct. The problem is modelled as a 2D-axisymmetric. The DGM results are compared to Actran TM solutions. As already mentioned in section 5.4, Actran TM has been validated for similar intake problems.

The numerical models for the acoustics analyses are constructed according to the description given in section 3.4. The impedance ($Z = \rho_0 c_0(2.06 - 0.02\mathrm{i})$ at 1300 Hz) and length of the liner are these used in the generic intake (see section 5.4). A single incident mode (24,1) at kR_{fan} = 30 with unit intensity is applied. Since uniform mean flows are only used in the acoustics analyses, no mean flow calculations are needed, and the mean flow velocity is set directly at the CAA mesh nodes (see section 3.3).

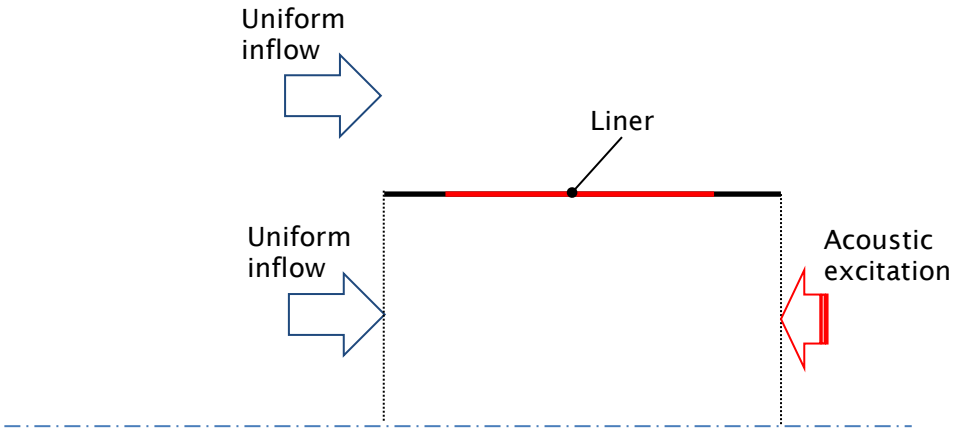

Figure C.1: A physical model of noise propagation and radiation from a straight cylindrical duct.

Two uniform mean flows corresponding to Mach numbers of 0.25 and 0.56 are considered in this study. These correspond to the mean flow Mach numbers at the fan plane and in the ambient used in the generic intake. Total pressure and temperature remain unchanged, i.e. p_{tot} = 101.5 kPa and T_{tot} = 288K.

The computational mesh dedicated for Actran TM calculations is shown in figure C.2 (a). It is unstructured mesh, created by a combination of triangular and quadrilateral quadratic finite elements.

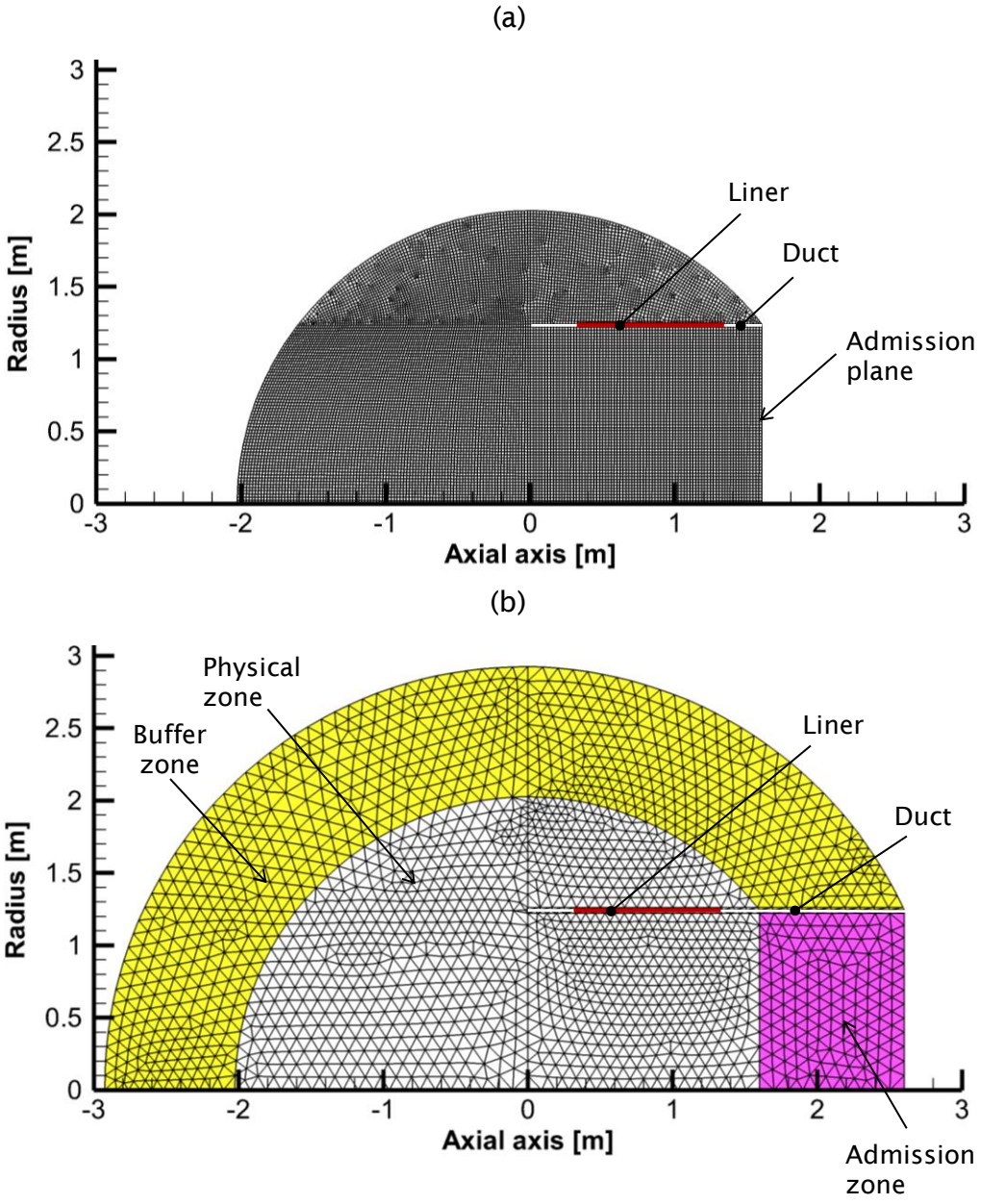

Figure C.2: Computational meshes used by (a) Actran TM and (b) Actran DGM for the investigation of inaccurate impedance modelling in the time domain when a straight cylindrical duct with uniform mean flow is considered.

The refinement is approximately 6 elements per upstream wavelength for the case of the higher mean flow Mach number. The numerical model has 60,199 degrees of freedom (NDOF). The mesh used by Actran DGM is shown in figure C.2 (b). It consists of physical zone, admission zone and buffer zone (see section 3.4 for details). This is unstructured mesh containing only triangular elements. The minimum mesh refinement is approximately 3-4 and 1-2 elements per upstream wavelength for the mean flows set to the Mach number of 0.25 and 0.56, respectively. The mesh is further refined along the liner. This gives element orders in the range from 2 to 4 for the mean flow Mach number 0.25, and in the range from 3 to 6 for the mean flow Mach number 0.56. The model sizes are 397,560 and 712,236 degrees of freedom, respectively, for the Mach numbers of 0.25 and 0.56. The length of the admission and buffer zones corresponds to approximately 9 and 4 axial upstream wavelengths, respectively, for the lower and higher mean flow velocity cases.

Results of the SPL along the wall for the lined duct are shown in figure C.3 for the mean flow set to Mach numbers of 0.25.

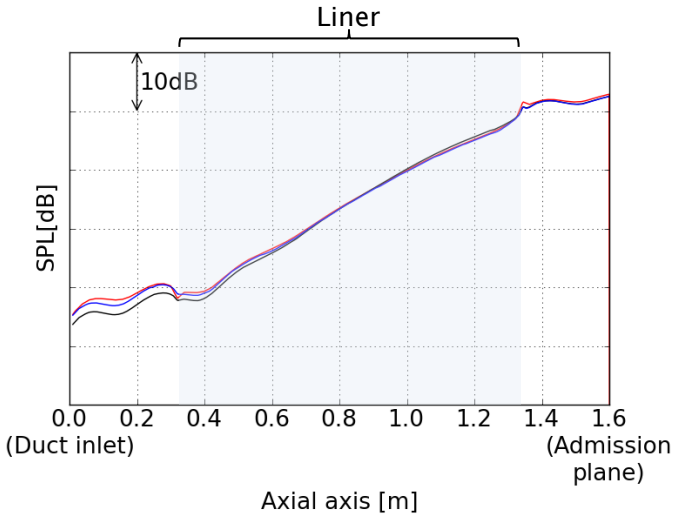

Figure C.3: Comparison of the SPL along the duct wall between Actran TM and DGM, both with Myers boundary condition, for lined ($Z = \rho_0 c_0(2.06 - 0.02\mathrm{i})$ at 1300 Hz) case with the uniform mean flow of Mach number 0.25. A single incident mode (24,1) with kR_{fan} = 30. Solid red line: Actran TM solution; solid black line: Actran DGM solution obtained with default settings of the liner model; solid blue line: Actran DGM solution obtained with 4 times reduced radius in the spatial filter used in the liner model.

The discrepancies, i.e. the inaccuracy along the liner and at the end of the liner, between Actran TM and DGM solutions reported in section 5.3.1 for a cylindrical duct with uniform liner are also captured here when the DGM with default settings of the liner model is used. Although the differences now are less pronounce, e.g. 2dB at the end of the liner instead of 5dB. In order to verify the statement made in section 5.3.1 that the discrepancies can be attributed to the spatial filtering applied in Actran DGM, we now perform the DGM calculation with 4 times reduced radius which determines the area used in the spatial filter applied in the liner model (see section 2.7.6 for details). This is the smallest value of the radius which gives a stable DGM solution. The SPL comparison along the duct wall shown in figure C.3 confirms clearly that much better accuracy can be obtained when less stringent spatial filtering is applied. Very good agreement is now achieved in terms of the predicted rate of attenuation and the SPL value at the end of the liner. The maximum observed (local) discrepancy is below 1dB. Furthermore, the rapid increase in the SPL at the end of the liner is now well captured by the DGM.

The next step is then to increase the mean flow velocity to obtain the mean flow Mach number 0.56.

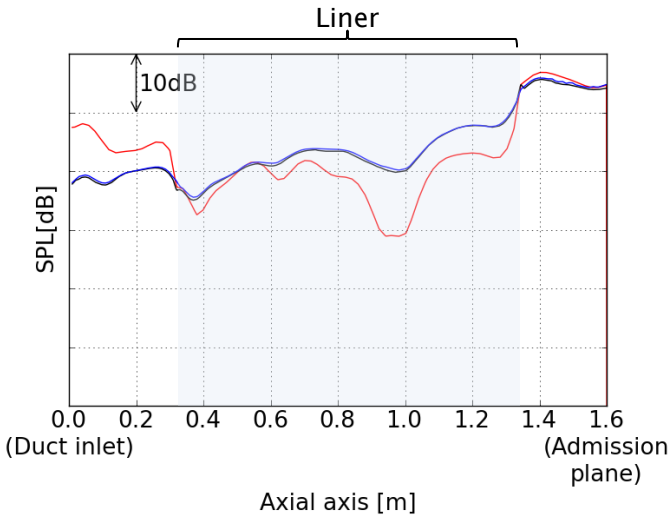

Figure C.4: Comparison of the SPL along the duct wall between Actran TM and DGM, both with Myers boundary condition, for lined ($Z = \rho_0 c_0(2.06 - 0.02\mathbf{i})$ at 1300 Hz) case with the uniform mean flow of Mach number 0.56. A single incident mode (24,1) with kR_{fan} = 30. Solid red line: Actran TM solution; solid black line: Actran DGM solution obtained with default settings of the liner model; solid blue line: Actran DGM solution obtained with default settings of the liner model and refined 4 times mesh along the liner.

This is achieved by changing the aerodynamic parameters of the mean flow. The numerical models used by Actran TM and DGM remain unchanged. The SPL comparisons between Actran TM and DGM along the duct wall are shown in figure C.4. In the case of the higher mean flow velocity, significantly larger discrepancies along the liner are observed. This behaviour seems to be justified, since the convective term in the Myers boundary condition contains the mean flow velocity vector. The general character of the DGM solution along the liner agrees well with that obtained in section 5.4.2.3 for the lined generic intake. All features reported for the generic intake are captured here as well, i.e. the inaccuracy of approximately 5 to 10 dB along the liner and the discrepancies at the liner discontinuities, particularly at the end of the liner. However, the discrepancy at the end of the liner is much smaller in the straight duct. This can be explained by the fact that the mean flow velocity is much higher (Mach number of approximately 0.7) at the end of the liner in the generic intake.

In the case of the mean flow with the Mach number of 0.56, despite many attempts, a stable solution has not been obtained for reduced local area used in the spatial filter applied in the liner model. Therefore, the accuracy of the liner model, when less stringent spatial filtering is applied, has not been assessed in this case.

Finally, we verify the accuracy of the liner model for the mean flow with the Mach number of 0.56 when a very fine mesh is used along the liner. This is performed to avoid the high-order spatial discretisation along the liner and to minimize the discontinuities between the element faces which belong to the liner (for more details on the liner model see section 2.7.6). Actran DGM mesh generated for this study is shown in figure C.5. The only difference, when compared to the initial DGM mesh, is that the mesh is 4 times refined along the liner. This gives element orders in the range from 1 to 6, and the model now has 919,704 degrees of freedom. The SPL comparison between the DGM results obtained with different mesh resolutions along the liner is shown in figure C.4. The comparison clearly shows no influence of the mesh refinement on the accuracy of the liner model.

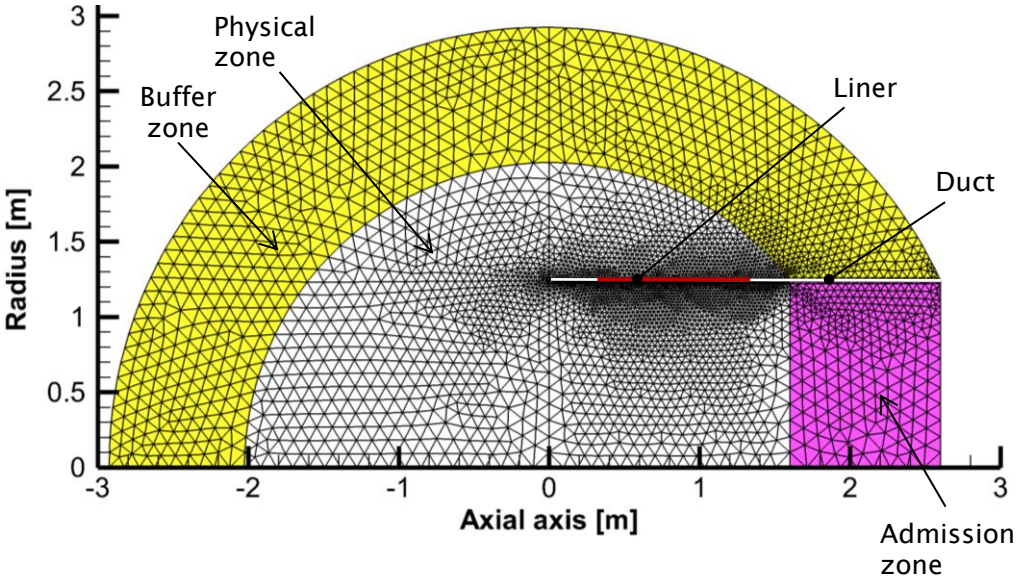

Figure C.5: The computational mesh with the 4-times refinement along the liner used by Actran DGM for the investigation of inaccurate impedance modelling in the time domain when a straight cylindrical duct with uniform mean flow is considered.

D Acoustic intensity for homentropic and irrotational mean flows

In the case of source-free region, the acoustic total energy is conserved and the following relation is satisfied

$$\frac{\partial \mathrm{E}}{\partial \mathrm{t}} + \boldsymbol{\nabla} \cdot \mathbf{I} = 0. \tag{D.1}$$

For homentropic and irrotational mean flows, the acoustic energy density E and intensity can be defined as follows [178];

$$\mathbf{I} = \left(\frac{p'}{\rho_0} + \boldsymbol{u}' \cdot \boldsymbol{u}_0\right)\left(\rho_0 \boldsymbol{u}' + \frac{p'}{{c_0}^2}\boldsymbol{u}_0\right), \tag{D.2}$$

and

$$\mathrm{E} = \frac{p'^2}{2\rho_0 {c_0}^2} + \frac{\rho_0 \boldsymbol{u}'^2}{2} + \rho'(\boldsymbol{u}' \cdot \boldsymbol{u}_0). \tag{D.3}$$

If the flow is steady or periodic and free from acoustic sources the average of the energy (equation (D.1)) over time implies that

$$\boldsymbol{\nabla} \cdot \bar{\boldsymbol{I}} = 0, \tag{D.4}$$

where $\bar{\boldsymbol{I}}$ is the time-averaged acoustic intensity.

Hence, we find that the acoustic power crossing any surface S is defined by

$$P = \int_S \bar{\boldsymbol{I}} \cdot \boldsymbol{n} dS. \tag{D.5}$$

The time-averaged acoustic intensity over a period is given by

$$\bar{\boldsymbol{I}}(\boldsymbol{x}) = \frac{1}{T}\int_T \mathbf{I}(\boldsymbol{x}, t)\mathrm{dt}. \tag{D.6}$$

Therefore the acoustic intensity given by Eq. (D.2) can be averaged in time according to

$$\bar{\boldsymbol{I}}(\boldsymbol{x}) = \frac{1}{T}\int_{T}\left(\frac{p'}{\rho_0} + \boldsymbol{u}'\cdot\boldsymbol{u}_0\right)\left(\rho_0\boldsymbol{u}' + \frac{p'}{{c_0}^2}\boldsymbol{u}_0\right)\mathrm{dt}. \tag{D.7}$$

Note that flow and acoustic quantities are physical. This implies that in the time domain they exist only in the real half of the complex domain. The acoustic quantities are given by Eq. (2.16). Applying some trigonometry rules and using the fact that the average of the fluctuating power over a period is zero, it can be shown that in the frequency domain the acoustic intensity for the homentropic and irrotational flows is given by

$$\bar{\boldsymbol{I}}(\boldsymbol{x}) = \frac{1}{2}\left[\mathrm{Re}\{\tilde{p}\tilde{\boldsymbol{u}}^*\} + \rho_0\mathrm{Re}\{(\boldsymbol{u}_0\cdot\tilde{\boldsymbol{u}})\tilde{\boldsymbol{u}}^*\} + \frac{1}{{c_0}^2}\,\boldsymbol{u}_0(\boldsymbol{u}_0\cdot\mathrm{Re}\{\tilde{p}\tilde{\boldsymbol{u}}^*\}) + \frac{1}{{c_0}^2\rho_0}\boldsymbol{u}_0|\tilde{p}|^2\right]. \tag{D.8}$$

Bibliography

[1] “Annex 16 — Environmental Protection.Volume I — Aircraft Noise,” International Civil Aviation Organization, Montreal, 2008.

[2] M. J. Smith, Aircraft Noise, Cambridge: Cambridge University Press, 1989.

[3] “Getting to grips with aircraft noise,” Airbus Customer Services: Flight Operations Support & Line Assistance, Blagnac, 2003.

[4] J. Bottcher, “International Civil Aviation Organization (ICAO),” 20-21 October 2004. [Online]. Available: legacy.icao.int/icao/en/atb/.../BIP_2_2_jb.pdf . [Accessed 16 January 2012].

[5] “Advisory Council for Aeronautics Research in Europe (ACARE),” [Online]. Available: http://www.acare4europe.com/. [Accessed 16 January 2012].

[6] “Flightpath 2050 Europe’s Vision for Aviation,” Publications Office of the European Union, Luxembourg, 2011.

[7] “Rolls-Royce,” [Online]. Available: http://www.rolls-royce.com/reports/environment_report_07/reducing-en-impact/noise-reduction.html. [Accessed 16 January 2012].

[8] The Jet Engine 5th edition, Rolls Royce Technical Publications, 2005.

[9] “ICAO Environmental Report, Aviation and Climate Change,” International Civil Aviation Organization, Montreal, 2010.

[10] J. F. Groeneweg, T. G. Sofrin, E. J. Rice and P. R. .. Gliebe, “Turbomachinery Noise,” in *Aeroacoustics of Flight Vehicles: Theory and Practice, Vol. 1: Noise Sources*, Woodbury, Acoustical Society of America, 1995, pp. 151-209.

[11] W. Eversman, “Theoretical Models for Duct Acoustic Propagation and Radiation,” in *Aeroacoustics of Flight Vehicles: Theory and Practice, Vol. 2: Noise Control*, Woodbury, Acoustical Society of America, 1994, pp. 101-163.

[12] J. Tyler and T. Sofrin, “Axial flow compressor noise studies,” *Transactions*

of SAE, vol. 70, p. 209–332, 1962.

[13] P. F. Joseph and M. G. Smith, “Aircraft noise,” in *Advanced Applications in Acoustics, Noise and Vibration*, London, Spon Press, 2004, pp. 292-346.

[14] U. W. Ganz, “Boeing 18-inch Fan Rig Broadband Noise Test (NASA / CR-1998-208704),” Langley Research Center, Hampton, 1998.

[15] P. Joseph and A. Parry, “Rotor/wall boundary layer interaction broadband noise in turbofan engines,” in *7th AIAA/CEAS Aeroacoustics Conference*, Maastricht, 2001.

[16] G. M. Lilley, “Jet Noise Classical Theory and Experiments,” in *Aeroacoustics of Flight Vehicles: Theory and Practice, Vol. 1: Noise Sources*, Woodbury, Acoustical Society of America, 1995, pp. 211-289.

[17] C. K. W. Tam, “Jet Noise Generated by Large-Scale Coherent Motion,” in *Aeroacoustics of Flight Vehicles: Theory and Practice, Vol. 1: Noise Sources*, Woodbury, Acoustical Society of America, 1995, pp. 311-390.

[18] C. Tam and M. Golebiowski, “On the Two Components of Turbulent Mixing Noise from Supersonic Jets,” *AIAA Paper,* pp. 96-1716, 1996.

[19] C. K. Tam, “Jet Noise: Since 1952,” *Theoretical and Computational Fluid Dynamics,* vol. 10, p. 393–405, 1998.

[20] M. . J. Fisher, G. A. Preston and C. . J. Mead, “A modelling of the noise from simple coaxial jets part II: With heated primary flow,” *Journal of Sound and Vibration,* vol. 209, p. 405–417, 1998.

[21] J. R. Mahan and A. Karchmer, “Combustion and Core Noise,” in *Aeroacoustics of Flight Vehicles: Theory and Practice, Vol. 1: Noise Sources*, Woodbury, Acoustical Society of America, 1995, pp. 483-517.

[22] E. Envia, A. G. Wilson and D. L. Huff, “Fan Noise: A Challenge to CAA,” *International Journal of Computational Fluid Dynamics,* vol. 18, no. 6, pp. 471-480, 2004.

[23] J. Coupland, A. Wilson, N. Pollard, S. Uellenberg, C. Breard and J. Diamond, “Demonstration of a CFD-CAA Methodology to Predict Buzz-Saw Noise Propagation to the Aircraft,” in *13th AIAA/CEAS Aeroacoustics Conference (28th AIAA Aeroacoustics Conference)*, Rome, Italy, 2007.

[24] R. Self, “Jet noise prediction using the Lighthill acoustic analogy,” *Journal of Sound and Vibration,* vol. 275, p. 757–768, 2004.

[25] D. Bodony and S. Lele, “On the current status of jet noise predictions using large-eddy simulations,” *AIAA Journal ,* vol. 46, pp. 364-380, 2008.

[26] A. Uzun and M. Y. Hussaini, “High-Fidelity Numerical Simulations of a Round Nozzle Jet Flow,” in *16th AIAA/CEAS Aeroacoustics Conference*, 2010.

[27] W. Liu, J. W. Kim, X. Zhang, D. Angland and B. Caruelle, “Landing-gear noise prediction using high-order finite difference schemes,” *Journal of Sound and Vibration,* vol. 332, p. 3517–3534, 2013.

[28] C. K. W. Tam and J. C. Webb, “Dispersion-relation-preserving finite difference schemes for computational acoustics,” *Journal of Computational Physics,* vol. 107, p. 262–281, 1993.

[29] C. K. Tam, “Computational Aeroacoustics: An Overview of Computational Challenges and Applications,” *Intemational Joumal of Computational Fluid Dynamics,* vol. 18, no. 6, pp. 547-567, 2004.

[30] G. Ashcroft and X. Zhang, “Optimized prefactored compact schemes,” *Journal of Computational Physics,* vol. 190, p. 459–477, 2003.

[31] B. Van Antwerpen, R. Leneveu, S. Caro and P. Ferrante, “New advances in the use of Actran/TM for nacelle simulations,” in *14th AIAA/CEAS Aeroacoustics Conference*, Vancouver, 2008.

[32] K. S. Brentner and F. Farassat, “An analytical comparison of the acoustic analogy and Kirchhoff formulation for moving surfaces,” *AIAA Journal,* vol. 36, p. 1379–1386, 1998.

[33] J. Ffowcs Williams and D. Hawkings, “Sound generation by turbulence and surfaces in arbitrary motion,” *Philosophical Transactions of the Royal Society,* vol. 264, no. Ser. A,, p. 321 – 342, 1969.

[34] F. Farassat and G. P. Succi, “The prediction of helicopter rotor discrete frequency noise,” *Vertica,* vol. 7, no. 4, p. 309–320, 1983.

[35] R. J. Astley, “Numerical methods for noise propagation in moving flows, with application to turbofan engines,” *The Acoustical Society of Japan,* vol. 30, no. 4, 2009.

[36] I. D. Roy and W. Eversman, “Improved Finite Element Modeling of the Turbofan Engine Inlet Radiation Problem,” *Journal of Vibration and Acoustics,* vol. 117, no. 1, pp. 109-115, 1995.

[37] W. Eversman, “Mapped infinite wave envelope elements for acoustic radiation in a uniformly moving medium,” *Journal of Sound and Vibration,* vol. 224, no. 4, p. 665–687, 1999.

[38] J. Manera, R. Leneveu, S. Caro and J. Mardjono, “Broadband Turbomachinery Noise: Exhaust Noise Computations with Actran/TM and Actran/DGM,” in *15th AIAA/CEAS Aeroacoustics Conference*, Miami, 2009.

[39] J. Manera, G. Lielens, S. Caro, B. J. Tester and L. de Mercato, “Shear Layer Modelling with a Finite Element Model - Variants of the Munt Problems,” in *13th AIAA/CEAS Aeroacoustics Conference*, Rome, 2007.

[40] Y. Özyörük, E. Alpman, V. Ahuja and L. N. Long, “Frequency-domain prediction of turbofan noise radiation,” *Journal of Sound and Vibration,* vol. 270, pp. 933-950, 2004.

[41] Y. Özyörük and B. J. Tester, “Application of frequency-domain linearized Euler solutions to the prediction of aft fan tones and comparison with experimental measurements on model scale turbofan exhaust nozzles,” *Journal of Sound and Vibration,* vol. 330, p. 3846–3858, 2011.

[42] Y. Özyörük and V. Ahuja, “Numerical Simulation of Fore and Aft Sound Fields of a Turbofan,” *AIAA Journal,* vol. 42, no. 10, pp. 2028-2034, 2004.

[43] Y. Park, S. Kim, S. Lee and C. Cheong, “Numerical investigation on radiation characteristics of discrete-frequency noise from scarf and scoop aero-intakes,” *Applied Acoustics,* vol. 69, p. 1258–1269, 2008.

[44] N. Chevaugeon, J.-F. Remacle, X. Gallez, P. Ploumhans and S. Caro, “Efficient Discontinuous Galerkin Methods for solving acoustic problems,” in *11th AIAA/CEAS Aeroacoustics Conference*, Monterey, 2005.

[45] S. K. Lele, “Compact Finite Difference Schemes with Spectral-like Resolution,” *Journal of Computational Physics,* vol. 103, pp. 16-42, 1992.

[46] N. Schoenwald, L. Panek, C. Richter and F. Thiele, “Investigation of Sound Radiation from a Scarfed Intake by CAA-FWH Simulations using

Overset Grids," in *13th AIAA/CEAS Aeroacoustics Conference*, Rome, 2007.

[47] J. W. Kim and R. D. Sandberg, "Efficient parallel computing with a compact finite difference scheme," *Computers & Fluids,* vol. 58, p. 70–87, 2012.

[48] C. Richter, J. A. Hay, L. Panek, N. Schonwald, S. Busse and F. Thiele, "A review of time-domain impedance modelling and applications," *Journal of Sound and Vibration,* vol. 330, p. 3859–3873, 2011.

[49] Y. Reymen, M. Baelmans and W. Desmet, "On the Performance of the Quadrature-Free Discontinuous Galerkin Method on Hexahedral and Tetrahedral Grids for Linearized Euler Equations," in *14th AIAA/CEAS Aeroacoustics Conference*, Vancouver, 2008.

[50] M. Bauer, J. Dierke and R. Ewert, "Application of a Discontinuous Galerkin Method to Predict Airframe Noise (AIAA 2009-3175)," in *15th AIAA/CEAS Aeroacoustics Conference*, Miami, 2009.

[51] R. D. R. Rinaldi, A. Iob and R. Arina, "An efficient discontinuous Galerkin method for aeroacoustic propagation," *International Journal for Numerical Methods in Fluids ,* no. Published online in Wiley Online Library (wileyonlinelibrary.com). DOI: 10.1002/fld.2647, 2011.

[52] R. Leneveu, B. Schiltz, S. Laldjee and S. Caro, "Performance of a DGM scheme for LEE and applications to aircraft engine exhaust noise," in *14th AIAA/CEAS Aeroacoustics Conference*, Vancouver, 2008.

[53] A. Klöckner , T. Warburton, J. Bridge and J. S. Hesthaven, "Nodal discontinuous Galerkin methods on graphics processors," *Journal of Computational Physics,* vol. 228, no. 21, pp. 7863-7882, 2009.

[54] A. Corrigan, F. Camelli, R. Lohner and J. Wallin, "Running Unstructured Grid Based CFD Solvers on Modern Graphics Hardware," in *19th AIAA Computational Fluid Dynamics*, San Antonio, 2009.

[55] N. Gödel, N. Nunn, T. Warburton and M. Clemens, "Scalability of Higher-Order Discontinuous Galerkin FEM Computations for Solving Electromagnetic Wave Propagation Problems on GPU Clusters," *IEEE Transactions on magnetics,* vol. 46, no. 8, 2010.

[56] W. Reed and T. Hill, “Triangular mesh methods for the neutron transport equation,Tech. Report LA-UR-73-479,” Los Alamos Scientific Laboratory, 1973.

[57] H. L. Atkins, “Continued Development of the Discontinuous Galerkin Method for Computational Aeroacoustic Applications,” NASA Langley Research Center, Hampton, 1997.

[58] B. Cockburn and C. Shu, “TVB Runge-Kutta local projection discontinuous Galerkin finite element method for conservation laws II: general framework,” *Mathematics of Computation,* vol. 52, pp. 411-435, 1989.

[59] B. Cockburn, S. Lin and C. Shu, “TVB Runge-Kutta local projection discontinuous Galerkin finite element method for conservation laws III: one dimensional systems,” *Journal of Computational Physics,* vol. 84, pp. 90-113, 1989.

[60] B. Cockburn, S. Hou and C. Shu, “The Runge-Kutta local projection discontinuous Galerkin finite element method for conservation laws IV: the multidimensional case,” *Mathematics of Computation,* vol. 54, pp. 545-581, 1990.

[61] B. Cockburn and C.-W. Shu, “The Runge-Kutta discontinuous Galerkin method for conservation laws V multidimensional systems,” *Journal of Computational Physics,* vol. 141, no. 2, p. 199–224, 1998.

[62] B. Cockburn and C.-W. Shu, “Runge–Kutta Discontinuous Galerkin Methods for Convection-Dominated Problems,” *Journal of Scientific Computing,* vol. 16, no. 3, 2001.

[63] H. L. Atkins and C.-W. Shu, “Quadrature-free implementation of discontinuous Galerkin method for hyperbolic equations,” Institute for Computer Applications in Science and Engineering, Hampton, 1996.

[64] F. Q. Hu, M. Y. Hussaini and P. Rasetarineray, “An Analysis of the Discontinuous Galerkin Method for Wave Propagation Problems,” *Journal of Computational Physics ,* vol. 151, p. 921–946, 1999.

[65] F. Q. Hu and H. L. Atkins, “Eigensolution Analysis of the Discontinuous Galerkin Method with Nonuniform Grids I. One Space Dimension,” *Journal of Computational Physics,* vol. 182, pp. 516-545, 2002.

[66] F. Q. Hu and H. L. Atkins, “Two-dimensional Wave Analysis of the Discontinuous Galerkin Method with Non-Uniform Grids and Boundary Conditions,” in *8th AIAA/CEAS Aeroacoustics Conference*, Breckenridge, 2002.

[67] M. Ainsworth, “Dispersive and dissipative behaviour of high order discontinuous Galerkin finite element methods,” *Journal of Computational Physics,* vol. 198, p. 106–130, 2004.

[68] C. Peyret and P. Delorme, “Dicontinuous Galerkin Method for Computational Aeroacoustics,” in *12th AIAA/CEAS Aeroacoustics Conference*, Cambridge, Massachusetts, 2006.

[69] R. Leneveu, B. Schiltz, J. Manera and S. Caro, “Parallel DGM scheme for LEE applied to exhaust and bypass problems,” in *13th AIAA/CEAS Aeroacoustics Conference*, Rome, 2007.

[70] B. Schiltz, R. Leneveu, S. Caro, Y. Druon and A. Mosson, “Exhaust noise prediction of realistic 3D lined turbofans submitted to strong shear layers,” in *AIAA/CEAS Aeroacoustics Conference*, Miami, 2009.

[71] R. Astley, R. Sugimoto and P. Mustafi, “Computational aero-acoustics for fan duct propagation and radiation. Current status and application to turbofan liner optimisation,” *Journal of Sound and Vibration,* vol. 330, p. 3832–3845, 2011.

[72] Actran DGM 12.2 User’s Guide, Mont-Saint-Guibert: Free Field Technologies SA, 2012.

[73] G. K. Batchelor, An Introduction to Fluid Dynamics, Cambridge: Cambridge University Press, 1967.

[74] E. F. Toro, “The Equations of Fluid Dynamics,” in *Riemann solvers and numerical methods for fluid dynamics: a practical introduction, (Third Edition)*, Berlin, Springer-Verlag, 2009, pp. 1-40.

[75] M. E. Goldstein, “Aeroacoustics,” Lewis Research Center, Cleveland, 1974.

[76] S. W. Rienstra and A. Hirschberg, “An Introduction to Acoustics,” Eindhoven University of Technology, Eindhoven, 2013.

[77] W. Eversman and R. J. Beckemeyer, “Transmission of Sound in Ducts

with Thin Shear Layers—Convergence to the Uniform Flow Case," *Journal of the Acoustical Society of America,* vol. 52, no. 1, pp. 216-220, 1972.

[78] B. J. Tester, "Some aspects of "sound" attenuation in lined ducts containing inviscid mean flows with boundary layers," *Journal of Sound and Vibration,* vol. 28, no. 2, p. 217–245, 1973.

[79] K. U. Ingard, "Influence of fluid motion past a plane boundary on sound reflection, absorption, and transmission," *Journal of the Acoustical Society of America,* vol. 31, no. 7, p. 1035–1036, 1959.

[80] K. Myers, "On the acoustic boundary condition in the presence of flow," *Journal Sound and Vibration,* vol. 71, p. 429–434, 1980.

[81] S. W. Rienstra, "Impedance Models in Time Domain including the Extended Helmholtz Resonator Model," in *12th AIAA/CEAS Aeroacoustics Conference*, Cambridge, Massachusetts, 2006.

[82] K. -Y. Fung and H. Ju, "Time-domain Impedance Boundary Conditions for Computational Acoustics and Aeroacoustics," *International Journal of Computational Fluid Dynamics,* vol. 18, no. 6, pp. 503-511, 2004.

[83] Y. Özyörük and L. N. Long, "A time-domain implementation of surface acoustic impedance condition with and without flow," in *2nd AIAA/CEAS Aeroacoustics Conference, State College*, Pennsylvania, 1996.

[84] Y. Özyörük, L. N. Long and M. G. Jones, "Time-domain numerical simulation of a flow-impedance tube," *Journal of Computational Physics,* vol. 146 , no. 1, pp. 29-57 , 1998.

[85] C. K. W. Tam and L. Auriault, "Time-Domain Impedance Boundary Conditions for Computational Aeroacoustics," *AIAA Journal ,* vol. 34, no. 5, pp. 917-923, 1996.

[86] C. Richter, F. H. Thiele, X. Li and M. Zhuang, "Comparison of Time–Domain Impedance Boundary Conditions by Lined Duct Flows," in *12th AIAA/CEAS Aeroacoustics Conference*, Cambridge, Massachusetts, 2006.

[87] M. G. Jones, W. R. Watson and T. L. Parrott, "Benchmark Data for Evaluation of Aeroacoustic Propagation Codes with Grazing Flow," in *11th AIAA/CEAS Aeroacoustics Conference*, Monterey, 2005.

[88] K. -Y. Fung, H. B. Ju and B. TallaPragada, “Impedance and its time-domain extensions,” *AIAA Journal,* vol. 38, no. 1, pp. 30-38, 2000.

[89] H. Ju and K. -Y. Fung, “Time-Domain Impedance Boundary Conditions with Mean Flow Effects,” *AIAA Journal,* vol. 39, no. 9, pp. 1683-1690, 2001.

[90] Y. Reymen, M. Baelmans and W. Desmet, “Time-Domain Impedance Formulation based on Recursive Convolution,” in *12th AIAA/CEAS Aeroacoustics Conference (27th AIAA Aeroacoustics Conference)*, Cambridge, 2006.

[91] X. Y. Li, X. D. Li and C. K. Tam, “Construction and Validation of a Broadband Time Domain Impedance Boundary Condition (AIAA 2011-2870),” in *17th AIAA/CEAS Aeroacoustics Conference*, Portland, 2011.

[92] N. Chevaugeon, J.-F. Remacle and X. Gallez, “Discontinuous Galerkin Implementation Of The Extended Helmholtz Resonator Model In Time Domain,” in *12th AIAA/CEAS Aeroacoustics Conference*, Cambridge, Massachusetts, 2006.

[93] Actran 12.2 User’s Guide, Mont-Saint-Guibert: Free Field Technologies SA, 2012.

[94] B. J. Tester, C. J. Powles, N. J. Baker and A. J. Kempton, “Scattering of Sound by Liner Splices: A Kirchhoff Model with Numerical Verification,” *AIAA Journal,* vol. 44, no. 9, 2006.

[95] B. J. Tester, “The propagation and attenuation of sound in lined ducts containing uniform or "plug" flow,” *Journal of Sound and Vibration,* vol. 28, no. 2, p. 151–203, 1973.

[96] S. W. Rienstra, “A classification of duct modes based on surface waves,” *Wave Motion,* vol. 37, p. 119–135, 2003.

[97] E. J. Brambley and N. Peake, “Classification of aeroacoustically relevant surface modes in cylindrical lined ducts,” *Wave Motion,* vol. 43, p. 301–310, 2006.

[98] E. J. Brambley, “Fundamental problems with the model of uniform flow over acoustic linings,” *Journal of Soundand Vibration,* vol. 322, p. 1026–1037, 2009.

[99] E. J. Brambley, “A well-posed boundary condition for acoustic liners in straight ducts with flow,” *AIAA Journal,* vol. 49, no. 6, p. 1272–1282, 2011.

[100] S. W. Rienstra and M. Darau, “Boundary-layer thickness effects of the hydrodynamic instability along an impedance wall,” *Journal of Fluid Mechanics,* vol. 671, p. 559–573, 2011.

[101] G. Gabard, “A comparison of impedance boundary conditions for flow acoustics,” *Journal of Sound and Vibration,* vol. 332, p. 714–724, 2013.

[102] Y. Aurégan and M. Leroux, “Experimental evidence of an instability over an impedance wall in a duct with flow,” *Journal of Sound and Vibration,* vol. 317, p. 432–439, 2008.

[103] D. Marx, Y. Aurégan, H. Bailliet and J. -C. Valière, “PIV and LDV evidence of hydrodynamic instability over a liner in a duct with flow,” *Journal of Sound and Vibration,* vol. 329, p. 3798–3812, 2010.

[104] D. Marx, “A piecewise linear mean flow model for studying stability in a lined channel,” *Journal of Sound and Vibration,* vol. 331, p. 3809–3823, 2012.

[105] E. J. Brambley, “Surface modes in sheared boundary layers over impedance linings,” *Journal of Sound and Vibration,* vol. 332, p. 3750–3767, 2013.

[106] G. Gabard and E. J. Brambley, “A full discrete dispersion analysis of time-domain simulations of acoustic liners with flow,” *Journal of Computational Physics,* vol. 273, p. 310–326, 2014.

[107] C. K. Tam, H. Ju and E. W. Chien, “Scattering of acoustic duct modes by axial liner splices,” *Journal of Sound and Vibration,* vol. 310, p. 1014–1035, 2008.

[108] Y. Özyörük and L. N. Long, “Time-Domain Calculation of Sound Propagation in Lined Ducts with Sheared Flows,” *AIAA Journal,* vol. 38, no. 5, pp. 768-773, 2000.

[109] S. Zheng and M. Zhuang, “Verification and Validation of Time-Domain Impedance Boundary Condition in Lined Ducts,” *AIAA Journal,* vol. 43, no. 2, pp. 306-313, 2005.

[110] T. L. Parrott, W. R. Watson and M. G. Jones, “Experimental Validation of a

Two-Dimensional Shear Flow Model for Determining Acoustic Impedance," NASA Langley Research Center, Hampton, 1987.

[111] E. J. Brambley, "Viscous boundary layer effects on the Myers impedance boundary condition," in *15th AIAA/CEAS Aeroacoustics Conference*, Miami, 2009.

[112] Q. Zhang and D. J. Bodony, "Direct numerical simulation of three-dimensional honeycomb liners with turbulent boundary layer," in *18th AIAA/CEAS Aeroacoustics Conference*, Colorado Springs, 2012.

[113] C. K. Tam, N. N. Pastouchenko, M. G. Jones and W. R. Watson, "Experimental validation of numerical simulations for an acoustic liner in grazing flow: Self-noise and added drag," *Journal of Soundand Vibration,* vol. 333, p. 2831–2854, 2014.

[114] L. Sbardella, B. J. Tester and M. Imregun, "A time-domain method for the prediction of sound attenuation in lined ducts," *Journal of Sound and Vibration,* vol. 239, p. 379–396, 2001.

[115] L. di Mare, A. I. Sayma, J. Coupland and M. Imregun, "Acoustic Liner Models in a general purpose CFD Code," in *11th AIAA/CEAS Aeroacoustics Conference*, Monterey, 2005.

[116] K. W. Thompson, "Time Dependent Boundary Conditions for Hyperbolic Systems," *Journal of Computational Physics,* vol. 68, pp. 1-24, 1987.

[117] R. Hixon, "Radiation and Wall Boundary Conditions for Computational Aeroacoustics: A Review," *International Journal of Computational Fluid Dynamics,* vol. 18, no. 6, pp. 523-531, 2004.

[118] F. Q. Hu, "Absorbing Boundary Conditions," *International Journal of Computational Fluid Dynamics,* vol. 18, no. 6, pp. 513-522, 2004.

[119] T. Colonius, "Modeling artificial boundary conditions for compressible flow," *Annual Review of Fluid Mechanics,* vol. 36, p. 315–45, 2004.

[120] J. P. Berenger, "A perfectly matched layer for the absorption of electromagnetic waves," *Journal of Computational Physics,* vol. 114, p. 185–200, 1994.

[121] F. Q. Hu, "On Absorbing Boundary Conditions for Linearized Euler Equations by a Perfectly Matched Layer," *Journal of Computational*

Physics, vol. 129, p. 201–219, 1996.

[122] C. K. W. Tam, L. Auriault and F. Cambuli, “Perfectly Matched Layer as an Absorbing Boundary Condition for the Linearized Euler Equations in Open and Ducted Domains,” *Journal of Computational Physics,* vol. 144, p. 213–234, 1998.

[123] F. Q. Hu, “A Stable, Perfectly Matched Layer for Linearized Euler Equations in Unsplit Physical Variables,” *Journal of Computational Physics,* vol. 173, p. 455–480, 2001.

[124] F. Q. Hu, “A Perfectly Matched Layer absorbing boundary condition for linearized Euler equations with a non-uniform mean flow,” *Journal of Computational Physics,* vol. 208, p. 469–492, 2005.

[125] M. Israeli and S. A. Orszag, “Approximation of radiation boundary conditions,” *Journal of Computational Physics,* vol. 41, no. 1, pp. 15 - 135, 1981.

[126] S. K. Richards, X. Zhang, X. X. Chen and P. A. Nelson, “The evaluation of non-reflectingboundary conditions for duct acoustic computation,” *Journal of Sound and Vibration,* vol. 270, p. 539–557, 2004.

[127] C. P.-B. D., “Sound propagation in a fluid flowing through an attenuating duct,” *Journal of Fluid Mechanics,* vol. 4, pp. 393-406, 1958.

[128] O. C. Zienkiewicz, R. L. Taylor and J. Z. Zhu, The Finite Element Method: Its Basis and Fundamentals, Elsevier Butterworth-Heinemann, 6th Edition, 2005.

[129] E. F. Toro, Riemann solvers and numerical methods for fluid dynamics: a practical introduction (Third Edition), Berlin: Springer-Verlag, 2009.

[130] J. S. Hesthaven and T. Warburton, “Nodal High-Order Methods on Unstructured Grids. I. Time-Domain Solution of Maxwell’s Equations,” *Journal of Computational Physics,* vol. 181, p. 186–221, 2002.

[131] B. Cockburn, G. E. Karniadakis and C.-W. Shu , Discontinuous Galerkin Methods: Theory, Computation and Applications (Lecture Notes in Computational Science and Engineering), Springer , 2000.

[132] J.-F. Remacle, J. E. Flaherty and M. S. Shephard, “An Adaptive Discontinuous Galerkin Technique with an Orthogonal Basis Applied to

Compressible Flow Problems," *Society for Industrial and Applied Mathematics,* vol. 45, no. 1, p. 53–72, 2003.

[133] G. Gabard, "Wave-based Discontinuous Galerkin Methods for the Linearized Euler Equations in the Frequency Domain," in *13th AIAA/CEAS Aeroacoustics Conference*, Rome, 2007.

[134] J. Qiu, B. C. Khoo and C.-W. Shu, "A numerical study for the performance of the Runge–Kutta discontinuous Galerkin method based on different numerical fluxes," *Journal of Computational Physics,* vol. 212, p. 540–565, 2006.

[135] S. K. Godunov, "A difference method for numerical calculation of discontinuous solutions of the equations of hydrodynamics," *Mat. Sb. (N.S.),* vol. 47(89), no. 3, p. 271–306, 1959.

[136] J. S. Hesthaven and T. Warburton, Nodal Discontinuous Galerkin Method, Algoritms, Analysis and Applications, Springer, 2010.

[137] J. C. Butcher, Numerical methods for ordinary differential equations, John Wiley & Sons, 2003.

[138] F. Q. Hu, M. Y. Hussaini and J. L. Manthey, "Low-Dissipation and Low-Dispersion Runge–Kutta Schemes for Computational Acoustics," *Journal of Computational Physics,* vol. 124, p. 177–191, 1996.

[139] T. Toulorge and W. Desmet, "Optimal Runge.Kutta schemes for discontinuous Galerkin space discretizations applied to wave propagation problems," *Journal of Computational Physics,* vol. 231, p. 2067–2091, 2012.

[140] L. Liu, X. Li and F. Q. Hu, "Nonuniform time-step Runge–Kutta discontinuous Galerkin method for Computational Aeroacoustics," *Journal of Computational Physics,* vol. 229 , p. 6874–6897, 2010.

[141] B. Seny, J. Lambrechts, T. Toulorge, V. Legat and J. F. Remacle, "An efficient parallel implementation of explicit multirate Runge-Kutta schemes for discontinuous Galerkin computations," *Journal of Computational Physics,* vol. 256, p. 135–160, 2014.

[142] ANSYS FLUENT documentation (Release 14.0), Canonsburg: ANSYS, Inc., 2011.

[143] D. C. Wilcox, Turbulence Modeling for CFD, DCW Industries, 2006.

[144] “Python Programming Language – Official Website,” [Online]. Available: http://python.org/. [Accessed 27 2 2012].

[145] W. J. Chun, Core Python Programming, Second Edition, Prentice Hall, 2006.

[146] L. Piegl and W. Tiller, The NURBS book, 2nd edition, Berlin: Springer-Verlag, 1997.

[147] ANSYS ICEM CFD documentation (Release 14.0), Canonsburg: ANSYS, Inc., 2011.

[148] Tecplot - User’s Manual, Bellevue: Tecplot, Inc, 2013.

[149] J. D. Hunter, “Matplotlib: A 2D graphics environment,” *Computing In Science & Engineering,* vol. 9, no. 3, pp. 90-95, 26 03 2007.

[150] R. Munt, “The interaction of sound with a subsonic jet issuing from a semi-infinite cylindrical pipe,” *The Journal of Fluid Mechanics,* vol. 83, no. 4, pp. 609-640, 1977.

[151] D. G. Crighton, “The Kutta condition in unsteady flow,” *Annual Review of Fluid Mechanics,* vol. 17, pp. 411-45, 1985.

[152] B. Noble, Methods based on the Wiener-Hopf Technique, New York: Pergamon, 1958.

[153] G. Gabard and R. Astley, “Theoretical model for sound radiation from annular jet pipes: far- and near-field solutions,” *Journal of Fluid Mechanics,* vol. 549, pp. 315-341, 2006.

[154] R. J. Astley, I. Achunche and R. Sugimoto, “Validation of CAA prediction of noise radiated from turbofan intakes,” in *16th International Congress on Sound and Vibration*, Krakow, 2009.

[155] I. Achunche, J. Astley and R. Sugimoto, “Prediction of Forward Fan Noise Propagation and Radiation from Intakes,” in *15th AIAA/CEAS Aeroacoustics Conference (30th AIAA Aeroacoustics Conference)*, Miami, Florida, 2009.

[156] P. G. Drazin and W. H. Reid, Hydrodynamic Stability, Cambridge: Cambridge University Press, 1981.

[157] B. J. Tester, G. Gabard and Y. Özyörük, “Influence of mean flow gradients on fan exhaust noise predictions,” in *14th AIAA/CEAS Aeroacoustics Conference*, Vancouver, 2008.

[158] L. Lapworth, “Hydra-CFD: A Framework for Collaborative CFD Development,” in *International Conference on Scientific and Engineering Computation (IC-SEC)*, Singapore, 2004.

[159] N. C. Ovenden and S. W. Rienstra, “Mode-Matching Strategies in Slowly Varying Engine Ducts,” *AIAA Journal,* vol. 42, no. 9, pp. 1832-1840, 2004.

[160] C. . L. Morfey and M. J. Fisher, “Shock-wave radiation from a supersonic ducted rotor,” *The Aeronautical Journal of the Royal Aeronautical Society,* vol. 74, pp. 579-585, 1970.

[161] M. J. Fisher, B. J. Tester and P. J. Schwaller, “Supersonic fan tone noise prediction,” in *AIAA 98-2249*, 1998.

[162] A. McAlpine and M. J. Fisher, “On the prediction of "Buzz-saw" noise in aero-engine inlet ducts,” *Journal of Sound and Vibration,* vol. 248, no. 1, p. 123–149, 2001.

[163] A. McAlpine and M. J. Fisher, “On the prediction of "buzz-saw" noise in acoustically lined aero-engine inlet ducts,” *Journal of Sound and Vibration,* vol. 265, p. 175–200, 2003.

[164] P. R. Spalart and S. R. Allmaras, “A one-equation turbulence model aerodynamic flows,” in *AIAA 30th Aerospace Sciences Meeting and Exhibit*, Reno, 1992.

[165] S. Shahpar and L. Lapworth, “PADRAM: Parametric Design an Rapid Meshing System for Turbomachinery Optimisation,” in *ASME Turbo Expo*, Atlanta, 2003.

[166] P. Moinier, J. D. Muller and M. B. Giles, “Edge-based Multigrid Schemes and Preconditioning for Hybrid Grids,” *AIAA Journal,* vol. 40, no. 10, pp. 1954-1960, 2002.

[167] D. Mueller, H.-J. Schulz, G. Zitouni and W. Baumann, “Europe's Largest Aero Acoustic Test Facility for Aero Engine Fans - The Development and Operation of the AneCom AeroTest Anechoic Chamber,” in *11th AIAA/CEAS Aeroacoustics Conference*, Monterey, 2005.

[168] "X-noise," [Online]. Available: http://www.xnoise.eu/index.php?id=387. [Accessed 11 02 2014].

[169] A. H. Nayfeh and D. P. Telionis, "Acoustic propagation in ducts with varying cross-sections," *Journal of the Acoustical Society of America,* vol. 54, no. 6, pp. 1654-1661, 1973.

[170] S. W. Rienstra, "Sound transmission in slowly varying circular and annular lined ducts with flow," *Journal of Fluid Mechanics,* vol. 380, p. 279–296, 1999.

[171] S. W. Rienstra, "Sound propagation in slowly varying lined flow ducts of arbitrary cross-section," *Journal of Fluid Mechanics,* vol. 495, pp. 157-173, 2003.

[172] S. Felix and V. Pagneux, "Mulitmodal analysis of acoustic propagation in three-dimensional bends," *Wave Motion,* vol. 36, p. 157–168, 2002.

[173] S. Felix and V. Pagneux, "Sound attenuation in lined bends," *Journal of the Acoustical Society of America,* vol. 116, p. 1921–1931, 2004.

[174] E. J. Brambley and N. Peake, "Sound transmission in strongly curved slowly varying cylindrical ducts with flow," *Journal of Fluid Mechanics,* vol. 596, pp. 387-412, 2008.

[175] A. McAlpine, A. Daymond-King and A. Kempton, "Sound radiation from a flanged inclined duct," *Journal of the Acoustical Society of America,* vol. 132, no. 6, pp. 3637-3646, 2012.

[176] J. A. Hamilton and R. J. Astley, "Acoustic Propagation on Irrotational Mean Flows Using Transient Finite and Infinite Elements," *AIAA Journal,* vol. 43, no. 1, pp. 124-134, 2005.

[177] P. G. J. Schwaller, N. J. Baker, J. D. Tomlinson, P. Sijtsma and R. Hemmings, "Noise Validation of Model Fan Rig with Engine," in *12th AIAA/CEAS Aeroacoustics Conference*, Cambridge, 2006.

[178] C. L. Morfey, "Acoustic energy in non-uniform flows," *Journal of Sound and Vibration,* vol. 14, no. 2, p. 159–170, 1971.

[179] F. Nataf , "A new approach to perfectly matched layers for the linearized Euler system," *Journal of Computational Physics,* vol. 214, p. 757–772, 2006.

[180] S. A. Parrish and F. Q. Hu, “Application of PML absorbing boundary condition to aeroacoustic problems with an oblique mean flow,” in *13th AIAA/CEAS Aeroacoustics Conference*, Rome, 2007.

[181] T. Toulorge and W. Desmet, “Curved Boundary Treatments for the Discontinuous Galerkin Method Applied to Aeroacoustic Propagation,” in *15th AIAA/CEAS Aeroacoustics Conference*, Miami, 2009.

[182] M. Siebenborn, V. Schulz and S. Schmidt, “A curved-element unstructured discontinuous Galerkin method on GPUs for the Euler equations,” Cornell University library, 14 01 2013. [Online]. Available: http://arxiv.org/abs/1208.4772. [Accessed 28 05 2013].

[183] I. Babuska and B. Q. Guo, “The h, p and h-p version of the finite element method; basis theory and applications,” *Advances in Engineering Software,* vol. 15, pp. 159-174, 1992.